ELECTRONIC RECOLLISIONS IN A STRONG LASER FIELD

A Thesis
Presented to
The Academic Faculty

by

Adam J. Kamor

In Partial Fulfillment
of the Requirements for the Degree
Doctor of Philosophy in the
School of Physics

Georgia Institute of Technology
December 2013

ELECTRONIC RECOLLISIONS IN A STRONG LASER FIELD

Approved by:

Professor Turgay Uzer, Advisor
School of Physics
Georgia Institute of Technology

Professor Markus Kindermann
School of Physics
Georgia Institute of Technology

Dr. Cristel Chandre
CNRS
Centre de Physique Theorique, Marseille, France

Professor Michael Shatz
School of Physics
Georgia Institute of Technology

Dr. Claire Berger
CNRS
Institut Neel, Grenoble, France

Professor Predrag Cvitanovic
School of Physics
Georgia Institute of Technology

Date Approved: 1 November 2013

To my wife,

Elisabeth

ACKNOWLEDGEMENTS

First, I would like to thank my committee members and thesis readers, whose comments and careful considerations have helped shape this thesis. They have gone above and beyond in providing insights and drawing on past experience to help make the contents more clear and concise to potential readers.

Second, I must mention the staff at both my home institution, Georgia Tech, and also my french institution Aix-Marseille University. The constant support from the finance, IT, and maintenace departments at both institutions has assisted me greatly in performing research.

Thirdly, I would like to extend my most sincere gratitude to my two advisors, without whom I would not be writing this thesis. Professor Turgay Uzer (Georgia Tech) and Dr. Cristel Chandre (CNRS) have helped me grow as a scientist, presenter, and writer. Without their patient and careful instruction I would not have been able to perform this research, and indeed, without their personalities and support I most likely would not have finished the PhD program. While not an advisor, I must also mention a fellow graduate student/friend, Francois Mauger. His instruction, especially at the beginning of my thesis, was an important component in my development as a graduate student. Also, without him, my trips to Marseille, France would have been a good deal less fun.

Finally, I would like to thank my family. Specificaly my parents, whose nurturing and support for the past twenty six years have helped shape who I am as a person. Also, my wife, Elisabeth, whose constant support as I pursued this research has been a much needed boost.

TABLE OF CONTENTS

LIST OF TABLES

LIST OF FIGURES

SUMMARY

Unusual and challenging ionization processes take place when an atom or molecule is placed in the presence of a super intense, ultra short laser field. One such process is the ionization and subsequent return of an electron to the ionic core. The electron carries with it the energy it has absorbed from the laser field and this energy drives different atomic phenomena such as high harmonic generation or multiple ionization. The mechanism of the electron return is often referred to as the "three-step" model. In this model, an electron is first ionized at the peak amplitude of the laser field. Once ionized, a change in the direction of the laser field forces the electron to return to the parent ion and causes a subsequent recollision. The purpose of this thesis is to examine in great detail the recollision process, its mechanisms, and its dependence on physical parameters (such as laser intensity and ellipticity) for a number of physically interesting scenarios.

CHAPTER I

INTRODUCTION

1.1 A primer on double ionization

An important area in atomic and molecular physics is the probing of matter at the electronic scale. For example, a chemical bond is simply the sharing of the electronic density between two atoms. To better understand this sharing, theoretical predictions are possible, i.e. based on electronegativity, or the covalent or ionic nature of the bond. However, from the experimental point of view, a direct probing of this density is also desirable. Probing, for example, the large scale structure of a crystal or network solid, is possible with different types of electron microscopes. However, at the electronic level (both spatially and temporally) these methods fail. Other techniques, still in their infancy, are being developed to observe matter directly at this (currently) shortest possible time scale. Atto-second ($= 10^{-18}$ seconds) physics, at the interface of atomic, molecular, and laser physics holds great promise in this regard.

In brief, experimentalists can use very strong (on the order of 10^{15} watts per centimeter squared) laser pulses to ionize atoms and molecules, giving access to their structure. While laser pulses are of femto-second duration [13], sub-femto second pulses are also available under suitable circumstances [5]. These sub-femtosecond (attosecond) pulses are generated when ionized electrons "recollide" with their parent ion/molecule, causing a release of radiation. This radiation can be harnessed to generate pulses of atto-second duration. Atto-second pulse generation, which gives access to electron dynamics on their natural timescale, relies entirely on the release of radiation due to the recollision of the electron with its parent ion or molecule. An example of a typical radiation spectrum is shown in figure 1. In this figure a

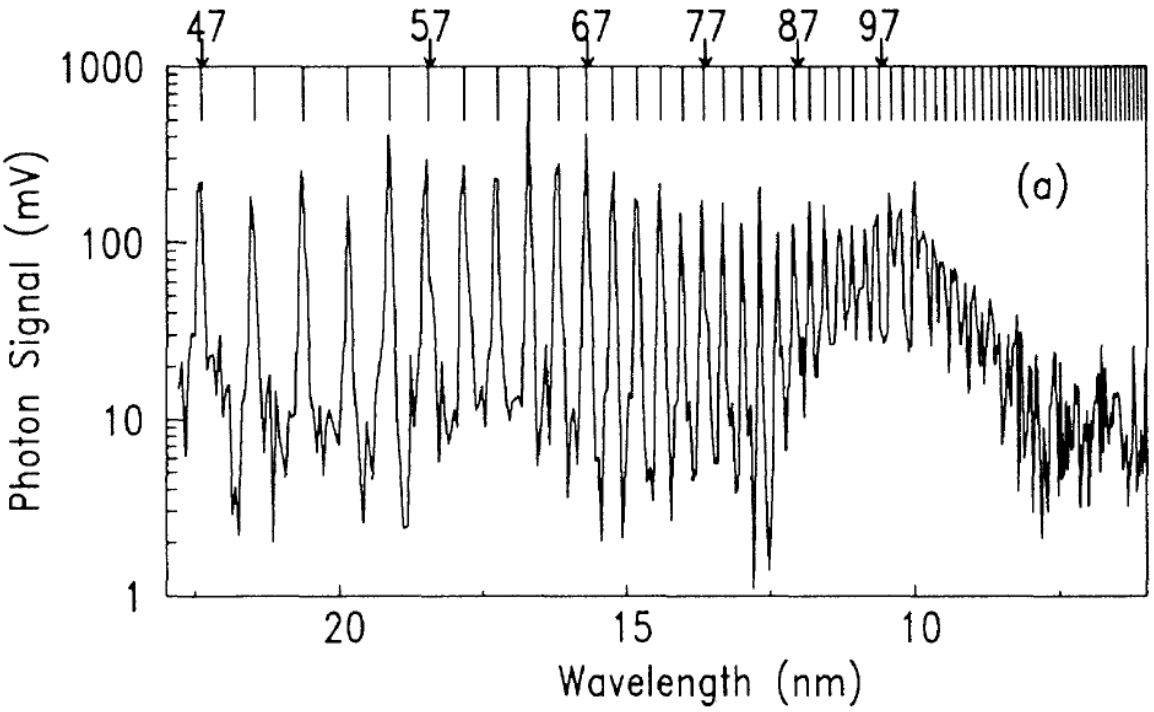

Figure 1: Reproduced from [2]. High harmonic generation spectra of Neon at $I = 10^{15}$ W $\cdot$ cm^{-2}.

plateau in the photon signal (radiative energy) is visible until approximately 11 nm, after which a drop-off in intensity quickly occurs. The plateau with an accompanying sudden drop-off is typical of high harmonic generation radiation spectra, which will be discussed later. A major point of Ch. 3 is explaining this drop-off in terms of a purely classical model.

This thesis, which focuses mainly on the recollision dynamics of atoms and electrons exposed to intense laser pulses, will first give some background and insights to the reader, in order to provide some additional historical and practical context into the recollision process. In the early nineties experiments showed the laser intensity dependence of the ionization of atoms in strong laser fields [3]. In figure 2, we see the single and double ionization probabilities of Helium as a function of the laser intensity. The experimental results for double ionization (DI) match closely the theoretical predictions (solid line) in the high intensity regime (around 4×10^{15} W $\cdot$ cm^{-2}). The theoretical prediction is based on the single active electron model (SAE) where the

effect of the second electron is averaged into the shielding from the core that the active electron experiences. Intuitively this makes sense. When the laser is sufficiently strong the independent ionization of the electrons is possible. Of course, once the first electron is ionized, it is indeed harder to ionize the second electron, however, with a strong laser this is feasible. At low intensity (around 4×10^{14} W $\cdot$ cm^{-2} for this experiment) single ionization (SI) is likely, however, the double ionization rate, while lower than at higher intensity, is still many orders of magnitude above the theoretically predicted value. This route to DI at low intensity, is actually dependent on the interaction of the two electrons, which explains the failure of the theoretical model. The DI process can be expressed more schematically as well. Calling our target species $\mathcal{X}$, we represent the independent double ionization of the electrons as the two step process:

$$\begin{aligned} \mathcal{X} &\rightarrow \mathcal{X}^{+} + e^{-} \\ \mathcal{X}^{+} &\rightarrow \mathcal{X}^{2+} + e^{-}. \end{aligned}$$

This process is often referred to as sequential double ionization (SDI) in the literature, and it is this name which will be used in this manuscript. Likewise, the alternative route to double ionization, which occurs at lower intensity, can be expressed as

$$\mathcal{X} \rightarrow \mathcal{X}^{2+} + 2e^{-},$$

which in the literature is referred to as non-sequential double ionization (NSDI). A third option, known as recombination, is also possibile. In this situation a double ionization event does not occur because the ionized electron returns to the core with insufficient energy so that it is re-captured by the Coulomb field. In this situation energy is released via radiation in the form of high harmonics of the laser field. The amount of energy released depends on which energy level the newly captured electron is placed, but often recombination to the ground state is assumed.

It is the second route, NSDI, which is the primary focus here. This process, which will shortly be shown to be intimately linked to electronic recollision, is one of nature's strongest manifestations of electron correlation.

1.1.1 Focusing on NSDI

The NSDI process is often characterized by the frequently cited "three-step scenario" [6] or simply the "rescattering model" [14, 15]. This model has been of great importance to the strong field physics community and has been referred to as "the keystone of strong-field physics" [13]. A schematic of the mechanism is shown below, in figure 3. The mechanism itself can be broken into three steps.

1. One of the electrons (henceforth labelled as the "outer" electron) ionizes at a maximum of the laser field via tunnelling with an initial momentum of $p_0 = 0$ (panel 1) and moves into the unbound space (panel 2).

2. As the laser field changes direction the outer electron, whose motion is dictated almost entirely by the laser field, moves toward the ion (panel 3).

3. The electron, which has gained energy from the laser field, can initiate several different atomic phenomena such as the ionization of additional electrons, recombination – resulting in the release of radiation (HHG), fragmentation, or the excitation of vibrational and rotational modes in molecules.

This model, while overly simple, has been accurate in making experimental predictions, such as the maximum energy an ionized electron can bring back to the core. Recall this is related to the cut-off in the HHG spectra of fig. 1. The model makes several stringent assumptions. In the first step, when the electron ionizes, it is assumed that it does so by tunneling through the Coulomb barrier (perturbed by the laser field). Upon exiting the barrier its momentum must be zero. Up to now, there is no conclusive experimental confirmation that tunneling takes place, and therefore the

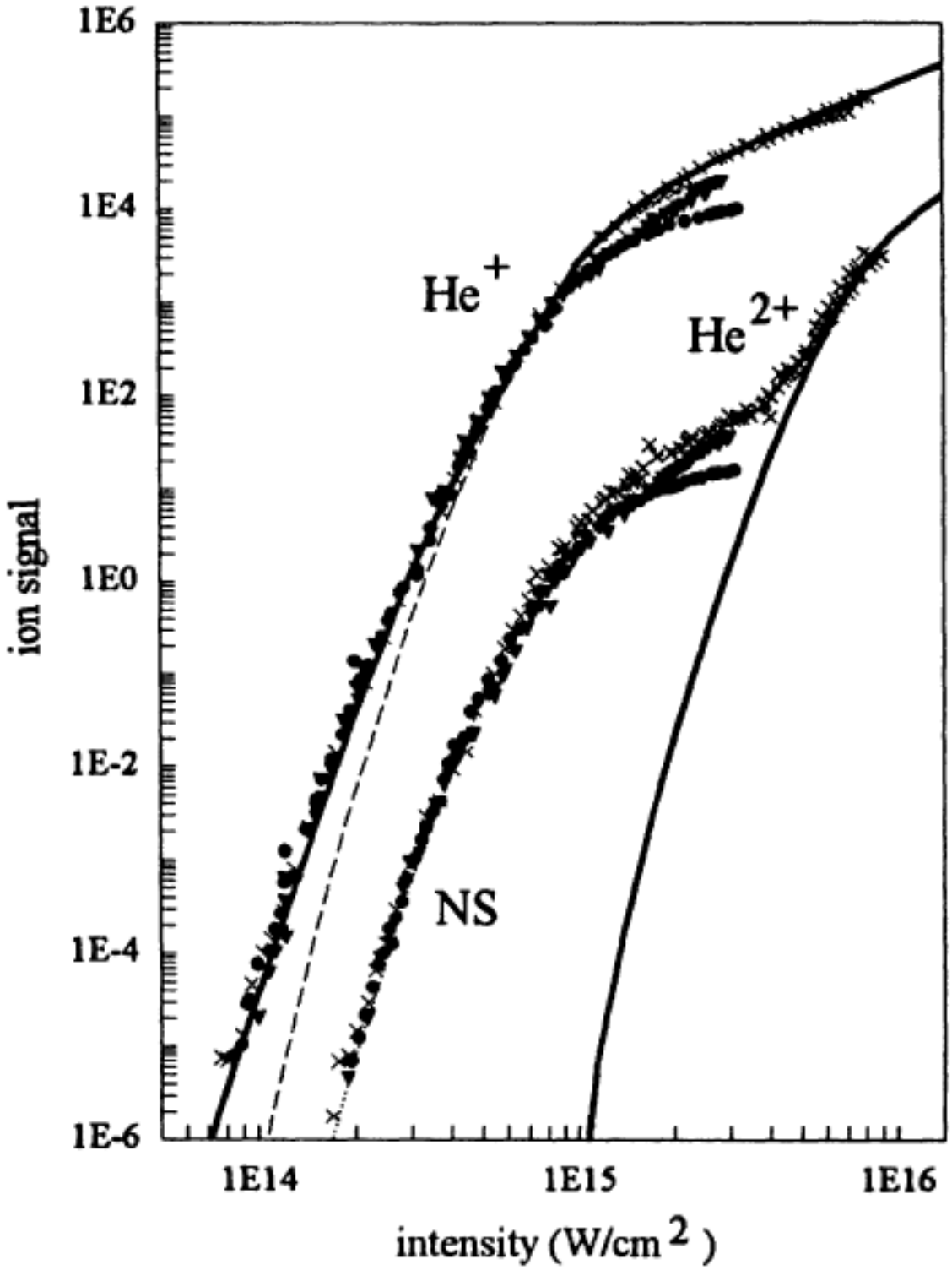

Figure 2: Reproduced from [3]. Single and double ionization probabilities of Helium. The pulse is linearly polarized and 100 femto-seconds long. The wavelength is taken to be 780 nm. The solid curve is a theoretical prediction for the sequential double ionization rate.

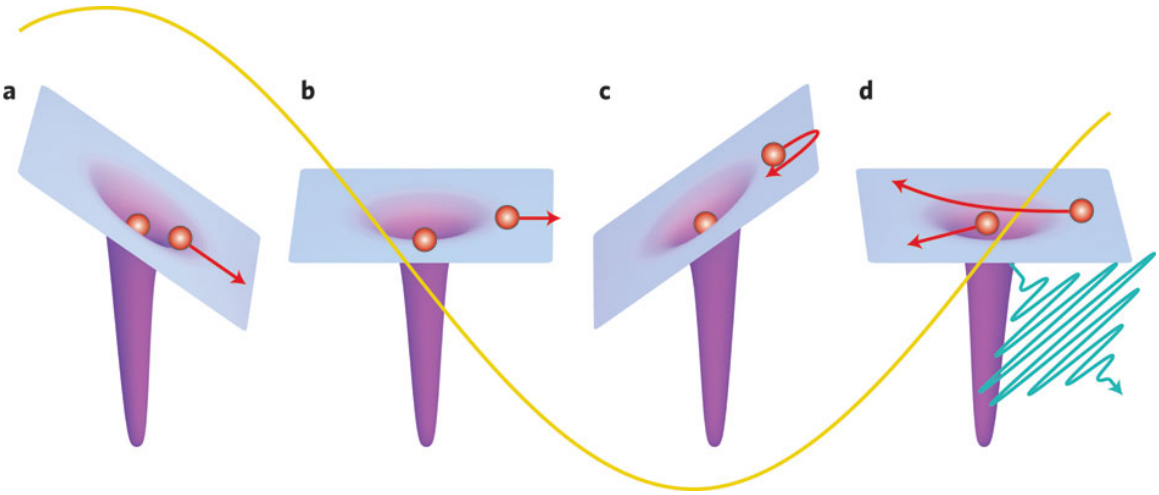

Figure 3: Reproduced from [4]. An optical pulse interacts with the Coulomb interaction of the electron with the core.

assumption that $p_0 = 0$ has no experimental basis. Finally, once ionized, the Coulomb field is entirely neglected. The motions of the electron are dictated entirely by the laser field. This assumption is debatable. In fact, at typical laser intensities the laser field and Coulomb field are of the same order of magnitude at peak field amplitude nearby the maximum of the combined potential. In Ch. 3 we introduce corrections to this "three-step scenario" which allows for an internally consistent model which is purely classical.

Multi-electron ionization and HHG are two common outcomes of an electronic recollision. In multi-electron ionization, a double ionization probability curve (such as the one shown in figure 2), will exhibit what is referred to as a "knee" shape in the NSDI regime. This "knee" shape is considered to be "the principal signature of NSDI" [16]. A recollision of an electron, followed by a recombination with the core leads to HHG. This radiation can be harnessed in useful ways, such as the design of new light sources in the atto-second pulse regime [17]. A schematic of HHG is shown in figure 4.

This process, ionization and then a subsequent return makes intuitive sense for a sinusoidally shaped, linearly polarized laser field. The motion of an already ionized

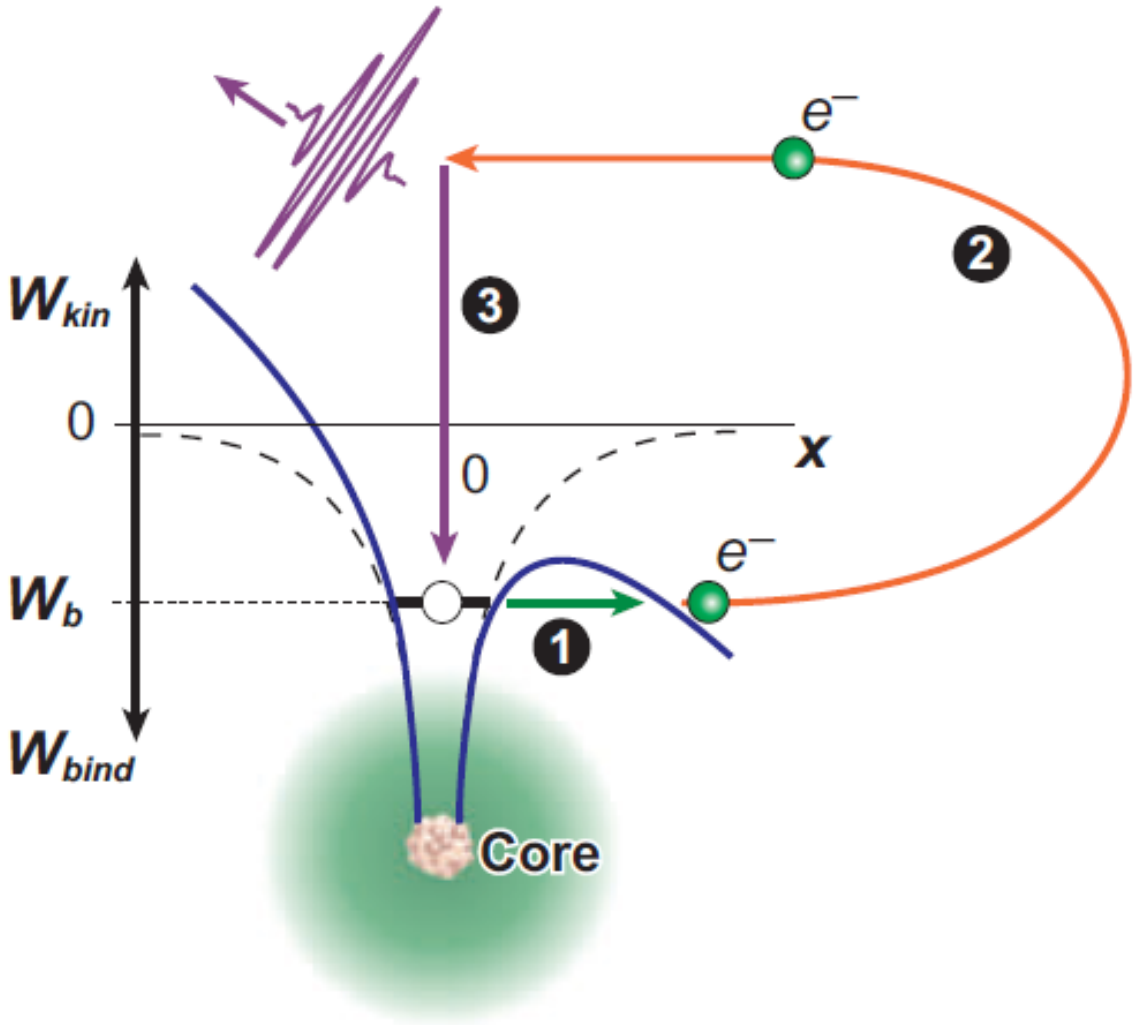

Figure 4: Reproduced from [5]. A schematic of Corkum's three-step scenario [6]. (1) Electron ionizes. (2) Electron returns to the core. (3) Electron recombines with the core, releasing high harmonics. This process is known as high harmonic generation (HHG).

electron takes place primarily along the polarization axis, which gives a strong spatial preference for a recollision to occur. However, the light polarization is often used by experimentalists as a control knob with which one can fine tune various physical processes. Therefore the effects of the laser ellipticity must be investigated as well.

1.1.1.1 The difference ellipticity makes

Thinking of the laser ellipticity as a continuously variable parameter, it has two extremes. The first, which has already been mentioned, is linear polarization (LP). On the other extreme is circular polarization (CP) where as a function of time the laser field (whose magnitude remains constant) traces out a circle in the polarization plane. Historically, it has been thought that recollisions in a CP field are not possible due to the apparent lack of preference for the inward radial direction (which pulls the already ionized electron back to the core). Instead, the electron moves away from the core in a spiraling motion. This notion was supported by experimental results performed in the early nineties such as the one highlighted in the left panel of figure 5. We see that there is strong agreement between the experimental results (triangles) and the theoretical prediction (which assumes the independence of the two electrons), unlike the case for LP (see figure 2), which implies that nowhere is electron-electron correlation (i.e. a recollision) significant. However, since then conflicting experimental results have appeared which do show a NSDI channel in double ionization rates, as evidenced by the "knee". As an example, the right panel of figure 5 shows a strong DI enhancement at low intensity, which is indicative of the existence of NSDI. From a historical point of view, the same panel is interesting as well. The view that CP fields would prevent recollisions (and hence NSDI) was such a firmly held belief that when these results were first published many in the community were surprised. The views of the community at this time (and to a lesser extent in the present day) are well described by the following quotes:

> "If the polarization is circular, then as soon as any portion of the wavepacket emerges from the atom or molecule, it gets pulled by the field in constantly changing directions —first away from the ion, then laterally, and so on. The cusplike motion ensures that the wavepacket never returns to the ion of its birth." [18]

and

> "...only a slight ellipticity of the laser polarization [away from LP] will ensure that the electron never returns to the environment of the ion" [6]

To give some weight to these quotes, and the feelings of the community at large the first quote can be found in a review of recollision physics from Physics Today, 2011. The second quote, which is contained in the same article as the "three step scenario", discussed earlier, has been cited slightly over 2,100 times.

The consensus that recollisions do not exist in a CP field is due mainly to a popular, gross simplification of the system. There is no exact solution to the dynamics of an electron moving in a combined laser and Coulomb field despite intensive efforts to find one starting with Volkov in the thirties. However, the dynamics can be solved exactly when one leaves out the Coulomb field. This omission of the Coulomb field, known as the "Simple-man model" [6], is assumed true in a wide range of situations, and does not support recollisions in CP. However, we will show in chapter 3 that indeed, this simplification is not valid and when a Coulomb field is included recollisions in CP are possible.

This idea, that CP fields do not support recollisions, was a main focus of research during the thesis, and in some of the following chapters the effects of the laser ellipticity will be explained using simple, predictive models which directly contradict the above quotes.

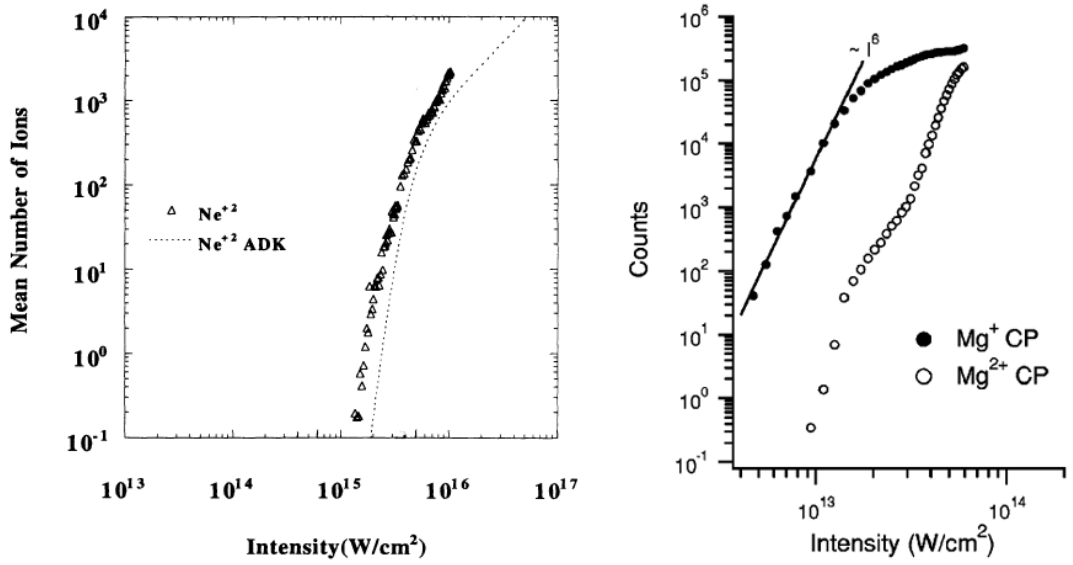

Figure 5: Left panel: Reproduced from [7]. Experimental double ionization curves for Neon (triangles) with a circularly polarized laser. The wavelength is taken as 614 nm and the pulse length is 120 femto seconds. A sequential theoretical model is shown by the dashed line. Right panel: Reproduced from [8]. Double ionization curves for Magnesium with a circularly polarized laser. The laser wavelength is taken as 800 nm and the pulse length is 120 femto seconds.

1.1.2 Numbers of the field

To get a sense of the popularity of the field, in figure 6 we show the total number of citations per year for articles related to "strong field recollision" (left panel) and "nonsequential double ionization" (right panel). We see that since 1992 the number of citations per year has experienced strong growth, up to the most recent year for which statistics are available. In addition to a growing number of citations, "recollision" based papers enjoy on average 24 citations per publication while "NSDI" based papers experience 30 citations per publication on average.

1.2 Thesis work

This thesis work, performed from the summer of 2009 to the fall of 2013, took place primarily at the Georgia Institute of Technology with lengthy excursions to Marseille, France from February 1 to March 1 of 2011, February 1 to August 1 of 2012, and May

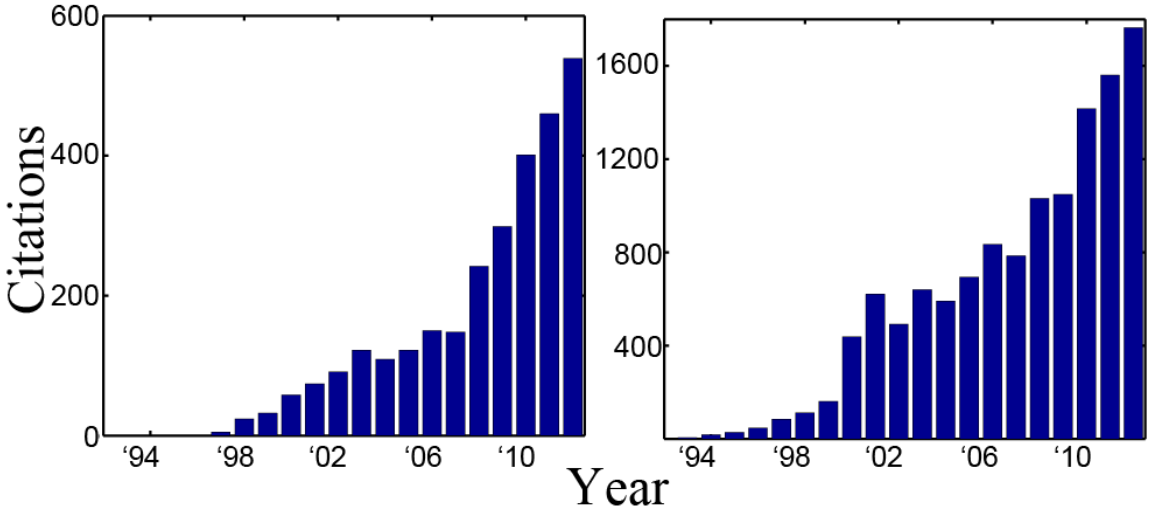

Figure 6: Citations as a function of the year for papers related to "strong field recollisions" (left panel) and "nonsequential double ionization" (right panel). Data retreived from Web of Science.

1 to July 1 of 2013. In addition, the results were shown at several conferences such as Montreal (QDI Conference, 2009), Paris (RNL, 2012), Tokyo (ATTO-ICOMP, 2011), and Atlanta, Ga. (DAMOP, 2011).

My long stays in France were mainly funded through the Chateaubriand Fellowship, a grant from the Office of Science and Technology of the French Embassy which encourages scientific collaboration between American and French laboraties. In addition to long visits, I am also a graduating with a PhD diploma from Aix-Marseille University (my French institution) thanks to a Co-tutelle agreement between Aix-Marseille University and the Georgia Institute of Technology. While in Marseille, I worked at the Centre de Physique Théorique (CPT), a laboratory of approximately 100 theoretical physicists located in Luminy, a suburb of Marseille.

This thesis primarily focuses on the recollision process in atoms and molecules. A recolliding electron can be considered an agent of many different physical processes. It could lead to the multiple ionization (double, triple, etc.) of some target species. When multiple ionization does not occur, i.e. the ionized electron is re-captured by the ion, radiation is released which can be harnessed by the experimentalist for a

plethora of purposes, such as high harmonic generation (HHG), different color lasers, and obtaining atto-second pulse trains. Therefore, to have a better understanding of how recollision is affected by experimental parameters, e.g. target species, laser polarization, wavelength, and intensity, is of great importance to the experimentalist.

1.2.1 Models

Rydberg atoms are a prime example in atomic physics of a classically-treatable system. The justification lies in the fact that the electron is loosely bound, existing in a state with a large quantum number. With such a large quantum number the difference between energy levels is small and the discretization which occurs in quantum mechanical systems approaches a continuum which can be represented classically. Of course in our systems, the electron is generally not loosely bound (initially our modelled electrons begin on the ground state), and the analogy to Rydberg states is not valid. However, the main electronic processes of interest to us are those involving electron-electron collision, or scattering. We therefore take the view of Paul Corkum, a leading figure in the strong field physics community —the electrons can be treated as classical plasmas [6]. Recall that for the laser intensities associated with NSDI, i.e. intensities present in this thesis, the electronic energy is large compared to the photon energy and we are dealing with "mainly electron physics rather than atomic physics" [16].

Howevever, what happens before ionization? Initially, the electron(s) begin in a bounded state of the atom. In this situation the quantum energy levels are far apart and the discretization is pronounced. We choose a micro-canonical ensemble of initial conditions, and generally do not focus on single electron trajectories. In fact, the questions we address in this thesis have to do with already ionized electrons, and what happens before ionization is often not interesting. However, of important note is the actual act of ionization. When originally conceived, the "three step scenario"

assumed an electron would tunnel through the Coulomb barrier and emerge with zero momentum on the other side. Of course classically tunneling is not possible, however, we consider tunneling to be an inessential assumption for the processess we are interested in. We evolve our electron trajectories classically from an ensemble of initial conditions, and do not enforce any constraints on the dynamics (such as zero initial momentum after ionization).

In addition to physical justifications for a classical treatment there are practical considerations as well. The most potent of which is the numerically intractability of the quantum mechanical system. To quote a review article in Contemporary Physics

> "...ab initio methods will remain confined to double ionisation of helium. Non-sequential triple and higher ionisation of heavier atoms as well as NSDI with account of more than two active electrons will be out of reach to such methods for a long time to come." [13]

As an example, below is a model for a single electron in the presence of a LP field.

$$\hat{H} = \frac{\hat{p}}{2} + E_0 \hat{x} \sin \omega t \tag{1}$$

$\hat{x}$ and $\hat{p}$ are the quantum position and momentum operators. The laser field is parameterized by its amplitude, E_0 and its wavelength ω. The interaction of the laser field with the electron is taken in the dipole approximation. The oscillatory motion of the electron is characterized by its quiver radius, which is the amplitude of the electronic motion. In this case, the quiver radius goes as E_0/ω^2. Likewise, the momentum, which also oscillates, scales as E_0/ω. Therefore, a quantum simulation must have on the order of $N \propto E_0/\omega^2 \cdot E_0/\omega = E_0^2/\omega^3$ points. If we would like to model multiple electrons, or work in more than a single spatial dimension the number of points, N will scale exponentially with the product of both aforementioned factors. The final scaling law can be written as

$$N \propto \left(\frac{E_0^2}{\omega^3}\right)^{(\text{\# of electrons} \quad \times \quad \text{\# of spatial dimensions})}.$$

Conversely, in a classical model, the system is described by a set of ordinary differential equations (derived from Hamilton's equations). The laser parameters E_0 and ω do not affect significantly the numerical complexity, and most important, computation time scales linearly with both the number of spatial dimensions and the number of electrons. While quantum computations (those that can be accomplished) often take place in large, massively parallelized computing facilities, the classical counterpart can be computed on a regular desktop PC.

The validity of our justifications given above is shown in the success of the classical models, measured by the ability of simple, classical models to closely re-create experimental results and fully quantum computations. In reference to the above quote, which states the needs of fully quantum calculations in the context of current computing power, the authors have this to say about the ability of full classical models:

> "It turns out that sufficiently high above the threshold, that is, for sufficiently high laser intensity, the classical and the quantum-mechanical results are virtually indistinguishable." [13]

A middle ground, between a fully quantum or classical treatment of the problem also exist [19]. These are semi-classical models, which assume tunnel ionization of the outer electron, but then allow for a classical dynamics to take effect afterwards.

The justifications given above for our choice of a classical framework should not be too much of a surprise. Studying ionized electrons (and their subsequent recollisions) is similar in some way to the study of Ryderg atoms (atoms in which the electron is loosely bound), which may be treated classically [20]. In addition, there is a strong

similarity between celestial mechanics and atomic physics (at least this specific subfield), due to the identical nature of the gravitational and Coulomb potentials. In fact, this similarity has been exploited for almost an entire century, beginning with the Bohr model of the atom. It is also used in the current day. For example, the theory of chemical reaction rates, or Transition State Theory, can be modelled in a way very similar to asteroid capture [21, 22, 23]. Another example is that of the Restricted Three Body Problem (RTBP, Sun-Jupiter-Asteroid), which can be used to study electron dynamics of multi-electron of Rydberg atoms. We hope to further make use of the aforementioned similarities in our specific research, electron recollision dynamics.

The work in this manuscript is performed entirely in a Hamiltonian framework and we make use of tools from nonlinear dynamics to gain insights into our systems. Our Hamiltonians are derived from models developed in the next chapter. In a Hamiltonian framework the state of the system is given by its position in phase space, where the (conjugate) momenta are given equal importance to spatial position of the electron. This means that the dimensionality of the system is doubled because each position has a corresponding momentum. Various methods will be used to reduce the dimension of phase space, such as the use of conserved quantities, Poincaré sections, and reduced models.

Our main methodology is as follows:

1. **Identify, construct, and analyze reduced models.**

   Reduced models, which will be covered in great detail in the next chapter, have the benefit of being low-dimensional. They are constructed from a detailed analysis of the dynamics of a full model. As a quick example, imagine a two electron system in which one of the electrons has ionized. The ionized electron, far from the ionic core (and the non-ionized electron), is truly only influenced by the laser field. In this situation a reduced model can be built which neglects the

Coulomb interaction of both the non-ionized electron and the nucleus. This new Hamiltonian would be of lower dimensionality (since the position and momenta of the non-ionized electron are absent).

2. **Identify and analyze invariant structures of the system**

   Our method is to study the collective behavior of an ensemble of trajectories rather than individual ones. For this purpose we use all the tools of modern nonlinear dynamics, invariant structures being a prominent example [24]. Invariant structures exist in phase space and are left invariant (unchanged) by the dynamics. In this thesis, fixed points, periodic orbits, tori, and manifolds will all be discussed and investigated. These invariant objects give a skeleton which the dynamics follow [24]. The analysis can be broken down into several parts. First, the structure, whatever it is, must be found. This typically comes down to finding periodic orbits in phase space with the Newton-Raphson algorithm. Next, the properties of the structure must be found, i.e. is it stable or unstable? Finally, we ascertain its effect on the dynamics both for a qualitative analysis of the dynamics and an examination of the properties of the structure.

   Of paramount importance (as will be shown in the following chapters) are periodic orbits, which are given the special name of *recolliding periodic orbits* or RPOs [25]. These are orbits which regulate the electronic recollision process. They do so by having a short period, are not too unstable, and have a spatial extent which allows for the electron to move sufficiently far away from the core to ionize, before being brought close to the core again.

3. **Impact on experimental observables**

   With an understanding of the dynamics, via an analysis of the invariant structures we want to understand their effect on the system. Most importantly, the role of periodic orbits (and other structures) in double ionization rates, HHG

spectra, momentum distributions, and other experimental observables.

1.2.2 Numerical tools

With classical models, the physical system is represented by a system of ordinary differential equations. Often times, when a statistical analysis must be performed, it may be necessary to integrate on the order of 10^6 different initial conditions. Several different numerical integration schemes have been used throughout this thesis. Additionally, these various integration schemes have been implemented on a variety of devices. Table 1 shows the different possible combinations of algorithm used (including the programming language) and the hardware on which the algorithm was implemented. The top row corresponds to the different algorithms where "RK" stands for a Runge-Kutta 4th order integration scheme, which in Matlab is implemented via ODE45, while in C++ it was developed by myself. Likewise, "Symp" corresponds to a symplectic integrator, again implemented by myself, which was adapted from the literature [26]. Symplectic integrators are useful for Hamiltonian systems because they are designed such that the symplectic two-form $dq \wedge dp$ is conserved at each time step, i.e. that the transformation from $(\mathbf{q}_0, \mathbf{p}_0) \rightarrow (\mathbf{q}_1, \mathbf{p}_1)$ is canonical. Therefore, symplectic integrators are particularly well suited to long integration times when other schemes would lead to an unacceptable amount of energy dissipation. In the leftmost column, "GPU" stands for graphics processing unit, which is the hardware device responsible for graphical acceleration. We made use of both an NVIDIA GeForce GTX 660 Ti and a NVIDIA Geforce GTX Titan. It is generally a many-cored, highly parallelized device well suited for numerical computations. It can be programmed in almost standard C via a set of library functions, e.g. OpenCL (AMD and ATI) and CUDA (nVidia). The "Desktop" entry is a standard Intel Core i5 machine with 8 GB of RAM, while the "Cluster" entry is a shared, high performance computing

Table 1: Combination of numerical integration algorithms and hardware platforms used

	C++/RK	C++/Symp	Matlab/RK	Matlab/Symp
GPU	X	X		
Desktop			X	X
Cluster	X	X	X	X

center available to members of the Center of Nonlinear Science, through the Partnership for an Advanced Computing Environment (PACE) at Georgia Tech. A typical job generally consists of 40 to 60 computing cores, with the ability to run compiled C++ code and Matlab. Each choice of hardware has pros and cons. For speed, the GPU and cluster are ideal. In fact, for single precision work, a single GPU is several hundred times faster than the desktop (and 3 or 4 times faster than the cluster). The cluster, while fast, is not so convenient because files must be transfered to the local machine for analysis. Likewise, the desktop, while slowest, is the easiest to use. In regards to software, Matlab is the easiest language to learn and to develop. Many algorithms which are useful for a scientific programming, are already professionally implemented such as the already mentioned Runge-Kutta integrator (ODE45) and a Newton-Raphson (fsolve) solver. C++ is a language which is harder to master, however, it is significantly faster than Matlab and is best suited for integrating large numbers of trajectories. However, there is no easy way to plot data (especially interactively) in C++ and typically we save our data in binary files which can later be opened in Matlab for analysis.

CHAPTER II

REDUCED MODELS

2.1 Introduction

The purpose of this chapter is to build and provide justification for the Hamiltonian models which will be used in the remainder of the text. These models will be used in a variety of situations, where the number of modelled electrons and the number of spatial dimensions will vary. However, the key underpinnings of the model are always the same. Briefly, all models have these in common: An effective potential between charged bodies, an interaction term between charged particles and the laser field, and assumptions made about the relativistic effects, nuclear mass, and different time and length scales.

For readers not familiar with the terms taken from nonlinear dynamics which will be used throughout the rest of the thesis it is recommended to read the appendix

2.2 Relativistic effects

Let us first examine a 1 degree of freedom (DOF), time dependent Hamiltonian which models an electron moving under the influence of a LP laser field.

$$\mathcal{H} = \frac{p^2}{2m} + E_0 x \sin \omega t \tag{2}$$

where we have chosen a sinusoid as the laser term, with frequency ω, and amplitude E_0. We can solve this system analytically by applying Hamilton's equations, which yield

$$p\left(t\right) = \frac{E_0}{\omega}\left[\cos \omega t - 1\right] + p_0 \tag{3}$$

for the momentum.

For a strong laser field, the initial momentum, is insignificant compared to the momentum gained by the laser field and we therefore assume

$$v_{max} \approx \frac{E_0}{m\omega}. \tag{4}$$

The boost parameter, β, of the Lorentz transformation becomes $\beta = v_{max}/c$, where c is the speed of light. In the atomic unit (a.u.) system, the electron mass, m, is unity and the speed of light, c, has the numerical value of $c = 1/\alpha \approx 137$, where α is the fine structure constant. Finally, we typically consider laser wavelengths of approximately 780 nm, which is equivalent to 0.0584 a.u. Requiring that $\beta \ll 1$ yields

$$\frac{E_0}{c\omega} \ll 1 \longrightarrow E_0 \ll 8. \tag{5}$$

The laser amplitude in atomic units can be converted to the more traditional $\mathrm{W} \cdot \mathrm{cm}^{-2}$ by the conversion

$$I = \left(\frac{5.142 \cdot 10^{11}}{2740} E_0\right)^2 \tag{6}$$

which implies that for $I \ll 2.25 \times 10^{18}\ \mathrm{W} \cdot \mathrm{cm}^{-2}$ we remain in the non-relativistic regime. Typically, we work with laser intensities not exceeding $10^{16}\mathrm{W}{\cdot}\mathrm{cm}^{-2}$ ($\beta \leq 0.07$), and we are therefore justified in not including relativistic effects.

2.3 Effect of Nuclear mass

Typically, we include a Coulombic interaction between the electron(s) and the nuclear core. We make the approximation, however, that the core remains stationary. The argument for doing so relies on the large mass of the core compared to an electron (a single proton/neutron is approximately 1800 times heavier than an electron) and the relatively short duration of the pulse.

We take Hamiltonian (2) to model the motions of the nucleus, and not the electron. We again arrive at Eq. 3 for the solution to the momentum. There are two

components. First, the time dependent term which is proportional to $E_0/(m\omega)$. This term represents the oscillatory motion of the nucleus due to the field. Its time average over a given laser cycle is zero and the amplitude is small compared to that of the electron because the mass of a nucleus is several thousand times larger than that of an electron. The initial momentum, p_0 will yield a $p_0\Delta t$ term in the displacement equation.

In a system where the nuclear mass is considered infinite, the energy levels go as $E_n = -\frac{Z^2}{2n^2}$. For the ground state of Hydrogen $E_1 = -\frac{1}{2}$. This total energy is the sum of the kinetic and potential energy. Assuming a soft-Coulomb potential (see sec. 2.4), with softening parameter a, this yields a maximum velocity of $v_{max} = \sqrt{m_e \frac{2-a}{a}}$, where m_e is the mass of the electron. For Hydrogen $a = 0.8$, yielding $v_{max} = 1.22\sqrt{m_e}$. Whereas in a system where we consider the motion of the nucleus, the energy levels are multiplied by the factor $\left(1 + \frac{1}{1836A}\right)^{-1}$, where A is the atomic weight ($A = 1$ for Hydrogen). Therefore, in the ground state of Hydrogen, the kinetic energy associated with the nucleus is approximately E_1/M_n, where M_n is the nuclear weight. This yields $v_{max} = \frac{1}{M_n}$, which is again several thousand times smaller than the corresponding initial velocity of the electron.

2.4 Soft Coulomb potential

The Coulomb potential between an electron and a particle with charge Z in the SI unit system reads

$$\begin{aligned} V(x,y,z) &= -\frac{1}{4\pi\epsilon_0}\frac{Z}{\sqrt{x^2+y^2+z^2}} \quad \text{which in atomic unites becomes} \\ &= -\frac{Z}{\sqrt{x^2+y^2+z^2}} \qquad \text{or simply} \\ &= -\frac{Z}{r} \end{aligned} \tag{7}$$

has a singularity at $r = 0$. In order to avoid this numerical issue, we introduce a soft-Coulomb potential, with softening parameter a [27, 28], also known as the Rochester

potential given by

$$V(x,y,z) = -\frac{Z}{\sqrt{r^2+a^2}} \tag{8}$$

This avoids singularity issues, while still retaining the key features of the physical potential. Similar issues also arise when implementing repulsive Couloumbic potentials between electrons. Again, the potential in atomic units would read

$$V(x_1,y_1,z_1,x_2,y_2,z_2) = \frac{1}{\sqrt{(x_1-x_2)^2+(y_1-y_2)^2+(z_1-z_2)^2+b^2}} \tag{9}$$

where we introduce an additional softening parameter, this time labelled b. The values of a and b are chosen based on the specific atom under consideration. In figure 7 we compare potentials (7) (solid red line) and (8) (dashed blue line).

Based on the work of this section, as well as sections 2.2 and 2.3 we can construct a field-free two electron Hamiltonian, i.e.

$$\mathcal{H}_{free}(\mathbf{x}_1,\mathbf{x}_2,\mathbf{p}_1,\mathbf{p}_2) = \frac{|\mathbf{p}_1|^2+|\mathbf{p}_2|^2}{2} - \frac{2}{\sqrt{\mathbf{x}_1^2+a^2}} - \frac{2}{\sqrt{\mathbf{x}_1^2+a^2}} \tag{10}$$

$$+\frac{1}{\sqrt{|\mathbf{r}_1-\mathbf{r}_2|^2+b^2}} \tag{11}$$

where the position and conjugate momenta of each electron are $\mathbf{x}_i$ and $\mathbf{p}_i$. This Hamiltonian, $\mathcal{H}_{free}$ is also used to generate initial conditions. We define the ground state energy, E_g as the sum of the first and second ionization potentials and find solutions to the implicit equation $\mathcal{H}_{free} = E_g$ which satisfy a microcanonical distribution.

2.4.1 Choosing the parameters a and b

From Hamiltonian (10) the softening parameters a and b must be chosen so that

1. Neither electron may ionize i.e. $\mathcal{H}_{free}(0,\infty,0,0) < E_g$
2. The space defined by the implicit equation $\mathcal{H}_{free} = E_g$, is not empty, i.e. $\{(\mathbf{x}_1,\mathbf{x}_2,\mathbf{p}_1,\mathbf{p}_2) : \mathcal{H}_{free}(\mathbf{x}_1,\mathbf{x}_2,\mathbf{p}_1,\mathbf{p}_2) = E_g\} \neq \emptyset$.

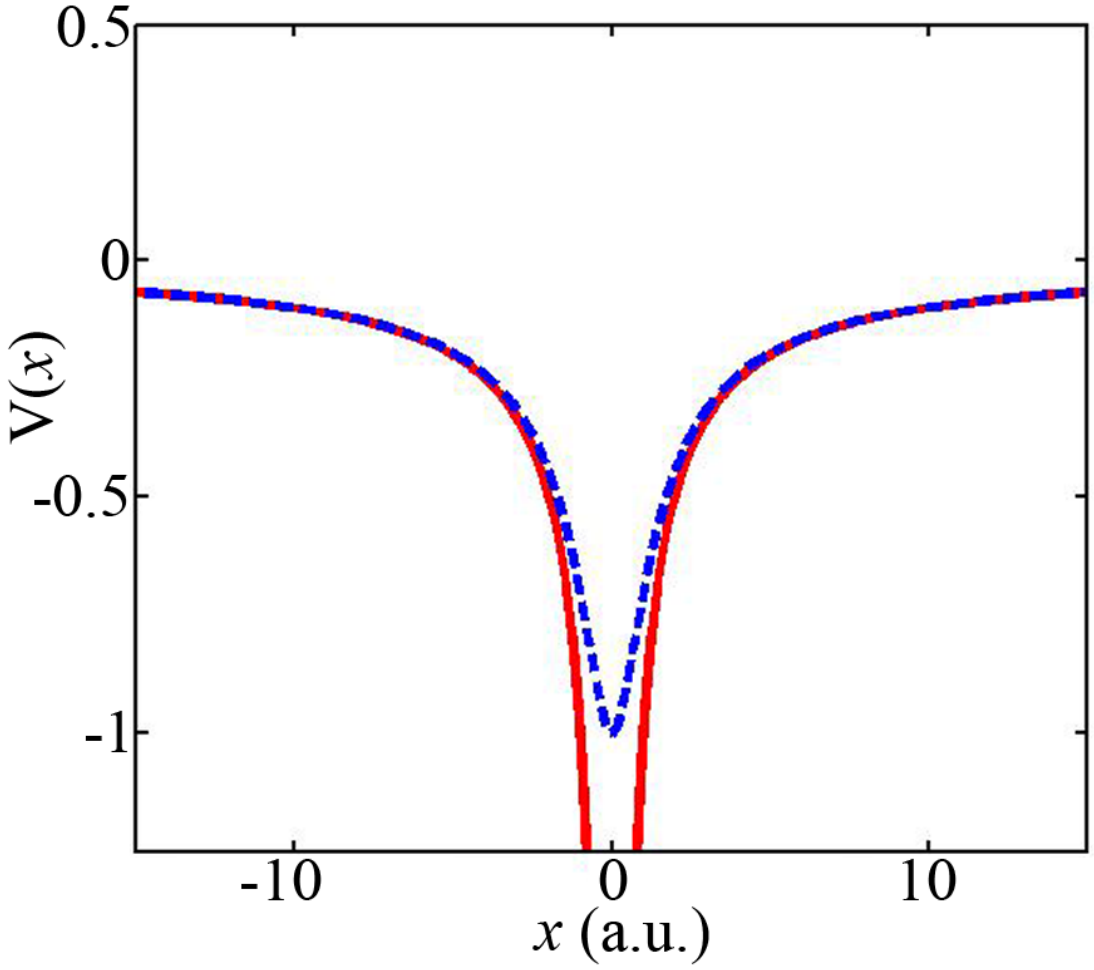

Figure 7: Comparison of the hard (red) and soft (dashed blue) Coulomb potentials. The soft Coulomb potential has $a = 1$.

	He	Ne	Mg	Ar	Xe	C_{60}
a	0.8	1	3	1.5	1.8	
E_1	24.59	21.56	7.65	15.76	12.13	7.6
E_2	54.42	40.96	15.04	27.63	21.21	

Table 2: Values of a and the first and second ionization potentials (shown in electron volts) [1] for different atoms.

For the first condition, no self-ionization, the condition reduceds to $a > \frac{-2}{E_g}$. Intuitively this makes sense. Without a laser field, i.e. an input of energy into the system, we want to avoid a situation whereby one electron moves to the bottom of the potential well allowing the other electron to move into the unbound space.

In order to get an upper bound on a we examine the second condition. When the potential term is at a minimum we are most likely to have an empty set. For the case when $a < b$ the potential is minimized when $x_1 = x_2 = 0$ and the potential becomes $-4/a + 1/b$. When $a > b$, the potential is minimized when the two electrons are equidistant from the nucleus on opposite sides. The electron positions becomes $x_1 = -x_2 = \sqrt{\frac{a^2-b^2}{3}}$. Taking these two conditions we arrive at the final result

$$\frac{-2}{E_g} < a < -\frac{3\sqrt{3}}{2E_g} \tag{12}$$

where we remove any restrictions on the choice of b. Throughout this manuscript we assign $b = 1$. The values of a, as already mentioned are atom specific. In table 2 we list the values of a chosen for each atom.

2.5 Laser polarization

The laser polarization, in addition, to the Coulombic interaction, is the main driver of electronic motion in our system, especially when the electron is ionized. From the view of an experimentalist, it is rather easy to vary the laser parameters and they can therefore be treated as experimental "control knobs" with which one can fine tune the physical processess under examination. A generic laser field is given below.

$$\mathbf{E}(t) = E_0 \left(\hat{x} \sin \omega t + \epsilon \hat{y} \cos \omega t\right). \tag{13}$$

The field amplitude is given by E_0, the field ellipticity is given by ϵ, and the frequency by ω. In this manuscript $\omega \approx 0.0584$ a.u., which translates to a wavelength of 780 nm (near-infrared). The ellipticity can be taken on the inclusive interval $[0, 1]$ where a LP field is $\epsilon = 0$ and a CP field is $\epsilon = 1$. Other ellipticities are given the broad name elliptical polarization, or EP. This definition of the laser field, from Eq. 13, will hold throughout this manuscript, with the exception of Ch. 7, where we introduce a multi-colored laser field.

2.5.1 Dipole approximation

The interaction of the laser field with the electron is represented by the dipole approximation [13]. Under this approximation, the laser wavelength is many orders of magnitude larger than the typically excursion distance of the electron, and therefore the electron sees a time dependent electric field that is spatially invariant.

Recall that for an electron in an electric, $\mathbf{E}$ with scalar potential $\mathcal{V}$ and a magnetic field $\mathbf{B}$ with vector potential $\mathbf{A}$ and also under the influence of a position dependent potential, $V(\mathbf{q})$, the equation of motion from Newton's Law gives

$$\ddot{\mathbf{x}} = e\left(\mathbf{E} + \mathbf{v} \times \mathbf{B}\right) - \nabla V(\mathbf{x}) \tag{14}$$

We claim that this is equivalent to the equations of motion generated under the Hamiltonian:

$$\mathcal{H}(\mathbf{q}, \mathbf{p}, t) = \frac{\left(\mathbf{p} - e\mathbf{A}(\mathbf{q}, t)\right)^2}{2} + V(\mathbf{q}) + e\mathcal{V}(\mathbf{q}, t) \tag{15}$$

This can be seen by first applying Hamilton's equations so that

$$\begin{aligned}
\dot{q}_i =& \frac{\partial \mathcal{H}}{\partial p_i} = p_i - eA_i(\mathbf{q}, t) \\
\dot{p}_i =& -\frac{\partial \mathcal{H}}{\partial q_i} = e\left(p_j - eA_j(\mathbf{q}, t)\right)\frac{\partial A_j(\mathbf{q}, t)}{\partial q_i} - \frac{\partial V(\mathbf{q})}{\partial q_i} - e\frac{\partial \mathcal{V}(\mathbf{q}, t)}{\partial q_i}
\end{aligned}$$

Taking from these equations, an expression for $\ddot{q}_i$ yields

$$\ddot{q}_i = \dot{p}_i - e\frac{\partial A_i(\mathbf{q}, t)}{\partial t} - e\frac{\partial A_i(\mathbf{q}, t)}{\partial q_j}\dot{q}_j.$$

We can now substitue the results for $\dot{q}_i$ and $\dot{p}_i$ into the equation above for $\ddot{q}_i$, which yields

$$\ddot{q}_i = e\left(p_j - eA_j\left(\mathbf{q},t\right)\right)\left(\frac{\partial A_j\left(\mathbf{q},t\right)}{\partial q_i} - \frac{\partial A_i\left(\mathbf{q},t\right)}{\partial q_j}\right) - \frac{\partial V\left(\mathbf{q}\right)}{\partial q_i} - e\frac{\partial A_i\left(\mathbf{q},t\right)}{\partial t} - e\frac{\partial \mathcal{V}\left(\mathbf{q},t\right)}{\partial q_i}.$$

The term, $\left(p_j - eA_j\left(\mathbf{q},t\right)\right)\left(\frac{\partial A_j(\mathbf{q},t)}{\partial q_i} - \frac{\partial A_i(\mathbf{q},t)}{\partial q_j}\right) = v_j\epsilon_{ijk}B_k = \left(\mathbf{v}\times\mathbf{B}\right)_i$ where ϵ_{ijk} is the Levi-Civita Tensor. Furthermore, $-\frac{\partial \mathbf{A}(\mathbf{q},t)}{\partial t} - \frac{\partial \mathcal{V}(\mathbf{q},t)}{\partial \mathbf{q}}$ is the expression of the electrical field $\mathbf{E}$.

From these expressions we recover the equation of motion generated from an application of Newton's law. We now employ the dipole approximation. Namely, that the spatial excursion of the electron is small compared to the wavelength of the laser field, ensuring that the laser term can be treated as spatially uniform, only depending on time, i.e.

$$\lambda \gg \text{ 10a.u.} \Rightarrow \begin{cases} \mathbf{A}\left(\mathbf{q},t\right) & \approx \mathbf{A}\left(t\right) \\ \mathcal{V}\left(\mathbf{q},t\right) & \approx \mathcal{V}\left(t\right) \end{cases}$$

.

We re-write Hamiltonian (15), keeping in mind the dipole approximation, as

$$\mathcal{H} = \frac{\left(\mathbf{p} - e\mathbf{A}\left(t\right)\right)^2}{2} + V\left(\mathbf{q}\right) + k \tag{16}$$

where we have also dropped the electric field scalar potential, $\mathcal{V}\left(t\right)$ because it has no effect on $\dot{\mathbf{q}}$ and $\dot{\mathbf{p}}$ and have autonomized the system by including the conjugate momentum to time, k. With our new Hamiltonian we undergo a canonical transformation via

$$\begin{aligned} \mathbf{v} =& \mathbf{p} - e\mathbf{A}\left(t\right) \\ \mathbf{x} =& \mathbf{q} \\ \tau =& t \\ h =& k - e\frac{\partial \mathbf{A}\left(t\right)}{\partial t}\cdot\mathbf{q} \end{aligned}$$

We can check that this transformation is indeed canonical by confirming that $dq_i \wedge dp_i = d\bar{q}_i \wedge \bar{p}_i$ where $\wedge$ is anti-commutative and bi-linear, and the bar denotes the transformed coordinates. Applying this identity to the above transformation yields

$$\begin{aligned} dx_i =& dq_i \\ dv_i =& dp_i - e\frac{\partial A_i(t)}{\partial t}dt \\ d\tau =& dt \\ dh =& dk - e\frac{\partial \mathbf{A}(t)}{\partial t}\cdot d\mathbf{q} - e\frac{\partial^2 \mathbf{A}(t)}{\partial t^2}\mathbf{q}dt \end{aligned}$$

so that

$$\begin{aligned} dx_i \wedge dv_i =& dq_i \wedge dp_i - e\frac{\partial A_i(t)}{\partial t}dq_i \wedge dt \\ d\tau \wedge dh =& dt \wedge dk + e\frac{\partial A_i(t)}{\partial t}dq_i \wedge dt - \frac{\partial^2 A_i(t)}{\partial t^2}q_i dt \wedge dt. \end{aligned}$$

By adding the above two equations and recalling that $d\alpha \wedge d\alpha = 0$ we confirm that $dx_i \wedge dv_i + d\tau \wedge dh = dq_i \wedge dp_i + dt \wedge dk$.

By applying this transformation, our new Hamiltonian becomes

$$\bar{H}(\mathbf{x}, \mathbf{v}, t, h) = \frac{|\mathbf{v}|^2}{2} + V(\mathbf{x}) + \mathbf{E}(t)\cdot\mathbf{x} + h$$

where the laser-electron coupling term is in the dipole approximation.

2.6 Qualitative analysis

From the justifications provided in the previous sections of this chapter we introduce now a complete model of two electrons operating in one, two, or three dimensions, under the influence of a laser field.

$$\begin{aligned} \mathcal{H} \;=\; & \frac{|\mathbf{p}_1|^2 + |\mathbf{p}_2|^2}{2} - \frac{2}{\sqrt{|\mathbf{x}_1|^2 + a^2}} - \frac{2}{\sqrt{|\mathbf{x}_2|^2 + a^2}} + \frac{1}{\sqrt{|\mathbf{x}_1 - \mathbf{x}_2|^2 + b^2}} \\ & + E_0 f(t)(\mathbf{x}_1 + \mathbf{x}_2)\cdot \begin{pmatrix} \sin\omega t \\ \cos\omega t \end{pmatrix}. \end{aligned} \tag{17}$$

where $\mathbf{x}_i$ and $\mathbf{p}_i$ are the position and conjugate momenta vectors while the other parameters have already been introduced. The function, $f(t)$ is the laser envelope. It is typically defined in a piece-wise manner whereby there is a two laser cycle linear ramp up, a 4 or 6 laser cycle plateau, and a two laser cycle linear ramp down. For a concrete example, consider the case where $\epsilon = 0$, i.e. LP. In this situation the laser-driven dynamics will take place almost entirely on the polarization axis of the laser field. Taking this axis to be the $\hat{x}$-axis, our Hamiltonian reduces to

$$\mathcal{H} = \frac{p_1^2 + p_2^2}{2} - \frac{2}{\sqrt{x_1^2 + a^2}} - \frac{2}{\sqrt{x_2^2 + a^2}} + \frac{1}{\sqrt{(x_1 - x_2)^2 + b^2}} + E_0 f(t)\,(x_1 + x_2)\sin\omega t \quad (18)$$

Applying Hamilton's equations yields a system of ODEs which can be solved numerically. The solution yields classical trajectories, i.e. the position and momenta of each electron as a function of time. The positions of both electrons are shown in figure 8 for two different sets of initial conditions. Without going into a detailed quantitative study of this figure, we can still glean much information from a quick qualitative review.

Both electrons begin at $t = 0$ bounded, and nearby the core. Slightly after one laser cycle the red trajectory ionizes, due to the influence from the laser field. Once it ionizes, and is far from the core, its dynamics is dictated almost entirely by the goings-on of the laser field (note the oscillatory motion of the ionized electron). This ionized electron returns to the core multiple times, however, note that at each fly-by its path is almost completely unperturbed. It is moving so fast, that although it is exchanging energy with the ionic core, its own path does not change, and it is still dictated entirely by its interaction with the laser field. Slightly before five laser cycles the electron collides with the core for a final time. Having imparted enough cumulative energy to the non-ionized electron, it too now ionizes, resulting in a double ionization. This qualitative description of the dynamics is useful and telling, however, not entirely accurate. Indeed, modelling the ionized electron as *only* interacting with

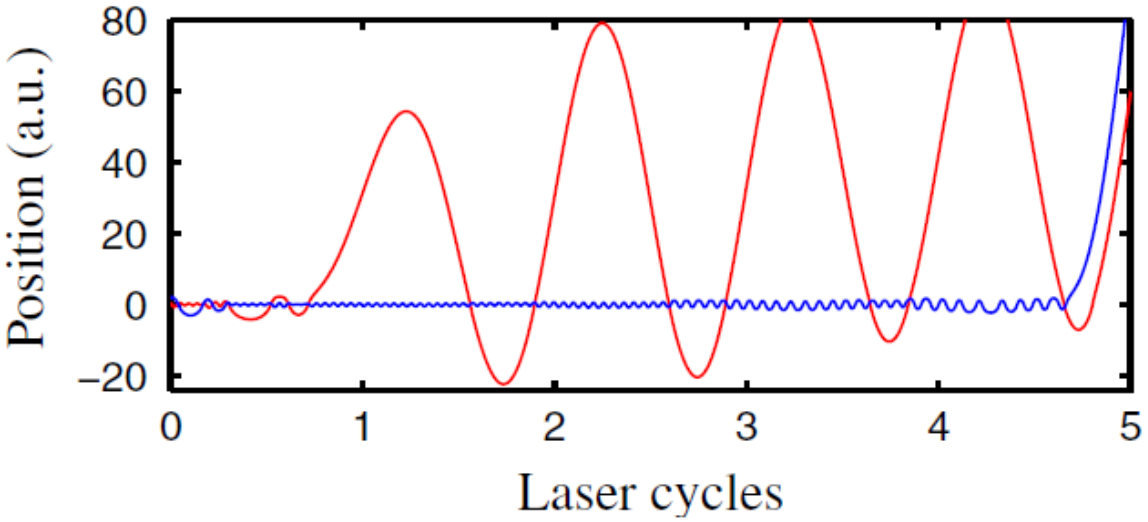

Figure 8: Reproduced from [9]. A typical solution of Hamiltonian (18) for the positions of the two electrons. The laser intensity is $I = 10^{15}$ W $\cdot$ cm^{-2} and the wavelength is 780 nm (0.0584 a.u.). The initial conditions are generated on the ground state energy surface of Helium with softening parameters $a = b = 1$.

the laser field (and not the Coulomb field) is useful from a qualitative point of view, but fails under a deeper, more quantitative scrutiny. As will be shown in Ch. 3 the effect of the Coulomb field plays a pivotal role in the recollision process, most notably in the maximum allowed return energy of the electron.

Reviewing the same trajectory again, now from the viewpoint of the blue trajectory is equally useful. After the ionization of the red trajectory the blue trajectory remains trapped, oscillating around the core. The amplitude of these oscillations is related to the energy of the electron. Furthermore, between recollisions of the red trajectory, the oscillations of the blue trajectory remain constant in amplitude. However, after a recollision, this amplitude increases slightly. This is because at each recollision, the red trajectory, which has gained energy in the field, imparts some of that energy back to the ion. After multiple recollisions the blue trajectory ultimately has received enough energy to itself ionize. Since the energy of the blue electron remains constant between recollisions, it can be modelled solely by its interaction with the core.

2.7 Reduced models

From the qualitative analysis performed above we construct two reduced models, known as the inner and outer electron models. These models are valid whenever there is a well established inner (e.g., blue trajectory above) and outer (e.g., red trajectory above) electron. The inner electron model,

$$\mathcal{H}_{inner}\left(\mathbf{x},\mathbf{p}\right)=\frac{\left|\mathbf{p}\right|^{2}}{2}-\frac{Z}{\sqrt{\left|\mathbf{x}\right|^{2}+a^{2}}} \tag{19}$$

includes only the interaction of the non-ionized electron and the core. It does not include the correlation with the other electron and the interaction of the laser field. The Coulomb charge, Z, can be varied. Typical values are $Z=1$ for a one electron model and $Z=2$ for a two electron model. The outer electron model,

$$\mathcal{H}_{outer}\left(\mathbf{x},\mathbf{p},t\right)=\frac{\left|\mathbf{p}\right|^{2}}{2}+E_{0}\mathbf{x}\cdot\begin{pmatrix}\sin\omega t\\ \cos\omega t\\ 0\end{pmatrix}, \tag{20}$$

on the other hand includes only the interation with the laser field, neglecting all Coulombic potentials. Both models, inner and outer, give a rough idea of the dynamics. A hybrid model, useful for studying one electron systems in general, includes both the Coulomb attraction to the core and the laser field. We refer to this model as simply the one electron model. It can be written as

$$\mathcal{H}_{outer}\left(\mathbf{x},\mathbf{p},t\right)=\frac{\left|\mathbf{p}\right|^{2}}{2}-\frac{Z}{\sqrt{\left|\mathbf{x}\right|^{2}+a^{2}}}+E_{0}\mathbf{x}\cdot\begin{pmatrix}\sin\omega t\\ \cos\omega t\\ 0\end{pmatrix}. \tag{21}$$

The benefit of reducing the dynamics to simpler models is an issue of dimensionality. Hamiltonian (17), when using two spatial dimensions is a 4 degree of freedom (DOF) system, or a 8 dimensional phase space. However, the inner electron model, is only a 2 DOF or 4 dimensional phase space. When you take into account the conservation of the energy (time-independent Hamiltonian) and add a Poincaré section

the dynamics is restricted to a 2 dimensional manifold. The outer electron and one electron model, on the other hand is 2.5 DOF (counting time dependence as 1/2 a DOF), resulting in a 5 dimensional phase space. By taking a stroboscopic Poincaré section we can reduce the system to 4 dimensions.

In the following chapters we will make much use of reduced Hamiltonians when analyzing the dynamics.

CHAPTER III

SINGLE ELECTRON DYNAMICS IN A COMBINED COULOMB AND LINEARLY POLARIZED LASER FIELD

3.1 Introduction

The dynamics of an electron in a combination Coulomb and laser field is currently an unsolved problem of strong field physics. Approximations do exist which assume negligible contributions from the Coulomb field, however, a scenario fully taking into account the Coulomb field has never been shown. The implications of this are that the results generated from neglect of the Coulomb field, for example a maximum return energy of $3.17U_p$ (see below), are assumed to be correct even in the presence of the Coulomb field. In this chapter, we will show that the maximum return energy is indeed very close to $3.17U_p$, however, for reasons more subtle than anticipated.

In the previous chapter we introduced the concept of reduced Hamiltonian models. Recall, their advantage exists in their lower dimensionality and the justification of their use arises from our qualitative study of the dynamics of the two electron system. Hamiltonian (21) is a model for a single electron. It is valid for either single-electron systems, or a two electron system where the additional electron has already ionized. It is written below as

$$\mathcal{H}_{inner}\left(\mathbf{x},\mathbf{p},t\right)=\frac{\left|\mathbf{p}\right|^{2}}{2}+V\left(\left\|\mathbf{x}\right\|\right)+\mathbf{x}\cdot\vec{E}\left(t\right) \tag{22}$$

where $\vec{E}\left(t\right)=E_0\left(\hat{x}\sin\omega t+\epsilon\hat{y}\cos\omega t\right)$ is the laser field. The potential $V\left(r\right)$ is a generic, rotationally invariant potential. Later it will be replaced by potentials more specific to various target species, whether they be atoms or molecules. When the laser field is absent ($E_0=0$), the Hamiltonian becomes independent of time. This gives two conserved quantities. First, the angular momentum, because the Hamiltonian is only

a function of the radial distance $r = \sqrt{(x^2 + y^2)}$, and second the total energy, because the Hamiltonian is time independent. With two independent conserved quantities in a two degree of freedom system the Hamiltonian system is integrable.

Throughout this manuscript the parameter ϵ, the field ellipticity, will be varied. In general, we are interested in its two extremes, $\epsilon = 0$ and $\epsilon = 1$. When $\epsilon = 0$, we refer to the field as linearly polarized (LP) and when $\epsilon = 1$ we refer to the field as circularly polarized (CP). In this chapter we will mainly investigate the LP case, with some short comments on EP given at the end of the chapter. The results for CP will be given in the following three chapters.

3.2 Linear Polarization, 1 spatial dimension

In a LP field the dynamics can be reduced to a single spatial dimension, which is oriented in parallel to the laser's axis of polarization. The Hamiltonian can be written as

$$\mathcal{H}(x, p, t) = \frac{p^2}{2} - \frac{Z}{\sqrt{x^2 + 1}} + E_0 x \sin \omega t \tag{23}$$

where we have explicity written the laser field as $E(t) = E_0 \sin \omega t$ and dropped the vector notation from our phase space coordinates. As a means of investigating this system in detail, we have chosen a soft Coulomb potential (see Sec.2.4), where we keep the softening parameter fixed at $a = 1$ and allow the Coulombic charge, Z, to vary. The variation of Z will be shown to be important when analyzing the strong field approximation (SFA) and the "simple-man model" [6]. The "simple-man model" corresponds to $Z = 0$, whereas a full account of the Coulomb interaction corresponds to $Z = 1$. The SFA assumes a high intensity laser so that the dynamics is dominated by the laser field interaction. Written as it is above, Hamiltonian (23) has 1.5 degrees of freedom (DOF) and is therefore not integrable. However, by turning off the laser field ($E_0 = 0$) we remove the time dependence and we are left with a 1 DOF system, which is integrable.

3.2.1 Integrable Hamiltonian, H_0

The integrable Hamiltonian, H_0, associated with Hamiltonian (23) is written as

$$\mathcal{H}_0(x,p) = \frac{p^2}{2} - \frac{Z}{\sqrt{x^2+1}} = \mathcal{E}. \tag{24}$$

For values of $H_0(A) < 0$ phase space is bounded and spanned by invariant tori. This Hamiltonian can undergo a canonical transformation to action-angle variables in the bounded region of phase space, which allows for a deeper understanding of the phase space picture. The formula for the action,

$$\begin{aligned} A &= \frac{1}{\pi}\oint_{-x_m}^{x_m} p dx \\ &= \frac{2}{\pi}\oint_{0}^{x_m} \sqrt{2\mathcal{E} + \frac{2Z}{\sqrt{x^2+1}}} dx, \end{aligned}$$

where $\pm x_m$ are the turning points, results in an integral without an analytical solution.

These invariant tori are parameterized by their respective action, computed from the above equation. The invariant tori can best be visualized by a Poincaré section taken stroboscopically. We take initial conditions randomly from a box in phase space centered around the core region, $x = 0$. Closeby the core, initial conditions will satisfy $H_0(x,p) < 0$, and we therefore only allow initial conditions which remain bounded. In figure 9 we show the Poincaré section for the integrable Hamiltonian. These tori, which as the action, A increases, continue to increase their spatial extent, are bounded, but in the limit where $H_0(A) \to 0^-$ become unbounded in the sense that their turning points are located at $\pm\infty$.

3.2.2 Adding a perturbation

We are interested in what happens when we introduce the laser field, a time-dependent perturbation. From Kolmogorov-Arnold-Moser (KAM) theory [29, 30, 31, 32], we know that tori whose frequencies are rational multiples of the driving frequency, ω (or nearly rational multiples), will be the first to break. The breaking of these tori will

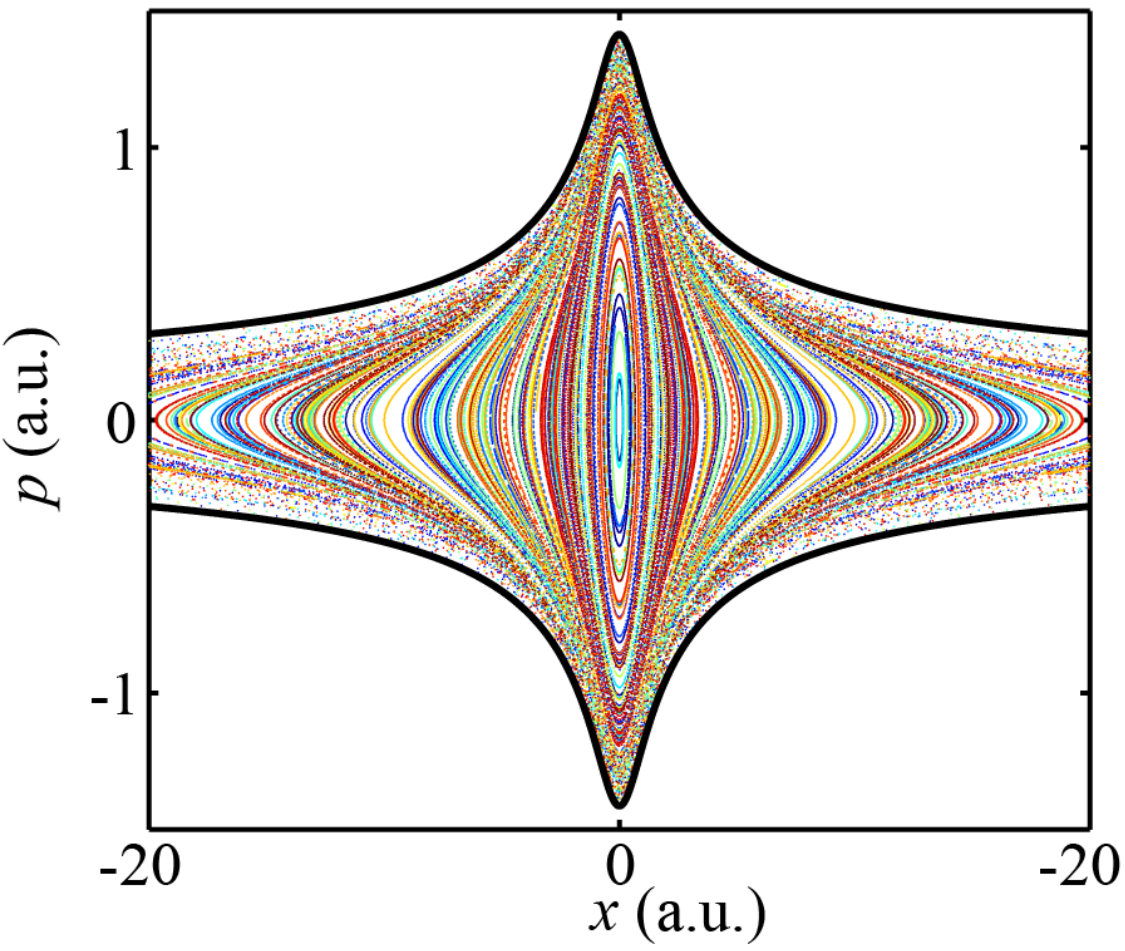

Figure 9: Poincaré section of Hamiltonian (24). Phase space is foliated by invariant tori. The thicker black lines show the boundary $H_0(x,p) = 0$.

result in the creation of elliptic and hyperbolic periodic orbits, by Birkhoff's theory, whose properties we will need to investigate in order to understand the dynamics.

In order to understand the resonance structure of the integrable Hamiltonian we will need to investigate the expression for the action, A, given above. This integral can be well approximated by a series expansion around the bottom of the Coulombic well [33], i.e. $x_m \approx 0$. However, this approximation fails at large values of the action. Instead, we evaluate the integral numerically to find $H_0(A)$. From Hamilton's equations, we know that the angle, $\omega_0(A) = \frac{\partial H_0(A)}{\partial A}$, which can also be computed numerically. With $\omega_0(A)$ known, we can establish the resonance condition $m\omega_0(A) - n\omega = 0$. Focusing on the $1:m$ resonances, for their shorter period, we find the action of the first four resonances, written as A_m, in figure 10 where we show a plot of $\frac{\omega_0(A)}{\omega}$ vs. A. The index m also gives the period of the orbit in units of laser cycles, i.e. the $m = 3$ orbit has a period of three laser cycles.

When the perturbation is turned on and some of the invariant tori break, elliptic islands appear, sandwiched between remaining tori. In figure 11 we show the same Poincaré section, however, for $E_0 \approx 5.3 \cdot 10^{-4}$ a.u., or $I = 10^{10}$ W $\cdot$ cm^{-2}. The resonances predicted by figure 10 are located by the black markers. The $m = 1$ resonance is marked by the "+" and the $m = 3$ resonance by the "•". The other resonances are also present, however, are not shown in the figure. At such a low value of E_0 these periodic orbits are still elliptic (see figure 12, left panel). These resonances, which are elliptic as the perturbation is turned on, also have hyperbolic counterparts (Birkhoff's theorem [34]). These hyperbolic orbits are part of the same resonance, and were on the same tori (before breaking) as the elliptical orbits shown in the figure. Their locations for $E_0 \ll 1$ are approximately symmetric about the x-axis to their elliptical counterpart. They are, however, of lesser interest, because they quickly become very unstable as the perturbation is increased, and hence have less of an effect on the dynamics. In the leftmost panels of figure 12 we show two

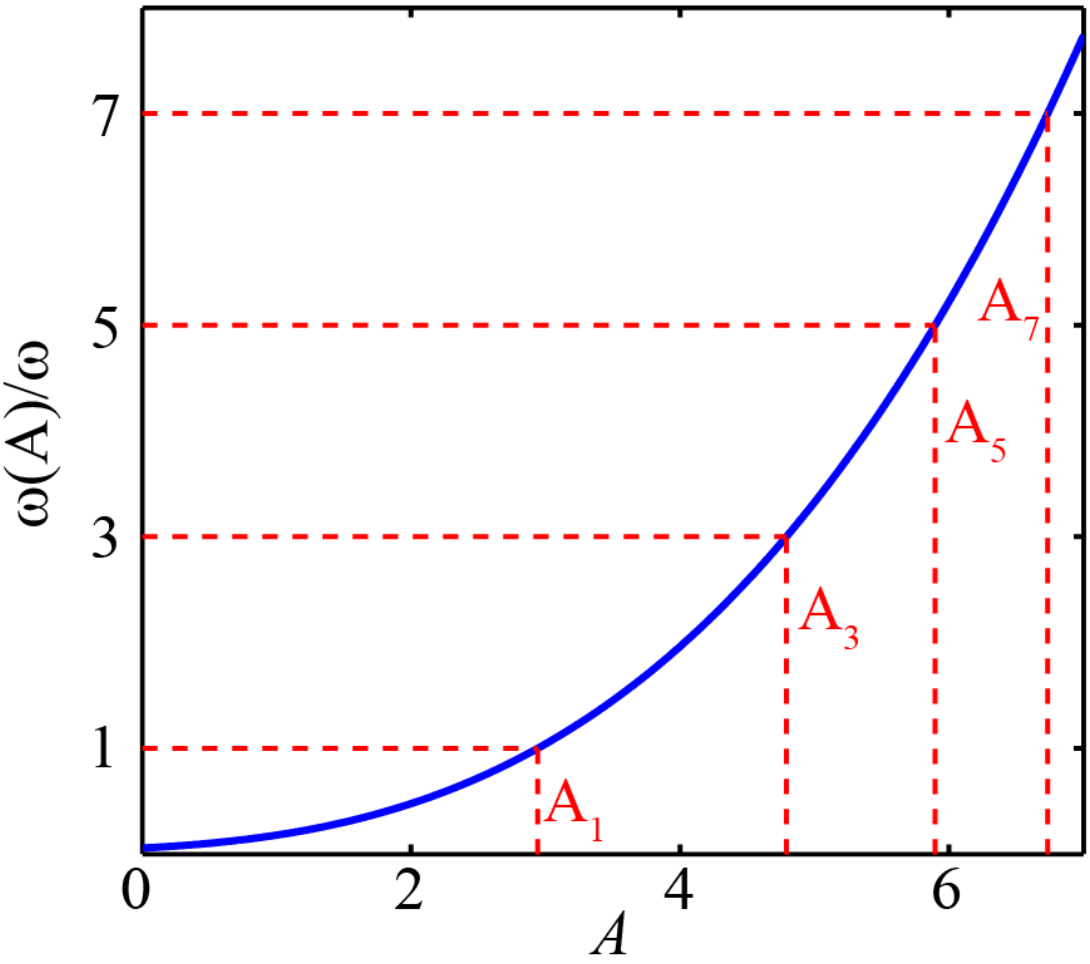

Figure 10: Dependence of $\omega_0(A)/\omega$ on the action, A. The first four resonances, $m = 1, 3, 5, 7$ are shown, with their corresponding actions, A_m.

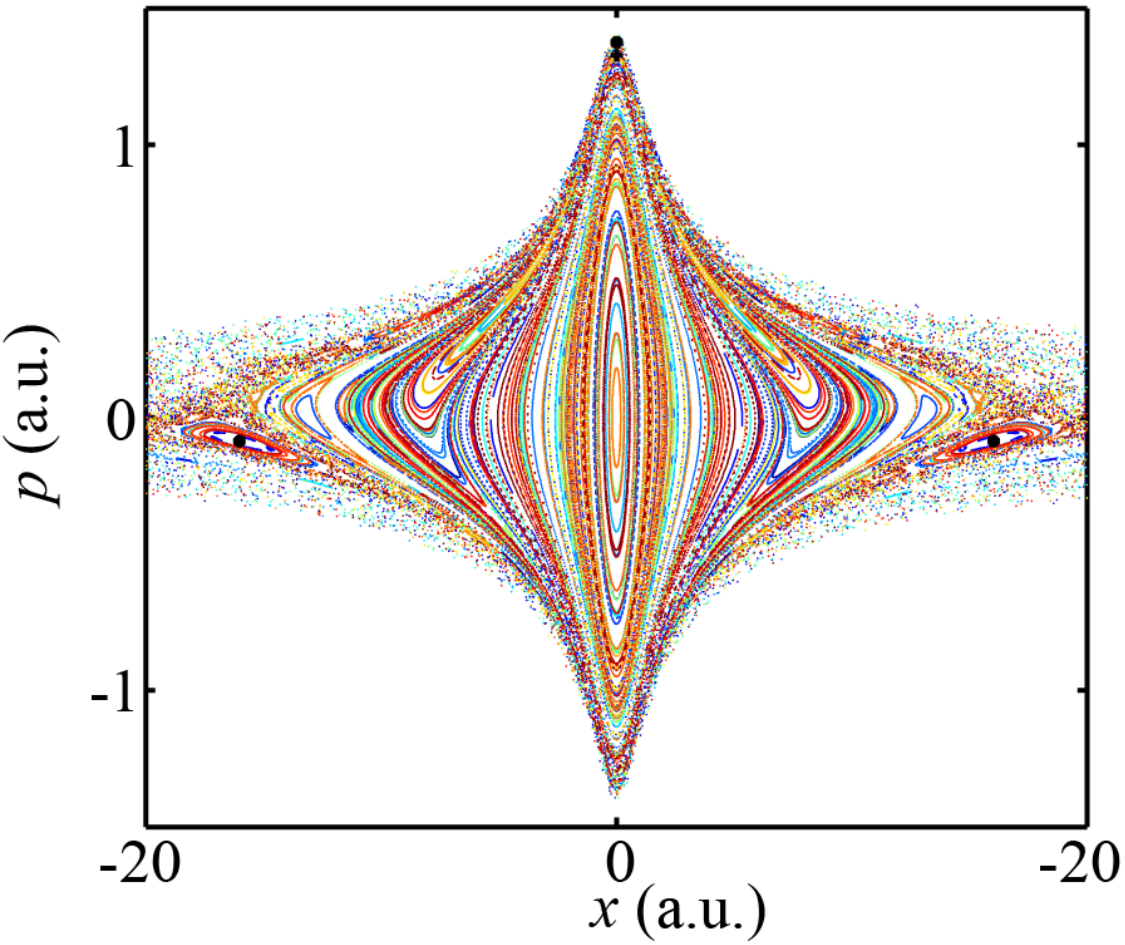

Figure 11: Poincaré section of Hamiltonian (23) at $I = 10^{10}$ W $\cdot$ cm^{-2}. The black markers show the placement of the $m = 1$ ("+") and $m = 3$ ("•") resonances, which at low intensity are elliptic islands.

additional Poincaré sections whereby the perturbation is now quite large, and the elliptical islands of figure 11 have disappeared. In fact, the periodic orbits associated with these elliptic islands still exist, however, they have bifurcated, and are now hyperbolic, making it difficult to resolve their location on a Poincaré section. To see this more clearly, the right panel of the same figure shows the bifurcation diagram for the $1:1$ (red) and $1:3$ (green) resonances). At both intensities used for the Poincaré sections on the left both orbits are now unstable.

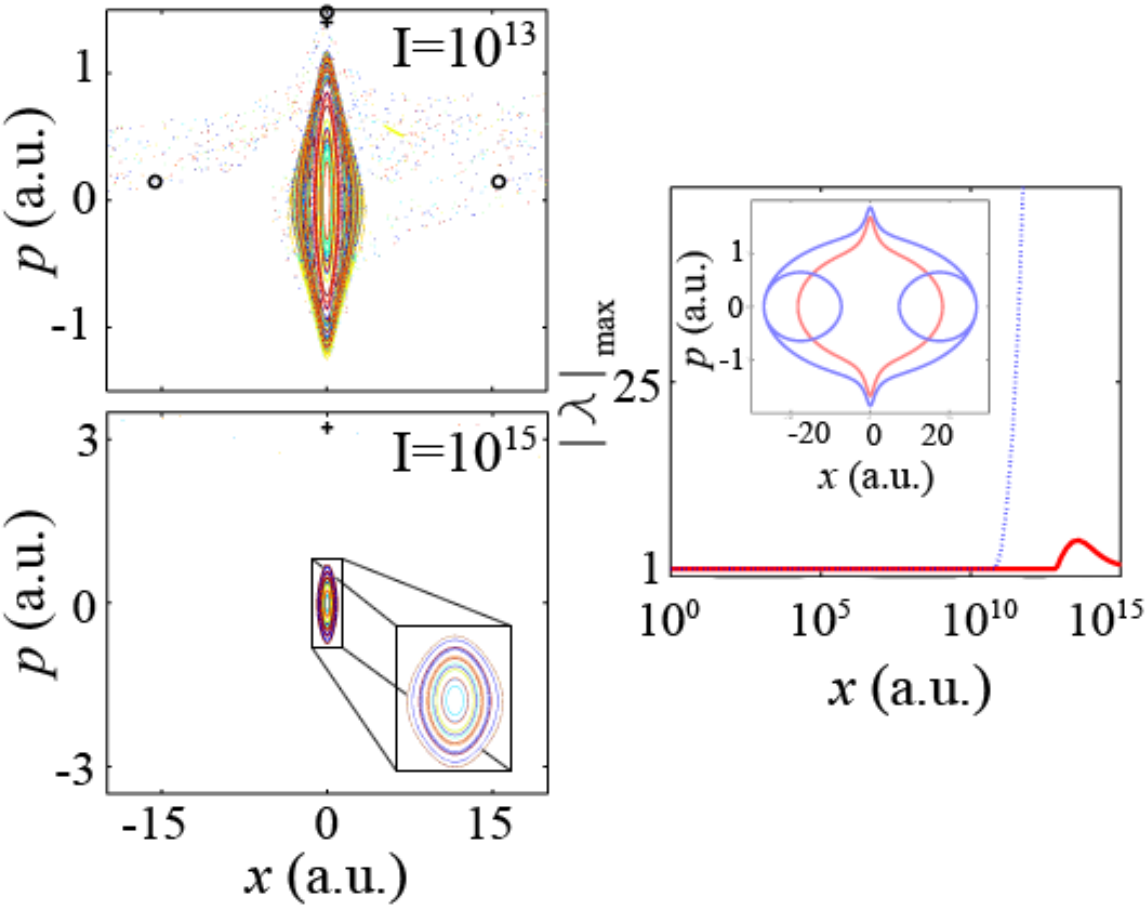

Figure 12: Left panels: Poincaré sections of Hamiltonian (23) at $I = 10^{13}$ W $\cdot$ cm^{-2} (top) and $I = 10^{15}$ W $\cdot$ cm^{-2} (bottom). The circle markers show the location of the $m = 3$ periodic orbit while the 'plus' sign shows the location of the $m = 1$ orbit. The inset of the bottom panel shows a blown up version of the bounded region. Right panel: Bifurcation diagram of the $m = 1$ (red) and $m = 3$ (blue) resonances. Inset: Phase space representation of the resonances at $I = 10^{14}$ W $\cdot$ cm^{-2}.

3.2.3 Dynamics of the system

The dynamics of this system can be analyzed in three parts. First, there are the non-ionizing trajectories, which remain in the bounded region. These are trajectories for which the attractive Coulomb potential dominates the ionizing effects of the laser field so that the electron always remains closeby the nucleus. We showed in the previous section (see figure 9) that this region is filled with invariant tori. Furthermore, the size of the bounded region decreases as the laser becomes stronger. Second, there are the trajectories which ionize and do not return. This dynamics has been explained previously by a phenomena known as recollision excitation with subsequent ionization, or RESI. A better understanding of this process can be found in the literature (see [35] and [36]). Briefly, an electron nearby the boundary of the bounded and unbounded regions exists in a state of limbo. It feels an almost equal pull between the ionizing effect of the laser field and the attractive nature of the Coulomb field. In this state, ionization ultimately will occur, however, it can take many periods of the laser field. Dynamically there exist a series of periodic orbits which exist in the narrow chaotic layer at the boundary which regulate the process. Finally, there are the trajectories which ionize and also return. The return process, as we will soon show, is controlled by the $1:m$ resonances. Interestingly these periodic orbits exist in the same chaotic layer as the orbits which control the RESI process. An examination of recolliding trajectories is useful in determining which orbits come into play.

From the bifurcation diagram of figure 12 we expect that at low intensity both resonances, $1:1$ and $1:3$ will affect the dynamics since they both have hyperbolic stability, however, with eigenvalues not too large. As we increase the intensity, however, the $1:3$ resonance should lose its influence on the dynamics because it becomes too unstable. In figure 13 this is precisely what we see. In the left panel we show a trajectory at $I = 10^{14}\ \mathrm{W}\cdot\mathrm{cm}^{-2}$ (blue) with the $1:3$ resonance superimposed on top. We see that the trajectory starts nearby the periodic orbit, follows it until moving

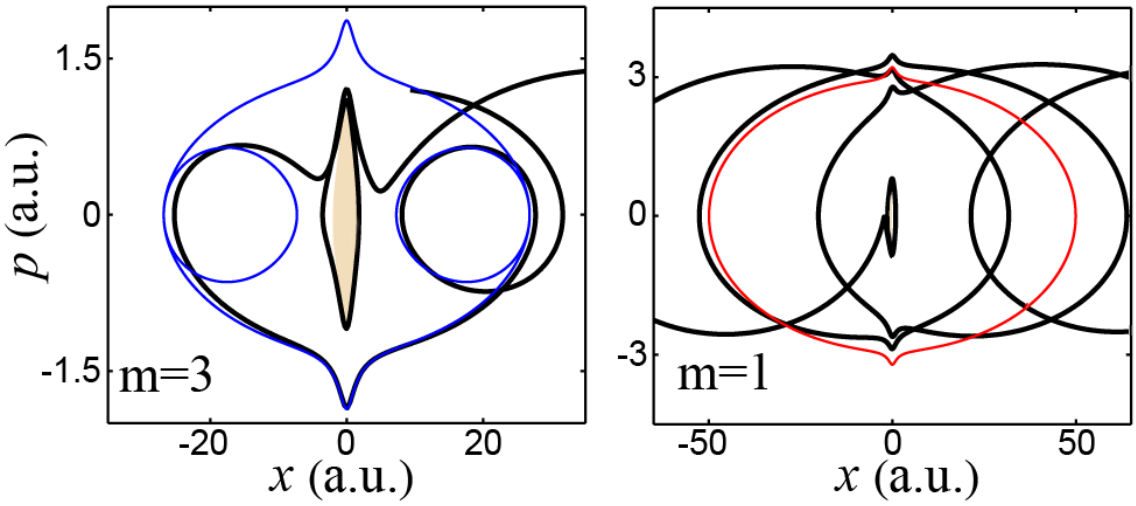

Figure 13: Left panel: A typical recolliding trajectory (black) of Hamiltonian (23) which follows the $1:3$ resonance, which is shown in blue for comparison. The intensity is taken to be $I = 10^{14}$ W$\cdot$cm^{-2}. Right panel: A typical recolliding trajectory (black) of Hamiltonian (23) which follows the $1:1$ resonance, which is shown in red for comparison. The intensity is taken to be $I = 10^{15}$ W $\cdot$ cm^{-2}. In both panels, the bounded region, a remnant for the integrable case, is shown in tan.

towards the bound region (light pink) which it circles until moving away not to return again. In fact, when the trajectory is nearby the bound region, its motion is similar to that of a trajectory undergoing the RESI process. From a dynamical perspective this is correct because the $1:m$ resonance and RESI orbits exist in the same chaotic layer. If we increase the intensity to $I = 10^{15}$ W $\cdot$ cm^{-2} we see a similar picture, however, for the $1:1$ resonance. This time, the trajectory starts nearby the bounded region (light pink), until ionizing, and subsequently returning to follow the periodic orbit (red) which it follows for a while until ionizing once more. These trajectories were chosen because they are representative of the recolliding dynamics happening at each intensity.

In addition to a trajectory analysis we perform a more statistical analysis as well. In figure 14 we show the density returns to the Poincaré section $p = 0$ for trajectories which have a recollision (in configuration space) via the colored density plot. Superimposed over this density (black markers) is the visualization of the unstable

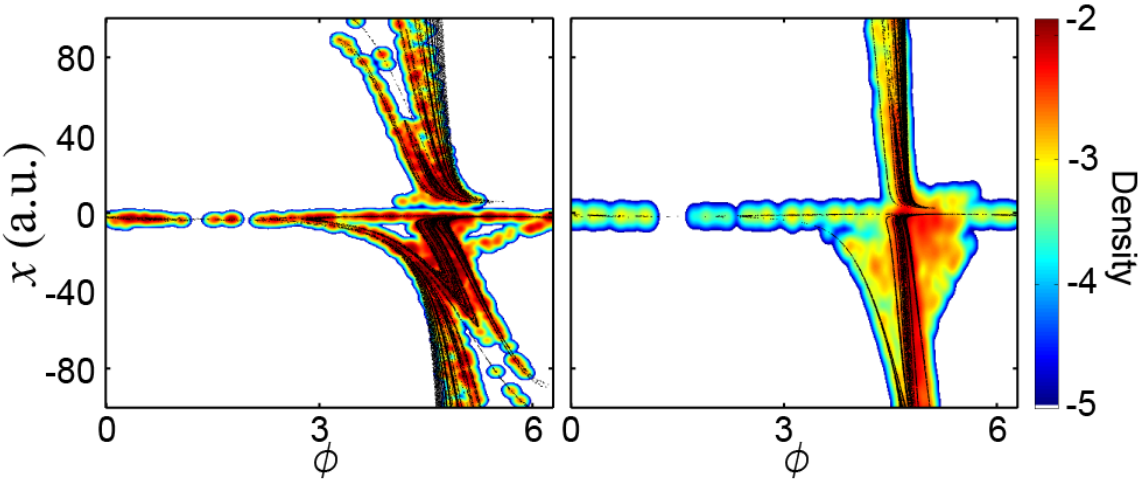

Figure 14: The colored surface is the density of returns to the Poincaré section $p = 0$ for electrons which undergo a recollision (in configuration space). The black lines are the visualization of the unstable manifold of the $m = 1$ periodic orbit. The left panel is $I = 10^{14}$ W $\cdot$ cm^{-2} and the right panel is $I = 10^{14}$ W $\cdot$ cm^{-2}.

manifold of the $m = 1$ resonance. In the left panel we use $I = 10^{14}$ W $\cdot$ cm^{-2} and in the right panel we use $I = 10^{15}$ W$\cdot$cm^{-2}. You can see that the manifold overlaps very strongly with the density of random recolliding trajectories, and in this way can be said to organize the recolliding dynamics. Similar manifolds for the other resonances, such as $m = 3$ look strikingly similar to the manifold of $m = 1$ which is expected because they exist in the same chaotic layer.

A brief note on stability: When we talk about stability, we are talking about the eigenvalues of the tangent flow (or monodromy) matrix which can be considered as an averaged effect of the dynamics for trajectories nearby the periodic orbit. A local stability can also be computed from the Hessian matrix. From Hamilton's equations applied to Hamiltonian (23) we have

$$\begin{aligned} \dot{x} &= p \\ \dot{p} &= \frac{-Zx}{(x^2+1)^{\frac{3}{2}}} - E_0 \sin \omega t \end{aligned}$$

which gives us the stability matrix

$$A(x) = \begin{pmatrix} 0 & 1 \\ -\alpha(x) & 0 \end{pmatrix} \tag{25}$$

where the matrix, $A(x)$ can be evaluated at points along the periodic orbit and the function $\alpha(x)$ is the second derivative of the soft Coulomb potential. The characteristic polynomial, $\chi(\lambda, x) = \lambda^2 + \alpha(x)$ has zeros when $\lambda = \pm\sqrt{-\alpha(x)}$. We know that when

$$\begin{aligned} \mathrm{Re}[\lambda] &> 0 \rightarrow \text{locally unstable,} \\ \mathrm{Re}[\lambda] &< 0 \rightarrow \text{locally stable,} \\ \mathrm{Re}[\lambda] &= 0 \rightarrow \text{locally marginal or elliptic.} \end{aligned}$$

Therefore, since $-\alpha(x) = \frac{Z\left(1-2x^2\right)}{\left(x^2+1\right)^{\frac{5}{2}}}$ we have that if $|x| > 1/\sqrt{2}$ the orbit is locally unstable, and if $|x| < 1/\sqrt{2}$ the orbit is of marginal stability locally (since λ will be imaginary). Likewise, the real component of λ is maximized when $-\alpha(x)$ is maximized as well, which occurs when $x = \pm\sqrt{3/2}$, which gives $\lambda \approx 0.45$. Furthermore, these results are indepenent of E_0, ω, and the periodic orbit! In figure 15 we show both the $m = 1$ and $m = 3$ resonances in the (x, p) plane where the color scale corresponds to $\mathrm{Re}[\lambda]$. We see that nearby $x = 0$ we have $\mathrm{Re}[\lambda] = 0$, however, at $x = \sqrt{1/2}$ the orbit first becomes unstable. Far away from the core region the orbit is unstable, however, only slightly. Keep in mind, therefore that the bifurcation diagrams of figure 12 do not tell the complete story. Trajectories under the influence of a specific $1 : m$ resonance are most likely to follow the resonance when far away from the core, where the orbit is least unstable, while they will oftentimes depart from the orbit near $x = 0$.

The recolliding dynamics of the one-dimensional, one-electron system, dictated by Hamiltonian (23), have been shown to be controlled by the $1 : m$ resonances. At low intensity, other orbits do indeed come into play, since more orbits are of low

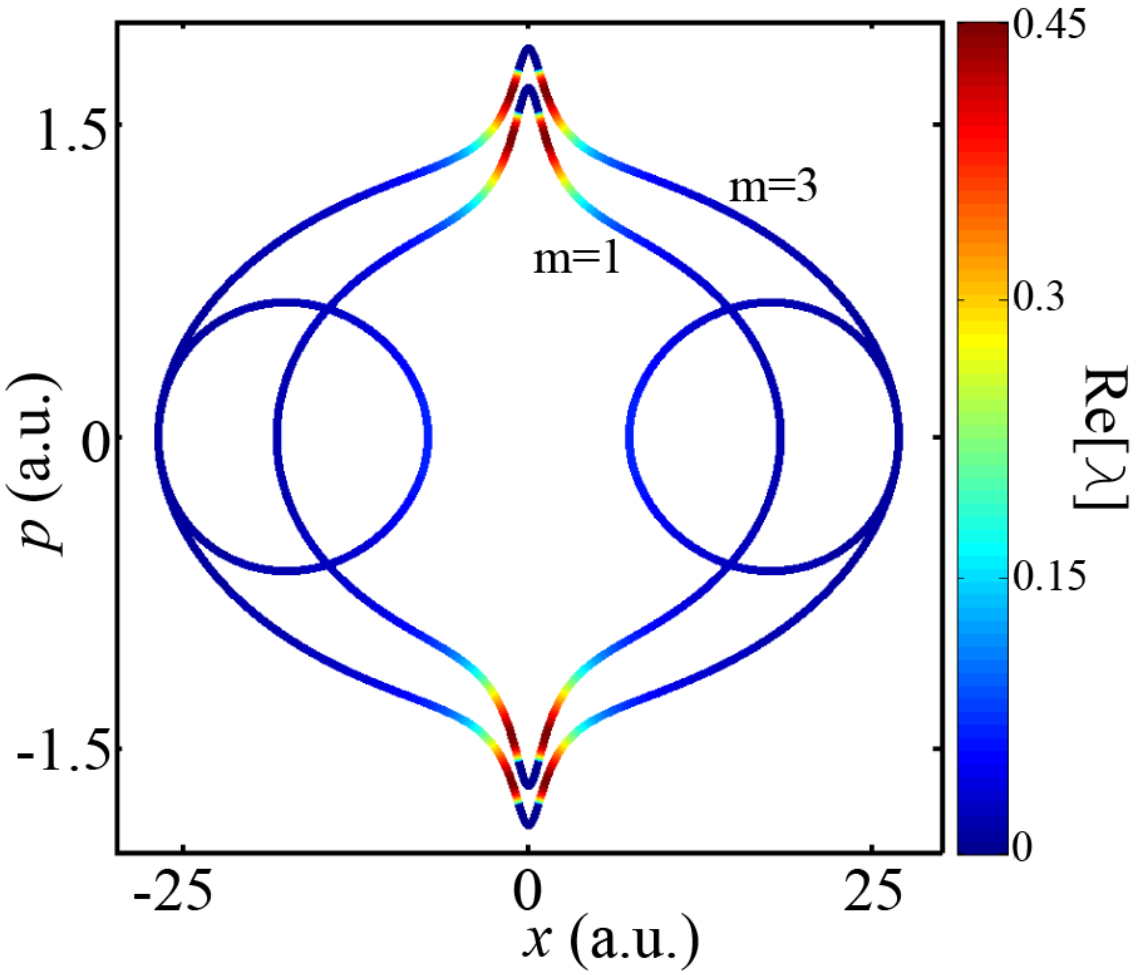

Figure 15: The $m = 1$ and $m = 3$ periodic orbits are shown at $I = 10^{14}$ W $\cdot$ cm^{-2} for $Z = 1$. The color bar indicates the local stability.

instability, however, it is the orbits of low period (or low value of m) which have the greatest influence on the dynamics. At high intensity, only the $1:1$ orbit can be seen as an imprint of the dynamics because the other orbits have either bifurcated, or are too unstable.

3.2.4 Electron returning with maximum energy

From the simple-man model (when $Z = 0$ in Hamiltonian (23)) it is known analytically that the maximum return energy of the electron, κ, given in units of the ponderomotive energy, $U_p = \frac{E_0^2}{4\omega^2}$, is $\kappa \approx 3.17$. However, as you begin to increase Z the problem of the maximum return energy cannot be solved analytically, and it becomes unclear what happens. There are several forces at play. On the way out, the Coulomb field slows the electron down. As a result, its turning point (where it stops) is closer to the nucleus than in the simple-man model. On the way back, both accelerations are in the same direction so the electron goes faster than in the simple-man. However, it starts from closer in.

From the viewpoint of the electron the Coulomb field has something of a cancelling effect on its return energy, qualitatively explained above. A more quantitative treatment is also desirable. We treat this problem by introducing a rescaling of Hamiltonian (23), given by

$$\bar{\mathcal{H}}\left(\bar{q}, \bar{p}, \bar{t}\right) = \frac{\bar{p}^2}{2} - \frac{\bar{Z}}{\sqrt{\bar{x}^2 + \bar{a}^2}} + \bar{x}\sin\phi + \bar{\mathcal{E}} \tag{26}$$

where

$$\begin{aligned}
\bar{t} =& \omega t \\
\bar{x} =& x\frac{\omega^2}{E_0} \\
\bar{p} =& p\frac{\omega}{E_0} \\
\bar{a} =& a\frac{\omega^2}{E_0} \\
\bar{Z} =& Z\frac{\omega^4}{E_0^3} \\
\phi =& \bar{t} + \phi_0
\end{aligned}$$

where ϕ_0 is the initial phase and the Hamiltonian is also autonomous. In what follows we drop the bars for simplicity. Hamilton's equations yield

$$\begin{aligned}
\dot{x} =& p \\
\dot{p} =& -\frac{Zx}{\left(x^2+a^2\right)^{\frac{3}{2}}} - \sin\phi.
\end{aligned}$$

Referring to the time of recollision as T, the trajectory must satisfy the equations $x\left(T\right) = 0$ and $p\left(T\right) = p_r$ where p_r is the recollision momentum. The change in momentum, $\Delta p = p\left(T\right) - p_0 = \Delta p_{sm} + \Delta p_z$ where we have separated the contributions coming from the laser field (Δp_{sm}) and the Coulomb field (Δp_z). The contribution from the laser field is straightforward to compute, i.e.

$$\Delta p_{sm} = -\int_0^T \sin\phi\left(t\right) dt = \cos\left(T+\phi_0\right) - \cos\phi_0$$

The contribution from the Coulomb field, however, relies on the approximation that the laser field is strong. We know that

$$\Delta p_z = -Z\int_0^T \frac{x\left(t\right)}{\left(x\left(t\right)^2+a^2\right)^{\frac{3}{2}}} dt$$

and, since we make the assumption that the laser field is strong, we allow for the approximation that $x\left(t\right) \approx x_{sm}\left(t\right)$, where $x_{sm}\left(t\right)$ is the solution to the simple-man

mode. A generic recolliding trajectory of the simple man model, ($Z = 0$) with initial condition (x_0, p_0, ϕ_0) has the solution

$$\begin{aligned} x(t) =& x_0 + (p_0 - \cos\phi_0)\, t + \sin(t + \phi_0) - \sin\phi_0 \\ p(t) =& p_0 + \cos(t + \phi_0) - \cos\phi_0. \end{aligned} \tag{27}$$

We have $x_{sm}(t) - x_{sm}(T) = x_{sm}(t) = (p_0 - \cos\phi_0)(t - T) + \sin(t + \phi_0) - \sin(T + \phi_0)$ where we expand around $t \approx T$ so that $x_{sm}(t) \approx (p_0 - \cos\phi_0)(t - T)$. We then make the transformation so that $\beta_0 = (p_0 - \cos\phi_0)$ and $\theta = (t - T)$ so that the

$$\begin{aligned} \Delta p_z =& -Z \int_{-T}^{0} \frac{\beta_0 \theta}{(\beta_0^2\theta^2 + a^2)^{\frac{3}{2}}} d\theta \\ =& -\frac{Z}{\beta_0} \left[-\frac{1}{\sqrt{(\beta_0^2\theta^2 + a^2)}} \right]_{-T}^{0} \\ \approx& \frac{Z}{\beta_0 a} \end{aligned}$$

We can now compute, ΔP given the contributions from the laser and Coulomb fields. $\Delta P = p(T) - p(0)$ so that $p(T) = p_0 + \Delta p_{sm} + \Delta p_z = p_r$.

$$\begin{aligned} p_r =& p_0 + \cos(t + \phi_0) - \cos\phi_0 + \frac{Z}{\beta_0 a} \\ =& \beta_0 + \frac{Z}{\beta_0 a} \end{aligned}$$

so that the kinetic energy

$$\begin{aligned} \frac{p_r^2}{2} =& \frac{\beta_0^2}{2} + \frac{Z}{a} + \frac{Z^2}{2\beta_0^2 a^2} \\ \approx& \frac{\beta_0^2}{2} + \frac{Z}{a}. \end{aligned}$$

If $p_0 = 0$ then the kinetic energy, $\frac{\beta_0^2}{2}$ gives the maximum return energy of the simple man, the oft-cited $3.17U_p$. In this situation, $\frac{p_r^2}{2} - \frac{Z}{a} \approx \frac{\beta_0^2}{2}$. In this way, we can see how the cancellation takes effect. The Coulomb field, increases the return momentum p_r such that the total return energy is roughly the same as that of the kinetic energy in the simple man model.

In figure 16 we show the dynamics, via the Poincaré section $x = 0$ for the simple-man model. The section is chosen to be $x = 0$ because this is the condition for a recollision to take place. The variable, ϕ, is the phase of the laser when the electron returns. The blue curve is the set of fixed points corresponding to the simple-man periodic orbit. The simple-man periodic orbit is the only orbit which exists when $Z = 0$, and can be found analytically. The initial condition is given by $(x_0 = 0, p_0 = E_0/\omega)$. Interestingly, this orbit, can be followed by continuity by increasing Z to the case when $Z = 1$, where it is actually the $m = 1$ resonance. The black points correspond to random initial conditions, generated on the Poincaré section, i.e. $x = 0$, $p < 0$, and $\phi \in [0, 2\pi]$. We see that there is a clustering of points around the periodic orbit, whereby points that begin close to the orbit stay close for some amount of time. The stability of the family of orbits at $Z = 0$ is parabolic. The largest kinetic energy of the orbit occurs when $\phi = \pi$ and the kinetic energy is precisely $2U_p$. We know analytically however, that when $Z = 0$ another trajectory exists which can bring back the maximum return energy of approximately $3.17U_p$. This trajectory exists at the very bottom of the distribution of black points where $\phi \approx 2.8$. The simple-man argument has been a long held truth of the strong-field physics community, and has been considered valid for $Z = 1$. This is despite the fact that the Coulomb field can be sufficiently strong, when compared to the laser term, even at high intensity. In the insets of figure 17 we show a comparison between the periodic orbit of the simple man model with that of the $m = 1$ resonance at $Z = 1$ for $I = 10^{14}$, and $I = 10^{15}$ W $\cdot$ cm^{-2} as we move from left to right. We see that at low intensity the two orbits are almost completely unrelated, but as you increase the intensity, and move towards the simple-man scenario, the orbits converge everywhere, except near the nucleus, i.e. $x = 0$, where the $m = 1$ orbit always has a slight, cusp-like increase in its momenta. This increase in momenta is due to the Coulomb potential and is the manifestation of the cancellation shown earlier. Likewise, the main figure of the panel

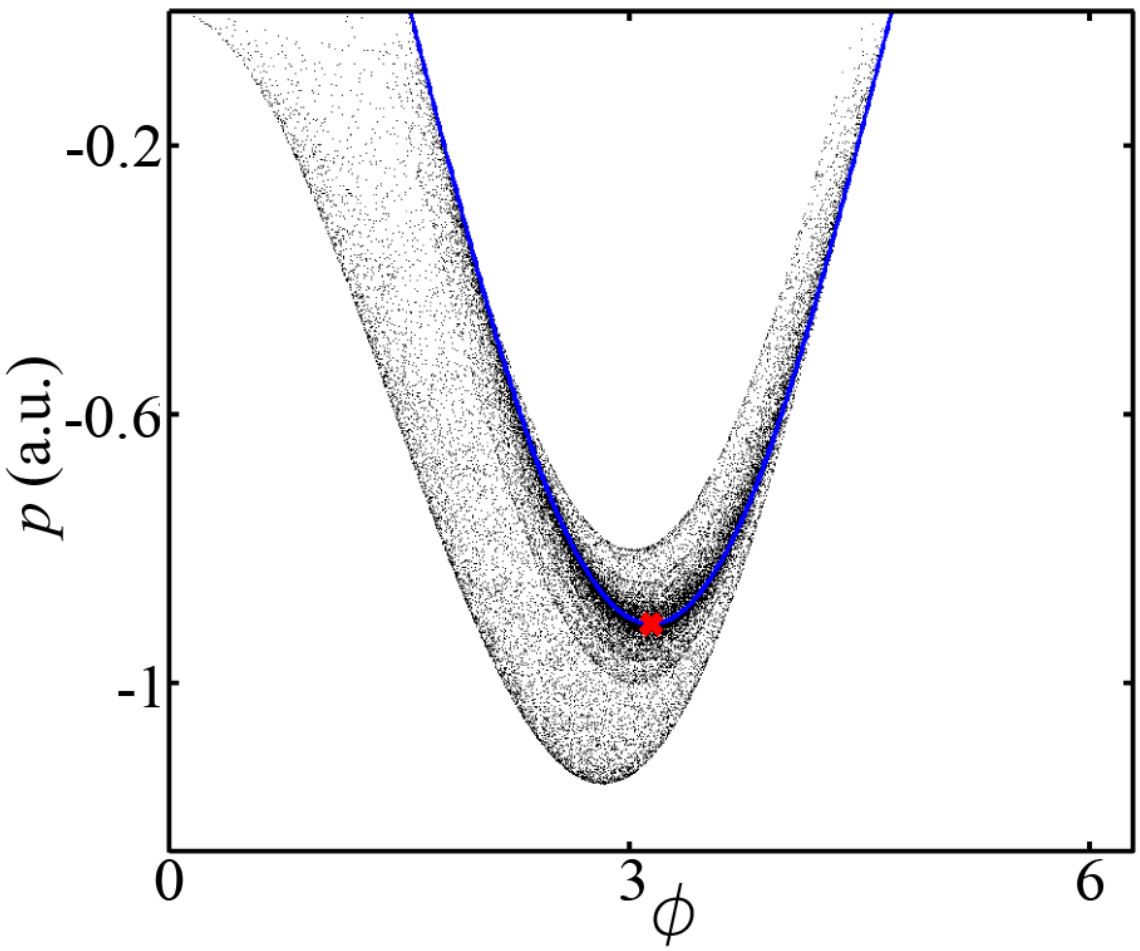

Figure 16: Poincaré sections of Hamiltonian (23) at $I = 10^{14}$ W $\cdot$ cm^{-2} for $Z = 0$, i.e. the simple-man scenario.

shows the return energy of both the $m = 1$ resonance (red curves) and the maximum return energy allowed by the dynamics (blue curves). In this situation, we consider the return energy to be the energy as the electrons reaches its point of closest return to the core. The solid lines correspond to the case when the return energy is taken to be the sum of the kinetic and potential energy, while the dashed lines only take into account the kinetic energy. In both situations, the return of the $m = 1$ orbit (red curves) converges to $2U_p$ (the same as the simple-man orbit), while the blue curves converges to $3.17U_p$. The convergence to $3.17U_p$ of the maximum return energy is expected, because as we increase the intensity, we approach the simple-man scenario, in which the laser field is dominant over the Coulomb field. However, even at high intensities such as $I = 10^{15}$ W $\cdot$ cm^{-2}, both blue curves are noticeably different than their convergent value. Most notable, however, is the difference between the two blue curves. It shows that the simple-man model is not valid at $Z = 1$ (at least for $I \leq 10^{15}$ W $\cdot$ cm^{-2}), otherwise, the inclusion of the Coulomb field in the energy calculation would be negligible. It has been shown above that the dynamics, even at $Z = 1$ allows for a maximum return of approximately $3.17U_p$. We've already given both a qualititative and quantitative explanation of why the simple-man model is valid above $Z = 0$ at the beginning of the section, i.e. the cancellation effect of the Coulomb field. However, we have not yet treated how the dynamics allows for a maximum return energy. In figure 18 we make use of the Poincaré section $x = 0$ to visualize the stable $\mathcal{W}^s$ and unstable $\mathcal{W}^u$ manifolds of the $m = 1$ resonance at $I = 10^{14}$ W $\cdot$ cm^{-2}. The orbit location on the section is designated by the red square and since the section is $x = 0$ each point can be viewed as a return of the electron. The maximum returning energy along the unstable manifold occurs at the largest (absolute value) of p, in this case $p \approx -1.94$ a.u., resulting in a return energy of approximately $4.24U_p$ (including the Coulomb potential). This is quite close to the solid red curve of figure 17 which was computed from trajectories with random initial

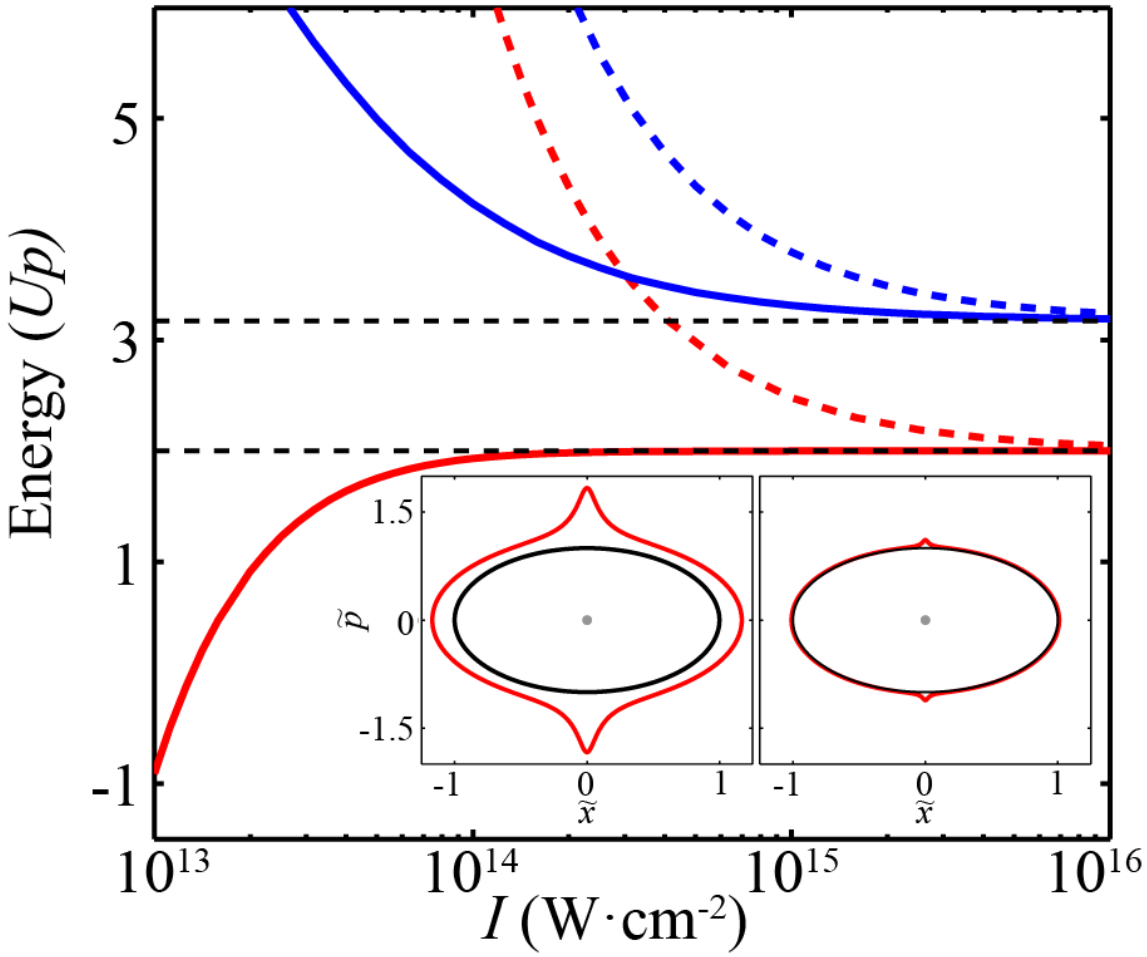

Figure 17: Maximum return energy (solid lines) and maximum return kinetic energy (dashed lines) accessible to the dynamics (blue) and on the periodic orbit $\mathcal{O}$ (red). Insets: The red orbits are the periodic orbits $\mathcal{O}$ at $I = 10^{14}$ (left) and $I = 10^{15}$ W·cm^{-2} (right), while the black orbit is the SFA periodic orbit (in the absence of Coulomb interaction). The $\tilde{x}$ and $\tilde{p}$ axes are scaled in units of E_0/ω^2 and E_0/ω, respectively.

conditions. When $Z \neq 0$, in order for a trajectory to return with maximum energy (or close to maximum energy) it must be following closely the unstable manifold of the $m = 1$ resonance. The case of $Z = 0$ is actually special, in the sense that the $m = 1$ orbit has parabolic stability, i.e. its stability cannot be determined from a linear analysis. A higher-order analysis does indeed show the orbit is unstable, however, only slightly. Therefore, a trajectory starting closeby the orbit along the unstable manifold would have to be integrated for a very long time to reach the maximum return energy. The color surface, placed on top of the manifolds, shows the regions in phase space where returns will take place. The color corresponds to exactly how many returns that will be. We see that areas which yield more returns lie closer to the manifolds, showing that it is indeed the manifolds which organize the recollision process (not just the dynamics of the trajectory which return with maximum energy). The bounding box surrounds the red, circular marker, which shows the point in phase space which leads to the trajectory which returns with maximum energy. The inset gives an exploded view of the bounding box for clarity. We see that the red marker is contained in the region known as the homoclinic tangle, where the stable and unstable manifolds intersect. The other areas of intersection, or homoclinic tangles, correspond to maximum return times for specific pulse durations. The longer the pulse is, the bigger is the maximum, and in order to reach the highest maximum return energy, the pulse has to be of infinite length–an impractical scenario. However, once more the differences between these maxima are not significant enough to be observed experimentally on HHG spectra. For instance, at the low intensity of 10^{14} W $\cdot$ cm^{-2}, the maximum return energy is 3.86 U_p after one laser cycle, and 4.24 U_p after 25 laser cycles. if the ponderomotive energy is low, this difference corresponds to a very small number of harmonics in the spectrum.

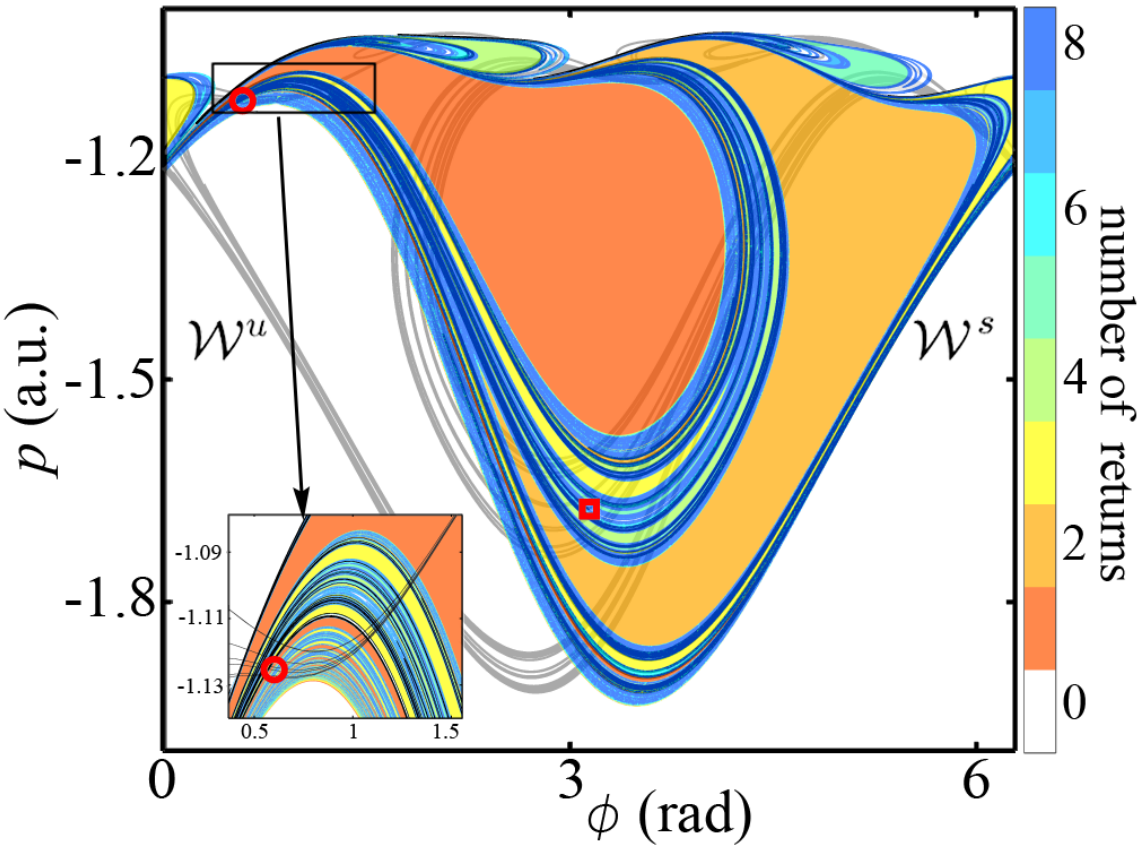

Figure 18: Stable ($\mathcal{W}^s$) and unstable manifolds ($\mathcal{W}^u$) of the periodic orbit $\mathcal{O}$ visualized on the Poincaré section $x = 0$. The intensity is $I = 10^{14}$ W $\cdot$ cm^{-2}. The red square marker corresponds to the location of the periodic orbit on the section. The colored areas correspond to regions in phase space (on the section) where trajectories return. The color scale denotes the number of returns. The trajectories initiated in the white region ionize without returning to the core, or remain bound by the Coulomb potential indefinitely. The bounding box on the top left of the figure is the region shown in the inset. The red circular marker denotes the initial condition which results in an electron returning with maximum energy.

3.2.5 High harmonic generation

The significance of the manifold picture of returning trajectories can be further illustrated in the quantum mechanial HHG distribution shown in figure 19. We solve the one dimensional Schödinger Equation (shown in atomic units)

$$i\partial_t \psi(x,t) = \left(-\frac{\Delta}{2} + \mathrm{V}(x) + \mathrm{E}(x,t)\right)\psi(x,t) \tag{28}$$

numerically with a split-operator method. The radiation field is computed from the Fourier transform of the dipole acclereration $\{\mathbf{R}_{\nu_{HHG}} = \mathcal{F}\left[< \psi(t) \left|\ddot{x}(t)\right| \psi(t) >\right](\nu_{HHG})\}$[37]. In the top two panels we initialize the wavepacket in the ground state of the quantum mechanical equivalent to Hamiltonian (23). In the top left panel we show the HHG spectra at the relatively low intensity of $I = 5 \cdot 10^{14}$ W $\cdot$ cm^{-2}. The vertical lines are the energy, given in harmonic numbers, at which we expect HHG cut-off to occur, given the formula, $E_c = (\kappa U_p + I_p)/\omega$. κ is determined by the curves shown in figure 17. For example, at $I = 5 \cdot 10^{14}$ W $\cdot$ cm^{-2}, we expect a maximum return energy of $\kappa \approx 4.5$ if we do not include the potential energy in the calculation, and $\kappa \approx 3.5$ if we do. The vertical lines in the other panels of the figure are also matched, both in color and line style, with figure 17. We see that a energy calculation which does not involve the potential energy misses the HHG cutoff by several tens of harmonics. In the right panel of the top row, where we move to the higher intensity of $I = 10^{15}$ W $\cdot$ cm^{-2}, the cut-off predictions are too close together, to determine which is more accurate. This is because at high intensity the solid and dashed blue lines of figure 17 have both almost converged to $\kappa \approx 3.17$. In the bottom panels of the same figure we show similar HHG spectra, however, for a scattering scenario. Figure 20 gives an illustration of our scattering scenario. We initialize the wavepacket on the $m = 1$ periodic orbit at the point where it is furthest from the core region (marked as $t = 0$). We then phase shift the laser so that it sends the wavepacket toward the core region. We cross the core at $t = 0.25$ and $t = 0.75$ laser cycles (modulus 1). The

harmonics generated from this event are what is shown in the figure. The intensities in the bottom row of figure 19 are the same as those used in the top row, however, unlike the top row, these new spectra each contain two plateaus and two cut-offs. These cut-offs are again contrasted with the expected cut-offs calculated with solid and dashed curves of figure 17. However, we now include the return energies of the $m = 1$ resonance (red curves of figure 17) for the first plateau, not present in the top row. In the low intensity case (left panel) we again see that the solid vertical lines, which include the potential energy in the calculation of κ are a much better prediction for the cut-off. This is true for both cut-offs. At higher intensity (right panel), again the cut-off associated with the blue curves is somewhat ambiguous in the sense that the two blue vertical lines are only a few wavenumbers apart. However, the first cut-off is clearly better predicited by a κ including the potential energy. We see that the simple-man model, which considers the Coulomb field to be neglible, cannot be used to predict HHG cut-off.

Indeed, the manifolds of the $m = 1$ resonance are not unique, in the sense that the manifolds of other orbits also bring back the maximum return energy. Figure 18 clearly shows the intersections of the stable and unstable manifold. Other resonant orbits of Hamiltonian (23) exist at the intersections of the these manifolds. The red and green circular markers correspond to the $m = 3$ and $m = 5$ resonances, respectively. Due to these heteroclinic connections, recolliding trajectories will experience influences from a combination of many resonant orbits, however, those orbits of shorter period, i.e. $m = 1$ and $m = 3$ will be more dominant.

3.3 A brief note on elliptical polarization

The orbits discussed already belong in the 1 DOF (plus time) system. However, to examine what happens when the laser field becomes ellipitical we must add an additional spatial dimension to account for the fact that in ellipticities other an linear

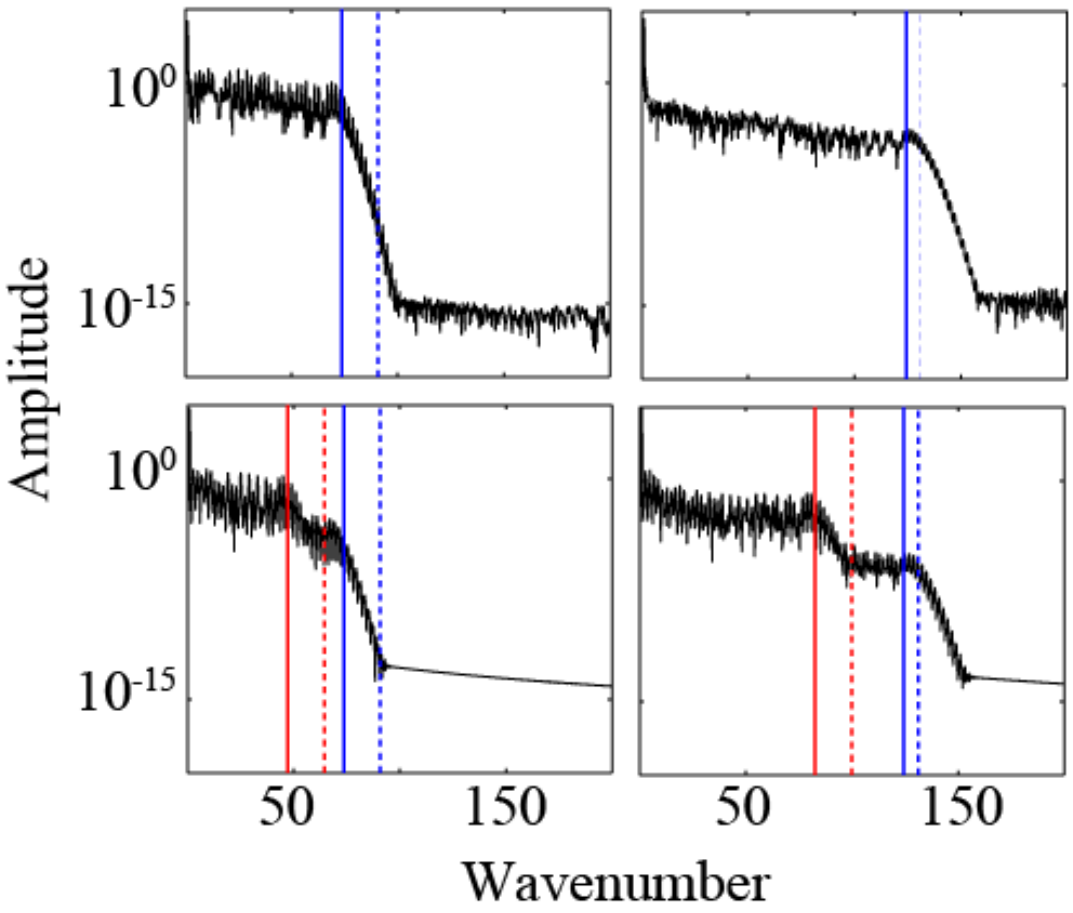

Figure 19: The top row shows the quantum mechanical high harmonic generation (HHG) spectra for $I = 5 \cdot 10^{14}$ W $\cdot$ cm^{-2} (left) and $I = 10^{15}$ W $\cdot$ cm^{-2} (right) with the wavepacket initialized in the ground state. The bottom rows show the HHG with the wave packet initialized at the outer left point of the $m = 1$ resonance with the laser field directing the wavepacket towards the core at $t = 0$. The intensities used in the left and right panels are the same as those used in the top row. In all panels the vertical lines mark the cut-off with the return energy found from their corresponding curve in figure 17. HHG is obtained from a numerical integration of the 1 dimensional Schrödinger equation via a split operator method.

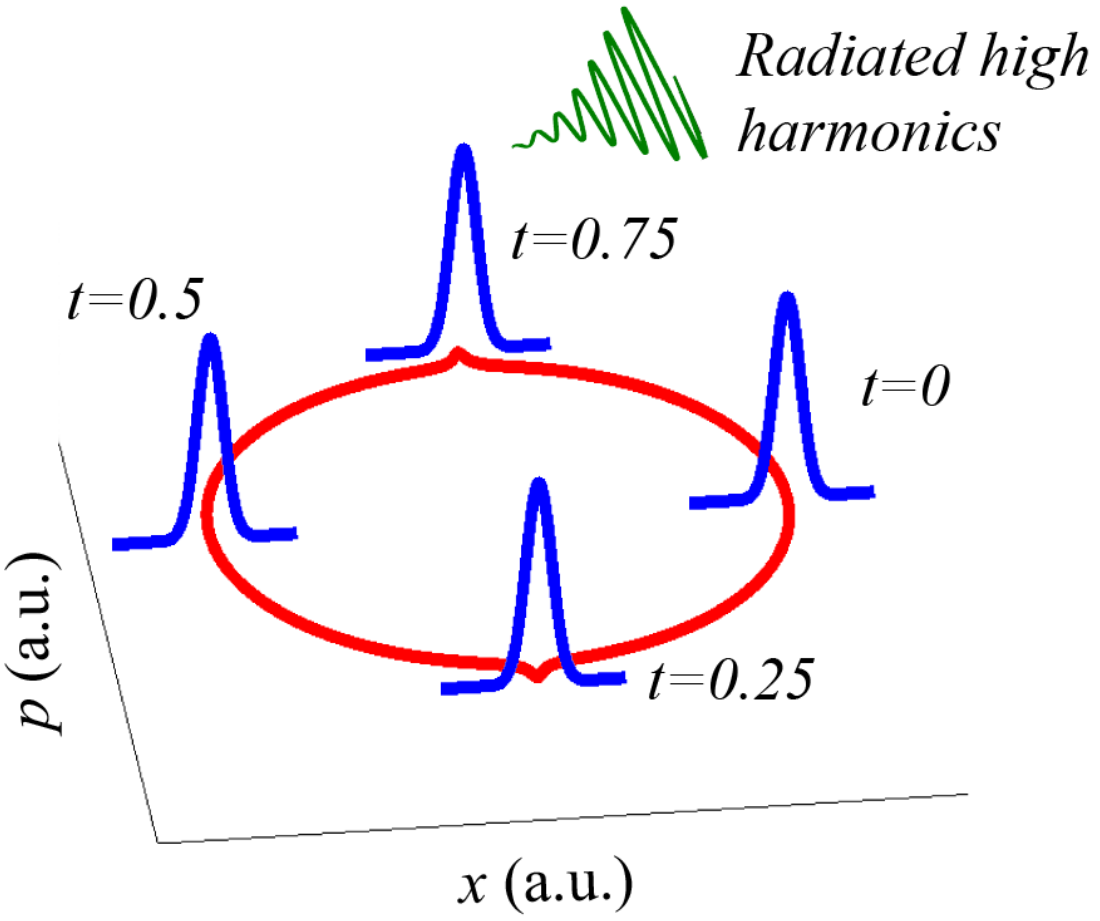

Figure 20: Illustration of the scattering scenario whose HHG spectra is shown in the bottom panels of figure 19.

the laser polarization exists on the plane, and not on the line. Hamiltonian,

$$\mathcal{H}_{inner}\left(x,y,p_x,p_y,t\right)=\frac{p_x^2}{2}+\frac{p_y^2}{2}-\frac{Z}{\sqrt{x^2+y^2+1}}+E_0\left(x\sin\omega t+\epsilon y\cos\omega t\right) \quad (29)$$

describes a one electron, two spatial dimension system, with ellipticity ϵ. E_0, while still the electric field amplitude, is now re-scaled by the factor $\frac{1}{\sqrt{(1+\epsilon^2)}}$ so that the time averaged Poynting vector remains constant in magnitude across the ellipticity range. The Hamiltonian is now 2.5 degrees of freedom (or 2 DOF + time) which introduces some additional complexity. Namely, the Poincaré sections utilized in the previous section are now four dimensional, and therefore, unless we wish to look at projections of the section (which introduces its own problems) we must rely on other methods.

Despite the additional degree of freedom, the periodic orbits shown in the previous section (derived from the resonance structure of Hamiltonian (23) can be extended to our new system. In figure 21 we show the bifurcation diagrams in the (ϵ, I) plane of the $m=1$ (left panel) and $m=3$ (right panel) periodic orbits discussed previously. The color scale denotes the absolute value of the largest eigenvalue associated with the periodic orbit at its respective value of I and ϵ. For the $m=1$ periodic orbit (left panel), the light grey curve, around the upper boundary of the diagram and along the line $\epsilon=1$ is used to denote where the orbit is elliptic ($|\lambda_{max}|=1$). Likewise, the region above the dashed black line shows where the periodic orbit has a sufficient spatial extent to affect the recolliding dynamics, i.e. qualifies as an RPO. We see that at low intensity and/or high ellipticity the $1:1$ resonance does not play a major role in the recollision process. For the periodic orbit $m=3$ (right panel), the orbit always qualifies as an RPO and does not bifurcate, hence no grey and/or black curves are necessary. Both orbits exist at higher intensity than is shown in the panels, however, we enforce a cut-off stability of $|\lambda_{max}|\leq 10^4$. Going beyond an analysis of the periodic orbits is difficult for the aforementioned reason of an additional DOF. In the previous section we gave a detailed explanation of the returning mechanism in LP (and we will

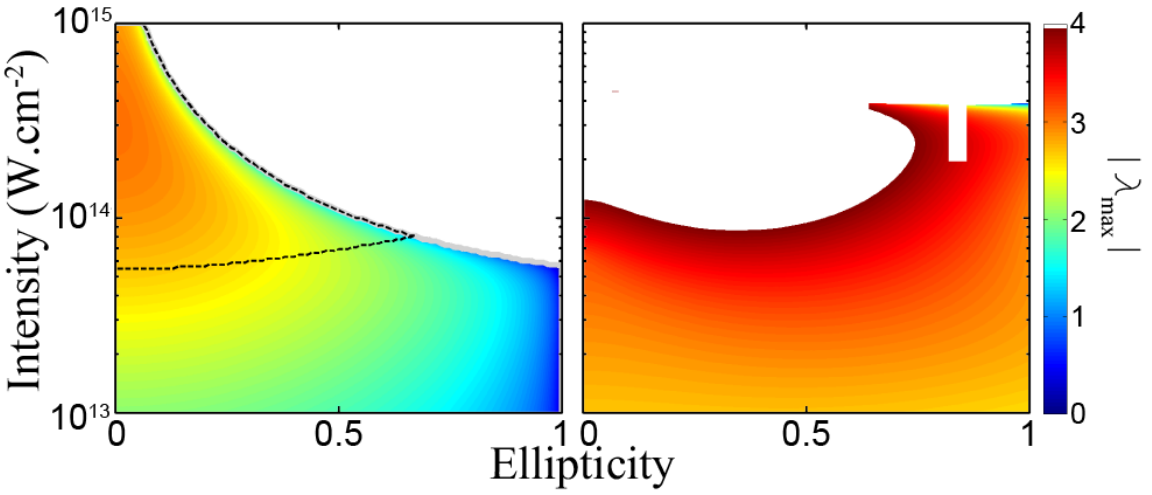

Figure 21: Bifurcation diagram of the $m = 1$ (left panel) and $m = 3$ (right panel) resonance in the (ϵ, I) plane. The light grey curve shows where the periodic orbit becomes elliptic ($|\lambda_{max}| = 1$), while the dashed black curves show where the respective orbit qualifies as an RPO. The color bar corresponds to the largest eigenvalue of the monodromy matrix in logarithmic scale.

do similarly for CP in the next chapter), however, the analysis of EP will require a new set of tools.

3.4 Conclusion

In this chapter we have explained recollisions in a linearly polarized field through phase space structures. Briefly, the single electron reduced Hamiltonian is integrable (Arnold-Liouville) when the laser field is turned off. With only a slight increase in the laser intensity invariant tori break, forming elliptical islands and hence periodic orbits. By Birkhoff's theorem, these elliptic periodic orbits have a hyperbolic periodic orbit associated with them which can also be found because they exist with approximately the same action and hence roughly between the same tori as their elliptical counterpart. We've shown, by examining random returning trajectories, that these orbits organize the recolliding dynamics. This has been shown by a comparison in phase space of the shape of the trajectories with the aforementioned orbits and by an analysis of Poincaré sections of random returning trajectories with stable and

unstable manifolds of orbits.

By examination of the stable and unstable manifolds of the periodic orbit associated with the $m = 1$ resonance we've seen that a trajectory closely following the manifold has the possibility of returning to the core with the maximum allowable kinetic energy. This is of special importance, because previously the maximum returning energy has been computed incorrectly by neglecting the Coulomb force which is inconsistent because the Coulomb field is required in the initial ionization step of the simple-man model. The manifold picture, however, is consistent in the sense that the Coulomb field is included, and indeed we show that the effect of the Coulomb field is self-cancelling in the sense that if it is entirely neglected one can still compute quantitatively correct maximum return energies. In following chapters we wil move away from linearly polarized laser fields into the circularly polarized regime

CHAPTER IV

SINGLE ELECTRON DYNAMICS IN A COMBINED COULOMB AND CIRCULARLY POLARIZED LASER FIELD

4.1 Introduction

Can an ionized electron be driven back to the core by an ultrastrong CP laser pulse? As explained in the introductory chapter, this is a high-stakes issue in attosecond physics since the returning electron, by carrying back the energy it has absorbed from the laser, can act as the agent of many key processes in intense laser physics [38], including the ultrafast imaging of macromolecules [39] and the design of new light sources through generation of ultrahigh harmonics [17]. The arguments explaining recollision with linear polarization, which were introduced in the prevoius chapter, also predict its absence in a CP field because ionized electrons tend to spiral away from the core [18]. When a knee was found for magnesium with a CP field [8] a decade ago, recollision was immediately ruled out as a possible explanation. Recently, we reconciled this surprise with other experimental results in CP [25] where no knee was observed [7], by showing that recollision is possible with CP [40] (see also references [41],[42]).

In this chapter we show that recollisions in CP result from a subtle compromise between the action of the strong laser field (which leads the electron away in a swirling motion) and the Coulomb attraction (which tends to recall it). Special families of RPOs turn out to be this compromise, similar to the LP case.

When the laser field is circularly polarized the magnitude of the laser field remains unchanged with respect to time. Only the direction of the field changes. We begin

with a Hamiltonian which models a single electron moving in two spatial dimensions under the influence of a circularly polarized field.

$$\mathcal{H}(x, y, p_x, p_y, t) = \frac{p_x^2}{2} + \frac{p_y^2}{2} + V(r) + E_0 (x \sin \omega t + y \cos \omega t) . \tag{30}$$

The potential, $V(r)$ where $r = \sqrt{x^2 + y^2}$ is rotationally invariant. In this chapter we use the soft-Coulomb potential of eq. 8 with $Z = 2$. The value of Z is a departure from the normally used value of $Z = 1$, however, the dynamics illustrated below do not qualitatively change with Z. From a physical view, choosing $Z = 2$ corresponds to a double ionized ion.

We transform to a frame co-rotating with the laser field such that it becomes a constant. This transformation, however, must be canonical so that the equations of motion can still be derived from Hamilton's equations.

4.2 Autonomizing the static frame Hamiltonian

First however, we introduce the autonomized version of Hamiltonian (30), referred to now as the static frame Hamiltonian. This is accomplished by adding the canonically conjugate pair (t, E), so that the new Hamiltonian, $\bar{\mathcal{H}}$ is conserved. Our transformation is $\bar{\mathcal{H}}(x, y, t, p_x, p_y, E) = \mathcal{H}(x, y, p_x, p_y; t) + E$. If we apply Hamilton's equations to the transformed Hamiltonian

$$\dot{t} = \frac{\partial \bar{\mathcal{H}}}{\partial E} = 1$$

$$\dot{E} = -\frac{\partial \bar{\mathcal{H}}}{\partial t} = -\frac{\partial \mathcal{H}}{\partial t} = E_0 \omega (x \cos(\omega t) - y \sin(\omega t))$$

where $\cdot$ represents differentiation with respect to our new evolution parameter τ. Hamilton's equations applied to the other pairs of conjugate variables are unchanged by this transformation.

4.3 Rotating Frame Hamiltonian

With an autonomized Hamiltonian we now perform the canonical change of coordinates into the frame co-rotating with the laser field.

This section can be skipped on a first reading, with the reader advancing directly to section 4.4.

$$\mathbf{\Omega}(\mathbf{t}) = \begin{pmatrix} \sin(\omega t) & \cos(\omega t) \\ \cos(\omega t) & -\sin(\omega t) \end{pmatrix} \tag{31}$$

such that

$$\begin{pmatrix} \bar{x} \\ \bar{y} \end{pmatrix} = \mathbf{\Omega} \begin{pmatrix} x \\ y \end{pmatrix} \tag{32}$$

and

$$\begin{pmatrix} \bar{p}_x \\ \bar{p}_y \end{pmatrix} = \mathbf{\Omega} \begin{pmatrix} p_x \\ p_y \end{pmatrix} \tag{33}$$

where the barred coordinates are measured in the rotating frame.

Furthermore, since $\mathbf{\Omega} = \mathbf{\Omega^{-1}}$ we can immediately say that

$$\begin{pmatrix} x \\ y \end{pmatrix} = \mathbf{\Omega} \begin{pmatrix} \bar{x} \\ \bar{y} \end{pmatrix} \tag{34}$$

and likewise for the momentum.

Applying the transformation $\mathbf{\Omega}(t)$ to our transformed Hamiltonian, $\bar{\mathcal{H}}$ yields yet another transformed Hamiltonian

$$\mathcal{K} = \frac{\bar{p}_x^2}{2} + \frac{\bar{p}_y^2}{2} + V(r) + E_0\bar{x} + E\left(\bar{x}, \bar{y}, \bar{t}, \bar{p}_x, \bar{p}_y, \bar{E}\right) \tag{35}$$

where $\mathcal{K}$ is also referred to as the Jacobi constant from its link to celestial mechanics. We must now find out how $E \to \bar{E}$ while remembering that in the end we must have a canonical transformation from

$$\begin{pmatrix} x \\ y \\ t \\ p_x \\ p_y \\ E \end{pmatrix} \xrightarrow{\text{canonical}} \begin{pmatrix} \bar{x} \\ \bar{y} \\ \bar{t} \\ \bar{p}_x \\ \bar{p}_y \\ \bar{E} \end{pmatrix} \tag{36}$$

.

In order to verify that the transformation is canonical it is sufficient to show that $\mathbf{J} = \mathbf{M^T J M}$, where $\mathbf{M}$ is the Jacobian matrix given by

$$\mathbf{M_{ij}} = \frac{\partial \xi_\mathbf{i}}{\partial \eta_\mathbf{j}} \tag{37}$$

where ξ is given by

$$\xi = \begin{pmatrix} q_1 & q_2 & \dots & q_n & p_1 & p_2 & \dots & p_n \end{pmatrix}^T \tag{38}$$

and n is the number of degrees of freedom in the system ($n = 3$ for our autonomized system) and η is a vector of identical form containing the new coordinates.

$\mathbf{J}$ is a $2n \times 2n$ symplectic matrix

$$\mathbf{J} = \begin{pmatrix} \mathbf{0} & \mathbf{1} \\ \mathbf{-1} & \mathbf{0} \end{pmatrix} \tag{39}$$

whose elements are $n \times n$ identity and zero matrices.

Our goal then is how to transform $E \to \bar{E}$ so that the overall transformation for $\eta \to \xi$ is canonical. We begin by calculating the matrix product $\mathbf{M^T J M}$.

$$\mathbf{M} = \begin{pmatrix} \sin\omega t & \cos\omega t & \omega\bar{y} & 0 & 0 & 0 \\ \cos\omega t & -\sin\omega t & -\omega\bar{x} & 0 & 0 & 0 \\ 0 & 0 & 1 & 0 & 0 & 0 \\ 0 & 0 & \omega\bar{p}_y & \sin\omega t & \cos\omega t & 0 \\ 0 & 0 & -\omega\bar{p}_x & \cos\omega t & -\sin\omega t & 0 \\ \frac{\partial\bar{E}}{\partial x} & \frac{\partial\bar{E}}{\partial y} & \frac{\partial\bar{E}}{\partial t} & \frac{\partial\bar{E}}{\partial p_x} & \frac{\partial\bar{E}}{\partial p_y} & \frac{\partial\bar{E}}{\partial E} \end{pmatrix} \tag{40}$$

$$\mathbf{J} = \begin{pmatrix} 0 & 0 & 0 & 1 & 0 & 0 \\ 0 & 0 & 0 & 0 & 1 & 0 \\ 0 & 0 & 0 & 0 & 0 & 1 \\ -1 & 0 & 0 & 0 & 0 & 0 \\ 0 & -1 & 0 & 0 & 0 & 0 \\ 0 & 0 & -1 & 0 & 0 & 0 \end{pmatrix} \tag{41}$$

When the matrix product is equated to $\mathbf{J}$ it provides us with conditions on the partial derivatives of $\bar{E}$ w.r.t the old coordinates, so that $\bar{E}\left(x, y, t, p_x, p_y, E\right)$ can be found. This process yields the following five equations

$$\begin{aligned} -\frac{\partial\bar{E}}{\partial x} - \bar{p}_x\omega\cos\omega t + \bar{p}_y\omega\sin\omega t &= 0 \\ -\frac{\partial\bar{E}}{\partial y} + \bar{p}_x\omega\sin\omega t + \bar{p}_y\omega\cos\omega t &= 0 \\ \frac{\partial\bar{E}}{\partial p_x} - \bar{x}\omega\cos\omega t + \bar{y}\omega\sin\omega t &= 0 \\ \frac{\partial\bar{E}}{\partial p_y} + \bar{x}\omega\sin\omega t + \bar{y}\omega\cos\omega t &= 0 \\ \frac{\partial\bar{E}}{\partial E} &= 1 \end{aligned}$$

which implies

$$\begin{aligned}
\frac{\partial \bar{E}}{\partial x} &= -\omega p_y \\
\frac{\partial \bar{E}}{\partial y} &= \omega p_x \\
\frac{\partial \bar{E}}{\partial p_x} &= \omega y \\
\frac{\partial \bar{E}}{\partial p_y} &= -\omega x.
\end{aligned}$$

With these 5 relationships we know that

$$\bar{E}\left(x, y, t, p_x, p_y, E\right) = E - \omega\left(x p_y - y p_x\right) \tag{42}$$

With this expression for $\bar{E}$, we can express our transformed Hamiltonian in the rotating frame completely in terms of the new coordinates. Furthermore, since $\bar{E}$ was solved for in a manner to guarantee $\mathbf{J} = \mathbf{M^T J M}$ we are assured that the transformation is canonical and that Hamilton's equations will hold with the new variables.

$$\mathcal{K} = \frac{\bar{p}_x^2}{2} + \frac{\bar{p}_y^2}{2} + V\left(\bar{r}\right) + E_0 \bar{x} + \bar{E} + \omega\left(x p_y - y p_x\right) \tag{43}$$

Now we make use of the transformation equation $\mathbf{\Omega}\left(t\right)$ to change $(x, p_x, y, p_y) \rightarrow (\bar{x}, \bar{p}_x, \bar{y}, \bar{p}_y)$ and we arrive at the final expression for the rotating frame Hamiltonian,

$$\mathcal{K}\left(\bar{x}, \bar{y}, \bar{t}, \bar{p}_x \bar{p}_y \bar{E}\right) = \frac{\bar{p}_x^2}{2} + \frac{\bar{p}_y^2}{2} + V\left(\bar{r}\right) + E_0 \bar{x} - \omega\left(\bar{x}\bar{p}_y - \bar{y}\bar{p}_x\right) \tag{44}$$

where we have set $\bar{E} = 0$, since it is constant. The addition of the final term, which is indeed a Coriolis term, is not surprising, since after all we are moving into a rotating frame. Therefore, the price to pay for an autonomized system is a mixed term in the Hamiltonian.

This Hamiltonian, referred to as the rotating frame Hamiltonian, will be used throughout the remainder of this section and also in chapter 5 (with $Z = 1$), however, we remove the "barred" notation for simplicity. The Hamiltonian, also refered to as

the Jacobi value, for its link to celestial mechanics, is time independent and therefore, conserved. Additionally, when the laser field is turned off ($E_0 = 0$), the angular momentum is also conserved because of the rotational invariance. This is especially important because with two conserved quantities our Hamiltonian is integrable (in regions of phase space which are bounded). In section 4.5.2 we focus especially on the case when $E_0 = 0$. Also, keep in mind that the potential was left generic, and this transformation is valid for any rotationally invariant potential.

4.4 Construction of the Zero-Velocity Surface

To better understand the dynamics generated by Hamiltonian (44) it is useful to construct the Zero Velocity Surface (ZVS). On this surface, the condition $\dot{x} = \dot{y} = 0$ is enforced, and the surface is therefore used to show the allowable region in configuration space.

From Hamilton's equations applied to Hamiltonian (44) we have

$$\dot{x} = p_x + \omega y,$$

$$\dot{y} = p_y - \omega x,$$

solving for p_x and p_y and plugging into Hamiltonian (44) while simultaneously enforcing the zero velocity condition that $\dot{x} = \dot{y} = 0$ yields the zero-velocity surface

$$\mathcal{V}(x, y) = -\frac{1}{2}\omega^2 \left(x^2 + y^2\right) + E_0 x + V(r).$$

In general, we show a cross section of this surface, along the line $y = 0$. Looking ahead, a 3D visualization of the surface is shown in chapter 5. In figure 22 we show the cross section of the ZVS for $y = 0$. In the left panel we show the ZVS for the integrable case while the right panel is $I = 10^{13}\,\mathrm{W}\cdot\mathrm{cm}^{-2}$. In the left panel $\mathcal{K} = -0.5$ gives a completely bounded dynamics while $\mathcal{K} = -0.34$ and $\mathcal{K} = -0.25$ both give a combination of bounded and unbounded dynamics. Likewise, in the right panel

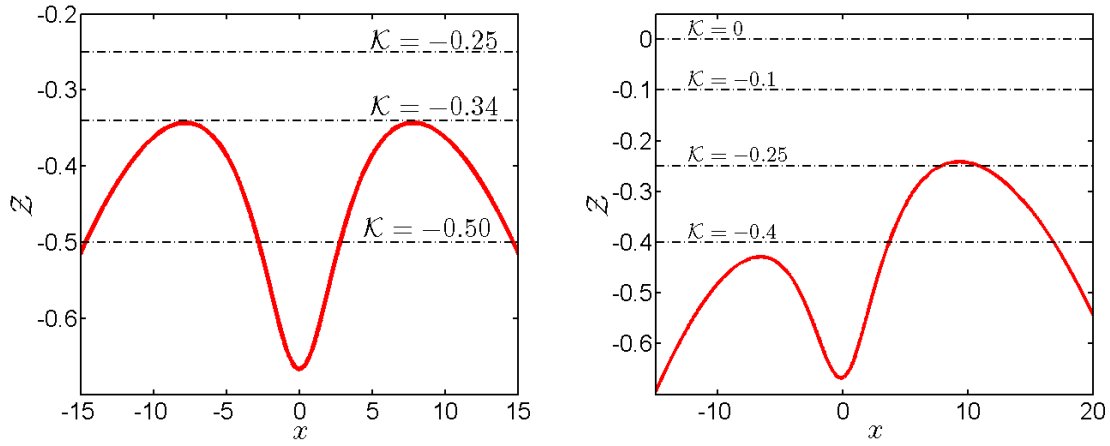

Figure 22: The left panel is the Zero Velocity Surface for the integrable case, $E_0 = 0$. Right panel is the Zero Velocity Surface for the non-integrable case of $I = 10^{13}$ W $\cdot$ cm^{-2}. The dashed horizontal lines correspond to the commonly used Jacobi values throughout the rest of this chapter. For both figures, $\omega = 0.0584$ a.u.

all Jacobi values shown correspond to a combination of bounded and unbounded dynamics.

4.5 Examining the dynamics

In order to understand the dynamics of this system, namely the driving mechanism behind recollisions, it is important to look at sample trajectories to gain a better intuition of the system. After an examination of these trajectories a scenario involving the structures in phase space can be constructed, keeping in mind the results from the LP case.

4.5.1 Samples of returning trajectories

In figure 23 we focus on the trajectories which exhibit a return. In the top two panels, the Jacobi value is fixed at $\mathcal{K} = -0.25$ whereas in the bottom panel the Jacobi value is $\mathcal{K} = -0.1$. In each panel the dashed black curve marks the return threshold of 5 a.u. Certain shapes come up often when examining recolliding trajectories. These shapes are highlighted in each of the panels. In the top two panels the same shapes come up in each trajectory. In the bottom panel the darker blue shape is similar to

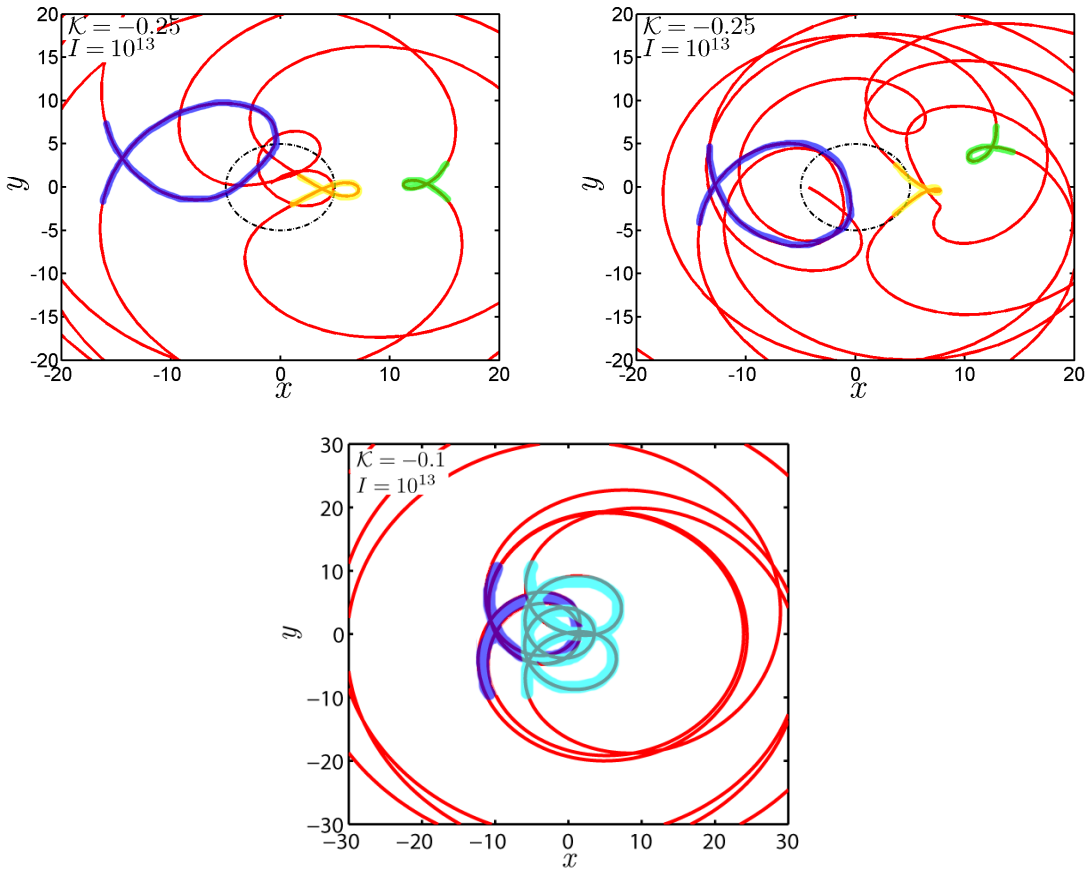

Figure 23: Several samples of returning trajectories. Segments of each trajectory which resemble the various periodic orbits in figure 26 are highlighed in blue ($\mathcal{O}_n$), green ($\mathcal{O}'_n$), and yellow ($\mathcal{H}_n$). For all panels $I = 10^{13}\ \mathrm{W \cdot cm^{-2}}$ and $\omega = 0.0584$ a.u.

the dark blue shapes in the top panel, but an additional shape, shown in light blue is also highlighted. It is easy to see that certain patterns repeat themselves across different trajectories and even different Jacobi values.

4.5.2 Integrability of the rotating frame Hamiltonian

To gain a better understanding of the returning trajectories shown in the previous section (especially the recurring patterns), we take a closer look at the dynamical system. First, we examine the integrable part of Hamiltonian (44), whereby $E_0 = 0$. The rotational invariance along with the time independence provides two constants of motion with which we can reduce the dimension of the dynamics. With a two degree

of freedom Hamiltonian and two constants of motion, our dynamics is integrable in the Arnold-Liouville sense, at least locally for regions which yield bounded trajectories. Of course, turning off the laser for Hamiltonian (44) seems artifical, because this Hamiltonian was generated by a transformation into a frame co-rotating with the laser field, itself. To ease this reluctance, however, recall that once we have made this transformation we can dissociate the Hamiltonian from the physical system it is meant to represent and simply treat it as a generator of a dynamics, whereby E_0 is simply another parameter.

As already mentioned, however, the system is only integrable when the dynamics is bounded in phase space. By construction of a Poincaré section we can get a sense for which parameter choices the dynamics will indeed be bounded. We choose as the Poincaré section $xp_x + yp_y = 0$. This section, shown in Cartesian coordinates is not an intuitive choice. However, by making the canonical change to polar coordinates,

$$\begin{aligned} r &= \sqrt{(x^2 + y^2)} \\ \theta &= \arctan \tfrac{y}{x} \\ p_r &= (xp_x + yp_y)/r \\ p_\theta &= xp_y - yp_x \end{aligned}$$

we see that the section is equivalent to $p_r = 0$ (with $\dot{p_r} > 0$), which corresponds to changes in sign of the radial momentum.

We show Poincaré sections for three different Jacobi values in figure 24. For $\mathcal{K} = -0.5$ phase space is bounded, which can also be seen by examining the Zero Velocity Surface (left panel, figure 22) which shows the limits in configuration space and therefore phase space is foliated by invariant tori. However, we see that for $\mathcal{K} = -0.34$, which is directly above the saddle-center, and especially for $\mathcal{K} = -0.25$ that higher values of p_θ correspond to unbound trajectories. These trajectories spiraling outward, and never returning to the core (or Poincaré section). The solid blue line

corresponds to the maximum p_θ value at which trajectories remain bounded.

In figure 25 we sample some of the periodic orbits which are found in the integrable system. Recall that in the integrable case their is a rotational invariance so that each orbit shown actually represents a family of orbits by rotation. However, for the orbits shown, where all periodic orbits intersect the x-axis, once the field is turned on this symmetry is broken and the only orbits which can persist are those which are symmetric about the x-axis. This symmetry can be seen by first examining Hamiltonian's equations applied to Hamiltonian (44),

$$\begin{aligned}
\dot{x} &= p_x + \omega y, \\
\dot{y} &= p_y - \omega x, \\
\dot{p}_x &= -E_0 - \frac{\partial V}{\partial x} + \omega p_y, \\
\dot{p}_y &= -\frac{\partial V}{\partial x} - \omega p_x.
\end{aligned}$$

Hamilton's equations dictate that if $\left(x^t, y^t, p_x^t, p_y^t\right)$ is a solution then $\left(x^t, -y^t, -p_x^t, p_y^t\right)$ must be as well when $t \to -t$.

In the aforementioned figure, we only show the orbits which can persist once the field is applied. Furthermore, we only show a small portion of the orbits which exist in the integrable case, focusing on the orbits, which, based on their shape, period, and nonlinear properties, are likely candidates to exert an influence on the dynamics of returning trajectories. The exception to this are the orbits found in the bottom row. Admittedly, *a priori* it is not clear why these orbits would be responsible for ionizations and returns, however, in Sec. 4.5.3 it will be clarified why they are included. In all panels the dashed black circle of radius 5 a.u. is used to show the return threshold, which we define as the maximum distance from the core an electron must reach after it has already ionized to be considered a returning trajectory. These orbits are followed by continuity, by increasing the intensity, into the NSDI regime.

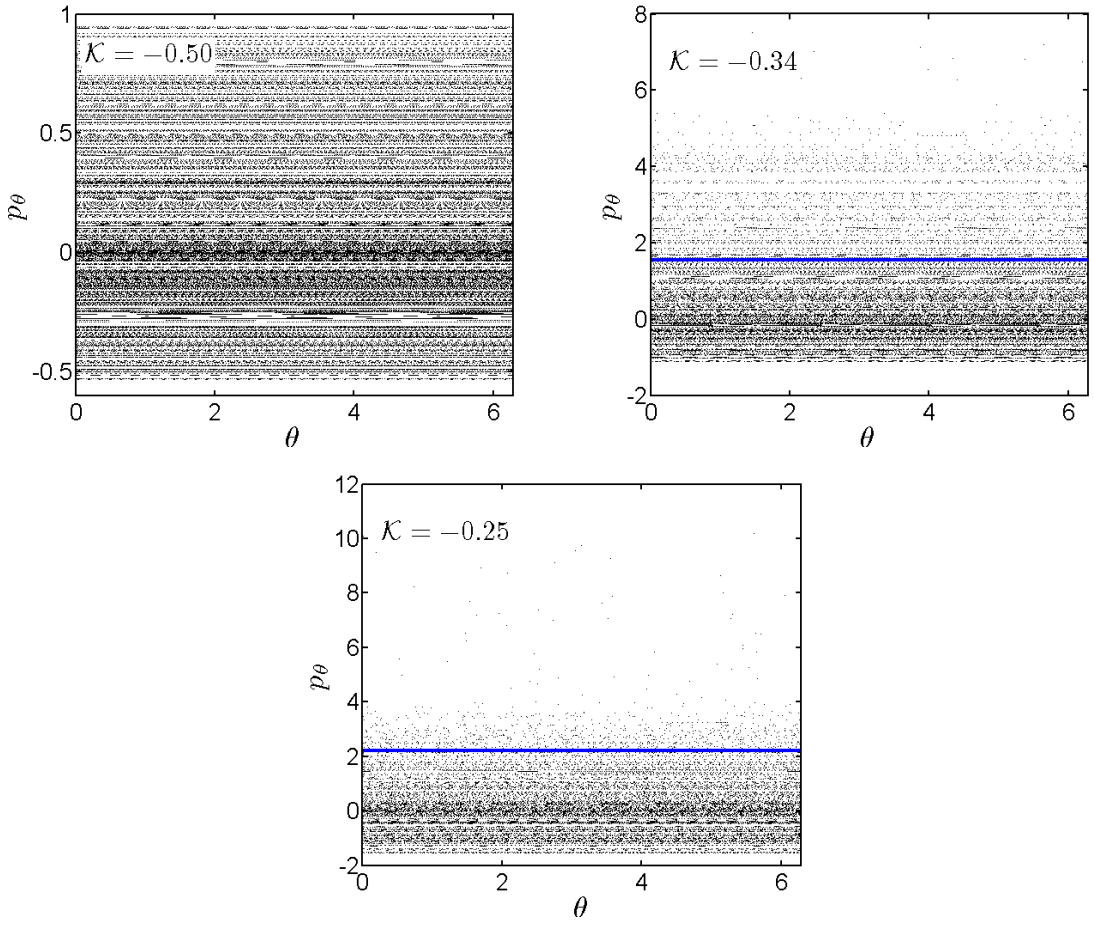

Figure 24: Poincaré sections for different Jacobi values in the integrable system. As the Jacobi value is increased the dynamics enters the unbound region of phase space. Compare the Jacobi values shown in the top left of each panel with their corresponding locations on the Zero Velocity Surface in the left panel of figure 22. The solid blue line indicates the largest value of the angular momentum (p_θ) for which the dynamics is bounded. For all figures, $E_0 = 0$ (integrable case) and $\omega = 0.0584$ a.u.

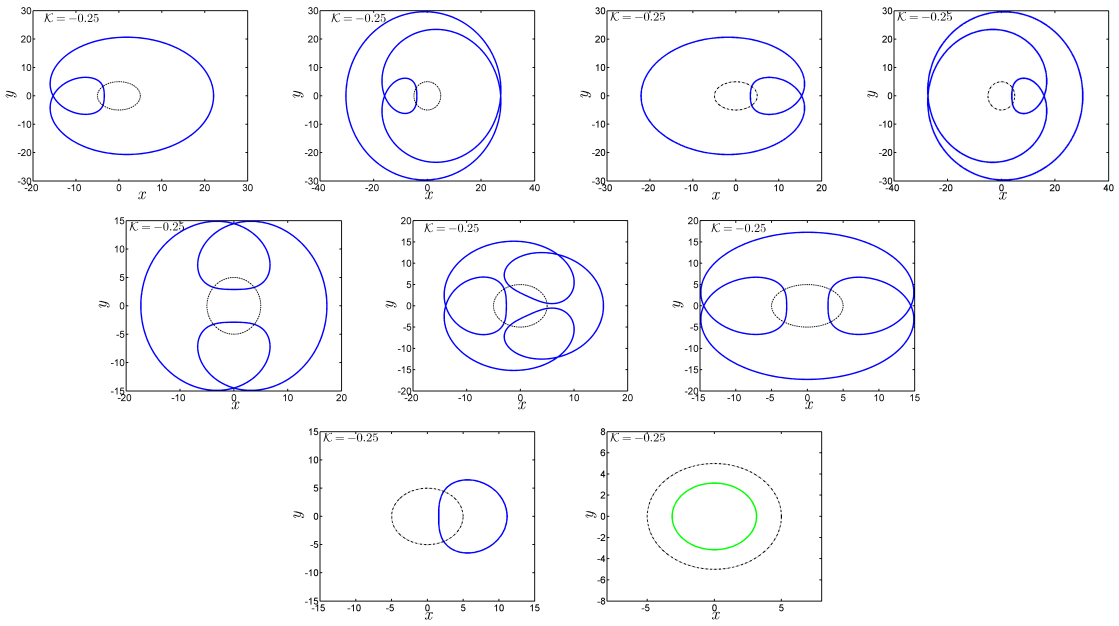

Figure 25: Periodic orbits in the integrable case, which based on their shape, are possible candidates for wielding influence on the dynamics of returning trajectories. In all panels $E_0 = 0$, $\mathcal{K} = -0.25$, and $\omega = 0.0584$ a.u.

4.5.3 Non-integrable case

An examination of the integrable system is useful, however, the non-integrable system (with the laser field turned on), is physically much more interesting, especially from the view point of an experimentalist. The orbits found in the previous section, in figure 25, can be followed by continuity as we increase the intensity (moving away from the integrable case). We choose as our case study the intensity $I = 10^{13}\,\mathrm{W}\cdot\mathrm{cm}^{-2}$ which is well situated in the NSDI regime. For the Jacobi value we choose $\mathcal{K} = -0.25$, which, according to the right panel of figure 22 is sufficiently high above the saddle-center to allow for widespread ionization (a prerequisite of a recollision).

In figure 26 we show these orbits for our new set of parameters. Each panel shows the corresponding orbit in the same panel of figure 25. With the exception of the two orbits shown in the bottom row it is clear that the orbits in the non-integrable case resemble their corresponding orbits in the integrable case. However, for the two periodic orbits on the bottom row it is not so clear. These orbits, originating in

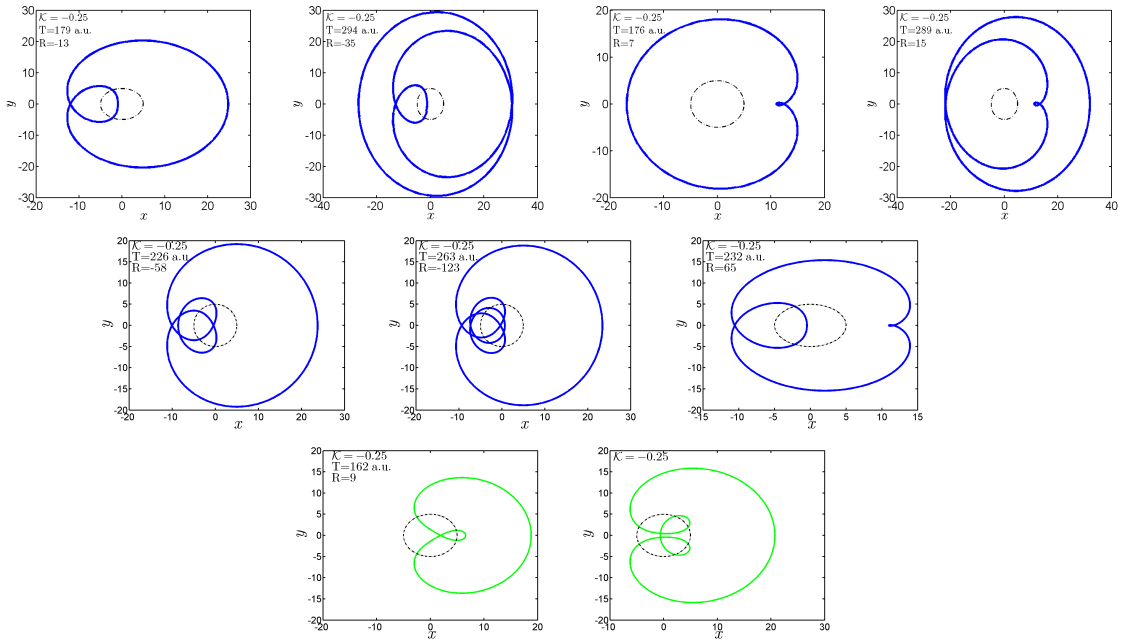

Figure 26: Recolliding periodic orbits from figure 25, which are possible candidates for affecting the dynamics of returning trajectories. The intensity is taken as $I = 10^{13}\ \mathrm{W} \cdot \mathrm{cm}^{-2}$ while $\mathcal{K} = -0.25$ and $\omega = 0.0584$ a.u.

the integrable case undergo a series of bifurcations which allow them to qualitatively resemble the orbits shown in figure 26. Here all of the orbits extend beyond the ionization threshold of 15 a.u. and return to with 5 a.u. of the ionic core. Therefore, we would say that all of the periodic orbits shown in figure 26 are indeed *recolliding periodic orbits*, already defined in the previous chapter.

These nine RPOs can be reduced further by grouping them into specific families of RPOs. The two leftmost RPOs in the top row are members of a family, which we denote by $\mathcal{O}_n$, where $n \in \mathbb{Z}^+$ denotes the number of returns to the Poincaré section $y = 0$. For brevity, we only show $\mathcal{O}_2$ and $\mathcal{O}_3$, however, high order members can also be found, however, their influence on the dynamics is diminished because as n increases so does their period. Additionally, the two rightmost panels in the top row are members of a family which we denote as $\mathcal{O}'_n$, again where $n \in \mathbb{Z}^+$ denotes the number of returns to the Poincaré section $y = 0$. Just like the case with $\mathcal{O}_n$, we only show the two simplest members of the family, $\mathcal{O}'_2$ and $\mathcal{O}'_3$. The families $\mathcal{O}_n$ and

$\mathcal{O}'_n$ are of special interest because they are the same orbits as those of the $1:m$ resonances of the previous chapter. The two families can be followed by continuity with the ellipticity parameter to $\epsilon = 0$. In the LP case both families are reduced to single orbits (since their is no longer a Jacobi parameter because the system is no longer autonomous) and they exist with $y = 0$ and $p_y = 0$, i.e. all dynamics is along the polarization axis. We can then make a reduction from two spatial dimensions (x, y) to a single spatial dimension, x, exactly like the LP problem from the previous chapter. It then becomes apparent that these orbits $\mathcal{O}_n$ and $\mathcal{O}'_n$ are the hyperbolic and elliptic $1:m$ resonances, respectively. For $m = 3$, we have $\mathcal{O}_2$ and $\mathcal{O}'_2$. Likewise, for $m = 5$ we have $\mathcal{O}_3$ and $\mathcal{O}'_3$, and so on. The other RPOs shown in figure 26 do not originate from this resonant family, however, they also play a role in the recollision process in CP. The RPOs in the second row do not compromise a family, however, they are just a small sampling the of available orbits which contain a variable number of inner loops at various positions, so long as the symmetry requirement is met. The leftmost panel in the bottom row is itself a family, in a similar vein to $\mathcal{O}_n$ and $\mathcal{O}'_n$. We only show the first element of the family, however, additional members are identified by an increasing number of loops surrounding the core region. We denote this family by $\mathcal{H}_n$. Finally, the rightmost panel in the bottom row shows an orbit, which we denote $\mathcal{U}$. It is not a member of a larger family but like all of the other RPOs shown it originates in the integrable case. Already, it is clear that potentially more orbits have a controlling interest in the recolliding dynamics as compared to the LP case.

4.5.3.1 Re-examining the trajectories of Sec. 4.5.1

The orbits (and their families) discussed in the previous section are responsible for the repeated patterns highlighted in figure 23. The blue highlight corresponds to $\mathcal{O}_n$, the green highlight corresponds to $\mathcal{O}'_n$, and the yellow highlight corresponds to $\mathcal{H}_n$. We label the orbits with an ambiguous index, n, instead of using a specific number

for each additional case because by inspection we cannot be certain which orbit in the respective family is actually being followed (if it is a single orbit at all). It is often the case that recolliding trajectories exhibit traits of multiple periodic orbits. Indeed, this is the case for both panels in the top row of the figure. As a trajectory moves around the chaotic sea the influence of the various periodic orbits located in the sea wax and wane depending on the proximity of the trajectory to the respective orbit. Note however, that not all periodic orbits are represented in the samples shown in figure 23. In order to better understand which periodic orbits can be considered fundamentally important in the returning mechanism we perform a quantitative and statistical study on a large number of returning trajectories. Finally, it is interesting to note that in the LP case from the previous chapter, two orbits (and their manifolds) dictate the entire recollision process. However, in the CP case, many more orbits appear to affect the dynamics. We would like to reduce the CP dynamics to the dynamics of a single orbit, if possible. In the following section, we perform a statistical analysis of returning trajectories, to determine exactly which orbits regulate the recollision process.

4.5.3.2 Linear Discriminant Analysis

Making use of common pattern recognition algorithms, namely Linear Discriminant Analysis (LDA), we can identify portions of trajectories under the influence of a given set of periodic orbits by examining key features of the trajectory in configuration space. For $\mathcal{K} = -0.25$, as described in the previous section it appears that only a few periodic orbits determine the return mechansim. These orbits are $\mathcal{O}_n$, $\mathcal{H}_n$, and $\mathcal{U}$ (see figure 26).

LDA is an algorithm, often used for pattern recognition, which finds a linear combination of features, of a given object, to classify the said object into a supplied group. The groups are determined by a set of training data, which are data, where

based on the features, the user determines to which group a given element belongs. In practice, the set of features are critical in determining the success rate of the algorithm. It is important to choose features which can be well differentiated across the various periodic orbits. In figure 27 we show the x position of the periodic orbit as a function of time for the three orbits $\mathcal{O}_2$, $\mathcal{H}_1$, and $\mathcal{U}$. However, since far away from the core region many of the periodic orbits are similar in appearance we show only the portions of the respective periodic orbits which are within the ionization threshold, of 15 a.u., which in this context we will refer to as the viewing radius. We see that each type of periodic orbit has a distinct shape when characterized by its x position. Unfortunately, the LDA algorithm cannot take as an input a high resolution time signal without running into numerical issues. Namely, the amount of training data must be large compared to the number of elements of our signal. For a time series signal (such as those shown in the bottom row of figure 27) the number of elements is quite large. Instead, we choose a much simpler set of features, which does not have the same problem. Namely, our features are

1. initial point of the time series, x_0,
2. final point of the time series, x_f,
3. number of local extremum,
4. the difference between the final and initial points, $x_f - x_0$.

With this feature set, LDA can successfully discriminate between the three different trajectory types. However, it does not make a distinction between members of the same family, i.e., the algorithm does not distinguish between $\mathcal{O}_2$ and $\mathcal{O}_3$, mainly because inside the viewing radius members of the same family look quite similar. For a given trajectory, the algorithm only analyzes segments which exist inside the viewing radius. For a given returning trajectory, multiple trajectory segments can be supplied.

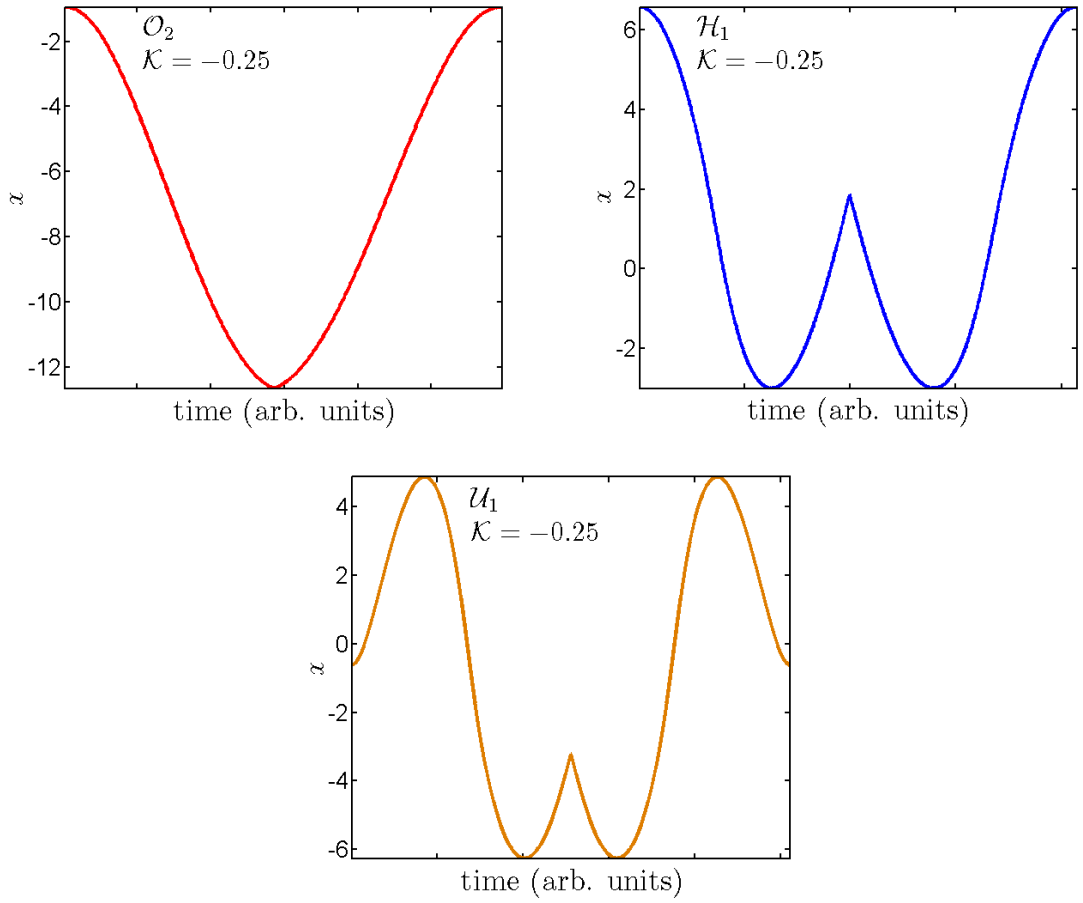

Figure 27: The top row shows the three periodic orbits which are most responsible for ionizations and returns for $\mathcal{K} = -0.25$ and $I = 10^{13}\,\mathrm{W}\cdot\mathrm{cm}^{-2}$. The dashed black curve is the viewing radius. The bottom row is the time series signal of the x position of each periodic orbit inside the viewing radius. For all panels $\omega = 0.0584$ a.u., $\mathcal{K} = -0.25$ and $I = 10^{13}\,\mathrm{W}\cdot\mathrm{cm}^{-2}$

For $\mathcal{K} = -0.25$ we show the frequency of each trajectory type in the left panel of figure 28 for various return thresholds. For each panel, the algorithm investigates approximately 450 trajectory segments. Starting in the left panel of the top row and moving clockwise we have a return threshold of 3 a.u., then 4 a.u. and finally 5 a.u. The blue bars correspond to the raw data, directly outputted from the algorithm, while the red bars correspond to the addition of an error correcting term. The final columns in each panel correspond to the trajectories which could not be properly labelled by the algorithm. In each panel, regardless of the data examined (non-adjusted vs. adjusted) and which return threshold used we observe that $\mathcal{O}_n$, $\mathcal{H}_n$ and $\mathcal{U}$ each play significant roles in the return process. The trajectories which could not be properly placed are generally as frequent as the least common orbit type, $\mathcal{O}_n$. This shows that we have chosen the correct three periodic orbits to look at because they are the three most common. The final panel, rightmost in the bottom row, is the residue curves of the three key periodic orbits. We see that at $\mathcal{K} = -0.25$ (dashed vertical line) that each of the orbits is slightly hyperbolic.

The analysis carried out on returning trajectories for $\mathcal{K} = -0.25$ can be replicated for additional Jacobi values. We repeat the same analysis, now for $\mathcal{K} = -0.1$, however, we focus on the orbits shown in figure 29. They are $\mathcal{O}_n$, $\mathcal{O}'_n$, $\mathcal{O}^*$, and $\mathcal{O}^{**}$. Notice how in the rightmost panel of the top row, where we show $\mathcal{O}'_2$ that the inner loop reaches far into the core region, well inside the return threshold of $r_{ret} = 5$ a.u. Recall that this was not the case for $\mathcal{K} = -0.25$ (see figure 26). The panels in the bottom row show orbits which played only a minimal role in the return process for $\mathcal{K} = -0.25$, however now their role is much more prominent. This is because the magnitude of the residue of both orbits is very large for $\mathcal{K} = -0.25$ (see right panel of figure 30) while for $\mathcal{K} = -0.10$ the residues are much closer to zero, while still remaining hyperbolic. The periodic orbit $\mathcal{U}$ and the family $\mathcal{H}_n$, which were quite common for returning trajectories at $\mathcal{K} = -0.25$ are now much less prevalent. For

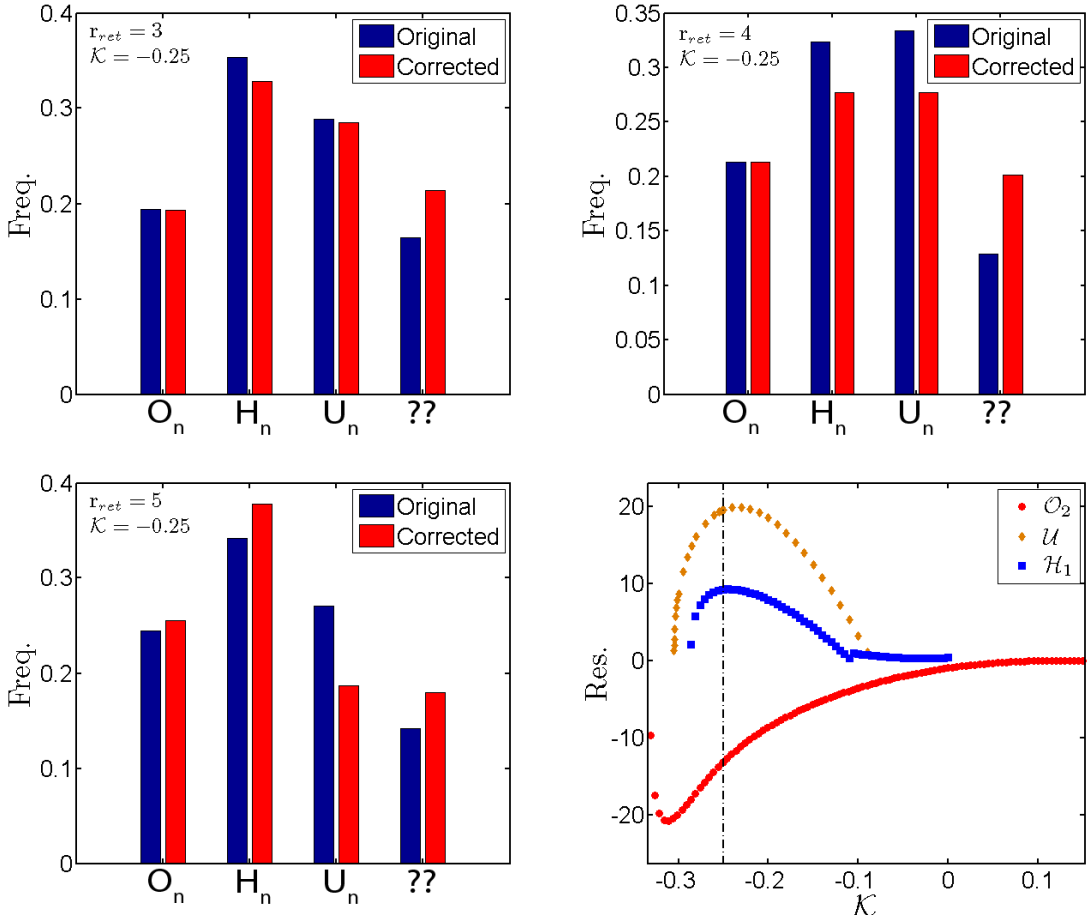

Figure 28: Histograms of the occurence of the three periodic orbits $\mathcal{O}_n$, $\mathcal{H}_n$ and $\mathcal{U}$. The blue bars correspond to the raw data while the red bars are the same data with an error correction added. The final column is the frequency with which the algorithm could not detect the underlying periodic orbit. The rightmost panel in the bottom row is a residue curve for the three periodic orbits with the Jacobi value $\mathcal{K} = -0.25$ marked by the vertical dashed black line. For all panels $I = 10^{13}\,\mathrm{W}\cdot\mathrm{cm}^{-2}$, $\mathcal{K} = -0.25$, and $\omega = 0.0584$ a.u.

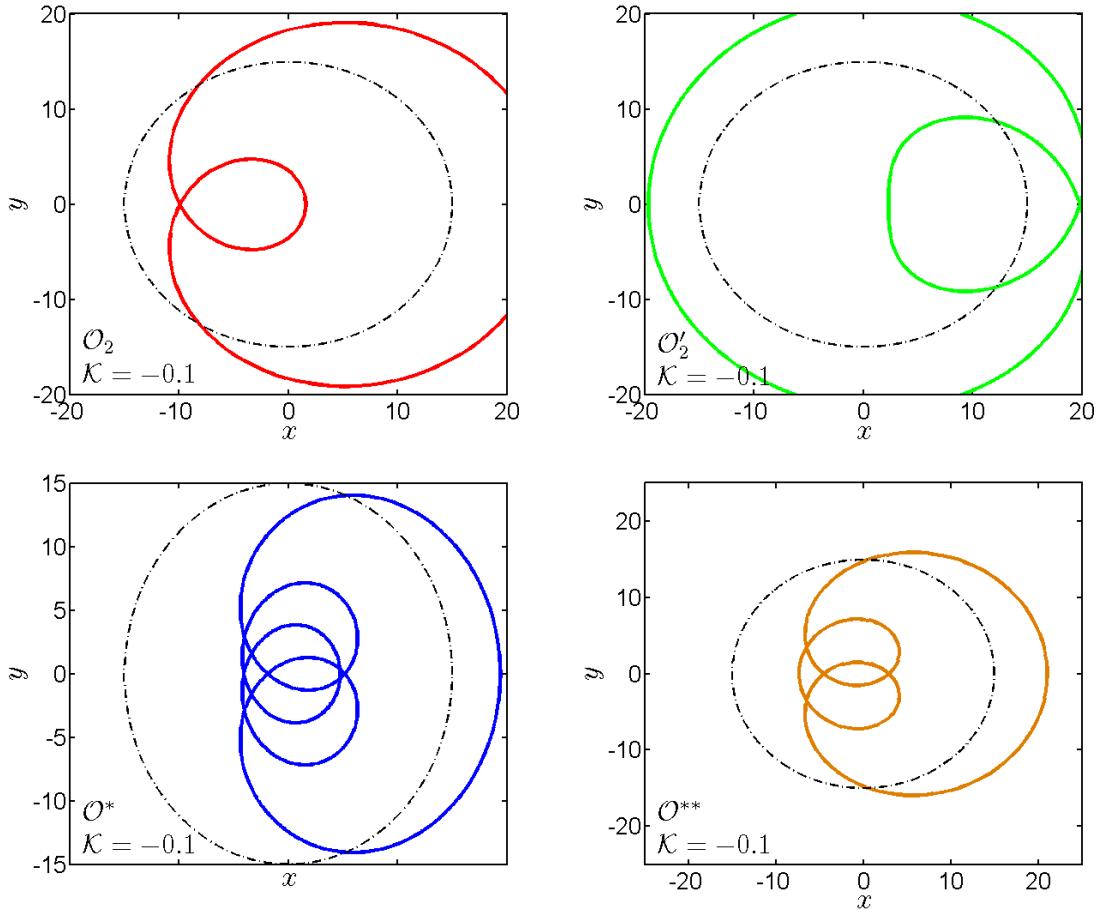

Figure 29: The four periodic orbits which are primarily responsible for ionizations and returns for $\mathcal{K} = -0.1$. The dashed black circle corresponds to the viewing radius, 15 a.u. For all panels $I = 10^{13}$ W $\cdot$ cm^{-2}, $\mathcal{K} = -0.1$, and $\omega = 0.0584$ a.u.

$\mathcal{U}$, the reason is not quite clear, however, the spatial extent of the periodic orbit is decreasing and while it does extend beyond the ionization threshold of 15 a.u., it is close. For the family $\mathcal{H}_n$, however, a period halving occurs for $\mathcal{H}_1$ at approximately $\mathcal{K} = -0.11$ and additionally as the Jacobi value increases the spatial extent of the orbit decreases and nearby $\mathcal{K} = -0.1$ the periodic orbit no longer extends past the ionization threshold of $r_{ion} = 15$ a.u.

In figure 30 we show the results of LDA on the returning trajectories for $\mathcal{K} = -0.1$. In the left panel we show the frequency with which each of the key periodic orbits is expressed while the right panel shows the residue curves of the periodic orbits. Like

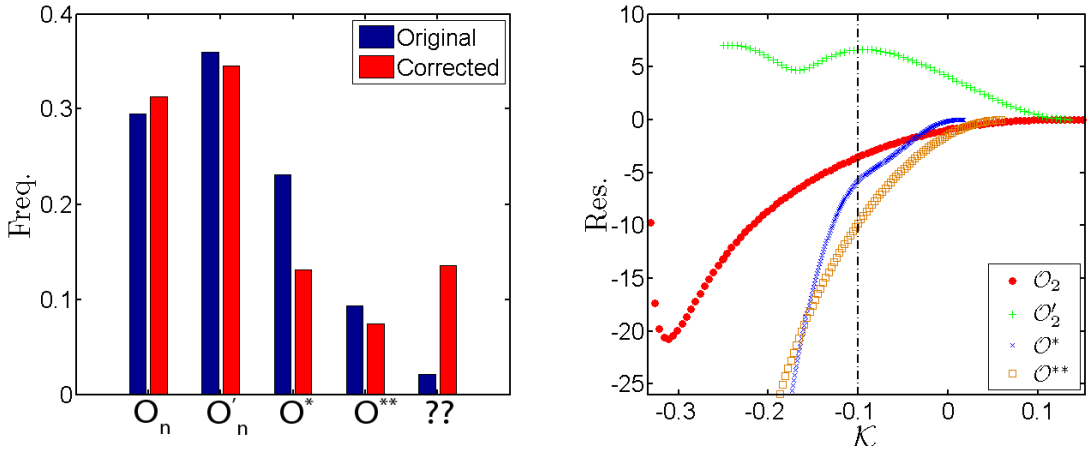

Figure 30: The left panel shows a histogram of the occurence of the four periodic orbits $\mathcal{O}_n$,$\mathcal{O}'_n$, $\mathcal{O}^*$, and $\mathcal{O}^{**}$. The blue bars correspond to the non-corrected data while the red bars are the same data with an error correction added. The final column is the frequency with which the algorithm could not detect the underlying periodic orbit. The right panel is a residue curve for the three periodic orbits with the Jacobi value $\mathcal{K} = -0.10$ marked by the vertical dashed black line. For all panels $I = 10^{13}\,\mathrm{W}\cdot\mathrm{cm}^{-2}$, $\mathcal{K} = -0.1$, and $\omega = 0.0584$ a.u.

the case for $\mathcal{K} = -0.25$, we again see that the frequency with which the trajectory segment could not be identified is approximately as small as the least common of the orbits, in this case $\mathcal{O}^{**}$. Note, however, that the 'corrected' data for the final column of the frequency plot is much larger than the 'original' column. This is because a large number of trajectory segments which were initially classified as $\mathcal{O}^*$ where actually misclassified, and actually their type could not be determined. However, although the cannot be determined column is large (approximately 13%), it is comprised of many different orbit types, and no one orbit was dominant. This demonstrates that the four periodic orbits selected as being dominant in the return mechanism at $\mathcal{K} = -0.1$ are indeed the correct choices.

LDA can be useful for determining the relative importance of different periodic orbits in the context of the returning mechanism. It allows us to gauge the relative importance of various periodic orbits, or more pointedly it allows us to confirm that a small set of selected periodic orbits is indeed primarily responsible for the return

mechanism in CP. We have confirmed the groups of periodic orbits which are responsible for ionizations and returns at two different Jacobi values, $\mathcal{K} = -0.25$ and $\mathcal{K} = -0.1$. We have shown that the return scenario differs slightly between these two Jacobi values because the relative importance of the periodic orbits varies. Namely, the family of periodic orbits $\mathcal{O}'_n$ does not play a role at $\mathcal{K} = -0.25$ because it does not approach sufficiently close to the core. Furthermore, the importance of $\mathcal{H}_n$ decreases as well as we transition from $\mathcal{K} = -0.25$ and $\mathcal{K} = -0.1$ while the opposite occurs for the orbit $\mathcal{O}^*$ and $\mathcal{O}^{**}$.

4.6 Conclusion

We have shown that the dynamics in a CP field is much richer than in the LP counterpart in the sense that many more orbits affect the dynamics of recollisions. Furthermore, since the Hamiltonian is autonomous, our conserved quantity, the Jacobi value, parameterizes familes of RPOs (as opposed to single instances of RPOs in LP). In the following chapter, we develop a predictive model for electronic recollisions in CP, which will utilize the properties of $\mathcal{O}_2$, one of the orbits analyzed by the LDA of this chapter.

CHAPTER V

A PREDICTIVE MODEL OF RECOLLISION FOR ATOMS AND MOLECULES

5.1 Introduction

In this short chapter, we will show that the family of key periodic orbits $\mathcal{O}_2$ can be used as a bellwether to the recollision process in a strong circulary polarized laser field. We find the necessary conditions for recollision-driven nonsequential double ionization to occur. The outlined mechanism is universal in that it applies equally well beyond atoms: The internal structure of the target species plays a minor role in the recollision process.

From the previous chapter we showed that several families of RPOs regulate the electronic recollision process in CP. This was accomplished using the one-electron model of Ch. 2 (Hamiltonian (21)). The benefit in understanding electronic recollisions is so that physical processes such as NSDI can be better explained. NSDI, however, is a two-electron process, relying on the returning electron to bring back sufficient energy to ionize the second electron. The Hamiltonian is different than the one electron system, since it includes a kinetic energy and attractive Coulomb potential for an additional electron. Furthermore, the electron-electron interaction must be included as well. So then, of foremost importance is determining if the RPOs found in the last chapter still regulate the dynamics in this more complicated system.

5.2 Sample of trajectories

A typical NSDI trajectory in a CP field for a two-active-electron atom appears in the left panel of Fig. 31: The dark electron (red online) recollides and causes the other

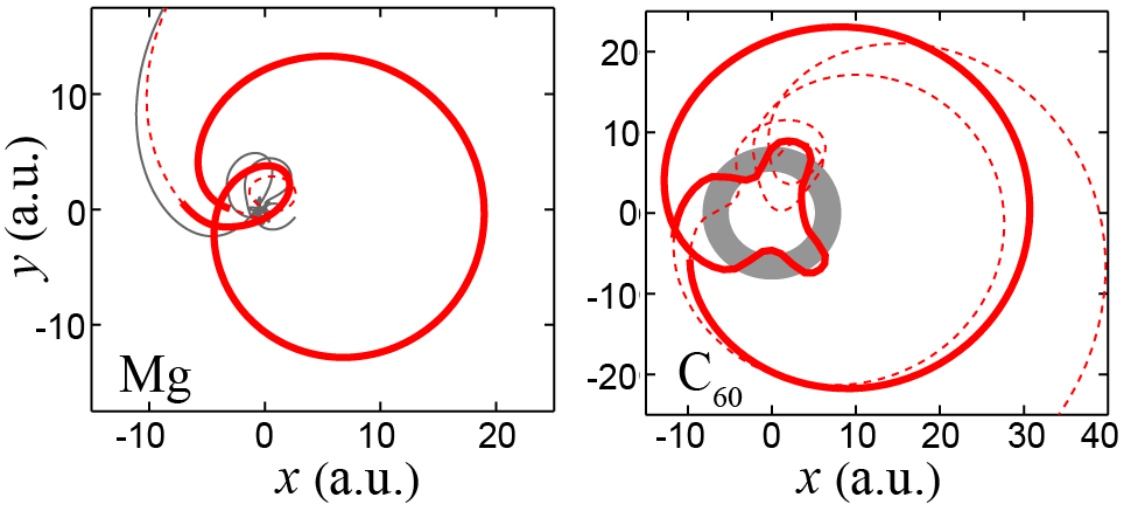

Figure 31: Left panel: Typical NSDI of Mg as modeled by Hamiltonian (46). The dark (red online) electron exhibits a recollision which causes the gray electron to ionize. Right panel: Typical one-electron trajectory of C_{60} which also exhibits a recollision [10]. The gray annulus represents the potential well. In both panels, the segment of the trajectory which is in bold mimics the shape of key periodic orbits. The laser parameters are 780 nm wavelength and an intensity of 5×10^{13} W $\cdot$ cm^{-2}. All trajectories are shown in the rotating frame.

electron (light gray), previously bound to the nucleus, to ionize. For comparison, the right panel of Fig. 31 displays a recolliding trajectory for C_{60} (buckminsterfullerene), where the gray annulus represents the potential well of the molecule. In both panels, we highlight the RPO signature in bold. We compare these recolliding trajectories with the periodic orbits of an already-ionized electron in Fig. 32 for each system respectively: The good agreement between the shapes of the RPOs of Fig. 32 and the sample trajectories of Fig. 31 (bold portions) forms the nub of our argument that specific periodic orbits drive recollisions.

The trajectories of Figs. 31 and 32 are represented in a frame rotating with the CP field (referred to as the rotating frame). They each consist of an interior loop, occurring in the down-field direction of the laser, which passes close to the nucleus (where the Coulomb attraction dominates the dynamics) and a farther reaching exterior loop which encloses the nucleus (where the laser field predominates). Comparing the RPO

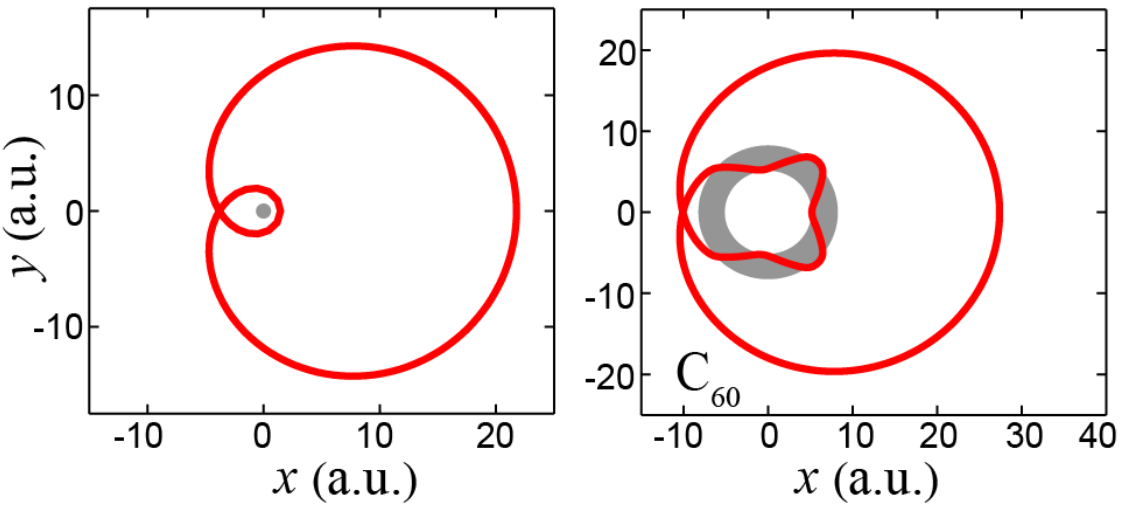

Figure 32: RPO corresponding to the highlighted trajectory portions in Fig. 31. The left panel corresponds to Hamiltonian (45) and the right panel to a one-electron Hamiltonian model for C_{60} [10].

in Fig. 32 for Hamiltonian (45) (left panel) and the same RPO for C_{60} (right panel), we observe striking similarities, despite the strong differences in the potentials. The only common feature between the two potentials is the Coulomb tail far from the core ($-1/r$ for $r \gg 1$) which results in a one electron model which we examine next.

5.3 Model

In the rotating frame the Hamiltonian modeling a one-electron dynamics has already been given by Hamiltonian (44) of Ch. 4, however we write it again here for convenience,

$$\mathcal{K} = \frac{p_x^2 + p_y^2}{2} - \frac{1}{\sqrt{x^2 + y^2}} + E_0 x - \omega \left(x p_y - y p_x \right). \tag{45}$$

For C_{60} we use a continuous approximation of the potential given in Ref. [10]. The phase space of Hamiltonian (45) is unbounded, but not all electrons can leave the core region and ionize. In particular if the Jacobi constant of the electron is smaller than the one corresponding to a specific Stark saddle point [43, 44, 20], the electron is stuck in the core region with no possibility for ionization. In Fig. 33, we display the limits of the domain accessible to the electron (in the configuration space of Hamiltonian (45)),

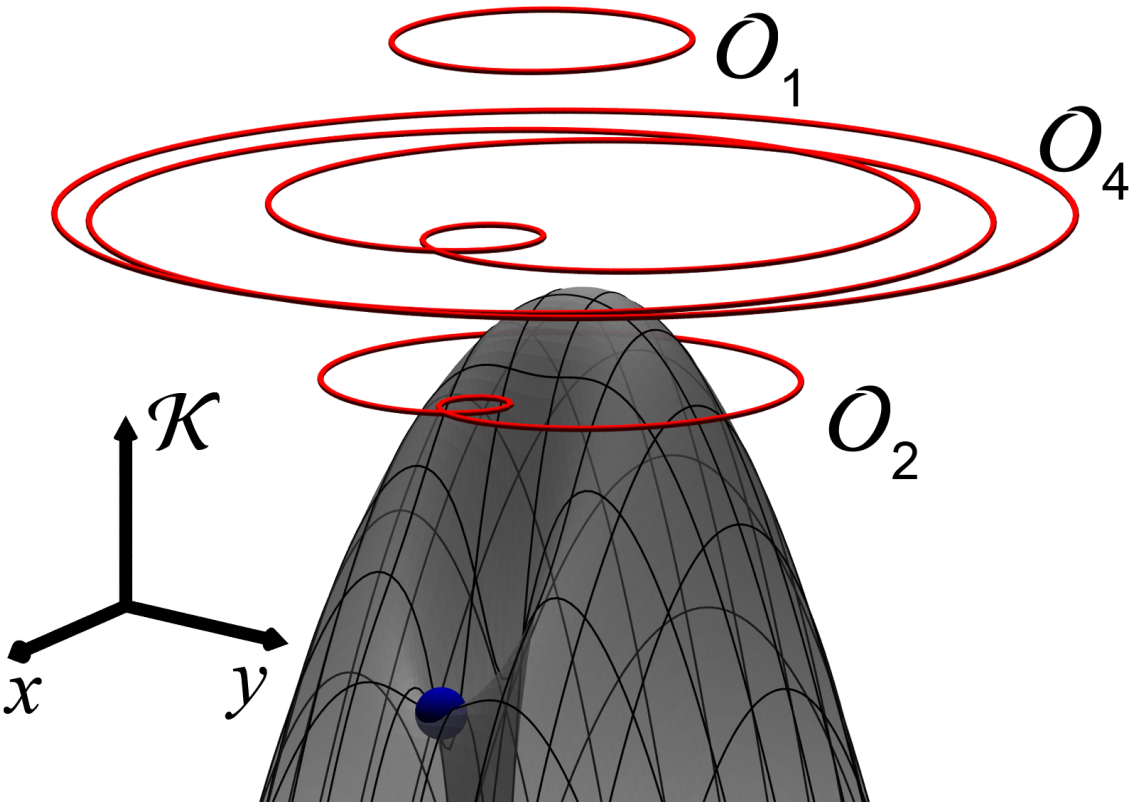

Figure 33: Limits of the accessible domain for an electron modeled with Hamiltonian (45). We display three RPOs of the family $\mathcal{O}_n$. The saddle point is marked by a sphere. The laser parameters are the same as in Fig. 31.

where the saddle point is indicated by a sphere.

As illustrated by Figs. 31 and 32, recollisions with CP are organized by certain types of periodic orbits. Only those periodic orbits which contain segments both close to and far away from the core play a role in recollisions and these are RPOs. The topologically simplest RPO consists of an off-centered circle and we found such an orbit for high values of the Jacobi constant (top orbit in Fig. 33). When followed by continuity as the Jacobi value is decreased, this orbit bifurcates into a family of periodic orbits which consist of an interior loop, in the down-field direction of the laser, and one or several exterior loops, leading to an excursion far from the core (like the highlighted regions of Fig. 31). We label these RPOs $\mathcal{O}_n$, where n corresponds to the number of loops in the periodic orbit (see Fig. 33). The interior loop is responsible for

the exchange of energy between the already-ionized electron and the core (or second) electron while the exterior loop is where the ionized electron gains energy from the laser field. Not all RPOs are equally important for recollision: Relevant orbits have a period which is much smaller than the pulse duration (so as to influence the motion of the already-ionized electron), and are weakly hyperbolic, so that an electron can stay close to them long enough to imitate their dynamics. We found a handful of such RPOs and their influence waxes and wanes with the choice of Jacobi value and intensity. For instance, the influence of $\mathcal{O}_4$ (middle curve in Fig. 33) can be seen on Fig. 2 of Ref. [40].

5.4 Two electron dynamics

The main outcome of the recollision is the modification of the core structure, leading to, e.g., NSDI. Recollisions exhibited by the two-electron Hamiltonian follow the organizing structures of the one-electron Hamiltonian (as seen in Fig. 31) and indeed it will be shown that these structures dictate the properties of the NSDI channel. The two-electron dynamics can be expressed by [45]

$$\begin{aligned}\mathcal{H} &= \frac{\|\mathbf{p}_1\|^2 + \|\mathbf{p}_2\|^2}{2} + V\left(\|\mathbf{r}_1\|\right) + V\left(\|\mathbf{r}_2\|\right) + \frac{1}{\sqrt{\|\mathbf{r}_1 - \mathbf{r}_2\|^2 + b^2}} \\ &\quad + E_0 f(t)\left(\mathbf{r}_1 + \mathbf{r}_2\right) \cdot \begin{pmatrix} \sin\omega t \\ \\ \cos\omega t \end{pmatrix}. \end{aligned} \tag{46}$$

Here $\mathbf{r}_{1,2}$ and $\mathbf{p}_{1,2}$ are the canonically conjugate positions and momenta of the two electrons in the lab frame. The potential is chosen as $V(r) = -2/\sqrt{r^2 + a^2}$, where a is the electron-core softening parameter [27, 28] which is adjusted to model the various atoms under investigation (we set $a = 3$ for Mg, $a = 1$ for Ne, $a = 1.5$ for Ar, and $a = 1.8$ for Xe). The pulse envelope is given by f. For the numerical results presented here, we consider a laser envelope with two laser cycle ramp-up, six cycle plateau, and a two laser cycle ramp-down. We find qualitatively similar results with other laser envelopes. Initial conditions of the respective atoms are taken from a

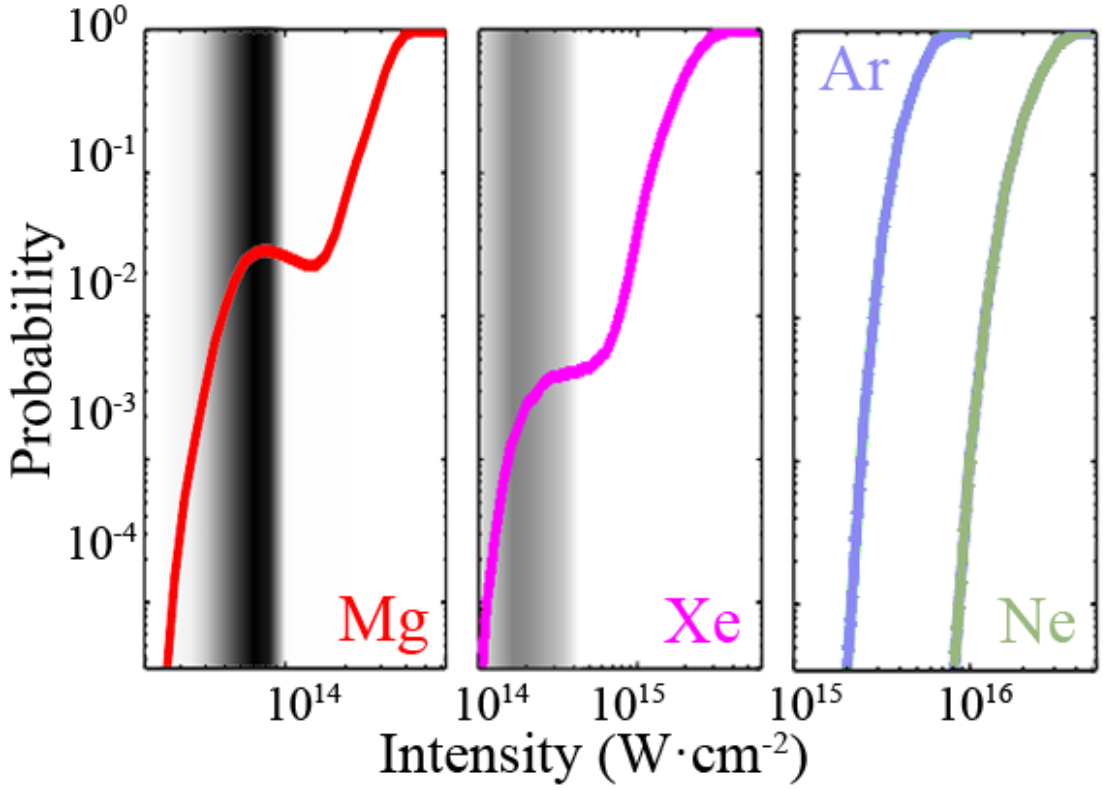

Figure 34: Curves: Double ionization yield for Mg (left panel) and Xe (middle panel), and Ar and Ne (right panel) obtained from Hamiltonian (46). In the two leftmost panels the gray shaded background is proportional to the probability that the three criteria for NSDI are satisfied (darker gray corresponds to a high probability). The laser wavelength is 780 nm.

microcanonical distribution on the ground state energy (defined as the sum of the two first ionization potentials. In this chapter we restrict Hamiltonian (46) to two spatial dimensions (fully three dimensional calculations follow the same organizational structure). In Fig. 34 we show the probability of double ionization, where we use a distance criterion for ionization, for Mg (left panel) and Xe (middle panel). Both atoms exhibit NSDI, which manifests itself in the knee enhancement, which is in contrast to Ar and Ne (right panel). Trajectory inspection shows that NSDI (when present) corresponds to recolliding trajectories.

In order to interpret the presence of a knee enhancement in the double ionization probability versus laser intensity, we consider the recollision mechanism driven by

RPOs. Given that RPOs are well defined for a constant laser envelope, we consider $f = 1$ and address recollisions happening during the plateau for the two-electron calculations. It should be noted that the analysis extends to events happening during the ramp-up, by considering a lower effective laser intensity. In order to be influenced by a RPO, a trajectory should get close to it and therefore have a Jacobi value compatible with those of the RPO family. The analysis of the recollision dynamics shows that the existence of an overlap between the Jacobi values for the pre-ionized electron and the domain of existence of the RPOs accurately predicts the existence of recollisions. From this observation, we derive a simplified predictive model for the existence of recollision and NSDI for a given atom. Given the similarity between the RPOs with different models, we use Hamiltonian (45) to determine the domain of existence of RPOs and restrict the analysis to $\mathcal{O}_2$, irrespective of the atom or molecule. Due to the ramp-up of the field the energy gained by each electron is $E_0 x_i^{(0)}$ where $x_i^{(0)}$ is the x-coordinate of the i^{th} electron at the beginning of the plateau. The generated distribution of Jacobi values corresponds to the colored areas in Fig. 35. The dark gray surface on each panel shows the domain of existence of the RPO $\mathcal{O}_2$ in the parameter space $(I, \mathcal{K})$ for Hamiltonian (45). Following the previous discussion, we estimate the probability of recollision as the proportion of pre-ionized electrons with the Jacobi values compatible with the existence of the RPO $\mathcal{O}_2$. Visually, it corresponds to the overlap between the gray and respective colored regions in Fig. 35. There is significant overlap between the surfaces for Mg, Xe, and C_{60} and the domain of existence of $\mathcal{O}_2$, therefore confirming that recollisions are expected for these targets (see also fig 31). In contrast, Ne and Ar do not show any overlap so recollisions are not expected for these atoms in the near infrared regime. Other RPOs, e.g., $\mathcal{O}_3$ and $\mathcal{O}_4$, can be included in the analysis. However, the results are very robust and do not change quantitatively because of the strong overlap in the domains of existence of the individual $\mathcal{O}_n$ in the parameter space $(I, \mathcal{K})$.

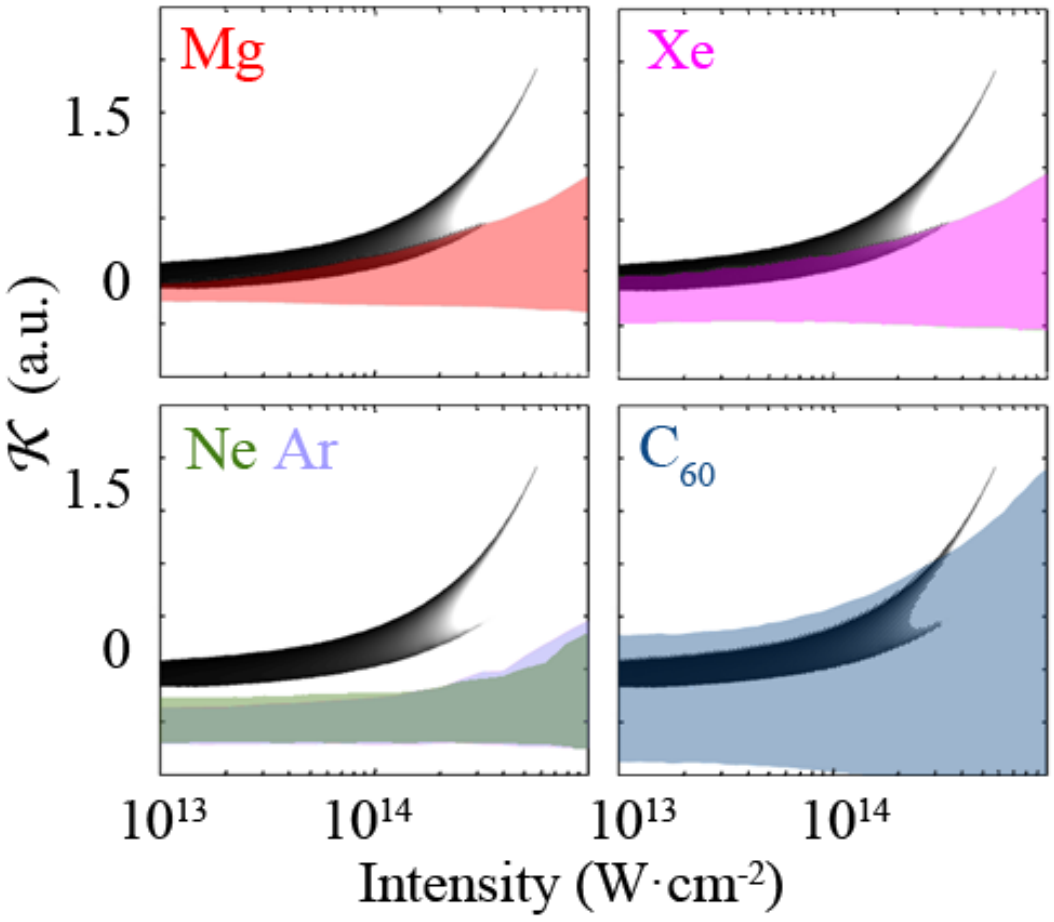

Figure 35: On each panel the dark gray surface represents the domain of existence of the RPO $\mathcal{O}_2$ for Hamiltonian (45). Its shading corresponds to the Greene's residue [11] of $\mathcal{O}_2$, which is an indication of its stability (darker shading corresponds to less unstable RPO). The light gray (colored online) surfaces are the distributions of Jacobi values of the pre-ionized electron for Mg, Xe, Ne and Ar, and C_{60}. The laser wavelength is 780 nm.

5.5 Energy criterion

Not every recollision leads to NSDI. For that to happen, the returning electron needs to bring sufficient energy to the core region in order to ionize the bound electron while remaining ionized itself. Based on this simple picture, we further refine the recollision criterion to predict the range of intensities where NSDI, and thus the knee in double ionization versus laser intensity, is expected. For a given recolliding trajectory, we define $\mathcal{K}_1$ (resp. $\mathcal{K}_2$) and $\mathcal{K}'_1$ (resp. $\mathcal{K}'_2$) as the Jacobi values of the pre-ionized (resp. core) electron before and after the recollision and we define η^2 as the energy exchange. Since the core electron is not screened by the pre-ionized electron, an effective charge of -2 is used to compute its Jacobi value from Hamiltonian (45). Assuming elastic recollisions leading to double ionization, the following inequalities hold:

$$\mathcal{K}'_1 = \mathcal{K}_1 - \eta^2 \quad > \mathcal{K}_\star, \tag{47a}$$

$$\mathcal{K}'_2 = \mathcal{K}_2 + \eta^2 \quad > \mathcal{K}_\star, \tag{47b}$$

where $\mathcal{K}_\star$ is the energy of the Stark saddle. Combining the two equations, we arrive at the condition $\mathcal{K}_1 + \mathcal{K}_2 > 2\mathcal{K}_\star$ which ensures that the returning electron is sufficiently energetic to trigger NSDI. In summary there are three necessary conditions for recollision-driven NSDI to occur:

1. the existence of an RPO (in a single active electron approximation) for Hamiltonian (45),

2. an overlap between the distribution of Jacobi values of the pre-ionized electron and the domain of existence of this RPO,

3. the pre-ionized electron brings in a sufficient amount of energy to free the second electron.

The first two conditions ensure that recollisions are possible, while the third criterion ensures that recollisions could lead to NSDI. Varying the intensity and estimating the

probability of these conditions provides the approximate intensity range where NSDI is possible. Referring back to Fig. 34 we compare these probabilities (gray surface) for Mg (left panel) and Xe (right panel) with their respective double ionization curves, as given by Hamiltonian (46). We see that the intensity range at which NSDI occurs, i.e., the location of the knee, is predicted well by the three conditions. Numerically, Xe shows NSDI at intensities approximately one order of magnitude larger than in Mg [46] (see also Fig. 34), in agreement with the probability to satisfy the three conditions. These predictions also agree with experimental findings [8, 47]. Finally, since the double ionization curves of Fig. 34 are computed with a ramp-up, the electron experiences an effectively lower intensity during the ramp-up. This results in double ionization curves which exhibit a cut-off intensity for the NSDI channel which is slightly higher than what is predicted from the three criteria.

5.6 Conclusion

Our discussion on recollision-driven events boils down to a few rules-of-thumb which apply to systems more complex than atoms. Molecular recollisions with CP are usually attributed to the spatial extent of the system, where the pre-ionized electron recollides at a different atomic center than the one it originates from [48]. In contrast, we have argued above that the excursion of the electron is much larger than the size of the molecule (see Fig. 31), and therefore the possibility of recollision in a CP field for molecules is not due to their spatial extent but mainly to how easily the first electron – the energy carrier – can be pre-ionized by the laser. For example, Ref. [48] reports a knee for NO and none for N_2 using a near-infrared CP field. The first ionization potentials of N_2 and Ar are close, whereas NO resembles Mg. Since there are no recollisions for Ar at this wavelength (see inset of Fig. 35), none should be expected for N_2. On the other hand, recollisions are expected for NO since they are plentiful in Mg. Furthermore, since the second electron is more tightly bound in NO than it

is in Mg, these recollisions need to bring back more energy for double ionization and hence experimentally NSDI is seen at higher intensity for NO than for Mg [8, 48].

CHAPTER VI

A BETTER UNDERSTANDING OF STRONG-FIELD IONIZATION OF FULLERENE VIA A BILLIARD MODEL

6.1 Introduction

The electrical and chemical properties of fullerenes, namely "buckyballs" and nanotubes, remain the focus of thorough investigations [10]. The Buckminsterfullerene molecule, C_{60}, is a prototypical nanocluster because of its stability and nearly spherical shape. In particular, it is an ideal cage in which to trap so-called endohedral atoms, resulting in molecular systems with peculiar properties [49], i.e., enhanced stability with respect to temperature. In recent years, there has been a significant interest in subjecting C_{60} to extreme conditions to probe its electronic and structural stability properties. A new class of experiments on C_{60} driven by strong laser pulses show that its ionization and fragmentation properties are very sensitive to the laser intensity and polarization [50]. In particular, the yields show remarkable changes with the ellipticity of the laser field.

In the previous chapter we investigated a model which predicts when electronic recollisions will occur. This model is independent of the potential used, as long as it is rotationally invariant. Hamiltonian (45) of Ch. 5 can be easily adapted to more complicated molecules, i.e. fullerene or C_{60} by simply replacing the soft-Coulomb potential with a more realistic potential. In Ref. [10] the authors provide a one electron potential of fullerene. The potential is exceedingly stiff (see fig. 36) (and non-continuous). This results in many difficulties during a numerical investigation. Instead, we focus on a billiard model.

A billiard, an almost canonical system of study in dynamical systems can be

useful for many reasons. Here, the purpose is to gain insight into the dynamics of a valence electron of the buckminsterfullerene molecule (C_{60}), which we will show to have a very stiff potential surface, suitable for a billiard adaptation. Of course, ultimately, for such a complex molecule, a billiard model will not suffice, however, as a first investigation, even this simple model provides a rich, complex dynamics which give useful insights into the system. Indeed, at the end of this chapter, we introduce a more complete model of C_{60}, and make comparisons between it and the billiard model.

Motivated by these findings, we consider the motion of an electron inside the valence shell of C_{60} subjected to a CP laser field. The goal is to understand the electronic dynamics prior to photoionization. In strong linearly polarized laser fields, the ionized electron can return to the remaining ion by recolliding with the cage [6, 51] when the laser field changes sign. This collision can lead to additional ionization or even fragmentation [50] of the molecule.

In particular, we investigate the classical dynamics of a one-electron model in the shell of fullerene C_{60} subjected to a strong circularly polarized laser field. In a circularly polarized field, the dynamics is best visualized in a frame co-rotating with the laser field where a conserved quantity emerges, the Jacobi constant [52]. All results presented in this paper are in the rotating frame in which the circularly polarized laser becomes a static field with definite upfield and downfield directions. We restrict the dynamics to a two-dimensional configuration space (the plane of polarization) for the valence electron. The valence electron feels an averaged potential, which, as we later show (Sec. 6.2.1), is very close to a spherical square well potential, where the electron bounces between the walls like a particle in an annular billiard. We choose a billiard model for its simplicity both analytically and numerically and because it serves as a faithful representation of the full model potential while not allowing ionization to occur.

Annular billiards occur in the literature in at least two contexts: Fermi acceleration and the study of quantum chaos by comparing classical and quantum mechanical computations [53, 54, 55, 56, 57, 58, 59, 60]. Chaotic dynamics arises either from pulsating boundaries or from an off-center inner wall. In our treatment the two walls are fixed and concentric. The main distinction here from other works on annular billiards is that in the rotating frame the electron moves along curved paths between successive wall collisions. The introduction of a Coriolis term into the Hamiltonian upon the transformation to the rotating frame is, of course, akin to introducing an effective uniform magnetic field (and another frequency, the Larmor frequency) in which an electron moves on a curved path [61, 62, 63, 64, 65]. The laser wavelength is taken as 780nm (corresponding to a frequency of 0.0584 a.u.) and its intensity is varied from zero to 10^{14} $\mathrm{W \cdot cm^{-2}}$, which are values consistent with what is routinely performed in experiments on C_{60} [10].

Our principal finding is that trajectories of the electron fall into three possible types which originate from specific parts of phase space. We identify various phase space structures which keep these trajectory types distinct from one another. Our classification is as follows: First there are "whispering gallery orbits" (WGO). These trajectories hit only the outer wall and their direction of travel, either clockwise or counterclockwise, is determined by which of the two regions in phase space where they originate. The second type, which we call "daisies" from their typical shape, hits both walls and can rotate either clockwise or counterclockwise. Both daisies and WGOs are called positive or negative based upon their direction of travel, counterclockwise or clockwise, respectively. The third type is mainly influenced by a very simple elliptic periodic orbit bouncing between the two walls in the downfield direction. The shape of these trajectories on the Poincaré section resembles a popular snack food, the Pringles curved potato chip, thus their designation as "pringle orbits."

We show that all the trajectories maintain their distinct characteristics with

changing intensity because of a special class of invariant tori which do not fulfill the usual twist hypothesis required by the Kolmogorov-Arnold-Moser (KAM) theorem. These tori are usually denoted as "twistless" tori or shearless curves (of the Poincaré map) or "meandering" curves when they are associated with separatrix reconnection [66, 67, 68]. Numerical studies show that these tori are very robust against perturbation, and are natural candidates for the partitioning of phase space into regions where well-defined, qualitatively distinct trajectories can be found.

The plan of this chapter is as follows: In Sec. 6.2, we introduce the model and dynamical rules of the billiard and its corresponding Hamiltonian and reflection guidelines. In Sec. 6.3, we give a qualitative analysis of different electron trajectories, and then relate them to the organization of phase space. Next, we analyze the dynamics by using Poincaré section and Frequency Map Analysis [69] in order to gain deeper insight into the properties and organization of phase space when the laser intensity is increased, and in particular concerning the role of twistless tori in the partitioning of phase space into three principal regions.

6.2 Dynamical Rules

6.2.1 Hamiltonian Model

A typical electron inside the shell feels the influence of the electrostatic potential created both by the positive charges of the nucleus and the electronic density, combined with the influence of the laser field. The effective single-particle potential is computed using density functional theory from a jellium approximation for the positive charge background [70]. It contains steep walls in the potential around the radius of fullerene ($r_0 = 6.69$ a.u.) [12, 70, 71, 72] with a certain thickness [73]. The Hamiltonian expressed in atomic units (a.u.) and in the dipole approximation, reads

$$\mathcal{H}(\mathbf{x}, \mathbf{p}, t) = \frac{|\mathbf{p}|^2}{2} + V(|\mathbf{x}|) + \mathbf{x} \cdot \mathbf{E}(t) \tag{48}$$

where $\mathbf{x} = (x, y)$ is the position of the electron in the polarization plane, $\mathbf{p} = (p_x, p_y)$ its canonically conjugate momenta and $|\cdot|$ denotes the Euclidean norm. The circularly polarized laser field is given by $\mathbf{E}(t) = E_0(\mathbf{e}_x \sin\omega t + \mathbf{e}_y \cos\omega t)$, where E_0 is the electric field amplitude, ω is the laser frequency, kept fixed at 0.0584 a.u., and $\mathbf{e}_x$ and $\mathbf{e}_y$ are unit vectors along the x and y axes, respectively. The laser intensity is the time averaged Poynting vector of our laser field and is related to E_0 by the relationship $I = \alpha E_0^2$, where $\alpha = 7.044 \times 10^{16}$ when laser intensity is measured in $\mathrm{W} \cdot \mathrm{cm}^{-2}$. Figure 36 shows the potential $V(r)$, where $r = |\mathbf{x}|$ as given in Ref. [12]. We note that the potential is very stiff at the boundaries of the shell. This is a common feature of various models for C_{60} [70, 71, 72]. This property holds for ions C_{60}^{q+} [71] also. An approximate potential consisting of a spherical square well potential, where the potential is equal to $-V_0$ for $r \in]r_0 - \delta, r_0 + \delta[$ and zero elsewhere, has been proposed in Refs. [74, 75]. This model has succeeded in explaining the oscillations in the photoionization cross-section of C_{60} [74]. We build a billiard model along these lines, where the steep walls of the potential are replaced with infinite walls and the dynamics in the annular region between the two walls is given solely by the interaction of the electron with the electric field, later referred to as the laser-driven dynamics:

$$\mathcal{H}(\mathbf{x}, \mathbf{p}) = \frac{|\mathbf{p}|^2}{2} + \mathbf{x} \cdot \mathbf{E}(t), \tag{49}$$

and reflection rules are applied whenever the trajectory reaches $r = r_{\mathrm{in}}$ or r_{out}, which are 5.14 a.u. and 8.24 a.u., respectively in our computations.

First, we perform a canonical change of variables into a rotating frame (with the laser field). The new coordinates $\left(\overline{x}, \overline{y}, \overline{p}_x, \overline{p}_y\right)$ are given by

$$\begin{pmatrix} \overline{x} \\ \overline{y} \end{pmatrix} = \mathbf{\Omega}(t) \begin{pmatrix} x \\ y \end{pmatrix}, \text{ and } \begin{pmatrix} \overline{p}_x \\ \overline{p}_y \end{pmatrix} = \mathbf{\Omega}(t) \begin{pmatrix} p_x \\ p_y \end{pmatrix},$$

where

$$\mathbf{\Omega}(t) = \begin{pmatrix} \sin\omega t & \cos\omega t \\ \cos\omega t & -\sin\omega t \end{pmatrix}.$$

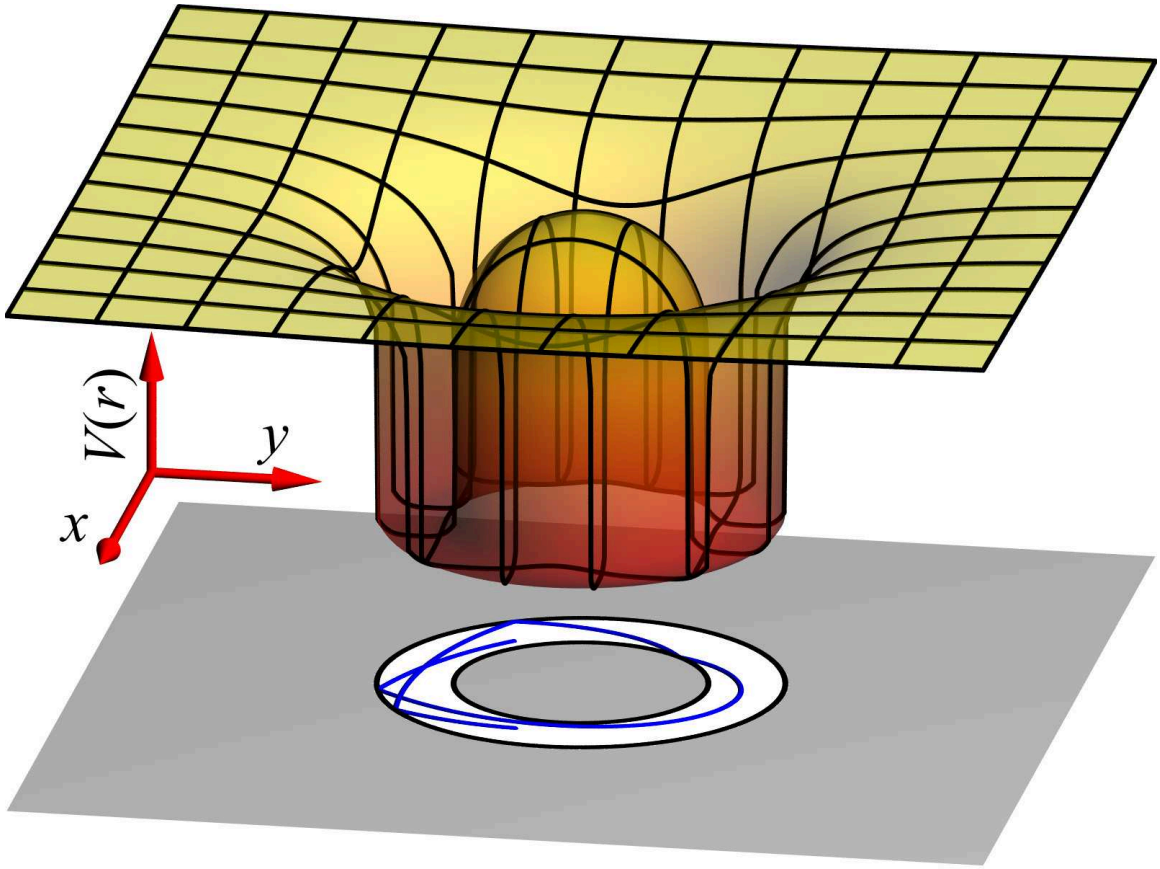

Figure 36: Potential V, felt by a valence electron in fullerene as given in Ref. [12]. The lower plane corresponds to the accessible billiard region (white space) with a sample trajectory (blue curve).

In the new set of variables, the Hamiltonian becomes time-independent and reads

$$\mathcal{K}(x, y, p_x, p_y) = \frac{p_x^2}{2} + \frac{p_y^2}{2} - \omega(xp_y - yp_x) + E_0 x, \tag{50}$$

where we have dropped the bars for simplicity. The resulting Hamiltonian has two degrees of freedom and the value of the Hamiltonian is the Jacobi constant of celestial mechanics [52].

6.2.2 Topology of phase space

The accessible part of phase space changes depending on the field frequency, amplitude, and the value of the Jacobi constant. A revealing way to visualize the accessible part in position space is to compute the zero velocity surface [52]. By applying Hamilton's equations to Eq. (50) we arrive at

$$\begin{aligned} \dot{x} &= p_x + \omega y, \\ \dot{y} &= p_y - \omega x, \end{aligned}$$

so that the Jacobi constant becomes

$$\mathcal{K}(x, y, \dot{x}, \dot{y}) = \frac{\dot{x}^2}{2} + \frac{\dot{y}^2}{2} - \frac{1}{2}\omega^2\left(x^2 + y^2\right) + E_0 x. \tag{51}$$

Setting $\dot{x} = \dot{y} = 0$ gives the Zero-Velocity Surface

$$\mathcal{V}(x, y) = -\frac{1}{2}\omega^2\left(x^2 + y^2\right) + E_0 x,$$

which charts the lower limit of the accessible parts of the billiard, as $\mathcal{K}$ is varied. A cross section of the zero-velocity surface is shown in Fig. 37 for $y = 0$. Depending on the value of $\mathcal{K}$, three possibilities arise: If $\mathcal{K}$ is smaller than $-\omega^2 r_{\text{out}}^2/2 - E_0 r_{\text{out}}$, then there is no accessible part to the dynamics. If $\mathcal{K}$ is between $-\omega^2 r_{\text{out}}^2/2 - E_0 r_{\text{out}}$ and $-\omega^2 r_{\text{in}}^2/2 + E_0 r_{\text{in}}$ then only a portion of the annular region is accessible. In this range of values, several truncations of the annulus are possible; in particular, we distinguish

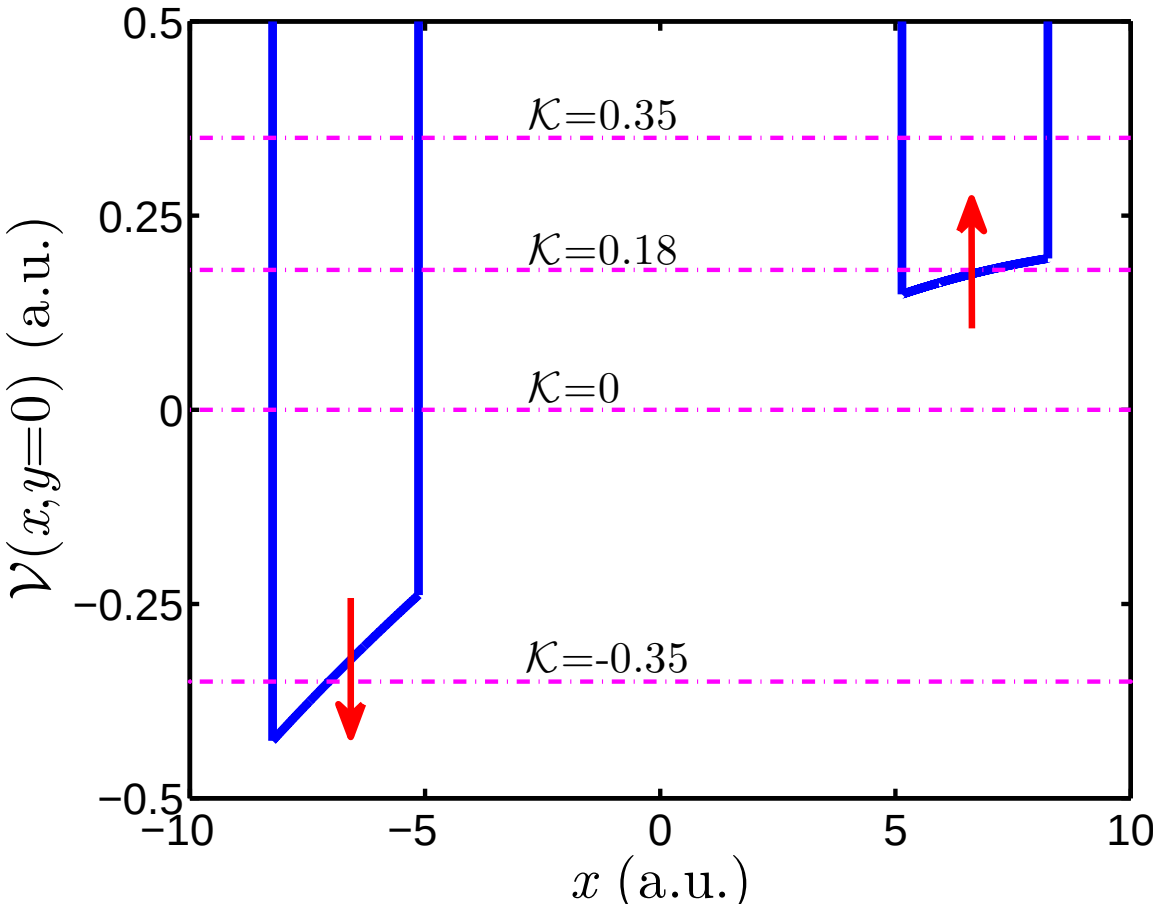

Figure 37: Section ($y = 0$) of the Zero-Velocity Surface in the accessible part of the billiard for $I = 10^{14}$ W $\cdot$ cm^{-2} and $\omega = 0.0584$ a.u. The red arrows show the deformation of the zero velocity surface as intensity is increased. The dashed horizontal lines are the Jacobi values used in Fig. 38 and Fig. 43.

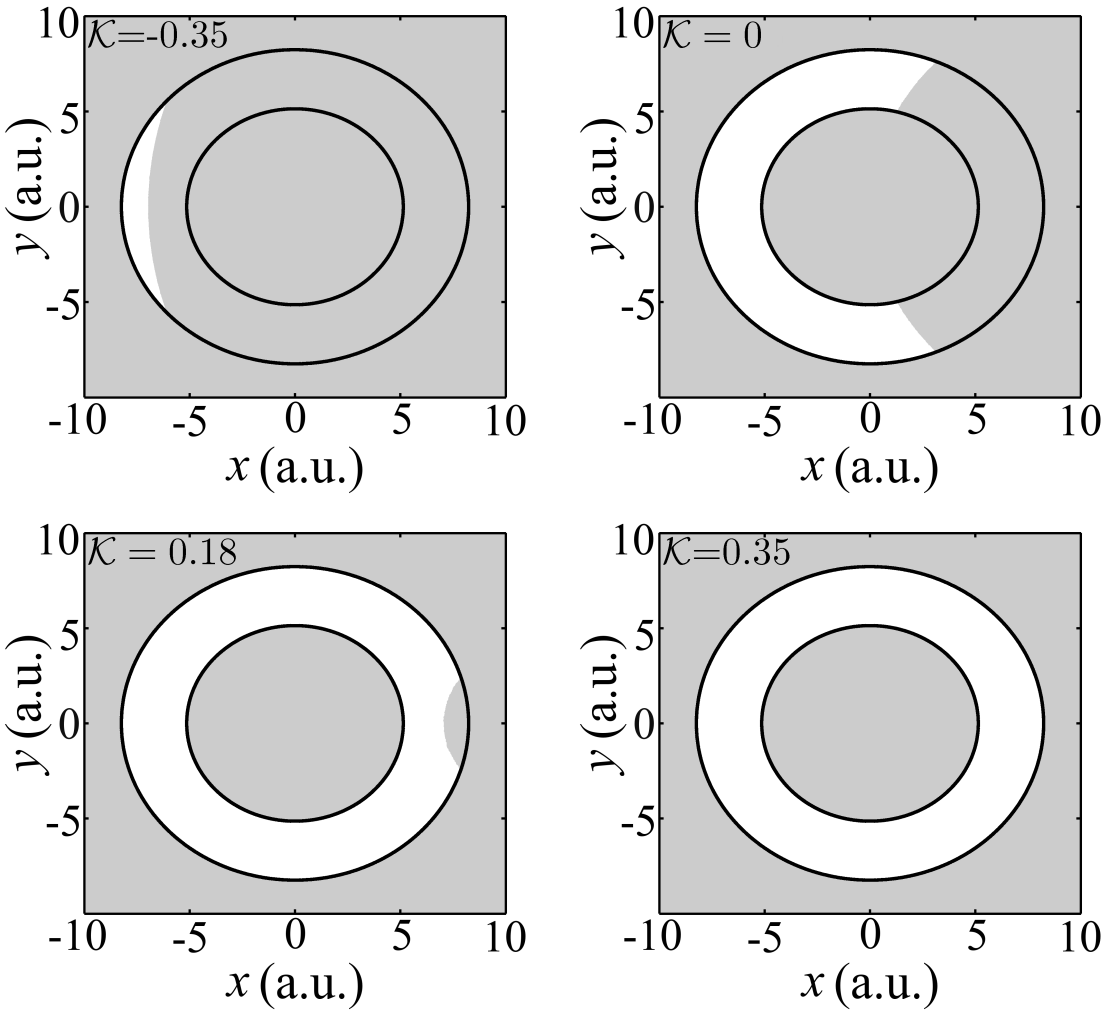

Figure 38: Accessible regions (white) of the billiard for different Jacobi values at $I = 10^{14}$ W $\cdot$ cm^{-2} and $\omega = 0.0584$ a.u. Jacobi values correspond to the dashed lines in Fig. 37.

two types: one which is homotopic to an annulus, and one which is only a portion of an annulus (see Fig. 38). For $\mathcal{K}$ larger than $-\omega^2 r_{\text{in}}^2/2 + E_0 r_{\text{in}}$, the entire annulus is accessible to the dynamics. As the laser intensity is increased, the difference between the right and left sides of the well is amplified. In this paper we mainly consider Jacobi constants larger than $-\omega^2 r_{\text{in}}^2/2 + E_0 r_{\text{in}}$ such that the full annular region of the billiard is accessible to the dynamics. For $I = 10^{14}$ W $\cdot$ cm^{-2} and $\omega = 0.0584$ a.u., this critical value of $\mathcal{K}$ is approximately equal to 0.15.

6.2.3 Dynamical rules

The dynamics is computed in a piecewise fashion because of the walls. It is composed of segments of laser-driven dynamics, as given by Hamiltonian (50), until the particle reaches one of the walls. At this instant, the reflection rule is applied which mimics an elastic scattering at the limit of an infinitely stiff potential.

Concerning the laser-driven dynamics, the equations of motions associated with Hamiltonian (50) are given by

$$\begin{aligned} x(t) &= \frac{E_0}{\omega^2} + \left(\left(x_0 - \frac{E_0}{\omega^2}\right) + p_{x,0}t\right)\cos\omega t \\ &\quad + \left(\left(p_{y,0} - \frac{E_0}{\omega}\right)t + y_0\right)\sin\omega t, \qquad (52a) \\ y(t) &= \left(y_0 + \left(p_{y,0} - \frac{E_0}{\omega}\right)t\right)\cos\omega t \\ &\quad - \left(\left(x_0 - \frac{E_0}{\omega^2}\right) + p_{x,0}t\right)\sin\omega t, \qquad (52b) \\ p_x(t) &= \left(p_{y,0} - \frac{E_0}{\omega}\right)\sin\omega t + p_{x,0}\cos\omega t, \qquad (52c) \\ p_y(t) &= \left(p_{y,0} - \frac{E_0}{\omega}\right)\cos\omega t - p_{x,0}\sin\omega t + \frac{E_0}{\omega}, \qquad (52d) \end{aligned}$$

where x_0, y_0, $p_{x,0}$, and $p_{y,0}$ are the initial conditions (at time $t = 0$).

At time $t = t_R$, the electron reaches either one of the two walls and we apply the reflection condition before a next phase of laser-driven dynamics. The reflection conditions are more easily expressed in polar coordinates as it corresponds to the radial momentum changing sign while the other coordinates are unchanged (see Fig. 39). By definition of the billiard, the rebound takes place at time $t = t_R$ satisfying

$$\sqrt{x^2(t_R) + y^2(t_R)} = r_i,$$

where i denotes the wall index, i.e., $i \in \{\text{in, out}\}$. Before the rebound (i.e., at $t = t_R^-$), we compute the radial momentum p_r from the value of (x, y, p_x, p_y) by $p_r = (xp_x + yp_y)/r$. Then, the rebound condition is given by a change of sign of the radial momentum

$$p_r\left(t_R^+\right) = -p_r\left(t_R^-\right).$$

As a consequence, the values of the momenta after the rebound, denoted p_x^+ and p_y^+, are given by

$$p_x^+ = -\frac{(x^2-y^2)p_x^- + 2xyp_y^-}{r^2}, \tag{53a}$$

$$p_y^+ = \frac{-2xyp_x^- + (x^2-y^2)p_y^-}{r^2}. \tag{53b}$$

We note that Hamiltonian (50) is left unchanged by the reflection rule, that is $\mathcal{K}\left(t_R^+\right) = \mathcal{K}\left(t_R^-\right)$, which is easily seen from the expression of the kinetic energy in polar coordinates which is equal to $p_r^2/2 + p_\theta^2/\left(2r_i^2\right)$.

6.2.4 Linearization of the flow

In this section, we consider the linear effect of the rebound condition on neighboring trajectories. The motivation for doing so is twofold: First the tangent rebound condition can be used to compute the tangent flow of trajectories to deduce the linear stability of periodic orbits. Second, as the billiard model corresponds to the limit of infinitely stiff potential for a Hamiltonian system, the billiard model should preserve the Hamiltonian structure. We have already checked that the rebound condition preserves the Hamiltonian, thus the last prescription is that the symplectic two-form is preserved, or equivalently the tangent rebound matrix is symplectic.

The tangent rebound matrix can be seen as an extension of the tangent flow [24] to include the impact of the rebound on neighboring trajectories (to first order). For that, we consider a first trajectory with initial conditions $x_0, y_0, p_{x,0}, p_{y,0}$ at $t = 0$ in the neighborhood of one of the two walls, i.e., $x_0^2 + y_0^2 \approx r_i^2$, where $i \in \{\text{in},\ \text{out}\}$, and such that the rebound time $t_R \ll 1$. Then, we look at the impact of a perturbation of these initial conditions to $x_0 + dx_0, y_0 + dy_0, p_{x,0} + dp_{x,0}, p_{y,0} + dp_{y,0}$ immediately after the rebound. Because the rebound time is not the same for the two trajectories, we have to consider a small laser-driven propagation before and after the rebound to deduce the tangent rebound properties. The situation is schematically depicted in Fig. 39.

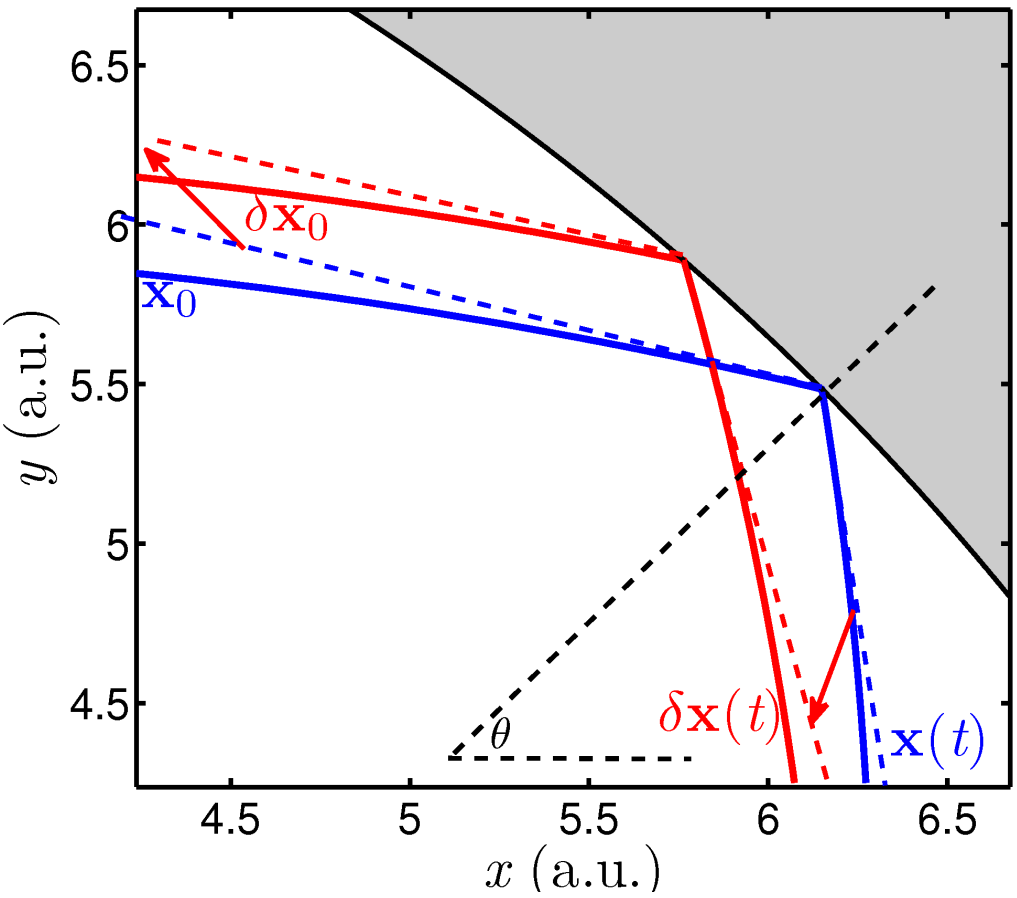

Figure 39: Schematic representation for computation of the rebound condition. The solid blue (dark) and red (light) lines are real trajectories, differing only by a small perturbation in the initial conditions. The dashed red and blue lines are representations of the linearized dynamics. The angle θ is the angle of rotation used in Hamiltonian (54).

The computation of the tangent rebound matrix is more easily seen in a rotated Cartesian set of coordinates $\tilde{x}, \tilde{y}, \tilde{p}_x, \tilde{p}_y$, for some angle θ to be specified later. In the rotated frame, the corresponding Hamiltonian reads

$$\begin{aligned} \mathcal{K}(x, y, p_x, p_y) &= \frac{p_x^2}{2} + \frac{p_y^2}{2} - \omega (x p_y - y p_x) \\ &\quad + E_0 x \cos\theta + E_0 y \sin\theta, \end{aligned} \tag{54}$$

where we have dropped the tildes for simplicity. Since we are only interested in the linear properties of the rebound condition, throughout this section we consider all the equations linearized to the first order.

As explained in Sec. 6.2.3, the dynamics is computed piecewise with a first stage of laser-driven propagation until the electron reaches the wall, then the rebound condition and finally a new stage of laser-driven propagation. In the rotated frame and before the rebound, i.e., $t < t_R$, the laser-driven dynamics given by Hamiltonian (54) yields

$$x(t) \approx x_0 + (p_{x,0} + \omega y_0)\, t, \tag{55a}$$

$$y(t) \approx y_0 + (p_{y,0} - \omega x_0)\, t, \tag{55b}$$

$$p_x(t) \approx p_{x,0} + (\omega p_{y,0} - E_0 \cos\theta)\, t, \tag{55c}$$

$$p_y(t) \approx p_{y,0} - (\omega p_{x,0} + E_0 \sin\theta)\, t, \tag{55d}$$

where we have neglected $O(t^2)$. At this stage, we select the rotation angle θ such that the perpendicular direction to the wall at the rebound is aligned with the x-direction for the unperturbed trajectory. We keep this fixed frame for the perturbed trajectory. An alternative way (which provides the same solution) is to consider a perturbed rotated frame (obtained by a rotation by an angle $\theta + d\theta$) to impose the same constraint (the direction perpendicular to the wall is the x-axis at the rebound) on the perturbed trajectory. As a consequence of the chosen angle θ, the rebound condition solely depends on the x-direction, such that $x(t_R) = r_i$, or equivalently

using Eq. (55a)

$$t_R \approx \frac{r_i - x_0}{p_{x,0} + \omega y_0}. \tag{56}$$

Besides, because of the circular shape of the billiard and the angle θ, at the rebound the y-component vanishes ($y\left(t_R\right) = 0$). However, for the perturbed trajectory, this condition does not apply. Since we consider the perturbed trajectory comparatively to the original one in the same rotated frame, it is easier for the purpose of the calculation to keep formally the y-components, knowing that it is actually equal to zero.

The next step for the trajectory dynamics is the rebound condition, at time $t = t_R$. Because of the orientation of the frame where the x-direction is aligned with the radial one, the rebound condition (53) becomes $\dot{x}\left(t_R^+\right) = -\dot{x}\left(t_R^-\right)$ and $\dot{y}\left(t_R^+\right) = \dot{y}\left(t_R^-\right)$ which implies to the momenta

$$p_x\left(t_R^+\right) = -p_x\left(t_R^-\right) - 2\omega y\left(t_R\right), \tag{57}$$

and $p_y\left(t_R^+\right) = p_y\left(t_R^-\right)$, while the positions are left unchanged.

Finally, after the rebound, the trajectory experiences a new phase of laser driven dynamics. Combining the rebound condition (57) with a linearized propagation similar to Eq. (55), one can write the dynamics after the rebound as a function of the initial conditions (before the rebound), such that

$$\begin{aligned}
x\left(t\right) &\approx x\left(t_R\right) + \left(p_x\left(t_R^+\right) + \omega y\left(t_R\right)\right)\left(t - t_R\right), \\
&\approx x_0 - \left(p_{x,0} + \omega y_0\right)\left(t - 2t_R\right), && \text{(58a)} \\
y\left(t\right) &\approx y_0 + \left(p_{y,0} - \omega x_0\right) t, && \text{(58b)} \\
p_x\left(t\right) &\approx -\left(p_{x,0} + 2\omega y_0\right) - 2\omega\left(p_{y,0} - \omega x_0\right) t_R \\
&\quad + \left(\omega p_{y,0} - E_0 \cos\theta\right)\left(t - 2t_R\right), && \text{(58c)} \\
p_y\left(t\right) &\approx p_{y,0} + 2\omega\left(p_{x,0} + \omega y_0\right)\left(t - t_R\right) \\
&\quad - \left(\omega p_{x,0} + E_0 \sin\theta\right) t, && \text{(58d)}
\end{aligned}$$

where the equations are linearized at the first order in time. With the explicit formula for the dynamics after the rebound, as given by Eq. (58), it is straightforward to compute the impact of the perturbation on the initial conditions by replacing $x_0, y_0, p_{x,0}, p_{y,0}$ with $x_0 + dx_0, y_0 + dy_0, p_{x,0} + dp_{x,0}, p_{y,0} + dp_{y,0}$ respectively. Because of the change of initial conditions, the rebound time is modified to $t_R + dt_R$ as well. Using Eq. (56) for the perturbed trajectory we end up with

$$dt_R = -\frac{dx_0}{p_{x,0} + \omega y_0} - \frac{r_i - x_0}{(p_{x,0} + \omega y_0)^2} \left(dp_{x,0} + \omega dy_0\right). \tag{59}$$

Finally, combining Eq. (58) with Eq. (59) it is possible to compute the perturbed dynamics after the rebound. We define the deviations dx, dy, dp_x, dp_y of the perturbed trajectory after the rebound. For instance, considering the x-coordinate, we obtain

$$\begin{aligned} dx &= -dx_0 - \frac{2\left(r_i - x_0\right)}{p_{x,0} + \omega y_0} \left(dp_{x,0} + \omega dy_0\right) \\ &\quad - \left(dp_{x,0} + \omega dy_0\right)\left(t - 2t_R\right). \end{aligned} \tag{60}$$

Since we are interested in the dynamics in the vicinity of the rebound, we consider the limits $x_0 \to r_i$ and $t \to t_R^+$ (such that $t \to 0$). As a consequence, we end up with $dx = -dx_0$ from Eq. (60). A similar procedure can be applied to the other components and summarized in the linear equation

$$\begin{pmatrix} dx \\ dy \\ dp_x \\ dp_y \end{pmatrix} = J_R \begin{pmatrix} dx_0 \\ dy_0 \\ dp_{x,0} \\ dp_{y,0} \end{pmatrix},$$

where J_R is the tangent rebound matrix given by

$$J_R = \begin{pmatrix} -1 & 0 & 0 & 0 \\ 0 & 1 & 0 & 0 \\ \left(4\omega p_y - 2E_0 \cos\theta - 2\omega^2 r_i\right) p_x^{-1} & -2\omega & -1 & 0 \\ 2\omega & 0 & 0 & 1 \end{pmatrix}, \tag{61}$$

using the conditions $x = r_i$, $y = 0$ and where p_x is taken *right before* the rebound on the wall. We note that the tangent rebound matrix is a symplectic matrix, which proves that the rebound condition (53) preserves the symplectic two-form, i.e.,

$$dx_0 \wedge dp_{x,0} + dy_0 \wedge dp_{y,0} = dx \wedge dp_x + dy \wedge dp_y.$$

The tangent flow is used to characterize the linear stability of invariant structures like periodic orbits. As for trajectories, their integration is carried out piecewise: the integration is composed of intervals of laser-driven propagation and rebound conditions. Between the rebounds, we integrate the tangent flow given by [24]

$$d_t J = \nabla \mathbf{F} \; J,$$

where $\nabla \mathbf{F}$ is the matrix of variations of the flow associated with Hamiltonian (54). Then, right after a rebound on one wall, the Jacobian matrix is equal to the product of the previous Jacobian matrix right before the rebound, denoted J^-, with the rebound matrix (61): Jacobian matrix after the rebound reads

$$J^+ = J_R J^-.$$

6.3 Analysis of the dynamics

A sampling of typical trajectories of the annular billiard for $I = 10^{12}$ W·cm^{-2} is shown in Fig. 40. These examples illustrate qualitatively the different types of observed trajectories already discussed in Sec. 6.1. In the top row we see that the trajectories only hit the outer wall and never the inner wall and are therefore "whispering gallery orbits", or WGOs. In the middle row we show "daisy orbits". They are qualitatively the same, hitting both walls successively and accessing the entire angular distribution of the billiard. Both WGO and "daisy orbits" keep a constant rotational direction, either clockwise or counterclockwise, which we denote negative or positive, respectively. In the bottom row, left panel we see a "pringle orbit", hitting both walls in

turn, however, limited only to the downfield region of the billiard. The simple two rebound trajectories located at both extremes of the upfield and downfiled region of the billiard are periodic orbits. The leftmost curve is an elliptic periodic orbit (stable) while the rightmost curve is a hyperbolic periodic orbit (unstable). In the bottom right panel is a trajectory which hits neither wall (see Sec. 6.3.1.1). In the following sections we connect these trajectories to phase space structures and their stability.

6.3.1 Poincaré Sections

Since the dynamical system has two degrees of freedom, a convenient way to visualize the dynamical organization of phase space is by Poincaré sections. Here we consider a Poincaré section with equation $p_r = 0$ in the direction $\dot{p}_r > 0$. The rebound condition (53) imposes a discontinuity in the radial momentum p_r at the rebound, such that formally the condition $p_r = 0$ is never reached during a rebound. However, we see the billiard as the limit of an infinitely stiff potential, and a smoother dynamics corresponding to Hamiltonian (48) would reach $p_r = 0$ before changing sign. As a consequence, we consider the rebounds on the walls as potential candidates for the Poincaré section. The electron either rebounds on the outer wall, meaning that the radial momentum changes from positive to negative values or the electron rebounds on the inner wall, so that the radial momentum changes from negative to positive values. In order to comply with the transverse condition $\dot{p}_r > 0$ we include only the collisions with the inner wall. Furthermore, because of the rebound condition (53) we note that p_θ, $x = r\cos\theta$, and $y = r\sin\theta$ are continuous under a rebound so that it is equivalent to record their values either directly before or after the rebound. The Poincaré section can be represented in several ways. A three-dimensional plot can be used where we plot (x, y, p_θ) or we can make a projection onto the plane (θ, p_θ) using the constant Jacobi constraint. Regardless of which method is chosen there are two types of points on the section: The first kind are points on the inner wall for which

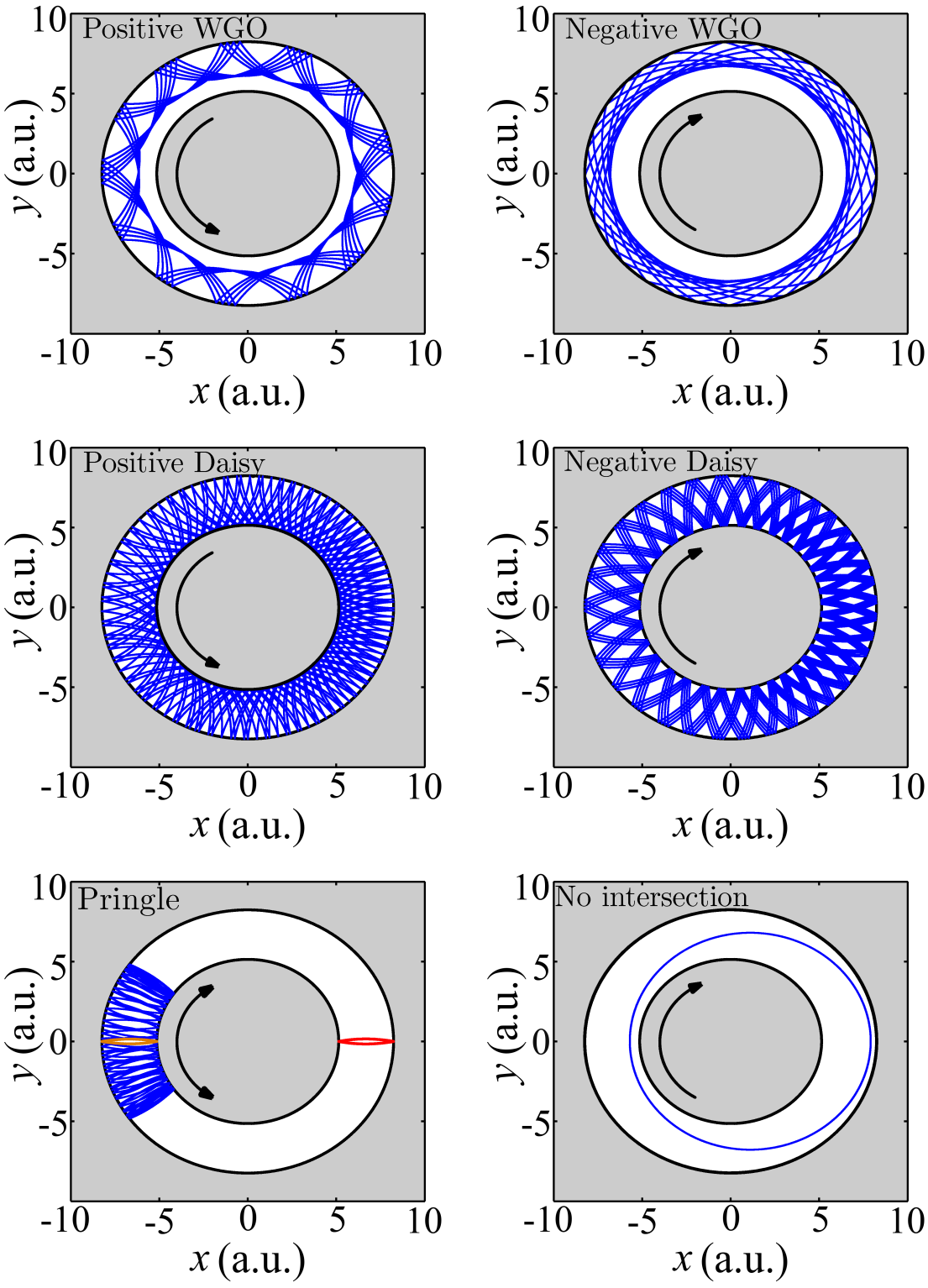

Figure 40: Trajectories of the annular billiard for $I = 10^{12}$ W $\cdot$ cm^{-2} and $\omega = 0.0584$ a.u. The trajectory type is shown in the top left corner of the panel and $\mathcal{K} = 0.35$ (see Fig. 37). The arrow shows the direction of travel of the trajectory. In the bottom left panel the simple two rebound orbits are periodic orbits. The downfield orbit (orange) is elliptic and the upfield orbit (red) is hyperbolic. The bottom right panel is a trajectory which hits neither wall for $\mathcal{K} = 2U_p \approx 0.002$ (see Sec. 6.3.1.1).

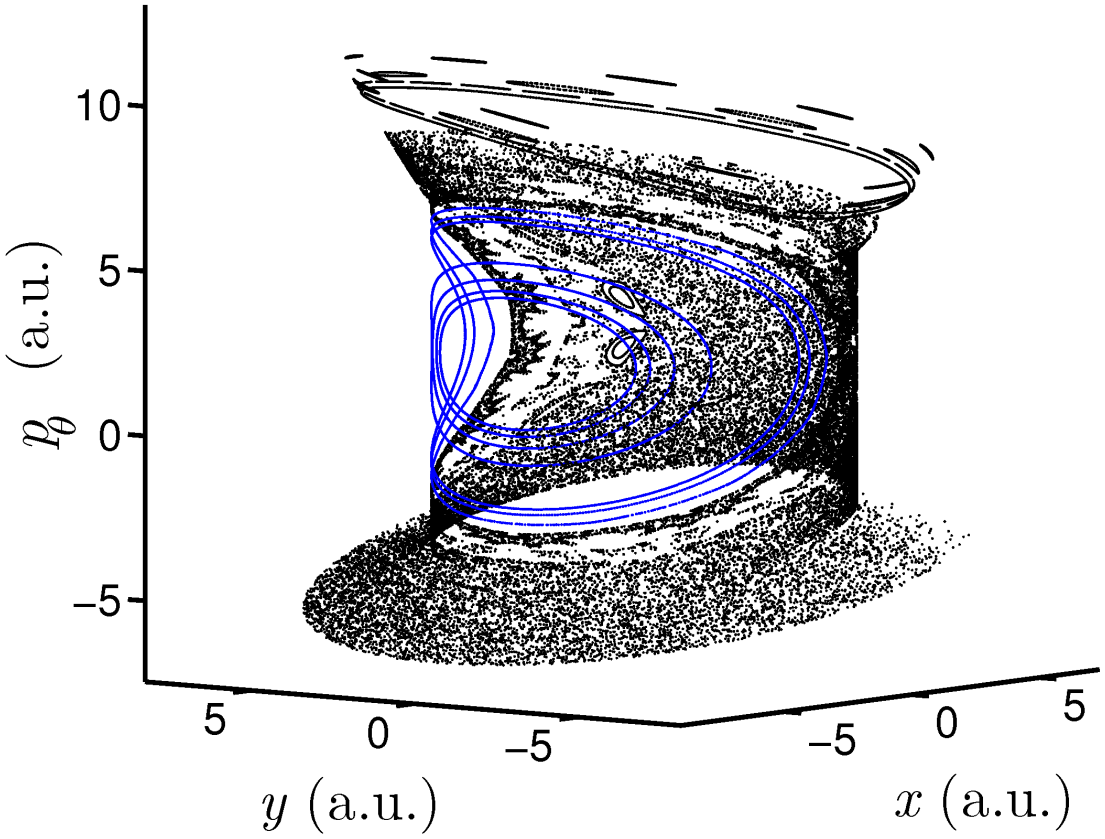

Figure 41: A Poincaré section for $I = 10^{14}$ W $\cdot$ cm^{-2}, $\omega = 0.0584$ a.u., and $\mathcal{K} = 0.35$. The blue trajectories (innermost) are the namesake of "pringle orbits". The corresponding two dimensional projection is displayed in Fig. 42, bottom right panel.

$r = r_{\text{in}}$ and p_r chosen so as to satisfy the condition on the Jacobi constant $\mathcal{K}$. The second kind are points for which $p_r = 0$ and r is chosen so as to satisfy $\mathcal{K}$. In this paper, for the sake of simplicity of our figures, we make use of the projection onto the two dimensional plane (θ, p_θ), however, we show the three dimensional counterpart in Fig. 41 where we have colored "pringle" trajectories in blue to illustrate their namesake shape.

6.3.1.1 *Trajectories which intersect neither wall*

It is natural to ask whether the choice of Poincaré section is a good one, i.e., do all trajectories intersect the Poincaré section? A small subset of trajectories which are noteworthy for both their peculiarity and the dynamics they showcase, do not intersect the Poincaré section $p_r = 0$. In that spirit we analyze the trajectories which do not collide with either wall. For such trajectories, $x^2 + y^2$ needs to remain between r_{in}^2 and r_{out}^2 at all times. The dynamics of these trajectories is governed by Hamiltonian (50). Using the translation $\tilde{x} = x - E_0/\omega^2$, $\tilde{p_x} = p_x$, $\tilde{y} = y$ and $\tilde{p_y} = p_y - E_0/\omega$, the Hamiltonian is mapped to

$$\tilde{\mathcal{K}} = \frac{p_x^2 + p_y^2}{2} - \omega(xp_y - yp_x) + \frac{E_0^2}{2\omega^2},$$

where we have dropped the tildes for simplicity. The dynamical features no longer depend on the value of E_0. The dynamics is better seen in polar coordinates, where the Hamiltonian becomes

$$\mathcal{K} = \frac{p_r^2}{2} + \frac{p_\theta^2}{2r^2} - \omega p_\theta + \frac{E_0^2}{2\omega^2}.$$

Since p_θ is a conserved quantity, the dynamics is that of a particle evolving in a potential equal to $p_\theta^2/(2r^2)$ and the particle will collide with a wall unless $p_\theta = 0$. In the case where, $p_\theta = 0$, p_r is constant, and it has to vanish so that no collision with the walls takes place. Therefore the only trajectories which do not hit a wall are circular orbits (since $\dot{r} = p_r = 0$). In the original coordinates, these circular periodic orbits are centered around $(x_0, y_0) = (E_0/\omega^2, 0)$ and they have a specific Jacobi constant of $2U_p$ where $U_p = E_0^2/(4\omega^2)$ is the ponderomotive energy. For this Jacobi constant, there exist a priori an infinite number of such orbits since the radius is not fixed. The only constraint on the radius is that the circular orbit has to fit inside the annulus.

Based on the laser parameters E_0 and ω, the existence and characterization of such orbits can be divided into several categories. For realistic fullerene parameters,

$(r_{\rm out} - r_{\rm in})/2 < r_{\rm in}$, which is considered here, the analysis can be grouped into four categories. Different parameters may lead to a different decomposition that can nevertheless be identified in a similar fashion (for instance the third point below may dissappear).

1. If E_0/ω^2 is larger than $r_{\rm out}$, then such trajectories do not exist because the center is outside the billiard.

2. If E_0/ω^2 is in between $r_{\rm in}$ and $r_{\rm out}$, then the circular orbits are on the right hand side of the inner wall of the annular billiard.

3. If E_0/ω^2 is in between $(r_{\rm out} - r_{\rm in})/2$ and $r_{\rm in}$, then such trajectories do not exist because none of the orbits can be fit inside the allowed region.

4. If E_0/ω^2 is smaller than $(r_{\rm out} - r_{\rm in})/2$, then the circular orbits surround the inner wall with a slight shift in the right direction.

The bottom panel of Fig. 40 shows a sample trajectory in the fouth category. In this example, the value $E_0/\omega^2 \approx 1.1$, which is less than $\rm r_{in}$ and hence the trajectory surrounds the inner wall, but is shifted slightly to the right. Except in rare cases (where E_0/ω^2 is equal to $r_{\rm in}$ or $r_{\rm out}$), if such orbits exist, then they exist as a continuous family. A linear stability analysis shows that these orbits are parabolic. In addition, given that $\dot{\theta} = -\omega$ (since $p_\theta = 0$), the particle turns clockwise.

Of course, these orbits remain exceptional, in the sense that they only exist at some particular value of the Jacobi constant $\mathcal{K} = 2U_p$. For $\omega = 0.0584$ a.u., all the orbits hit one wall at least for intensities larger than $I = 5.56 \times 10^{13}$ W $\cdot$ cm^{-2} or

intensities between 2.16×10^{13} W $\cdot$ cm^{-2} and 1.96×10^{12} W $\cdot$ cm^{-2}. The circular orbits confined in the right hand side of the annulus only exist for intensities between 2.16×10^{13} W $\cdot$ cm^{-2} and 5.56×10^{13} W $\cdot$ cm^{-2}. Finally, for intensities lower than 1.96×10^{12} W $\cdot$ cm^{-2} an infinite family of circular orbits surrounding the inner wall exist. Apart from the examples illustrated in this section all trajectories intersect, an infinite number of times, the Poincaré section. Therefore, we can safely keep our definition of the Poincaré section without missing important dynamics.

6.3.1.2 Varying the intensity

For $E_0 = 0$, Hamiltonian system (50) presents a continuous symmetry by rotation with two degrees of freedom, so it is integrable. We show the corresponding Poincaré section in Fig. 42 (top left panel). As expected, phase space is foliated by invariant tori.

When $E_0 > 0$ the system is no longer integrable and some invariant tori are expected to be broken. According to KAM theory, a large portion of invariant tori persist for E_0 small. In Fig. 42 we show the evolution of phase space as the laser intensity is varied. With increasing intensity we note the development of a resonance near $p_\theta \approx 2.5$. This resonance corresponds to the aforementioned two-rebound elliptic periodic orbit shown by the left most (downfield) orange curve in the bottom left panel of Fig. 40. This very robust elliptic periodic orbit (situated on the left hand side of the annulus) is extremely important in shaping the overall structure of phase space as intensity increases. Trajectories originating in this region cannot access the entire billiard in a way analogous to the librational motion in a pendulum. It is this librational motion which yields the "pringle orbits" already discussed at the beginning of this section. The behavior in the vicinity of this main resonance can be described roughly in the following way: The resonance is approximately located at $p_\theta = \omega r_0^2$, and this can be seen from the dynamical equation for θ, i.e., $\dot{\theta} = -\omega + p_\theta / r^2$. For a

given trajectory, if all the values of p_θ are larger than ωr_{out}^2, then the trajectory turns counterclockwise. If the values of p_θ are smaller than ωr_{in}^2 then it turns clockwise. In between, it oscillates between the two tendencies.

The Poincaré sections show that the phase space is highly regular over several decades of laser intensity. Chaotic regions of phase space develop near the hyperbolic periodic orbit which is a rebound between the two walls located in the upfield region, or the right-hand side of the annulus, and is shown in the rightmost curve in the bottom left panel of Fig. 40. Overall the structure of phase space looks very similar to that of a forced pendulum. In particular, the width of the main resonance zone grows like $\sqrt{E_0}$ or equivalently like $I^{1/4}$. However, we will see that there is a number of discrepancies of which twistless tori are the most significant ones. We readily observe that the lower part of phase space (negative angular momentum) is more chaotic than the upper one (positive angular momentum).

6.3.1.3 Varying the Jacobi value

With the intensity fixed at $I = 10^{14}$ W $\cdot$ cm^{-2} the Jacobi value can also be varied, keeping in mind that this variation affects the accessible regions of the billiard (see Sec. 6.2.2). We show the corresponding Poincaré sections in Fig. 43. Starting with the top left panel, the Poincaré section is contained inside the interval $\theta \in [2.45, 3.83]$ which agrees with the corresponding panel in Fig. 38, note also that the dynamics is highly regular. Besides, since the inner wall is not accessible for this Jacobi value, points on the section result directly from the condition that $p_r = 0$: A typical trajectory hits the outer wall but never reaches the inner one. For the top right panel, the inner wall is now accessible (see top right panel of Fig. 38) and the dynamics shows a mixed chaotic and regular behavior. In the regular region of the Poincaré section the trajectories are regular "pringle orbits", whereby the turning points in $\dot{\theta}$ are due to the dynamics (and not to the geometry of the billiard). Recall that the regular

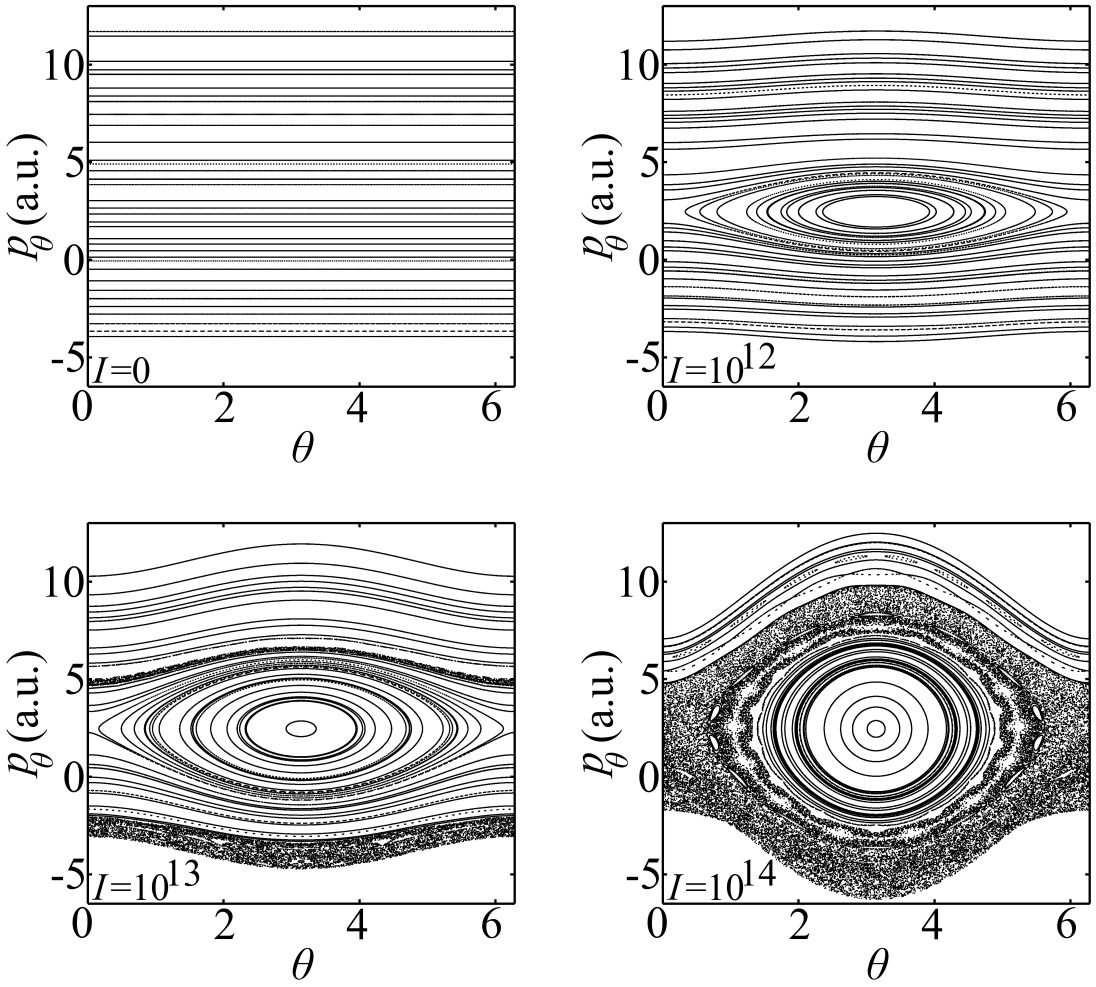

Figure 42: Poincaré sections for various values of the laser intensity. Starting in the top left panel we begin with $I = 0$ (integrable case) and moving left to right and up to down the intensity is increased. In all panels $\omega = 0.0584$ a.u. and $\mathcal{K} = 0.35$.

region does not span the entire region of accessible θ values. However, the trajectories originating in the chaotic region experience turning points in $\dot{\theta}$ because they hit the artificial walls imposed by the choice of Jacobi value. In the bottom panel the entire inner wall is accessible and only a small portion of the outer wall is inaccessible. The dynamics is still mixed, composed of a regular region with "pringle orbits", and a highly chaotic region where the trajectories hit the virtual walls imposed by the geometry of the configuration space. WGOs are not possible for these values of Jacobi constant. In fact, WGOs appear only when the entire annulus is accessible, e.g. in the bottom right panel of Fig. 42.

6.3.2 Partitioning of phase space

Because of the dimensionality of the billiard (two degrees of freedom) invariant KAM tori constitute barriers of transport which confine the (chaotic) dynamics to distinct regions of phase space. However, they are not robust enough to partition phase space at sufficiently high value of the intensity. Here, our analysis reveals the existence of much more robust invariant objects, namely twistless tori which are particularly relevant for the organization of phase space [66, 67], since they partition phase space at relatively high intensities into regions where the different types of trajectories occur. We next introduce a diagnostic tool for finding these tori.

6.3.2.1 Frequency Analysis

Frequency Analysis [69] is a practical tool in Hamiltonian systems for analysis of the dynamics. For integrable systems written in action-angle variables $(\mathbf{A}, \varphi)$, the method consists of plotting the frequency $\omega(\mathbf{A}) = \partial H_0/\partial \mathbf{A}$ as a function of $\mathbf{A}$, which is expected to be smooth for (sufficiently smooth) integrable systems. For nearly integrable systems, the frequency is computed by a windowed Fourier transform of a chosen observable. It is computed for an ensemble of trajectories, and plotted, for instance, as a function of the initial value of the action. From this analysis it

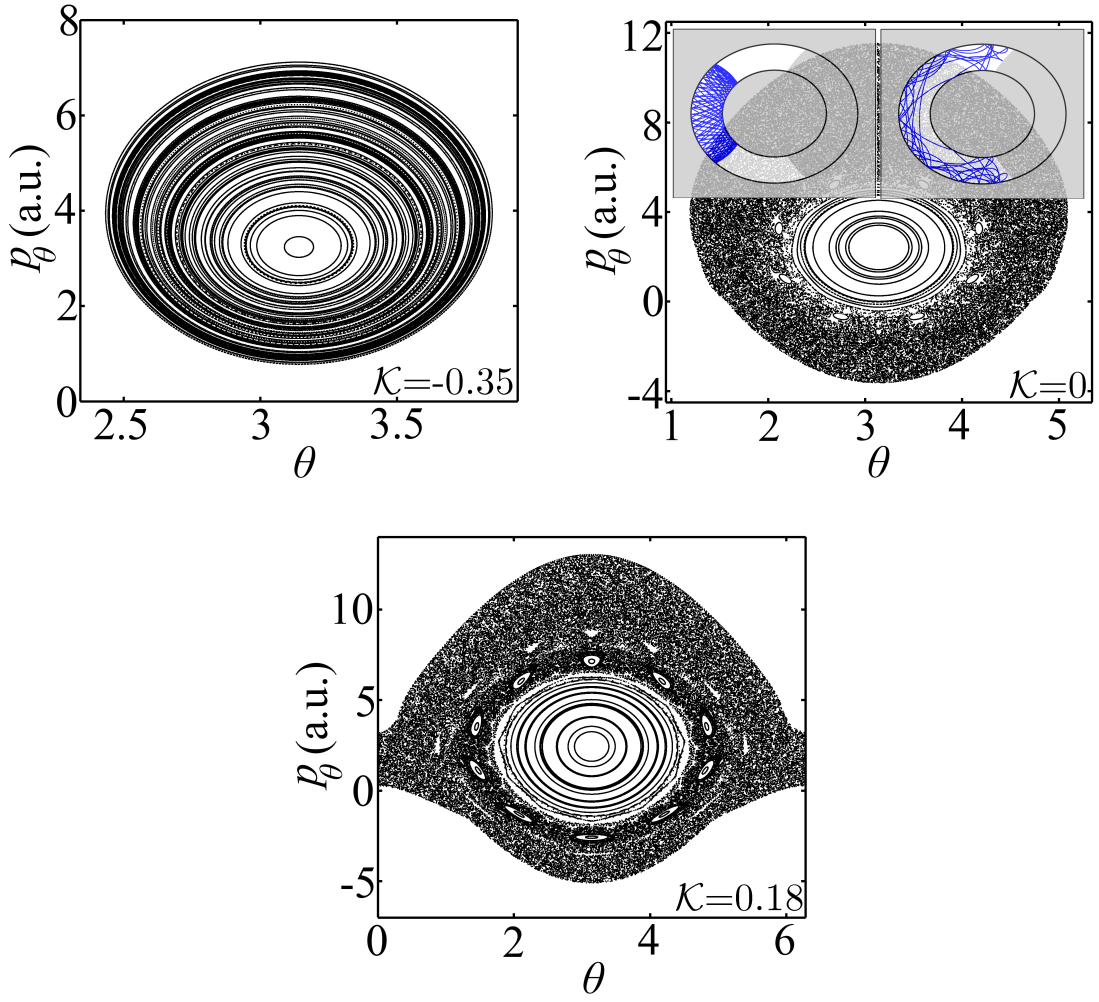

Figure 43: Poincaré sections for various values of $\mathcal{K}$ with $I = 10^{14}$ W $\cdot$ cm^{-2} and $\omega = 0.0584$ a.u. These Jacobi values are the same used in Fig. 37 and Fig. 38. The top right panel includes two trajectories. The left trajectory is taken from the "pringle" region and the right trajectory is taken from the chaotic region.

is possible to identify elliptic and hyperbolic islands, regular regions filled by KAM tori, and chaotic regions by their respective unique signatures. The elliptic islands are expressed as constant frequency plateaus, the hyperbolic orbits by cusps in the frequency, regular regions as apparently continuous curves, and chaotic regions as non-smooth sections. Frequency analysis can also identify regions where the twist condition is not satisfied, i.e., when ω is no longer a monotonous function of the action. In this case, the standard twist condition for the standard KAM theorem is not satisfied, and it gives rise to a new taxonomy of dynamical mechanisms, like separatrix reconnection and twistless tori [66, 67].

In Figure 44 we plot the frequency as a function of the initial momentum p_θ. The ensemble of trajectories are the series of points on the Poincaré section with initial conditions $\theta = \pi$ and various p_θ while imposing the Jacobi constraint to compute the other variables. The motivation is that for the integrable case p_θ is a conserved quantity. The frequency analysis of the integrable case (Fig. 44, upper panel) shows that the frequency is a continuously varying function of p_θ, as is expected. The most interesting feature is that the frequency map does not change monotonically with p_θ. This implies the existence of twistless tori located at the extrema of the frequency map, at $p_\theta \approx -3.03$ and $p_\theta \approx 6.11$. In the non-integrable case (Fig. 44, lower panel), we see the appearence of a plateau which corresponds to the "pringle orbits". In addition we notice some chaotic features in the insets, even if the overall behavior seems to be quite regular at this intensity. Furthermore, the frequency map still exhibits two extrema, again which correspond to twistless tori. A closer look at the frequency map around $p_\theta = -3.2$ and $p_\theta = 6.5$ (insets) reveals a rich dynamics with a succession of elliptic and hyperbolic orbits, even if the overall behavior seems to be quite regular.

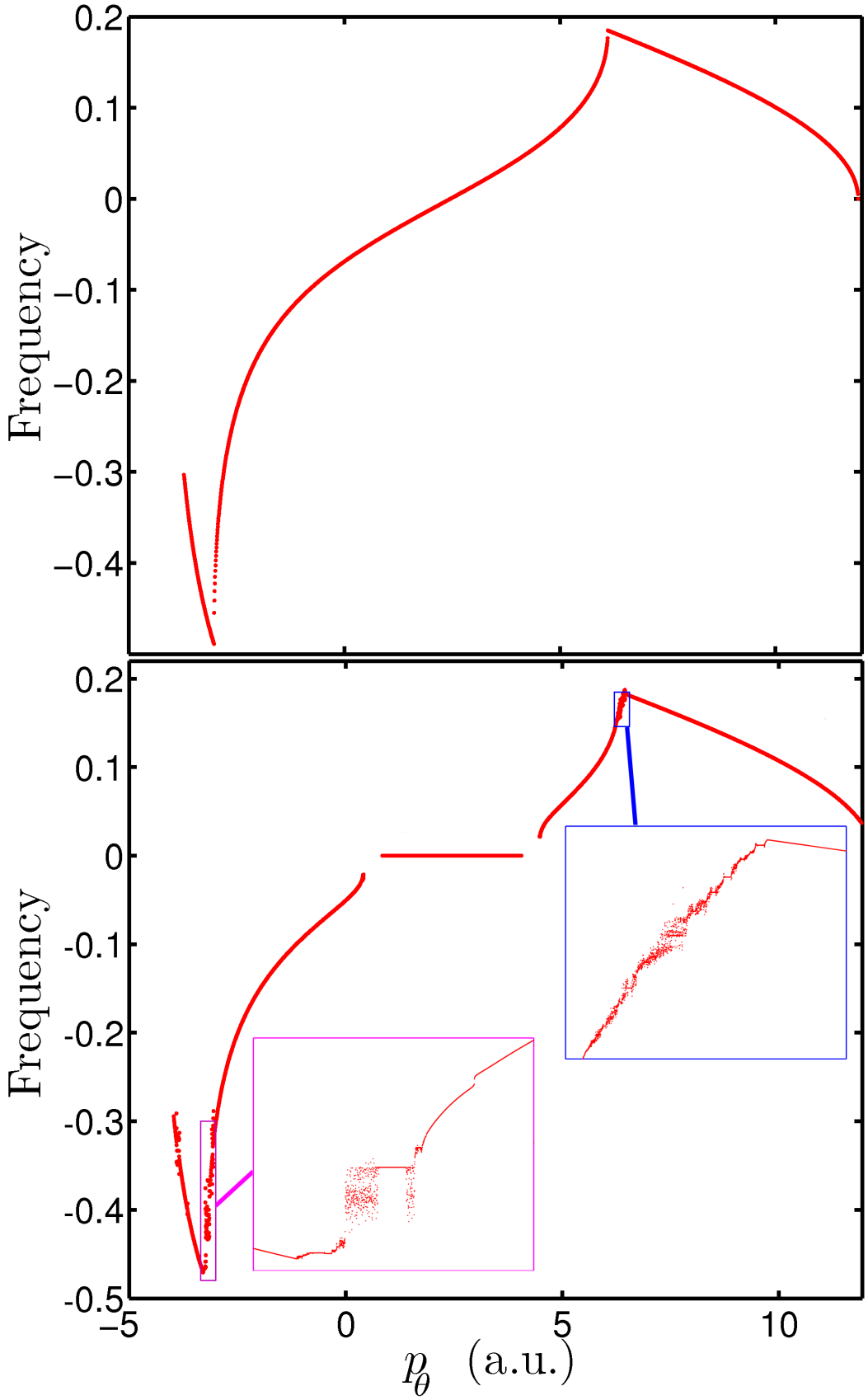
0.2
0.1
0
−0.1
−0.2
−0.3
−0.4
Frequency
0.2
0.1
0
-0.1
-0.2
-0.3
-0.4
-0.5
Frequency
−5
0
5
10
p_θ (a.u.)

6.3.2.2 Twistless tori

The aforementioned twistless tori are visualized by high resolution Poincaré sections. Figure 45 shows Poincaré sections with initial conditions nearby $p_\theta \approx 6.5$ (upper panel) and $p_\theta \approx -3.2$ (lower panel), corresponding to the local maxima in Fig. 44. Both Poincaré sections are similar in that they show well-developed chaotic regions sandwiched between two regular regions. The regular regions correspond to WGOs, shown in blue, and "daisy orbits", shown in red. Likewise, the chaotic region in both panels exhibits a stratification whereby a trajectory originating in one of these regions remains there and cannot pass to another chaotic region. The stratification is not due to KAM tori since KAM tori come in families. Instead it is caused by the existence of twistless tori, which, having dimension two, can partition phase space. In particular in the lower panel of Fig. 45, we recognize one of the signatures of twistless tori which is the meandering behavior (see for instance the interface between the orange and the dark red chaotic regions). The black line, superimposed over both panels, separates the two different possible ways of intersecting the Poincaré section. Points on the section above (resp. below) the black line for the upper (lower) panel are standard intersections of the flow with the Poincaré section in the sense that p_r changes sign smoothly before and after the intersection. Points below (resp. above) the black curve for the upper (lower) panel are collisions with the inner wall where the sign of p_r changes due to the rebound condition (see Sec. 6.3.1). As expected, all the WGO trajectories are below the black curve in the lower panel (since none of their points intersect the inner wall). The entire WGO region is regular. We also notice that all the "daisy orbits" are above the black curve, and this region is also mostly regular. Between these two regions is a strongly chaotic region with very few elliptic islands. Each of the chaotic regions (in both panels) has a portion above and below the black line. The range of θ where each chaotic region exists above (below) the black line gives the accessible region of the inner wall to the electron. Figure 46 illustrates how

the accessible region of the inner wall changes as one moves from WGOs to "daisies" in the lower panel of Fig. 45. Beginning with the WGOs, shown in blue, which have no points above the black line (no accessible region on the inner wall) we increase p_θ to the light blue region there is a small range of θ values for which the chaotic region is above the black line. The θ values are centered about $\theta = 0$ and they correspond to the area along the inner wall which is accessible to the electron. Moving again upwards in p_θ we pass by several more chaotic regions, each having a wider range of θ above the black line which allows for a wider range of the inner wall to be visited by the electron. The inner wall becomes more accessible until finally reaching the "daisy" region, shown in red. At this point, all intersections of the Poincaré section are above the black line covering $\theta \in [0, 2\pi]$ and therefore the entire inner wall is accessible. The four twistless tori which exist in this chaotic region are responsible for the discrete transition from WGOs to "daisy orbits". Likewise, a simiar feature can be observed for the upper panel of Fig. 45, nearby $p_\theta = 6.5$, however there are fewer chaotic regions and hence fewer twistless tori.

6.4 Conclusions on the billiard model

The motivation of our work stems from recent photoionization experiments in strong field of atoms and molecules in both circular and linear polarized light where a significant variation of the yields with polarization was observed [50]. We propose a rather simple dynamical model for the motion of a valence electron inside the valence shell of fullerene C_{60}, namely an annular billiard. We have investigated the dynamics when this electron is subjected to a circularly polarized laser field. We have shown that it exhibits three distinct types of trajectories: "whispering gallery", "daisy" and "pringle" orbits. These trajectories are found in distinct, identifiable regions of phase space for a wide range of laser intensity and Jacobi values. They are kept characteristically segregated from each other by the existence of twistless tori which partition

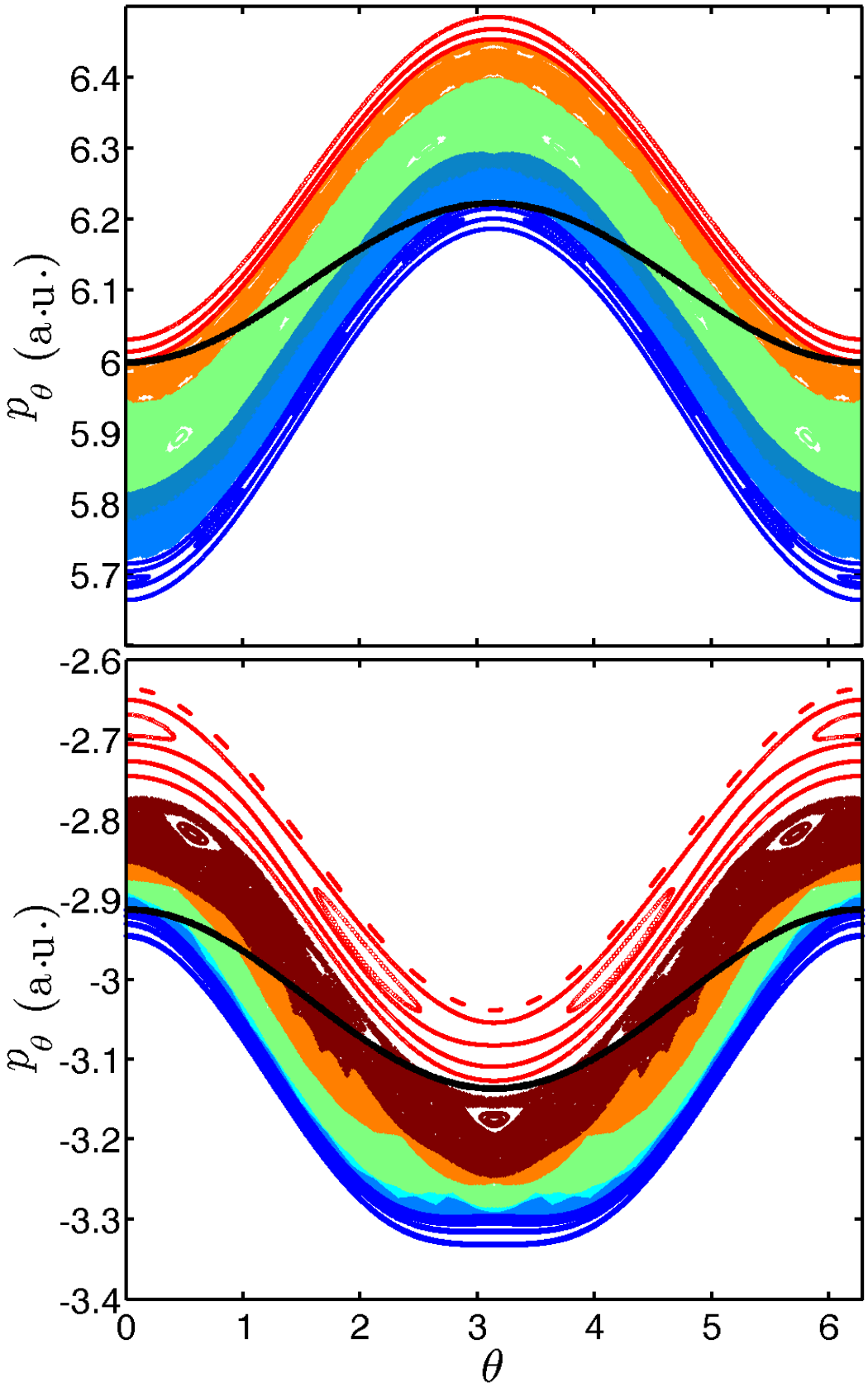
6.4
6.3
6.2
6.1
6
5.9
5.8
5.7
p_θ (a.u.)
-2.6
-2.7
-2.8
-2.9
-3
-3.1
-3.2
-3.3
-3.4
p_θ (a.u.)
0
1
2
3
4
5
6
θ

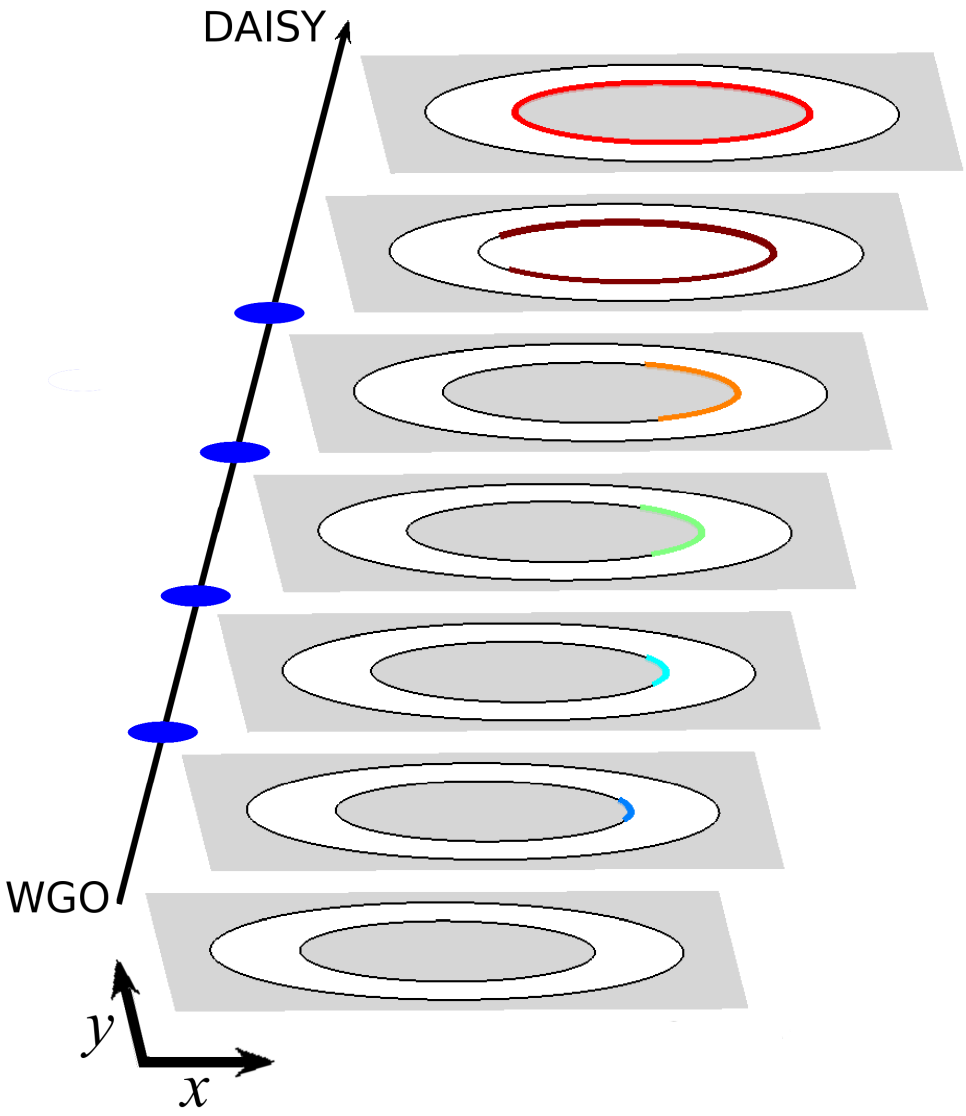

Figure 46: The transition scenario from whispering gallery orbits to "daisy orbits" is schematically represented via a graphic showing successive regions of the inner wall which can be visited by the electron. The color of the accessible region of the inner wall corresponds to the color of the chaotic regions in the bottom panel of Fig. 45. The blue ovals represent the twistless tori which separate the different chaotic regions.

phase space. The twistless tori are identified through a frequency analysis and are confirmed by generation of high resolution Poincaré sections. These twistless tori, blessed with high stability, exist in chaotic regions where KAM tori have been broken by the strong laser field. Because of the barriers they create, twistless tori, allow for a transition scenario from WGO to "daisy orbits" in both rotational directions, positive and negative.

In the greater context of this thesis, a rigorous study of the billiard model is useful because it is a warm-up to studying a "complete" model of fullerene, by which I mean a model with a continuous potential which allows for ionizations and returns. Of course, before ionizations and returns take place, the inner electron spends much time nearby the core. This study has allowed us to better understand the phase space structures which organize the motion of the inner electron, and provides a nice segway into ionizations (and subsequent returns).

6.5 Moving towards a more realistic potential

The jellium approximation used to approximate the positive charge background of fullerene [70] has been explicity expressed as a non-continuous potential in Ref. [12], Eq. (D1). However, the potential is not continous and is therefore not well suited for numerical analysis. We instead prefer to use a continuous, parameterized potential. Therefore, before we make a comparison between the billiard model and a more complete potential we must first choose an appropriately suited smooth potential.

6.5.1 Choosing a smooth potential

The proposed potential is given by Eq. (62).

$$V(r) = -\frac{\Delta r^{-1}}{\left(1 + \left|\frac{r-r_0}{\Delta r}\right|^{\alpha}\right)^{\frac{1}{\alpha}}} + \left(V_{min} + \frac{1}{\Delta r}\right)\left(1 - \frac{1}{1+\exp -\beta\left(r - r_0 - \Delta r\right)} - \frac{1}{1+\exp -\beta\left(r_0 - \Delta r - r\right)}\right) \quad (62)$$

Where $r_0 = 6.69$, $\Delta r = 1.56$, and $V_{min} = -1.5$. The two parameters α and β are allowed to vary such that in the limit $\alpha \to \infty$ and $\beta \to \infty$ the potential reduces to the square well potential of the billiard, as seen below.

$$V_\infty(r) = \begin{cases} {}^{-1}/_{|r-r_0|} & \text{for} \quad 0 < r < r_0 - \Delta r \text{ and } r_0 + \Delta r < r \\ V_{min} & \text{for} \quad r_0 - \Delta r < r < r_0 + \Delta r \end{cases} \tag{63}$$

In order to properly compare the dynamics generated from the potential of [12] and Eq. (62), we vary the parameters α and β. We select a choice of parameters that produce a potential with relatively soft walls that is only qualitatively similar to the potential found in [12]. This way, if the dynamics generated by both potentials are the same, we prefer to choose parameters that yield a soft potential, which will be easier to numerically integrate.

In figure 47 we superimpose the two potentials under different parameter values for Eq. (62). In the top panels β is kept constant at $\beta = 6$ and α is varied, while in the bottom panels α is kept constant at $\alpha = 3$ and β is varied. We see that as α is increased the top of the potential more closely resembles ${}^{-1}/_{|r-r_0|}$ and hence is a good fit to the potential in [12]. Likewise, as β is increased the walls become steeper and the bottom of the well becomes flatter. We choose $\alpha = 3$ and $\beta = 6$ because this combination yields a potential that is qualitatively similar to the potential of [12], however, the walls are not steep and therefore potential is not stiff and is easy to integrate numerically. We will refer to the potential given by Eq. (62) with $\alpha = 3$ and $\beta = 6$ as the smooth potential of fullerene and the system using this potential as the full model of fullerene.

With a suitable potential we can begin investigations into the full model fullerene.

6.5.2 Saddle point

Just like the case of the billiard, it is convenient to work in a rotating frame. Our new Jacobi value, shown below, is identical to that of the billiard with the addition

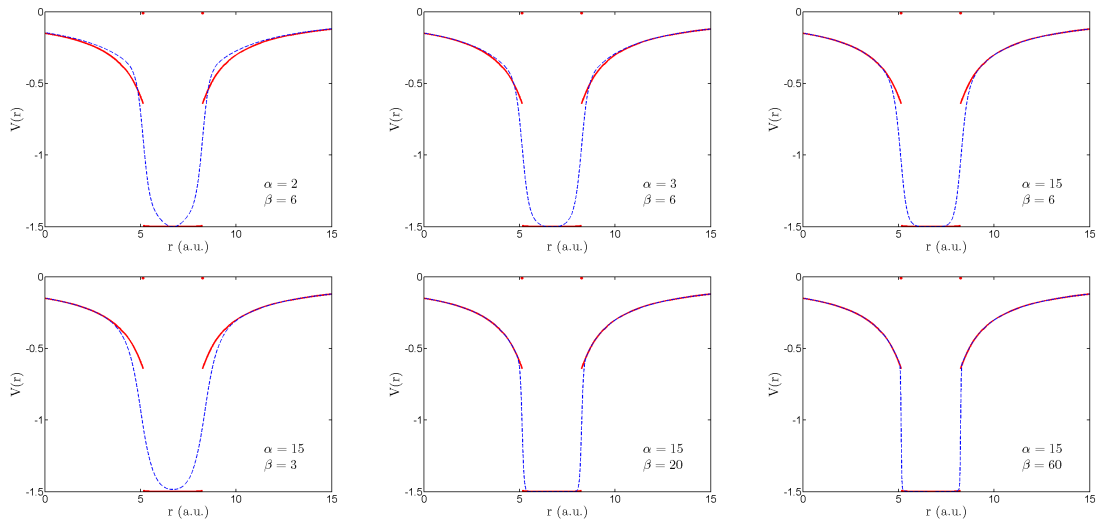

Figure 47: The potential of [12] is shown in solid red for all panels while potential (62) is shown by the dashed blue line. In the top row, α is varied while β remains constant and in the bottom row the opposite true.

of the smooth potential, $V(r)$.

$$\mathcal{K}(x, y, p_x, p_y) = \frac{p_x^2}{2} + \frac{p_y^2}{2} - \omega(xp_y - yp_x) + E_0 x + V(r), \tag{64}$$

We can furthermore define a Zero-Velocity Surface, as was done in Sec. 6.2.2 but this time it will be continuous. The zero velocity surface is useful for its aid in visualizing configuration space as well as its ability to show the saddle-center through which ionization and return are possible.

Applying the same techniques as were used in Sec. 6.2.2 we arrive at the expression of the zero velocity surface for a continuous potential,

$$\mathcal{V}(x, y) = -\frac{1}{2}\omega^2\left(x^2 + y^2\right) + E_0 x + V\left(\sqrt{x^2 + y^2}\right), \tag{65}$$

and we plot a comparison between the zero velocity surfaces of the billiard and of the full model in the left panel of figure 48. The zero velocity surface of the billiard has been taken from figure 37, however, we have shifted the entire surface downward 1.5 units so that it can be plotted directly on top of the zero velocity surface of the

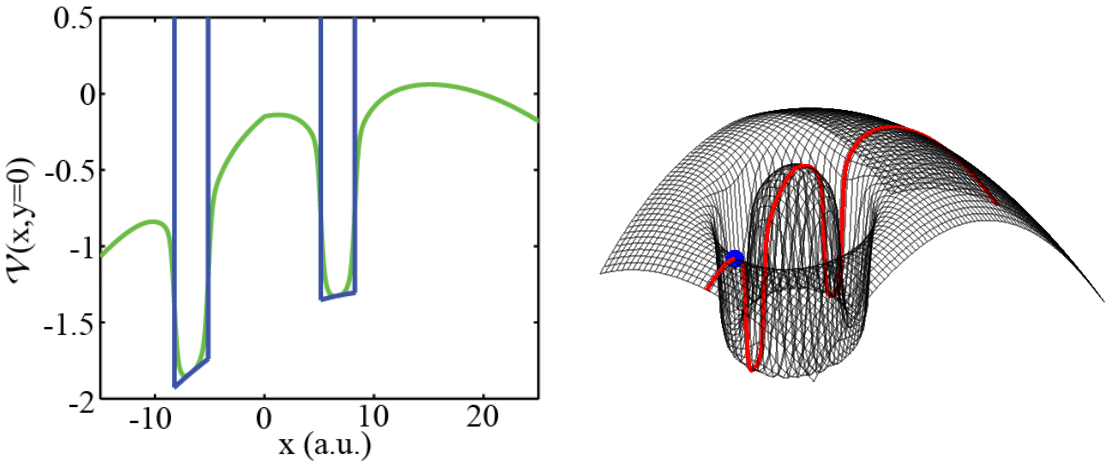

Figure 48: Left panel: A comparison of the Zero Velocity Surface for the billiard (shown in blue) and the potential of Eq.(62). Right panel: The Zero Velocity Surface for the full model of fullerene in two dimensions. The section along $y = 0$ is shown in red and a local extremum is highlighted by the blue marker.

full model. In the right panel we show a two dimensional zero velocity surface and highlight with a blue ball a local extremum known as the saddle-center.

The local extemum, classified as a saddle-center, is used to seperate phase space into a bounded and non bounded region. Of course, in the billiard, this point is absent because the potential walls are infinite, i.e. ionization is not allowed. However, for trajectories moving in the full model, the saddle-center acts as a window through which ionization may occur. Since the Jacobi value is conserved, trajectories which initially begin below the Jacobi value of the saddle center cannot ionize. On the contrary, trajectories which begin above the saddle-center may ionize, and then possibly recollide.

6.5.3 Trajectory analysis

In the case of the billiard model trajectories exhibited key characteristics which distinguished them from other trajectories based upon where they originated from in phase space. The same is true for the smooth potential. In figure 49 we show several trajectories integrated with potential (62). The trajectories are analogous to those

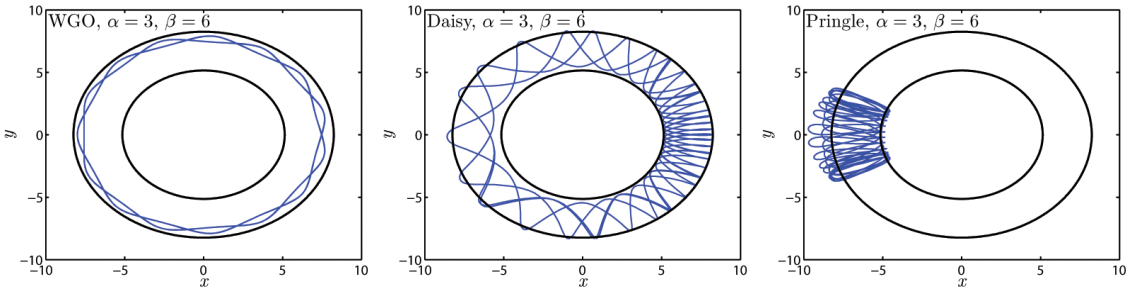

Figure 49: We illustrate trajectories from potential (62) with $\alpha = 3, \beta = 6$.

found in the billiard potential. Moving left to right across the row we see WGOs, daisy orbits, and finally pringle orbits. In order to properly define WGO and daisy orbits in the non-billiard potential, however, a redefinition is required. In the billiard system a WGO is one that does not hit the inner wall, however, there are no walls of constant radius in the full model. Therefore, a WGO is defined in a more qualitative sense to be trajectories which do not encroash too closely on the inner region of the potential. In a similar vein daisy orbits must alternatively move between the inner and outer wall regions. Of course, both orbits must access the entire range of θ, just as in the billiard model. We note that the trajectories of figure 49 very closely resemble their counterparts in the billiard model and have Jacobi values sufficiently below the saddle-center such that ionization is not possible.

6.6 Ionization time maps

One of the main purposes of switching to a more complete model of fullerene is to study ionization. As a first attempt, we initialize many trajectories with Jacobi values slightly above the saddle-center. All initial conditions, are generated on the Poincaré section, $p_r = 0$. An ionization is defined by a distance threshold criterion. In this case we say that an electron is considered ionized when $\sqrt{x^2 + y^2} > 30$ a.u. The total integration time is 20 laser cycles, however, ionization typically occurs much before then. With the criteria set, we integrate these trajectories and record how long ionization takes to occur. This type of computation is known as an ionization

time map. Some ionization time maps are shown in figure 50.

The color map varies between red and blue, with blue indicating a relatively quick ionization time and red indicating a longer ionization time. In figure 50 we show such an ionization time map for $I = 10^{14}$ W·cm^{-2} (top row) and $I = 10^{12}$ W·cm^{-2} (bottom row) and for a variety of Jacobi values above the saddle-center. As we move left to right across the columns we increase the Jacobi value further above the saddle-center, which washes out the fine structure of the ionization time maps. As the Jacobi value is increased above the saddle-center ionizations become more common and happen more quickly which can easily be seen in figure 50. In the top row we show results at high intensity and in the bottom row we show results at low intensity. Focusing on the top left panel, we see there is a fine structure. There is a large blue dot in the upper left of the figure and increasing distorted leaves which move counter-clockwise around the figure. The large blue dot is a region of quick ionization and each leave takes successively longer for ionization to occur.

In addition to constructing ionization time maps we can also look at distribution of ionization times such as those in figure 51. We see that the occurrence of ionizations is periodic, with maxima occurring with a period of roughly the laser period, $T = \frac{2\pi}{\omega} \approx 107$ a.u. This periodicity in the ionization time distribution (and decreasing count with each repetition) signals the existence of a periodic orbit responsible for ionization. A trajectory, moving through phase space, has an opportunity to ionize upon each nearby passing of the periodic orbit, which occurs roughly once every laser cycle.

1111

6.6.1 Globally, where does ionization originate?

The shape and bounds of the ionization time maps vary greatly depending on both Jacobi value and intensity. In the top row of figure 52 we show the ionization time

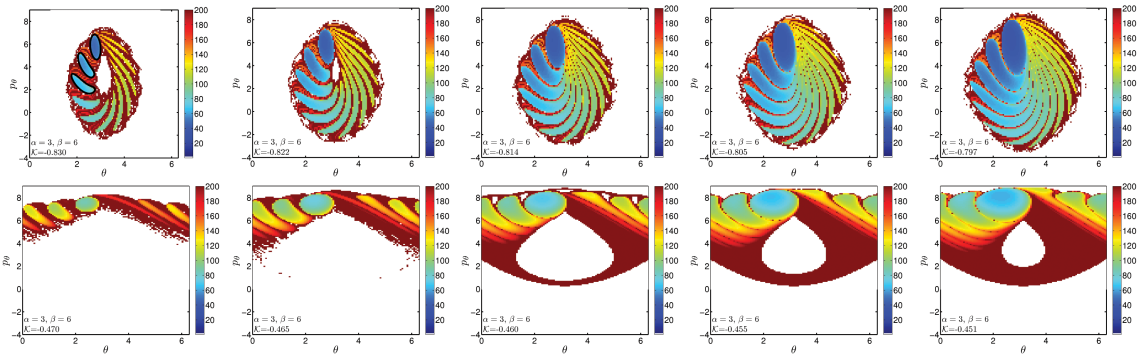

Figure 50: Ionization time maps for $I = 10^{14}$ W·cm^{-2} (top row) and $I = 10^{12}$ W·cm^{-2} (bottom row). As we move left to right across the panels the Jacobi value is 99%, 98%, 97%, 96% and 95% of the saddle-center energy. In the top right panel we show the intersections of the stable manifold of the Lyapunov orbit with the Poincaré surface.

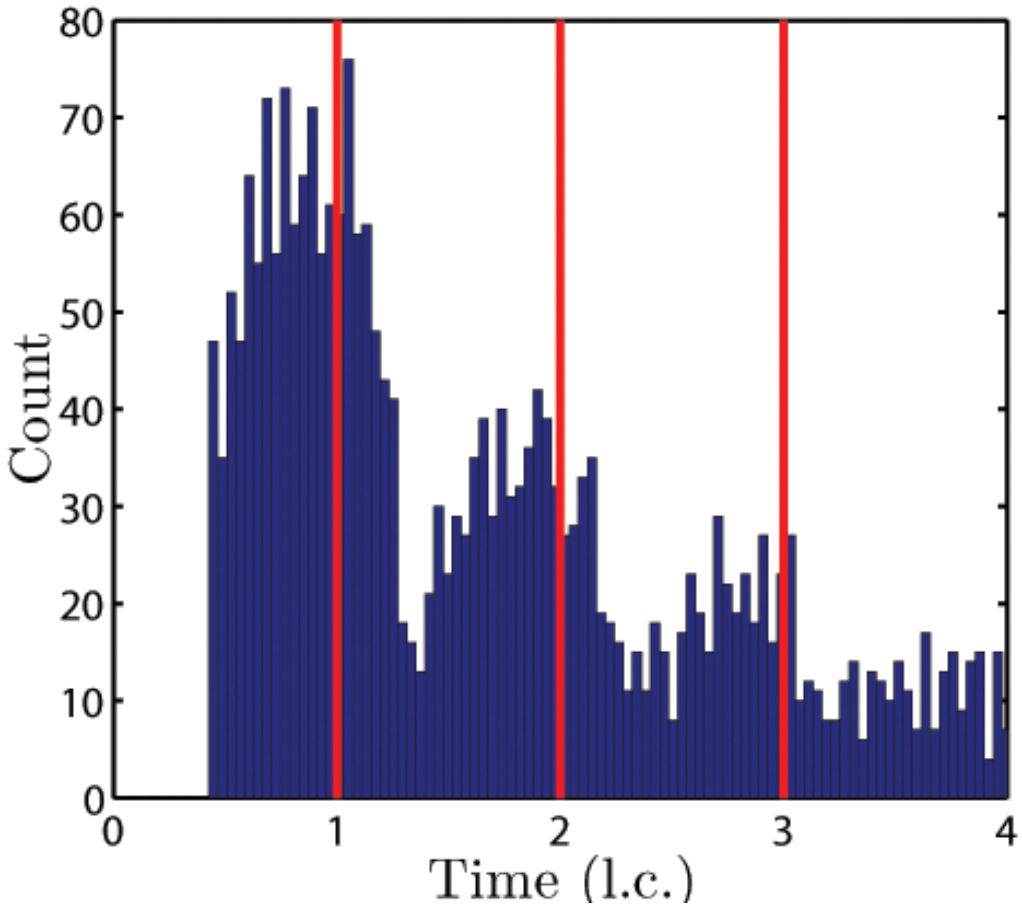

Figure 51: Ionization time histogram corresponding to the time map in the top left panel of figure 50. The red lines mark the completion of laser cycles 1,2, and 3.

maps of $\mathcal{K} = -0.830$ (99% the saddle-center energy) and $\mathcal{K} = -0.797$ (95% the saddle-center energy) for $I = 10^{14}$ W$\cdot$cm^{-2} surrounded by the corresponding Poincaré sections of non-ionizing trajectories in the first and third panels from the left, respectively. In both cases the ionization time map occurs in a chaotic sea surrounding by KAM tori. For $\mathcal{K} = -0.830$, however, the time map itself surrounds some remaining pringle orbits. This is not the case for $\mathcal{K} = -0.797$, however, because at this Jacobi value the periodic orbit has bifurcated. In the second and fourth panels on the top row, again relative to the left, we show full Poincaré sections used in $\mathcal{K} = -0.830$ and $\mathcal{K} = -0.797$, respectively, however, we have added in the Poincaré sections of several ionizing trajectories in blue while non-ionizing trajectories remain present in black. We see that there is no qualitative difference between the location of ionizing and non-ionizing trajectories for the two Jacobi values. The same analysis, however, is performed again in the bottom row for $I = 10^{12}$ W $\cdot$ cm^{-2} and there is a differnce now between $\mathcal{K} = -0.470$ (99% of the saddle-center energy) and $\mathcal{K} = -0.451$ (95% of the saddle-center energy), shown in the first and third panels from the left. We see that nearby the saddle-center ionization occurs only in a chaotic region which does not surround the pringle orbits. Likewise, farther away from the saddle-center the ionization time map again surrounds the pringle region.

In both cases, however, we notice that as we move farther from the saddle-center energy the region of ionization increases. This is expected because raising the Jacobi value (decreasing its magnitude) is equivalent to increasing the perturbation parameters E_0, which allows for more chaos and hence more ionization.

6.7 Lyapunov orbits

Figure 51 suggests a periodic orbit is responsible for ionization. From the zero velocity surface, we know that for Jacobi values sufficient close to the saddle-center that ionizing (and returning) trajectories must pass close by the saddle-center. With this

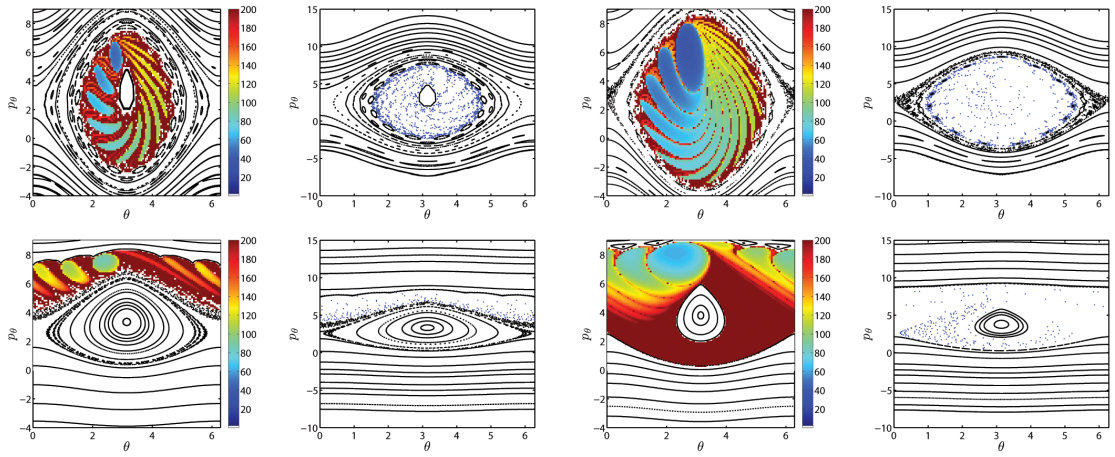

Figure 52: A comparison of ionization time maps and their corresponding Poincaré sections for $I = 10^{14}$ W $\cdot$ cm^{-2} in the top row and $I = 10^{12}$ W $\cdot$ cm^{-2} in the bottom row. The top row shows $\mathcal{K} = -0.830$ (99% the saddle-center energy) and $\mathcal{K} = -0.797$ (95% the saddle-center energy) in the first and third panels from the left while in the bottom row it shows $\mathcal{K} = -0.470$ (99% the saddle-center energy) and $\mathcal{K} = -0.451$ (95% the saddle-center energy). In the second and fourth panels on each row we show the full Poincaré section for the corresponding ionization time map. The black markers correspond to non-ionizing trajectories and the blue markers correspond to ionizing trajectories.

in mind, we examine a bifurcation of the saddle-center fixed point as the Jacobi value is increased.

For a given set of laser parameters the saddle-center is a fixed point of the system at a given Jacobi value. By increasing the Jacobi value above the saddle-center a bifurcation occurs and a periodic orbit develops which is often referred to as a Lyapunov orbit. These orbits are highly unstable and exist only close by the saddle-center. In the left panel of figure 53 we show the orbit in configuration space for the parameters used in the top left panel of figure 50 and the top row of figure 52. The grey and magenta lines represent the stable and unstable manifolds of the orbit. These manifolds are shown in the right panel of figure 53. The first several intersections of the stable manifold with the surface $p_r = 0$ are shown in black in the top left panel of figure 50. We see that these intersections are the islands of fast ionization on our time maps. The first intersection is the large blue spot of fastest ionization and the

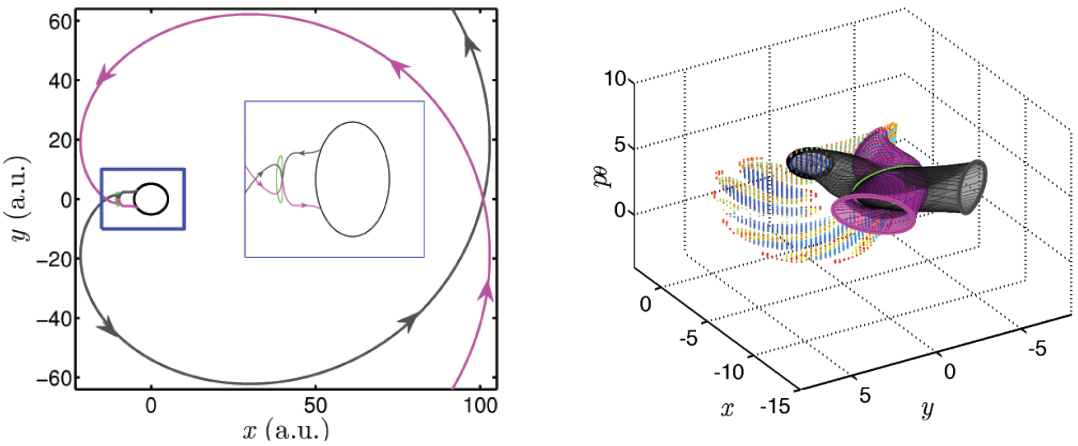

Figure 53: In the left panel the Lyapunov orbit is shown in green while the stable and unstable manifolds are shown in gray and magenta respectively. The blue box highlights the region displayed in the inset, which shows more detail nearby the Lyapunov orbit. In the right panel we show the manifolds in more detail, treating them as tubes of perturbed initial conditions. The tube of the stable manifold intersects the surface $p_r = 0$ at the thick black contour shown in the figure. The intersections of the stable manifold with the surface $p_r = 0$ are also shown in the top left panel of figure 50.

subsequent ionizations are the 'leaves' of fast ionization moving in a counter clockwise rotation around the time map.

With the top left panel of figure 50 in mind we can imagine initial conditions beginning on the large blue spot (or the subsequently smaller leaves) being drawn towards the Lyapunov orbit by the stable manifold. The Lyapunov orbit, existing relatively far from molecule where its attractive potential is weak, then allows ionization along its unstable manifold.

6.7.1 Global dynamics

We see from the second panel from the left on the top row of figure 52 that the Poincaré section of ionizing trajectories (blue markers) has holes, which appear to be a reflection about $\theta = \pi$ of the blue spots of the ionization time map. Along these

lines, we note that our system has a symmetry with $t \to -t$ such that

$$\begin{aligned} \theta &\to -\theta \\ r &\to r \\ p_\theta &\to p_\theta \\ p_r &\to -p_r \end{aligned}$$

so Hamilton's equations remain preserved. Therefore, these empty holes in the Poincaré section are simply highlighting the locations of the unstable manifolds intersection with the Poincaré surface. Accordingly, we show in the left panel of figure 54 a more detailed Poincaré section of the correspdoning blue region from figure 52. In the middle panel of the same figure the same Poincaré section, however, taken from initial conditions along the unstable manifold of the Lyapunov orbit. We see that the Poincaré sections from the left and middle panels are the same, even up to the fine structure which exists between the holes. Therefore, we can conclude that the dynamics of ionizing trajectories is driven by the unstable manifold of the Lyapunov orbit. Furthermore, in the rightmost panel of the figure we take the same initial conditions along the unstable manifold and choose a color scheme which assigns the final intersection with the Poincaré section as blue and the first intersection with the Poincaré as red with a discrete interpolation for between points. With this color scheme, remembering that the initial conditions are identical to those used in the middle panel, we generate a figure very similiar to an ionization time map. By treating the final intersection with the Poincaré section as a fast ionizing trajectory which have reversed time, which changes the unstable manifold to a stable manifold, and therefore, we confirm our earlier observation that the stable manifold and its intersections with the Poincaré section manifest themselves via the ionization time map.

Globally, we can now supply a concrete explanation of ionization near the saddle-center. The stable manifold of the Lyapunov orbit, as evidenced by the ionization time maps, acts as a conduit for trajectories to reach the continuum. Therefore, trajectories beginning inside the stable manifold (the large blue spot and leaves on the ionization time maps) are fast ionizing trajectories, whereas starting outside these large structures, yields a longer ionization time. The ionization time is longer because as the dynamics is driven by the unstable manifold, which does not act as a conduit to the continuum, it is up to the intersections of the stable and unstable manifolds to supply the necessary guidance to potentially ionizing trajectories to reach the continuum. Likewise, via observations made from figure 54 we observe that the unstable manifold drives the dynamics of ionizing trajectories.

6.7.2 Returns

Below the saddle-center ionizations, and therefore returns, are not possible. As the Jacobi value is raised above the saddle-center we expect the probability of return to increase. In the left panel of figure 55 we show a probability of return for a lower intensity, $I = 10^{13}$ W $\cdot$ cm^{-2}. Although the saddle-center is located at $\mathcal{K} = -0.566$ (vertical dashed black line), we see that returns do not occur in any significant amount until $\mathcal{K} \approx -0.39$, where the probability is roughly 10^{-5}. In the right panel, we use the Jacobi value $\mathcal{K} = -0.38$ and show a typical trajectory exhibiting a return. We see that the trajectory follows closely the Lyapunov orbit along the unstable manifold, moving away from the atom. After circling around the molecule several times, while increasing its distance to the core, the trajectory intersects itself in configuration space continues to circle the molecule, however, now with the radius decreasing. In fact, what is happening is a homoclinic connection of the manifolds of the Lyapunov orbit. A trajectory, moving away from the molecule along the unstable manifold, may switch to the stable manifold of the same orbit and return to the core. The existence

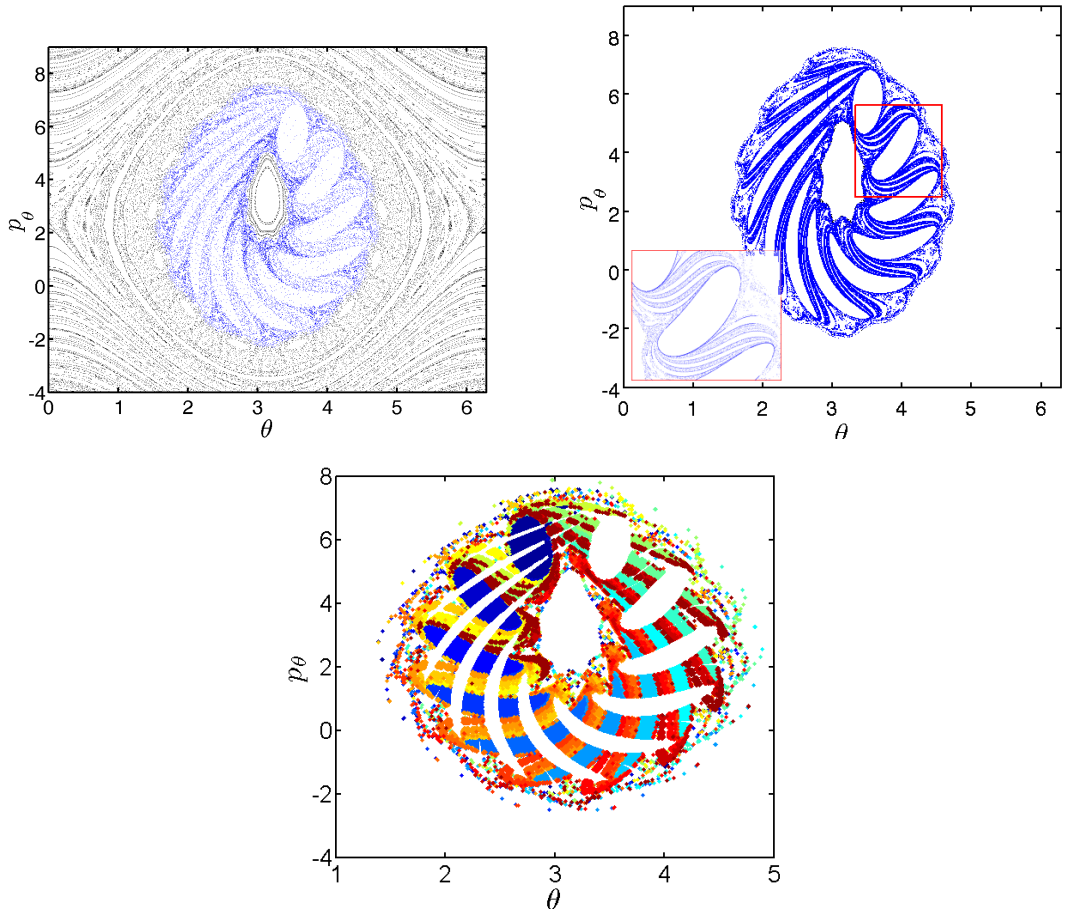

Figure 54: The left panel is a higher resolution version of the same blue region in figure 52. The middle panel is the same Poincaré section as shown in the left panel, however, initial conditions are taken along the unstable manifold of the Lyapunov orbit. The right panel is the same Poincaré section as the middle panel, with the same initial conditions, however, we assign a color to each point based on the time to ionization *from that point*. Blue is assigned a quick ionization time and red is assigned a slow ionization time.

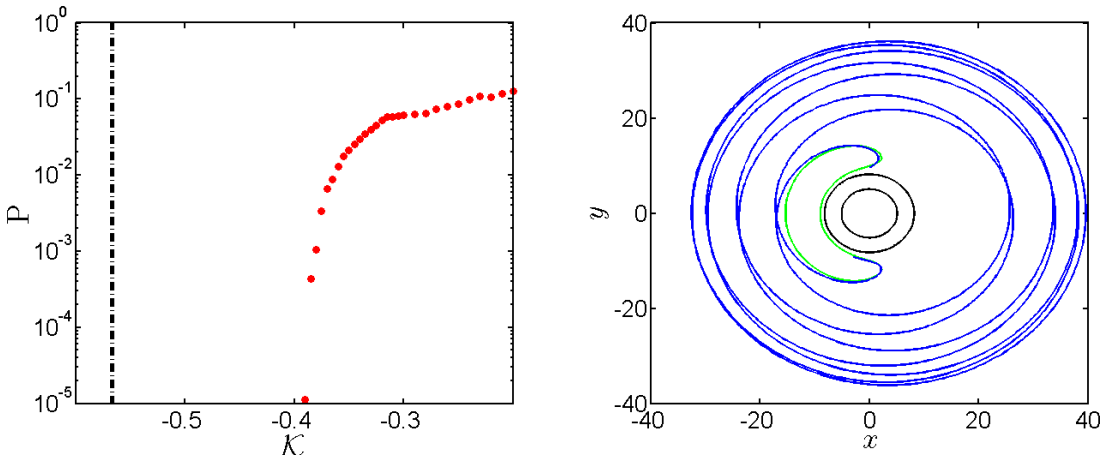

Figure 55: In the left panel the probability of return versus intensity is shown for $I = 10^{13}$ W $\cdot$ cm^{-2}. The vertical dashed line is the Jacobi value at the saddle-center. In the right panel we show a typical returning trajectory for $\mathcal{K} = -0.38$ in blue and the corresponding Lyapunov orbit in green.

of the homoclinic connection, however, depends on the laser parameters.

The ionization and return of trajectories with Jacobi values only slightly above the saddle-center provides for a rich, interesting dynamics. However, as we showed in Ch. 5 only a small percentage of trajectories, originating on the ground state energy surface of fullerene (and indeed other target species, for which the mechanisms outlined in this chapter also exist), possess Jacobi values sufficiently close to the core. In fact, most trajectories which ionize do so through the mechanism outlined in Ch. 5, i.e. RPOs.

6.8 Conclusions on the continuous potential

We have shown that the billiard model works surpisingly well when modelling the pre-ionization dynamics of the electron. To move into the ionized medium, however, the continuous potential must be used. We have shown that ionized trajectories originate from the chaotic sea only for Jacobi values which are sufficiently large. The recollision process, already studied in detail in Ch. 4 applies equally well to this more complicated system, and in fact, could be further used to generate an energy criterion which could

lead to predicitions on molecular fragmentations caused by electron recollision, for example.

CHAPTER VII

DOUBLE IONIZATION WITH A MULTI-COLORED LASER

7.1 Introduction

In this final chapter we depart from the single color laser field models which have so far been our primary focus. Instead, we perform a more statistical study of a two electron system leaving a study of the one electron dynamics to others. We consider the classical dynamics of a two-electron system subjected to an intense bichromatic linearly polarized laser pulse. By varying the parameters of the field, such as the phase lag and the relative amplitude between the two colors of the field, we observe several trends from the statistical analysis of a large ensemble of trajectories initially in the ground state energy of the Helium atom: High sensitivity of the sequential double ionization component, low sensitivity of the intensities where nonsequential double ionization occurs while the corresponding yields can vary drastically. All these trends hold irrespective of which parameter is varied: the phase lag or the relative amplitude. We rationalize these observations by an analysis of the phase space structures which drive the dynamics of this system and determine the extent of double ionization. These trends turn out to be mainly regulated by the dynamics of the inner electron.

Multiple ionization of atoms takes place at intermediate and high intensities when they are subjected to laser pulses [13]. The routes by which these multiple ionizations occur can be quite complicated. Two main routes have been identified for the double ionization of two-active-electron systems (like the Helium atom subjected to linearly polarized laser pulses): a sequential process and a nonsequential one [13]. In the sequential process the field ionizes one electron after the other in an uncorrelated way.

In contrast, the electron-electron correlation plays an active role in the ionization of the second electron in the nonsequential process. More specifically, the field picks up an electron, and sends this electron to the remaining ion core to dislodge the second electron, according the so-called recollision (or 3-step) scenario [6, 14, 15].

It has been observed experimentally in a broad range of intensities that nonsequential double ionization (NSDI) (also referred to as correlated double ionization (CDI) [76]) yields can be many orders of magnitude larger than in the sequential double ionization (SDI) [also referred to as uncorrelated double ionization (UDI)] counterpart. Varying the intensity gives rise to a characteristic "knee" shape for the double ionization yield as a function of the laser intensity. This strong effect due to electron-electron correlation has been observed experimentally [77, 3, 78, 79, 80, 81, 48, 82, 83] and also theoretically using quantum [13, 84, 85, 86, 87, 88, 89, 90], semi-classical [91, 92, 93] and classical simulations [94, 91, 16, 95, 88, 96, 97, 9, 76].

In this thesis, we investigate the dynamics resulting from the interaction between helium atoms and a bichromatic linearly polarized laser field using a classical model. Classical means are entirely sufficient to produce the strong electron correlation needed to explain double ionization phenomena [16]. Atomic phenomena in intense bichromatic fields can be considered as an extension of the principles of coherent control into the nonlinear nonperturbative regime of laser-atom interactions [98, 99, 100, 101, 102, 103, 104, 105, 106, 107, 108, 109, 110, 111]. Furthermore, bichromatic pulses [112] and phase shaping [113] are natural tools in atomic control research because they offer practical control parameters such as polarization, amplitudes and phases. In particular it has been shown that it is possible to use the direction of transport in a ratchet by varying the phase lag in the bichromatic pulse [114]. Although the classical mechanisms of double ionization remain qualitatively the same as for a monochromatic laser field [9], the double ionization yields show a strong sensitivity to changes in the parameters of the laser field, namely the

phase lag between the two colors and their relative amplitudes. We explain this dependence using an analysis in terms of phase space structures. Our main result is that all these processes are regulated primarily by the dynamics of the inner electron which is the electron that remains bounded after the other one has been ionized. Remarkably, this electron, rather than being a spectator, is in fact the driver in the ionization process.

We consider a classical model with one spatial dimension for each electron which corresponds to the direction of polarization of the laser field. We denote the positions of the two electrons by x and y and set the origin at the nucleus. We call the canonically conjugate momenta of x and y, p_x and p_y respectively. We consider soft Coulomb potentials [27, 16, 95, 96, 9, 76] defined by two softening parameters a and b for the interaction between charged particles. The Hamiltonian of the system in the dipole approximation is obtained by the sum of the kinetic energy of the electrons, the soft Coulomb potentials between the two electrons and between the electrons and the nucleus, and the interaction of the electrons with the field:

$$H\left(x,y,p_x,p_y,t\right)=\frac{p_x^2}{2}+\frac{p_y^2}{2}+\frac{1}{\sqrt{\left(x-y\right)^2+b^2}} -\frac{2}{\sqrt{x^2+a^2}}-\frac{2}{\sqrt{y^2+a^2}}+\left(x+y\right)E\left(\omega t\right), \tag{66}$$

where $E\left(\omega t\right)$ is a bichromatic laser field, defined as:

$$E\left(\omega t\right)=E_0 f(\omega t)\left(\sin\left(\omega t\right)+\alpha\sin\left(k\omega t+\delta\right)\right), \tag{67}$$

where E_0 is the amplitude of the dominant mode, ω its frequency, $\alpha<1$ the ratio of the amplitudes of the two colors of the laser field, k characterizes the mode locking between the two components, and δ is the phase lag. Since the second laser is an additional energy input to the system, the intensity is scaled with α as $I_0\propto E_0^2\left(1+\alpha^2\right)$. The system has two and a half degrees of freedom, one for each electron and one half for time dependence. The envelope function f is chosen as a trapezoid with 2

laser cycle (l.c.) ramp up, 4 laser cycle plateau, 2 laser cycle ramp down, and zero elsewhere. In what follows, the wavelength is chosen to be 780 nm (corresponding to a frequency of $\omega = 0.0584$ a.u.) and $k = 3$. Except when we investigate the role of α, we set $\alpha = 0.45$ for numerical simulations, which corresponds to an additional intensity input of 20%. We consider the initial state to be the ground state of He, i.e. $\mathcal{E}_g = -2.24$ a.u. [115, 16]. We choose $a = 1$ to prevent auto-ionization (so that the energy surface is bounded in phase space). The second softening parameter b is chosen so as to allow a significant energy exchange during a recollision. Here $b = 1$ [28].

For insight into the dynamics of typical trajectories and to interpret the mechanisms at play which explain the statistical analysis, we present two kinds of studies as functions of the parameters of the field, E_0, α and δ in what follows: In Sec. 7.2, a statistical analysis of a large ensemble of trajectories, and in Sec. 7.3 an analysis of the phase space structures.

7.2 Statistical analysis

Starting from the classical model (66), we perform a statistical analysis of a large ensemble of trajectories (typically 150,000) initially on the ground state (with a microcanonical distribution [9]). At the end of the pulse, a trajectory can exhibit zero, one or two ionized electrons. In our calculations, an electron is considered ionized when its energy (defined as the sum of its kinetic energy and the Coulomb interaction with the nucleus) is positive, which corresponds to an electron free from the Coulomb potential well. A convenient observable is the probability of double ionization where the two electrons have a positive energy at the end of the pulse. This probability is commonly plotted as a function of the laser intensity. A signature of NSDI is a characteristic knee shape: In the intermediate intensity range, these yields are much higher (by several orders of magnitude) than expected from the uncorrelated sequential double ionization mechanism [13]. At high intensity, the yields reach saturation,

corresponding to double ionization of all the electrons of the ensemble. In what follows, we investigate the double ionization yields versus the intensity when the phase lag δ and the relative amplitude α are varied.

7.2.1 Varying the phase lag δ

In Fig. 56 we display several double ionization probability curves as a function of the laser intensity for different values of the phase lag δ (for $\alpha = 0.45$).

In the intermediate range of intensities (up to saturation of double ionization), we observe a significant variability of the double ionization probabilities and consequently of the characteristic features of the knee. More precisely, in the intermediate intensity range the level of double ionization yields greatly vary with δ by a factor of 3; however, when varying δ the range of intensity where the knee is located (around 5×10^{14} W cm^{-2}, vertical dashed-dotted lines in Fig. 56) does not change significantly. In the low intensity regime i.e., for intensities lower than 8×10^{13} W cm^{-2} there is a very weak dependence of δ in these yields. The same conclusions hold for other values of α. We note a significant impact of the phase lag in the resulting double ionization probability, meaning that adjusting this parameter can act as a control knob for both sequential and non-sequential processes. One advantage of varying the phase lag between the two components of the laser field is that no additional input of energy is required (as opposed to varying other parameters like α) since the mean value of the electromagnetic energy does not depend on δ.

In Fig. 57 we represent the double ionization yield as a function of δ for the intensity labeled by the vertical magenta continuous line in Fig. 56. The resulting curve has a bell shape with a maximum slightly shifted before $\delta = \pi$. More specifically, we observe a fast variation of the double ionization yield with changes of the phase lag around $\delta = 0$ and a flattening around $\delta = \pi$. This confirms the high sensitivity of the double ionization probability to the parameter δ.

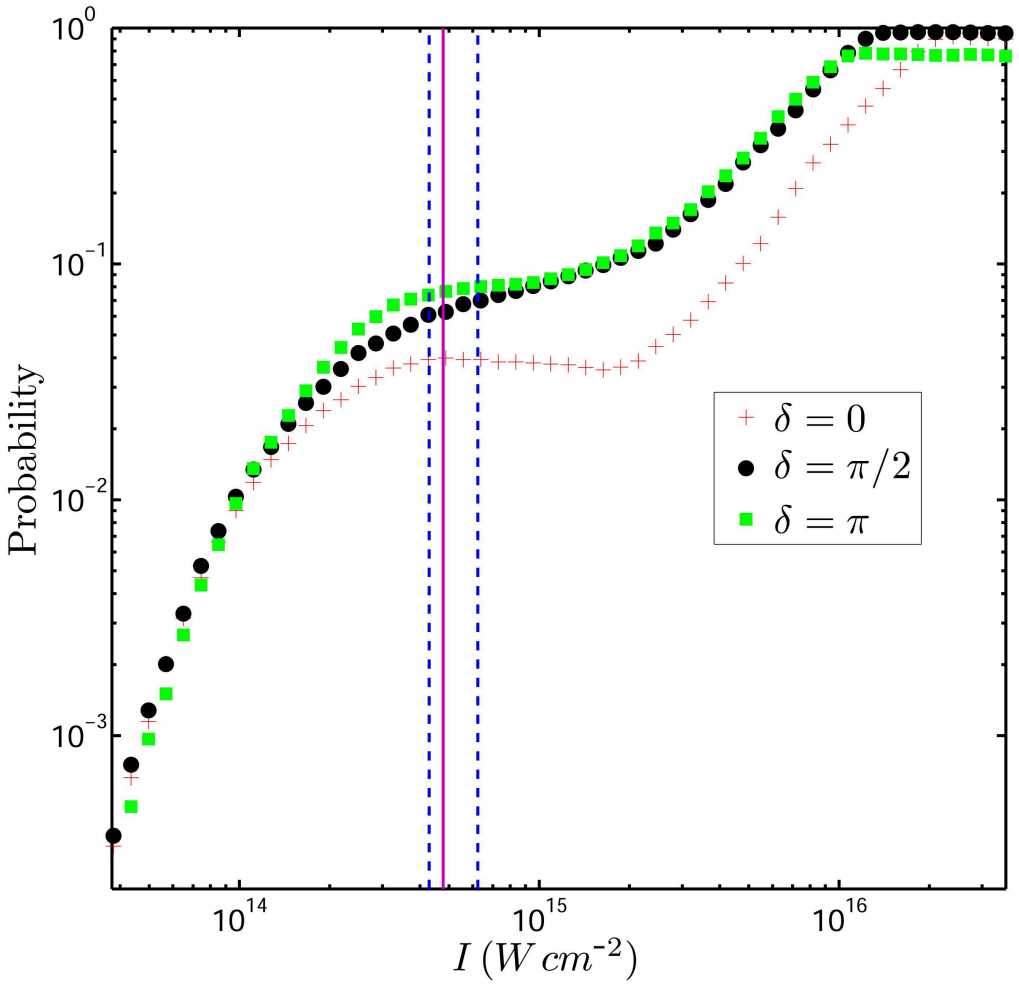

Figure 56: Probability of double ionization as a function of the intensity for $\alpha = 0.45$. The red crosses correspond to $\delta = 0$, the black circles to $\delta = \pi/2$, the green squares to $\delta = \pi$. We also indicate the range of variation of $I^{(c)}$ with δ as given by Eq. (79) (vertical dashed-dotted lines). The vertical magenta continuous line labels the intensity chosen in Fig. 57, 62, and 63.

Except for very low intensity (i.e. below 8×10^{13} W cm^{-2}) we observe qualitatively the same impact of δ on the double ionization yield (a bell shape almost centered around $\delta = \pi$). The precise value of the phase lag for which the probability is maximum depends on the laser parameters.

The value of δ for which we observe the first saturation of double ionization occurs when $\delta = \pi$. This value of δ does not depend on α (and is defined as soon as α is non-zero). We define $I^{(\mathrm{t})}(\delta)$ the intensity, as a function of the phase lag, for which saturation of double ionization is reached. Then, at high intensity, we note a great variability of $I^{(\mathrm{t})}(\delta)$ (the differences are of the order of 10^{16} W cm^{-2}) which is more than one order of magnitude larger that the range of variation of the knee.

7.2.2 Varying the relative amplitude α

After varying δ at fixed α, we keep δ fixed at π in order to investigate α's influence on the double ionization probability. We chose $\delta = \pi$ because it corresponds to the phase lag where the peak field amplitude is maximum (see Sec. 7.3.4). In Fig. 58 we represent the double ionization probability as a function of the intensity for different values of α. As for the variation of δ, we notice no significant dependence on the parameters at low intensities (below 8×10^{13} W cm^{-2}). In the intermediate intensity range, we notice that the probability greatly varies with α (more than a factor two) whereas the intensity at which the characteristic knee is developed does not change significantly. In the meantime, the UDI component also increases with α, and we notice a decrease of the intensity $I^{(\mathrm{t})}$ where double ionization is saturated. As a consequence we notice a flattening in the knee, the two CDI and UDI curves merging. As α is increased, the second color of the laser field becomes more important, hence δ is expected to have a more prominent role in controlling the system because the variation in probability becomes larger. This is confirmed by Fig. 59 where we have represented double ionization probabilities as a function of the intensities for $\alpha = 0.1$

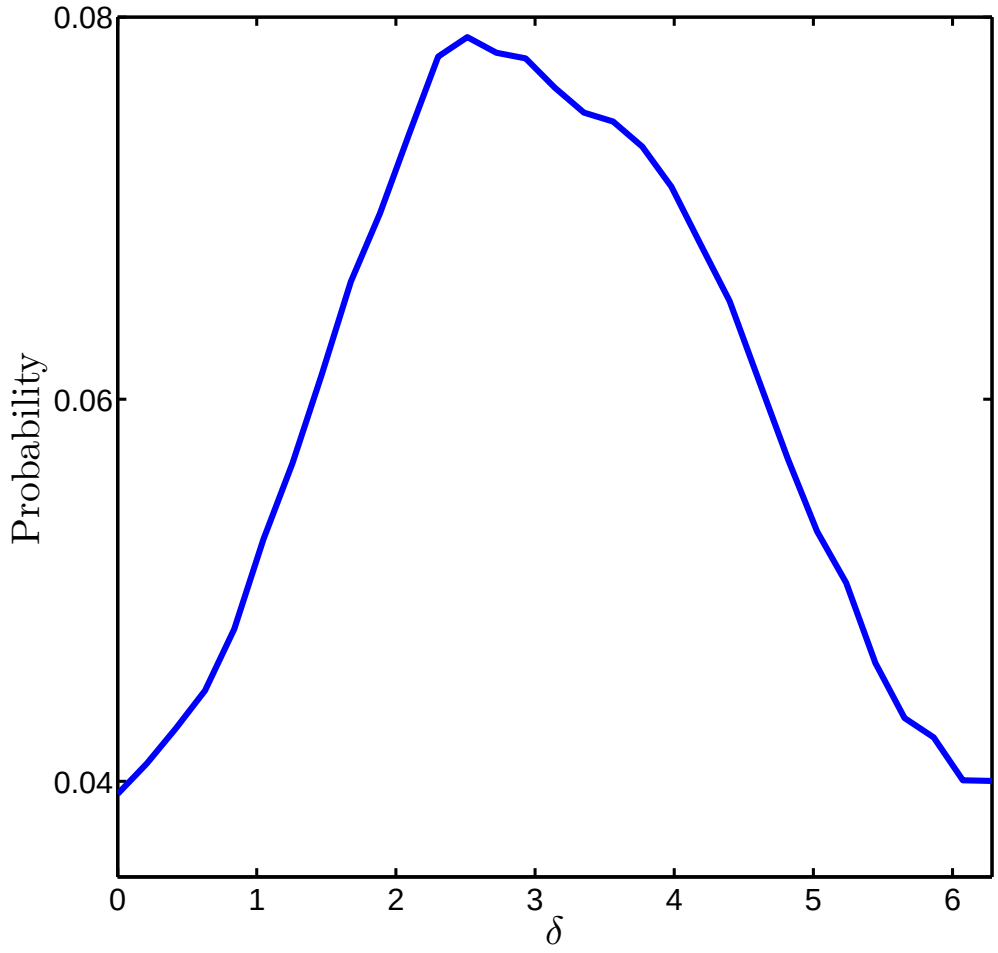

Figure 57: Double ionization probability as a function of δ for $\alpha = 0.45$ and the intensity labeled by the vertical magenta continuous line in Fig. 56 ($I = 4.78 \times 10^{14}$ W cm^{-2}).

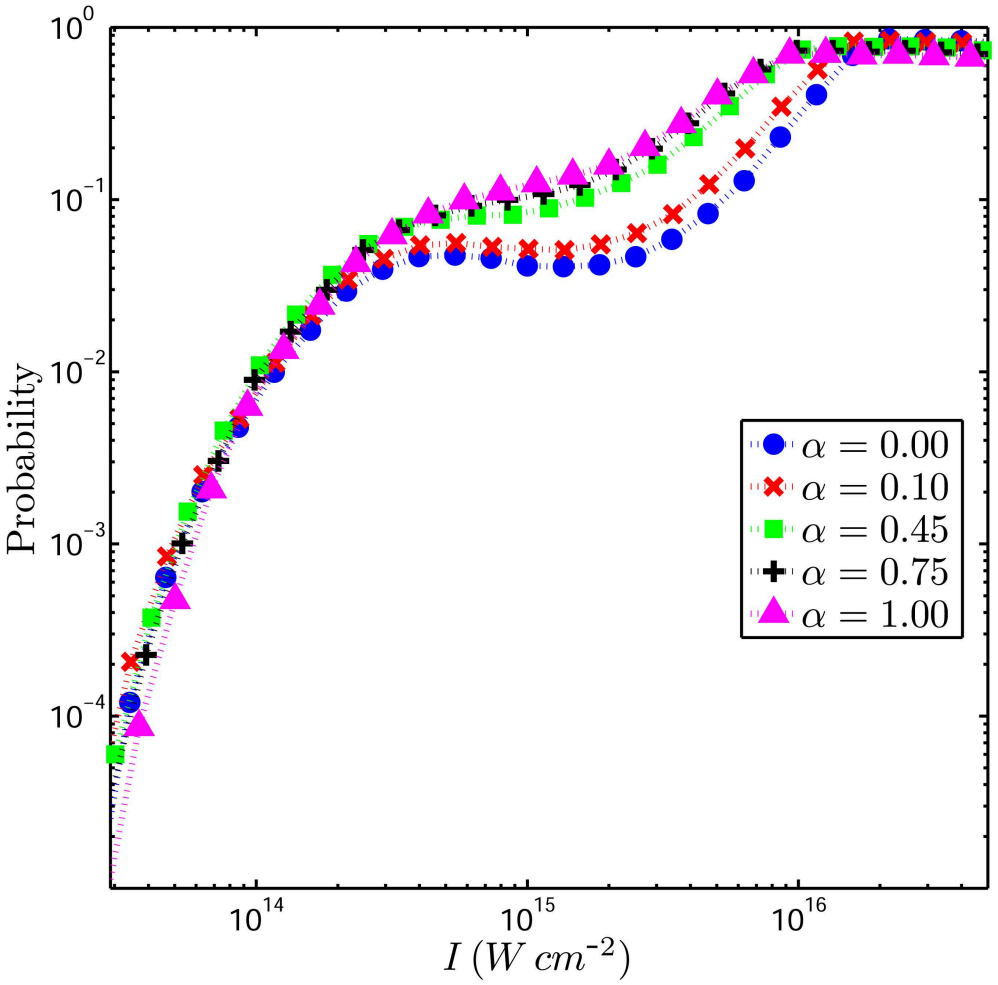

Figure 58: Double ionization probability as a function of intensity for different values of α. Blue circles correspond to $\alpha = 0$ (single laser), Red crosses to $\alpha = 0.10$, green squares to $\alpha = 0.45$, black plus signs to $\alpha = 0.75$ and magenta triangles correspond to $\alpha = 1.00$. Here $\delta = \pi$ for all curves.

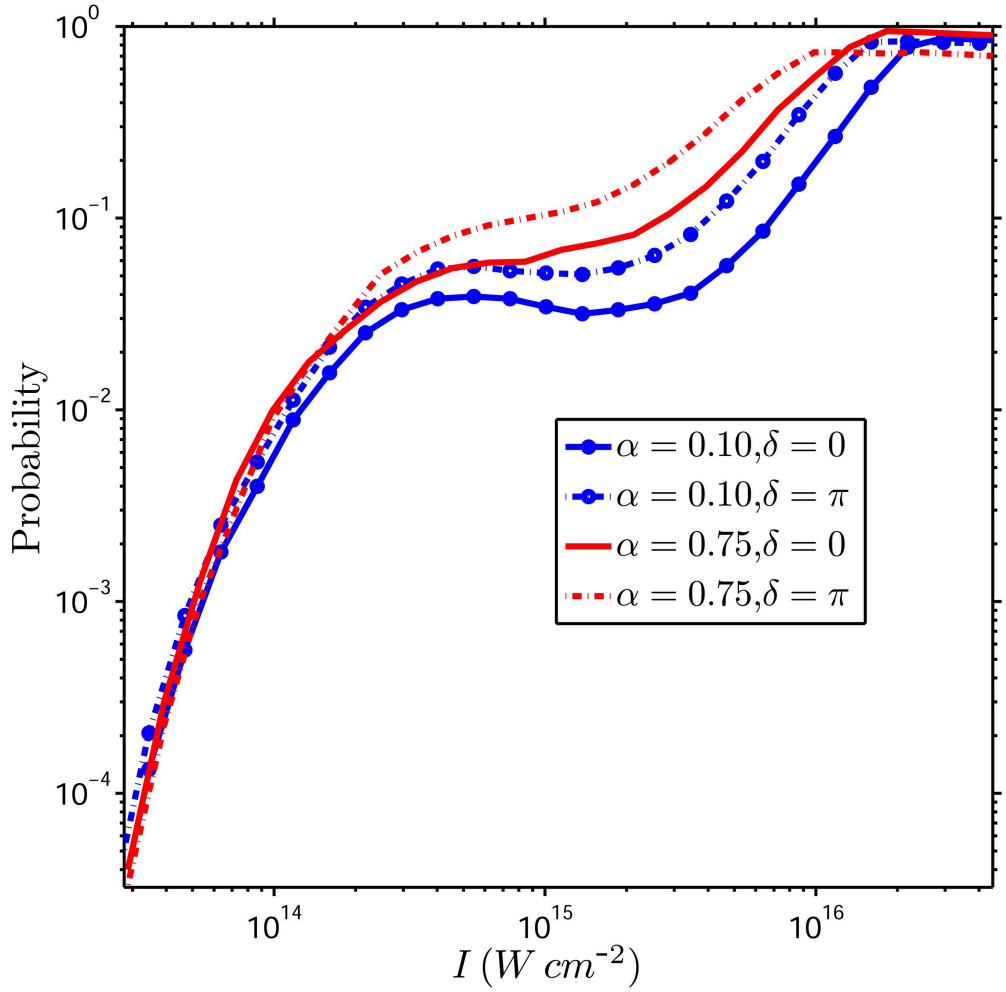

Figure 59: Double ionization probability as a function of the intensity for different values of δ. We keep α constant and equal to $\alpha = 0.1$ and $\alpha = 0.75$, respectively.

and $\alpha = 0.75$.

In summary, the statistical analysis shows these three main trends when changing the parameters of the field:

1. High sensitivity of the actual probability of double ionization,

2. High sensitivity of the intensity of saturation of the double ionization yields,

3. Low sensitivity of the intensity of knee regime (i.e. the CDI maximum).

In the next section, we analyze the dynamics of Hamiltonian (66) in terms of phase

space structures and we find results that support and explain these trends.

7.3 Nonlinear dynamical analysis

For the dynamical analysis of Hamiltonian (66) we follow the one performed in Ref. [9] for the monochromatic laser pulse. The analysis proceeds in the following way: First, without laser field ($E_0 = 0$), an outer electron and an inner one were identified from a periodic orbit analysis of the chaotic motion of typical trajectories. When the field is turned on, if the inner electron remains bounded, the atom may undergo a recollision which follows from the 3-step picture [6, 14] (the field picks up the outer electron, and upon reversal of the field, brings it back to the core and the two electrons share the collision energy).

7.3.1 Effective models

The dynamics of both electrons are accurately reproduced by reduced models except during recollisions [9]. These models allow one to derive the main properties of the double ionization curves versus intensity. We begin by investigating the behavior of typical trajectories. In Fig. 60, we represent the position of each electron (upper panel) and their energy (kinetic energy plus soft Coulomb potential, lower panel) as functions of time for a typical trajectory. We observe that one electron is first quickly ionized (the "outer" electron) while the other remains close to the core (the "inner" electron). Once ionized, the outer electron is driven mainly by the laser field and experiences large excursions from the core. In contrast, the inner electron experiences a competition between Coulomb interaction with the nucleus and the laser excitation. Without loss of generality, we assign x to the outer electron and y to the inner one. In the sample trajectory of Fig. 60 the inner electron (red curves) does not ionize until it collides with the outer electron (blue curves). Double ionization occurs at approximately 2.5 laser cycles, which can be confirmed by examining the energies of both electrons in the lower panel. We see that both electrons have positive energy

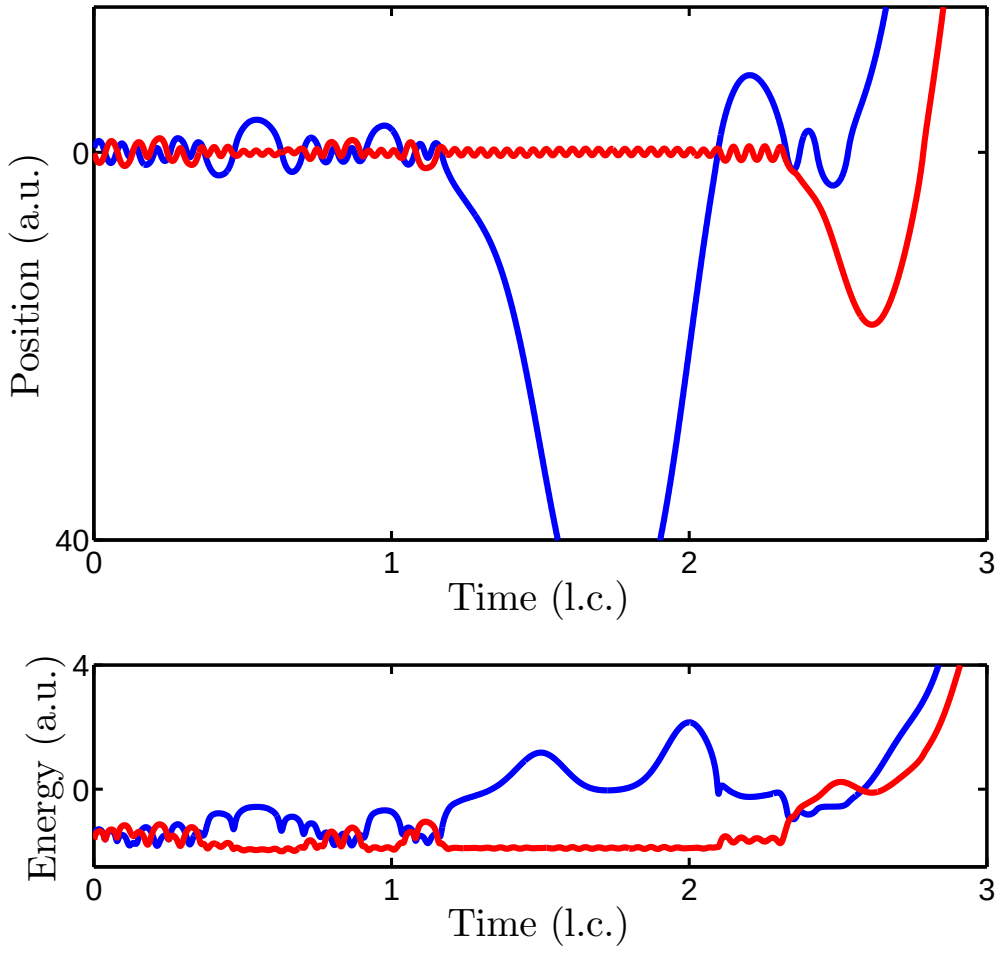

Figure 60: Typical nonsequential double ionization. We display the position (upper panel) and energy (as defined in the text, lower panel) of each electron as functions of time. The parameters are $I = 4.78 \times 10^{14}$ W cm^{-2}, $\alpha = 0.45$ and $\delta = 0$.

after this time (and thus are ionized). From this qualitative analysis, two reduced effective Hamiltonians are identified, $H_{\rm out}$ for the outer and $H_{\rm in}$ for the inner one:

$$H_{\rm out}\left(x, p_x, t\right) = \frac{p_x^2}{2} + xE\left(\omega t\right), \tag{68}$$

$$H_{\rm in}\left(y, p_y, t\right) = \frac{p_y^2}{2} - \frac{2}{\sqrt{y^2+1}} + yE\left(\omega t\right), \tag{69}$$

where we have neglected the interaction with other charges for the outer electron and have allowed the inner electrons to feel both the laser field and the attraction from the nucleus. For both electrons, we ignore the electron-electron interaction term since

they are assumed to be far away from each other between two recollisions. The main advantage of the above effective models is that their dimensions are lower than the one of Hamiltonian (66) (they both have one and a half degrees of freedom). Hamiltonian $H_{\rm out}$ is even integrable in the sense that one can explicitly give the expression of the trajectories as functions of the initial conditions. Hamiltonian $H_{\rm in}$ is not integrable but its dynamics can be analyzed qualitatively. In what follows, we analyze these two models as the parameters of the field are varied and correlate their dynamics with the double ionization curves plotted in Sec. 7.2 in order to support and explain the observed trends.

7.3.2 Dynamics of the outer electron

The trajectory of the outer electron [as governed by Eq. (68)] is given by

$$x\left(t\right) = x_0 + p_0 t + \frac{E_0}{\omega^2}\left(\sin\omega t + \frac{\alpha}{k^2}\sin\left(k\omega t + \delta\right)\right), \tag{70}$$

$$p_x\left(t\right) = p_0 + \frac{E_0}{\omega}\left(\cos\omega t + \frac{\alpha}{k}\cos\left(k\omega t + \delta\right)\right), \tag{71}$$

where $x_0 + E_0\alpha k^{-2}\omega^{-2}\sin\delta$ and $p_0 + E_0\omega^{-1}\left(1 + \alpha k^{-1}\cos\delta\right)$ are, respectively, the position and momentum of the outer electron at time $t = 0$. An important quantity is the maximum return kinetic energy of the outer electron: It gives the maximum amount of energy the outer electron can bring to the inner electron to trigger CDI. In addition, if the outer electron recombines, it gives the cutoff in harmonic generation for photon emission [112]. In order to compute this quantity we need to consider a shift of the field since the electron leaves the core at a certain phase ϕ of the field. The effective Hamiltonian is transformed into

$$H_{\rm out} = \frac{p_x^2}{2} + xE(\omega t + \phi).$$

Maximizing the kinetic energy $\mathcal{E}_{\rm max} = p_x(t_r)^2/2$ with respect to the recollision time t_r and the initial phase ϕ leads to the familiar condition that the maximum return energy is associated with trajectories leaving the nucleus with zero momentum [112].

As a function of the parameters of the laser field, this maximum kinetic energy is equal to

$$\mathcal{E}_{\max} = \kappa\,(\alpha, \delta)\, U_p, \tag{72}$$

where $U_p = E_0^2/(4\omega^2)$ is the ponderomotive energy and κ is only a function of α and δ. For $\alpha = 0$, we have $\kappa(0, \delta) \approx 3.17$ [6]. In Fig. 61, we represent $\kappa(\alpha, \delta)$ as a function of δ for various values of α. We notice that the amplitude of the variations of κ with δ increases with α. For a fixed value of α, the maximum return energy κ (in units of U_p) of the outer electron can vary significantly with δ (up to more than 2). For all values of α, the maximum of κ occurs at $\delta \approx 1.04$, while its minimum is obtained for $\delta \approx 3.99$. We notice that none of these values are related to the critical values of the phase lag for which we observe maximum of double ionization (around $\delta = \pi$) and saturation of double ionization. Thus, the origin of the amount of double ionization does not solely rely on the dynamics of the outer electron. It has to be complemented by the dynamics of the inner electron.

7.3.3 Dynamics of the inner electron

After the ionization of the outer electron, the inner electron experiences the combined action of the field and of the attraction from the nucleus only. Its Hamiltonian is given by Eq. (69). The competition between these two interactions leads to two distinct behaviors related to two distinct regions. Figure 62 represents these two regions in phase space: More specifically, we plot the distance of the inner electron from the nucleus after 10 laser cycles in the space of initial conditions $(y_0, p_{y,0})$ at $t = 0$. Note that the color map is in logarithmic scale. The red and green curves are two different Poincaré sections of an inner electron trajectory, taken stroboscopically with the laser period. They indicate that the dark region is filled with invariant tori where electrons are bound to the nucleus (for all time). The light region corresponds to ionizing electrons (after a transient time which depends on the initial conditions,

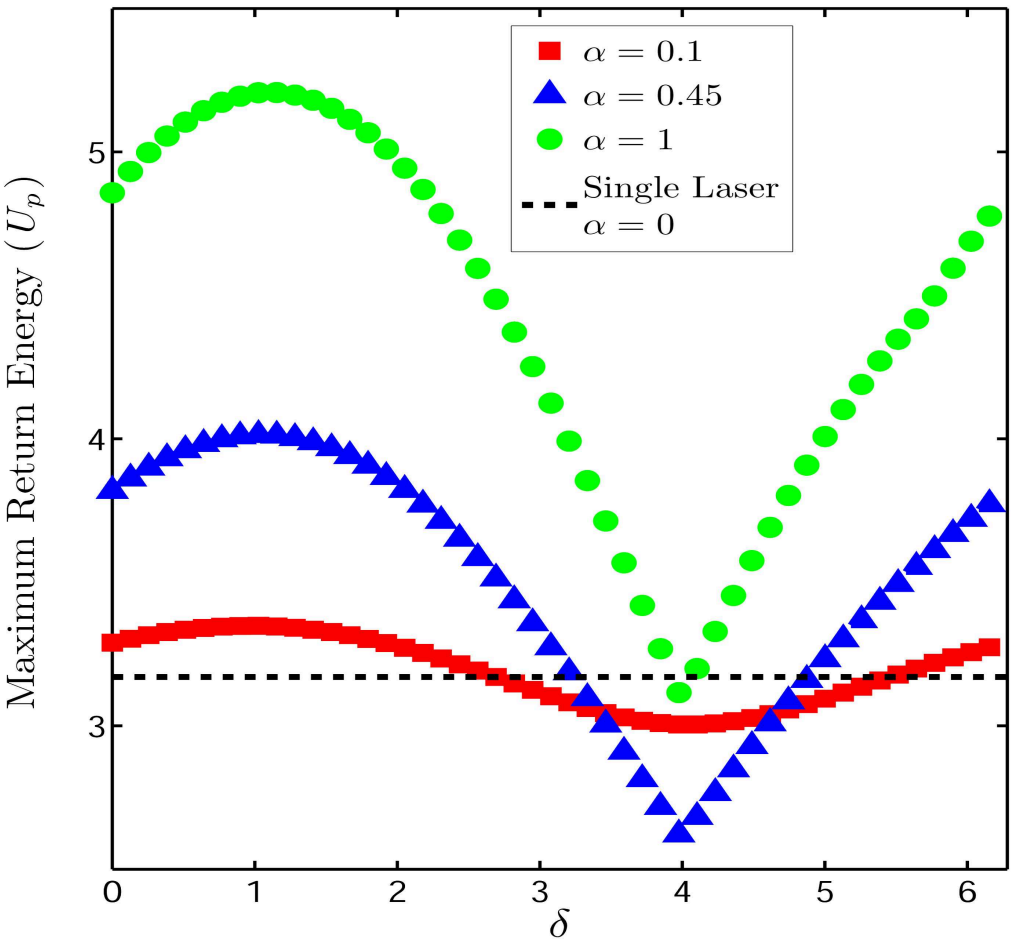

Figure 61: Maximum return energy of the outer electron as a function of δ in units of U_p. Red squares correspond to $\alpha = 0.10$, blue triangles to $\alpha = 0.45$, and green circles to $\alpha = 1.00$, while the dashed black line corresponds to the one laser system ($\alpha = 0$).

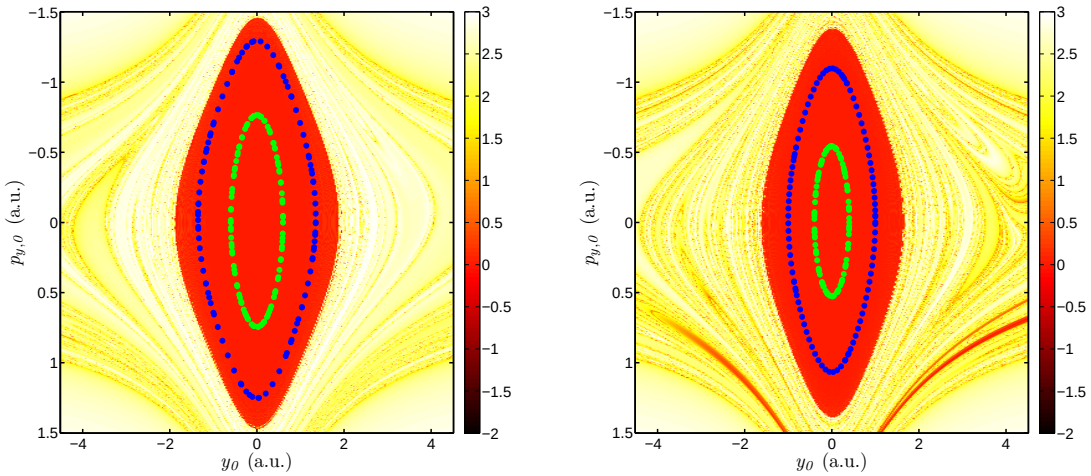

Figure 62: Laminar plots of inner electron dynamics as given by Hamiltonian (69) as a function of the initial conditions $(y_0, p_{y,0}, t = 0)$. For each initial condition, we represent the distance of the electron from the nucleus after 10 laser cycles. The distance is plotted in a logarithmic scale. In the left panel $\delta = 0$ and in the right panel $\delta = \pi$. The dashed curves are Poincaré sections of two typical trajectories in the bound region taken stroboscopically with the laser period. The parameters are $\alpha = 0.45$ and $I = 4.78 \times 10^{14}$ W cm^{-2} in both plots.

see the darker structures which spiral out). The rationale behind this dynamics is as follows: If the electron is close to the nucleus, then the Coulomb interaction dominates over the field and the electron is bound. If it is sufficiently far, the field dominates and the dynamics of the electron is unbounded, in a similar way as the outer electron. The maximum distance the inner electron can be from the nucleus while remaining bound is a function of the laser parameters.

7.3.4 Double ionization probability

Varying certain laser parameters leads to strong variations in the size of the bound region, which is pivotal in explaining the probability of double ionization. Hamiltonian (69) is not integrable. However, a close inspection of the dynamics of the inner electron in the bound region reveals that it is fairly insensitive to the field so we

consider another effective Hamiltonian in the bound region, namely

$$H_{\text{in}}^{*}\left(y,p_{y}\right)=\frac{p_{y}^{2}}{2}-\frac{2}{\sqrt{y^{2}+1}}, \tag{73}$$

which is integrable, its phase space being foliated by periodic orbits. There exists, at least locally, a canonical transformation which maps Hamiltonian (73) into action and angle variables. The action is defined by

$$A=\frac{1}{2\pi}\oint p_{y}dy.$$

When the field is present, most of the outer invariant tori are broken, whereas most of the inner ones close to the nucleus persist. We denote by $A_{m}\left(E_{0},\alpha,\delta\right)$ the action of the last invariant rotational torus which roughly corresponds to the boundary of the inner region. Figure 63 illustrates the dependence of $A_{m}\left(E_{0},\alpha,\delta\right)$ with δ as α and E_{0} are kept fixed for an intensity in the UDI regime ($I=4.78\times10^{15}$ W cm^{-2}). Numerically, we determine A_{m} by computing the volume of phase space for which the inner electron never ionizes during 2 laser cycle ramp up and 4 laser cycle plateau (see Fig. 63). At least qualitatively, the same trend is observed in the whole UDI regime (as well as the CDI regime), namely an inverted bell shape with fast variations of A_{m} around $\delta=0$ with a flattening and minimum centered around $\delta=\pi$.

An approximation to the size y_{m} of the inner region can be obtained by finding the local maximum of the effective potential (soft Coulomb potential plus laser excitation) at peak field amplitude. It is implicitly given by

$$M\left(\alpha,\delta\right)E_{0}=\frac{2y_{m}}{\left(y_{m}^{2}+1\right)^{3/2}}, \tag{74}$$

where $M(\alpha,\delta)$ is given by:

$$M\left(\alpha,\delta\right)=\max_{\tau\in[0,2\pi]}\left|\sin\tau+\alpha\sin\left(k\tau+\delta\right)\right|, \tag{75}$$

and corresponds to the peak field amplitude of the laser. In Fig. 64 we display the peak field amplitude as a function of δ. In the bound region, the energy of the inner

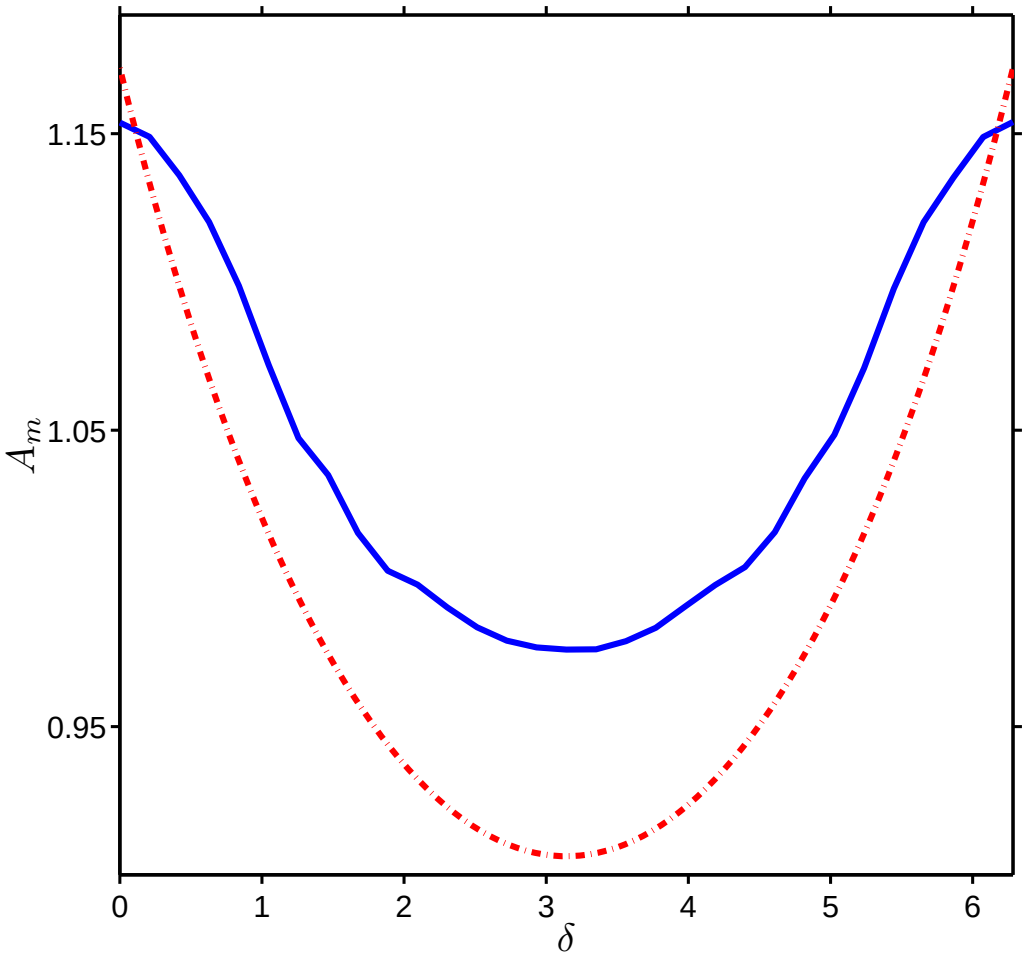

Figure 63: Action A_m of the outermost invariant torus as a function of δ for $\alpha = 0.45$ and $I = 4.78 \times 10^{14}$ W cm^{-2}. The solid line corresponds to the statistical data, while the dashed dotted line corresponds to the theoretical model, as given by Eq. (77).

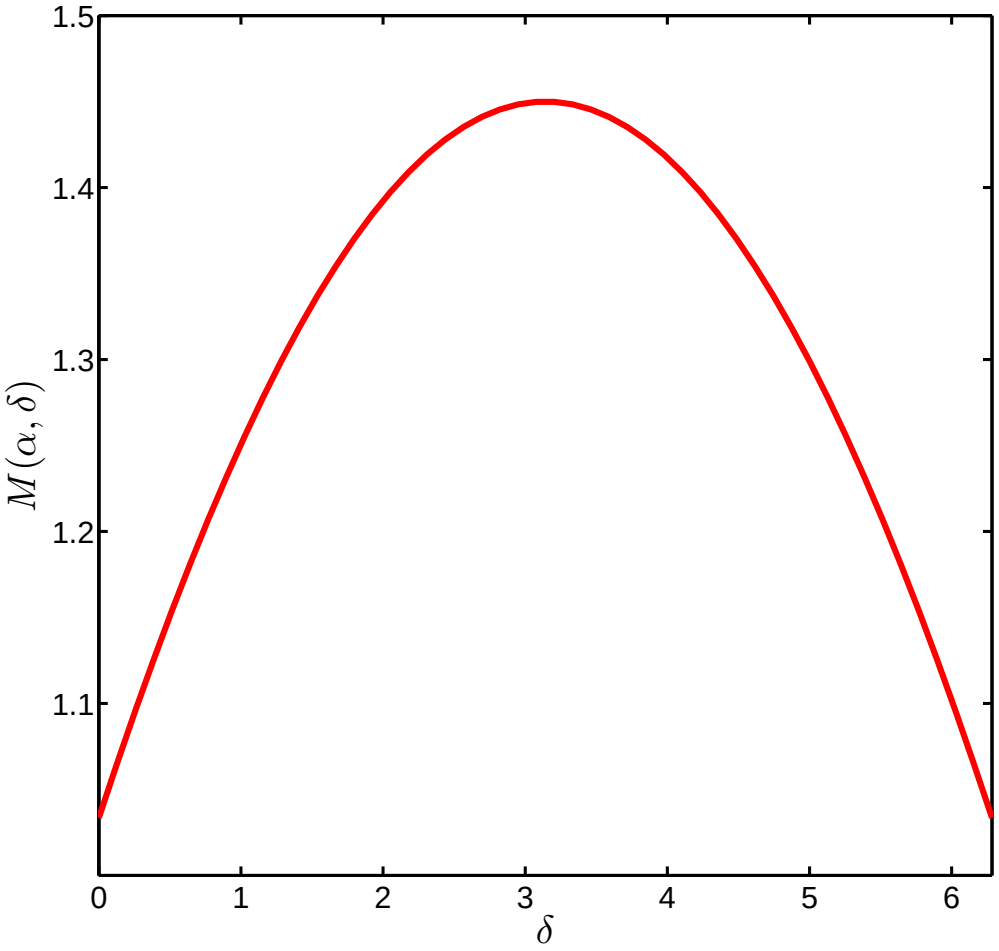

Figure 64: $M\left(\alpha = 0.45, \delta\right)$ as a function of δ, as given by Eq. (75).

electron, as defined by Eq. (69), does not vary much. Then, it is possible to relate it to the action A through the formula [76]

$$H_{\text{in}}(A) = -2 + \sqrt{2}\frac{\mathrm{e}^{\gamma A} - 1}{\gamma},$$

where $\gamma = -9\sqrt{2}/16$ (≈ -0.8). It can be inverted to express the action explicitly as a function of the energy

$$A = \frac{1}{\gamma} \ln\left(1 + \frac{\gamma}{\sqrt{2}}\left(H_{\text{in}} + 2\right)\right). \tag{76}$$

The outermost position y_m at peak field amplitude is associated with zero momentum, such that its energy H_m is equal to

$$H_m = H_{\text{in}}(y_m, 0, t_m) = -\frac{2}{\sqrt{y_m^2 + 1}} - E_0 M(\alpha, \delta)\, y_m.$$

Finally, the critical action A_m is obtained by plugging H_m into Eq. (76)

$$A_m = \frac{1}{\gamma} \ln\left(1 + \frac{\gamma}{\sqrt{2}}\left(2 - \frac{4y_m^2 + 2}{\left(y_m^2 + 1\right)^{3/2}}\right)\right), \tag{77}$$

where y_m is solution of Eq. 74. We compare this prediction with numerical evaluation of the action in Fig. 63. A careful analysis of A_m, as given by Eq. (77) shows that A_m is symmetric and minimum around $\delta = \pi$ for all α.

Sequential double ionization (UDI) corresponds to the situation when one electron is first ionized by the field, leaving the inner electron in the unbound region, so that the field sequentially ionizes the remaining electron. The amount of UDI is related to the volume of the bound region, therefore to A_m: the smaller the inner region (and thus A_m) the more likely it is for the inner electron to be found in the unbound region as well. Nonsequential (CDI) double ionization corresponds to the situation when the inner electron is first left in the inner region, and is then propelled, through a recollision, in the unbound region under the impact of the returning outer electron. As a result, it is easier for the outer electron to ionize the inner one if the bound region is small. Either way, for both CDI and UDI, we are expecting higher

double ionization probability when A_m is minimum (i.e. around $\delta = \pi$) and a strong sensitivity of the double ionization yield where A_m varies fast (i.e. around $\delta = 0$). It corresponds to what is observed in Fig. 57. The small discrepancy between $\delta = \pi$ and the actual maximum is due to nonlinear energy exchange processes during the recollision. In Fig. 61, we see that the kinetic energy of the outer electron upon return is not symmetric about $\delta = \pi$. In particular we see that the maximum return energy is rather small around π in comparison with slightly lower values of δ which explains that the maximum is expected to be slightly smaller than π.

The rate at which A_m changes with δ provides an explanation for the sensitivity of the probability to changes in δ which was discussed in Sec. 7.2.1. The action changes quickly in δ in the regions around $\delta = 0$ and slowly around $\delta = \pi$, which is the same trend observed for the rate of change in probability with δ from Fig. 57. This explains Observation 1 from the statistical analysis, in Sec. 7.2, namely that the double ionization yield is highly sensitive to the choice of phase lag.

7.3.5 Saturation of the double ionization probability

As explained before, CDI corresponds to the case where both electrons are left in the unbound region. An estimate of the size of the bound region is implicitly obtained through Eq. (74). An approximation of the amplitude of the field at which there is no inner region leads to an estimate of the intensity at which double ionization is saturated, meaning that all the trajectories double ionize. Equation (74) has a real solution if $E_0 M$ is smaller than $4/(3\sqrt{3})$ which leads to

$$E_0^{(\mathrm{t})}(\alpha, \delta) = \frac{4}{3\sqrt{3} M(\alpha, \delta)}.$$

The field is maximum for $\delta = \pi$ and its value is $M(\alpha, \pi) = 1+\alpha$. For this value of δ the critical value of the intensity at which all the trajectories double ionize is minimum. This is what is observed in Fig. 56 and 59. A numerical estimate of the range of variation of this critical intensity as a function of δ, corresponding to the amplitude

of variation of intensity between $E_0^{(t)}(\alpha, 0)$ and $E_0^{(t)}(\alpha, \pi)$ gives 1.1×10^{16} W cm^{-2} at $\alpha = 0.45$ which is what is observed in Fig. 56. A more precise approximation of the value of the intensity (as a function of the laser parameters) at which the bound region disappears is obtained by following the elliptic periodic orbit (with the period of the laser field) at the center of the elliptic island [9]. It explains Observation 2 from the statistical analysis, in Sec. 7.2, namely that the intensity of saturated double ionization greatly varies with the choice of the laser parameters.

7.3.6 Maximum of non-sequential double ionization

When one electron is bound to the nucleus after the other one has ionized, the only way through which it leaves the nucleus is by an exchange of energy with the outer electron when this one comes back to the core upon sign reversal of the laser field. Through this recollision the inner electron jumps from one invariant torus to another one (depending on the amount of energy exchanged), and it can even jump from one invariant torus to the unbound region. After it enters into the unbound region, it ionizes (solely due to the action of the field). A nonsequential double ionization corresponds to the situation when the exchange of energy allows the inner electron to jump from the bound region to the unbound one, while the outer electron keeps enough energy to remain ionized. The amount of energy exchanged as well as the size of the bound region are the two main reasons for the sensitivity of the nonsequential double ionization to changes in the parameters α and δ.

Using an equal sharing of the energy of the inner and outer electron [9], we derive a prediction for the intensity when the CDI probability is maximum. At $(y, p_y) = (0, 0)$, when the inner electron is bounded, its energy is $U_{\text{in}} = -2$, while at $(y, p_y) = (y_m, 0)$, when the inner electron is on the boundary (on the invariant torus with action A_m), its energy is $U_{\text{in}} = -2/\sqrt{y_m^2 + 1}$. This leads to a difference in energy of $\Delta\mathcal{E}_y = 2 - 2/\sqrt{y_m^2 + 1}$ which is the minimum energy required to ionize the inner electron in

one recollision. This energy comes from the outer electron, and when

$$\Delta\mathcal{E}_y = \frac{\mathcal{E}_{\max}}{2}, \tag{78}$$

the outer electron gives enough energy to ionize the inner electron (in one recollision) while keeping itself ionized as well.

The equal sharing relation can be solved in a manner very similar to the case of the one laser system [9] by making the assumption that double ionization occurs at peak field amplitude, as given by Eq. (74). Combining Eq. (78) with Eq. (74) yields the following approximation for $E_0^{(c)}$

$$E_0^{(\mathrm{c})} = \frac{4\omega}{\sqrt{\kappa}} - \left(\frac{2\omega}{\sqrt{\kappa}}\right)^{\frac{3}{2}}\sqrt{M} + \mathcal{O}\left(\left(\frac{2\omega}{\sqrt{\kappa}}\right)^{3}\right). \tag{79}$$

For numerically computed κ and M we can see from Fig. 65 that $I^{(\mathrm{c})}$ does not vary significantly with δ. Over the entire range of δ, the critical intensity $I^{(\mathrm{c})}$ varies by approximately 2×10^{14} W cm^{-2} which is compatible with the variations of $I^{(\mathrm{c})}$ as observed in Fig. 56. This variation is small compared to the variations of the laser intensity from 10^{13} to 10^{17} W cm^{-2} over the entire CDI and UDI regimes. It is also small compared to the variations of $I^{(t)}$ which are of the order of 10^{16} W cm^{-2}. It confirms Observation 3 from the statistical analysis, in Sec. 7.2, namely that the knee regime (and particularly the intensity for which CDI is maximum) is fairly insensitive to the laser parameters.

7.4 Conclusion

Using the statistical and nonlinear dynamical analysis we showed that the laser parameters α and δ can be used to control both the probabilities of double ionization and the rates of change of these probabilities both in the CDI and UDI regimes. This control acts on the outer electron by regulating the amount of energy it can bring to the core during a recollision. For the inner electron, the control depends on its stability, by changing the size of the bound area. Those two modulations act together to

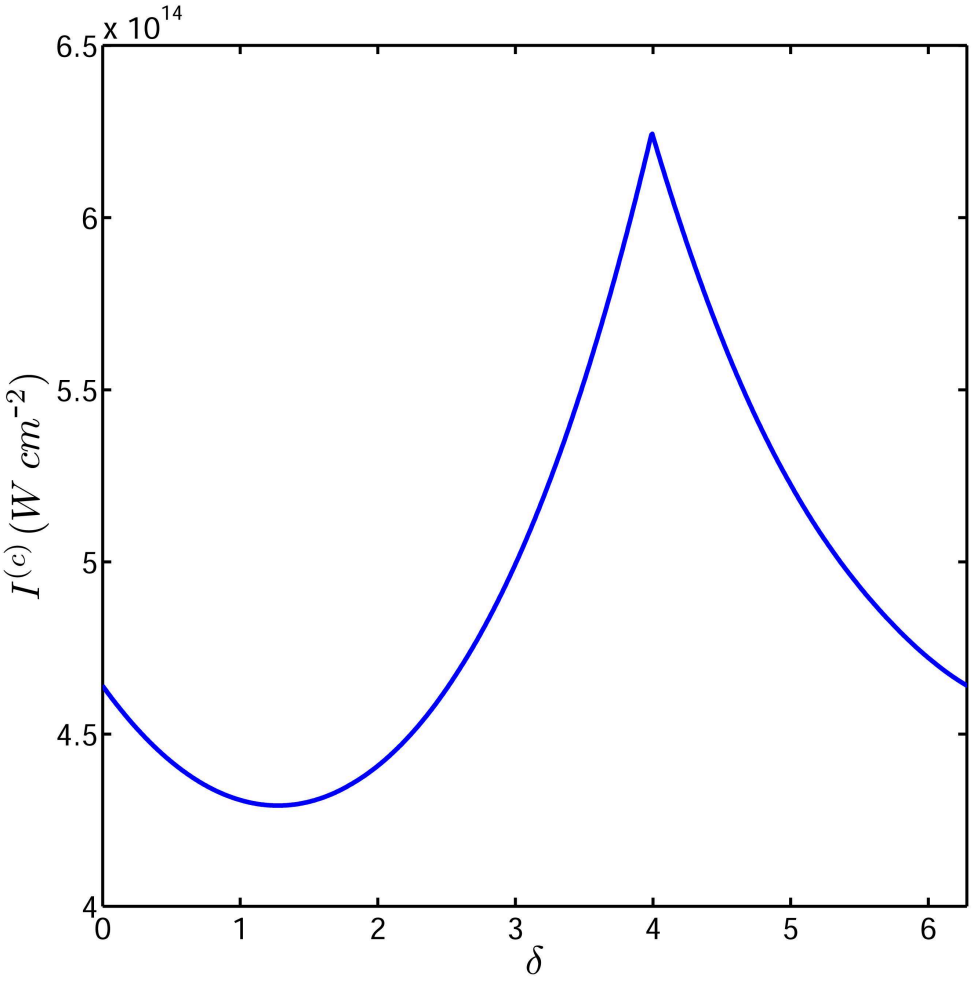

Figure 65: Expansion of $I^{(c)}$, where κ and M have been solved for numerically. For this plot $\alpha = 0.45$, $k = 3$, and $\omega = 0.0584$.

determine the double ionization probability, but it is the inner electron which has the strongest impact on its variations. In a nutshell, using the inner and outer electrons reduced models, we were able to explain the three observations obtained with the statistical analysis of the system: Namely the high sensitivity of the double ionization yield and saturation of double ionization with the choice of the laser parameters and the low sensitivity of the knee regime with the same parameters. This control helps in regulating the proportion of sequential versus nonsequential processes which occur in this atomic system.

CHAPTER VIII

CONCLUSION

The recollision scenario is at the heart of many key processes in strong field atomic physics. In this thesis, we've made use of classical, Hamiltonian models to better understand the one-electron dynamics in regards to recollisions. We've focused mainly on the ionizing and recolliding dynamics within the one-electron model; however, some time has also been spent on other aspects of the one-electron model. For example, we've investigated the non-ionizing dynamics of fullerene (Ch. 6) and also made a departure from the one-electron model by performing a statistical survey of NSDI in a two-color laser field (Ch. 7). Particular attention, however, has been paid to understanding HHG and NSDI as processes primarily dictated by recollisions. In this regard, an encompassing element of this work has been the introduction to the community of R-POs. We've shown that these "special" periodic orbits regulate the recolliding process as it pertains to recollision induced ionization and HHG.

8.1 Non-ionizing dynamics, etc.

We start by briefly recalling work performed which does not relate to HHG and NSDI. We investigated the valence electron dynamics of C_{60}, or fullerene, via a billiard model. We showed that there are several different organizing structures in phase space. Periodic orbits are responsible for the different types of very distinct electron trajectories present. Also, and perhaps more interestingly, there is a structure, known as a "meandering torus", which, by acting as a barrier in phase space, is responsible for the transition between different types of trajectories. A more complex, non-billiard, model of fullerene was also investigated. We showed that the non-ionizing dynamics are well represented by the billiard model, while the more complete model can be

useful for analyzing ionizations and subsequent recollisions.

We also performed a statistical analysis of double ionization in a Helium atom when a second laser (of a different frequency) is introduced. We showed that the inner electron dynamics are partly responsible for the effect the phase lag has on NSDI. As the phase lag is varied, the bounded region (where the inner electron resides) varies in size, making the inner electron easier (or harder) to ionize.

8.2 Recollision scenario

The recollision scenario presented in this thesis and supported in the literature (see [25]) relies on a collection of periodic orbits otherwise known as R-POs, or "recolliding periodic orbits". In the simple case of a linearly polarized field in a single spatial dimension (Ch. 3) we show that these R-POs come in a set of periodic orbits which are resonances from the perturbation of an integrable Hamiltonian. These resonant orbits control the dynamics of recolliding dynamics by acting as organizing structures in phase space. In fact, the HHG cut-off energy, dictated by the maximum return energy of the electron, is directly controlled by the unstable manifolds of the said periodic orbits. In the higher-dimensional case of a circularly polarized field we again find periodic orbits controlling the recollision process. However, due to the nature of the system (e.g. conserved quantities) each periodic orbit exists as a family parameterized by the energy.

8.3 High harmonic generation

The radiation released by a recolliding electron which recombines with the parent ion can be released as a series of high order harmonics of the driving laser field. These harmonics can be harnessed to generate atto-second duration pulses. The properties of these pulses are by large affected by the energy cut-off of the harmonic radiation. In the future, we hope to introduce additional perturbations to the R-POs (such as the addition of a second color to the laser term) to tweak the stability properties of

the orbits in hopes of increasing the maximum return energy.

8.4 Non-sequential double ionization

Non-sequential double ionization in a CP field has been investigated classically many times [25, 40, 116]. The contributions shown in this thesis pertain entirely to the recollision scenario (discussed above). Experimentally it was already known that Neon would not exhibit recollisions in a CP field [7]. The provided explanation put emphasis on the lack of a preferred direction in a CP field, resulting in an electron that is not pulled sufficiently radially inward. This explanation puts emphasis on the polarization of the field, not the properties of the atom. However, Magnesium was found to allow recollisions in CP [8]. This caused a re-thinking in the community, more than a decade ago, which has only recently begun to be settled [40, 18, 25]. In this thesis (as well as published work ([25])) we provide a classical, predictive model (Ch. 5) which explains the recollisions (or a lack thereof) in the context of R-POs. In brief, when the energy spectrum of the outer electron, which is dictated by the softening parameter, a (see Eq. 8), and the ground state energy E_g of the atom overlapped with the energies of different families of R-POs recollisions were expected. This model has proven useful not only for Neon and Magnesium, but predictions have also been made for Xenon, Argon, and the molecule fullerene.

APPENDIX A

CONCEPTS FROM NONLINEAR DYNAMICS

This section is intended to explain some of the terms from non-linear dynamics used in this thesis for readers from the AMO community. It is a brief introduction and the reader is suggested to look at [24] chapters 1-7, 11, and 13 for further details.

A.1 Hamiltonians

The Hamiltonian framework can be used to derive equations of motion for a certain class of dynamical system. For our purposes, the Hamiltonian of a particle with mass m moving in potential $V(\mathbf{q}, t)$ is expressed as the sum of the kinetic and potential energies, i.e.,

$$\mathcal{H}(\mathbf{q}, \mathbf{p}, t) = \frac{\|\mathbf{p}\|^2}{2} + V(\mathbf{q}, t), \tag{80}$$

where $\mathbf{q}$ and $\mathbf{p}$ are the canonically conjugate positions and momenta, respectively. In this situation the dimension of the system is N so that $\mathbf{q}, \mathbf{p} \in \mathbb{R}^N$. This Hamiltonian would be described as *non-autonomous* because its potential is explicitly time dependent. As a result of the time dependence the Hamiltonian is not conserved with time, i.e., $\frac{dH}{dt} \neq 0$. This can be shown by taking a derivative of the Hamiltonian w.r.t. time so that

$$\frac{dH}{dt} = \frac{\partial H}{\partial q}\dot{q} + \frac{\partial H}{\partial p}\dot{p} + \frac{\partial H}{\partial t} \tag{81}$$

where for simplicity we treat $\mathbf{q}$ and $\mathbf{p}$ as scalars. From Hamilton's equations we know that $\dot{q} = \frac{\partial H}{\partial p}$ and $\dot{p} = -\frac{\partial H}{\partial q}$ so by substituting these expressions into the above equation we show that

$$1111111\frac{dH}{dt} = \frac{\partial H}{\partial t}. \tag{82}$$

Therefore, the Hamiltonian is only conserved when $\frac{\partial H}{\partial t} = 0$, i.e. when the Hamiltonian is autonomous (no explicity time dependence) which is not the case for a system with a time dependent potential. This system would be referred to as $\left(N + \frac{1}{2}\right)$ DOF, or degrees of freedom. The N is from the dimension of the vectors $\mathbf{q}$ and $\mathbf{p}$ and the $\frac{1}{2}$ is generally used to denote the time dependence.

A Hamiltonian, however, can be *autonomized* (removing the time dependence) by the following procedure consisting of increase the dimension of phase space. First, we add to our Hamiltonian the quantity $\mathcal{E}$, which is the conjugate momenta of our new position variable t. Essentially, our goal is to increase the dimension of phase space by 2 by treating t and its conjugate $\mathcal{E}$ as additional phase space variables. In this way, t is now no different than the particle position (in real space) $\mathbf{q}$. Our new Hamiltonian

$$\mathcal{H}\left(\bar{\mathbf{q}}, \bar{\mathbf{p}}\right) = \frac{\|\mathbf{p}\|^2}{2} + V\left(\bar{\mathbf{q}}, t\right) + \mathcal{E} \tag{83}$$

where $\bar{\mathbf{q}} = (\mathbf{q}, t)$ and $\bar{\mathbf{p}} = (\mathbf{p}, \mathcal{E})$. The equations of motion for $\dot{\mathbf{q}}$ and $\dot{\mathbf{p}}$ (where the $\cdot$ denotes a time derivative w.r.t. our new evolution parameter, τ) are the same, however, we also now include $\dot{t} = \frac{\partial \mathcal{H}}{\partial \mathcal{E}} = 1$ and $\dot{\mathcal{E}} = -\frac{\partial H}{\partial t}$. In this way, by treating $(t, \mathcal{E})$ as phase space variables, the value $\mathcal{H} + \mathcal{E}$ is now conserved. We could now refer to the system as $(N + 1)$ DOF.

A.2 Jacobi values

The Jacobi value/constnat is a term used throughout the manuscript, specifically when referring to the one-electron model in a circulary polarized field. It is used to denote the energy of the system, or specifically, the value of the Hamiltonian in a rotating frame. It is used only in contexts where the Hamiltonian is autonomous and hence conserved (see above section). The name itself is borrowed from celestial mechanics, where the models and methods used are similiar (due to Coulomb/gravitational potential found in both systems).

The Jacobi value is used in this manuscript specifically for a one-electron model operating in two spatial dimensions, i.e. chapters 4 and 5. In section 4.3 of Ch. 4 we explicity show the calculation to autonomize the static frame Hamiltonian and then perform the change of variables into the rotating frame.

A.3 Integrability

The word "integrability" is used often throughout this thesis. It has a specific meaning, familiar to nonlinear dynamicists focusing on Hamiltonian systems. Put simply, when the number of independent conserved quantities (which are in involution) in the system is equal to the number of degrees of freedom the system is said to be integrable. It has nothing to do with the analytic solveability of the equations of motion. When a system is indeed integrable and configuration space is compact, we know that a canonical change of coordinates is possible (called action-angle coordinates) which allows the system to be solved quite trivially. The required transformation, however, is often difficult to compute. For integrable systems, phase space is foliated entirely by invariant tori and the dynamics is well understood. The actions are given by $A_n = \oint p_n dq_n$ such that $\mathcal{H}(\mathbf{q}, \mathbf{p}) = \mathcal{H}_0(\mathbf{A})$ with

$$\begin{aligned} \dot{\mathbf{A}} = -\frac{\partial \mathcal{H}_0}{\partial \theta} &\rightarrow \mathbf{A} = \text{const} \\ \dot{\theta} = \frac{\partial \mathcal{H}_0}{\partial \mathbf{A}} &\rightarrow \theta(t) = \theta_0 + \frac{\partial \mathcal{H}_0}{\partial \mathbf{A}} \end{aligned}$$

The solutions to the equations of motion shown above yields a dynamics which exists on a torus. The invariant tori of an integrable system are parameterized by the action, A, and the tori are invariant with respect to the dynamics because a trajectory on a given torus will remain on that torus.

A.4 Periodic orbits

It has been shown throughout this thesis that periodic orbits and other invariant objects (tori, manifolds, fixed points, etc) play an important role in organizing the

dynamics in phase space. Periodic orbits are objects that are closed loops in phase space which obey the dynamical equations of motion. The properties of periodic orbits, especially, is clarified here with attention focused on the case of Hamiltonian systems. In a canonical Hamiltonian system, the volume in phase space is conserved so for every contracting direction there must also exist an expanding direction. In order to determine the stability of an orbit, the Jacobian matrix, $\mathbf{J}$, must be solved numerically, along with the flow (Hamilton's equations). This is accomplished by solving the equation $\dot{\mathbf{J}} = \mathbf{AJ}$ with $\mathbf{J}(0) = \mathbf{I}_N$ where the matrix $\mathbf{A}$ is the stability matrix of the system (see Ch. 5 of [24]) and $\mathbf{I}_N$ is the identity matrix with N rows and columns. For a fixed point, $\mathbf{A}$ is constant and the solution for $\mathbf{J}$ is simple, however, for a periodic orbit $\mathbf{A}$ varies along the orbit and is non-constant and $\mathbf{J}$ must be computed numerically.

The eigenvalues of $\mathbf{J}$ come pair-wise in a Hamiltonian system. For a 1 DOF system, $\mathbf{J}$ is a 2×2 matrix and the eigenvalues of $\mathbf{J}$ will come in a pair. When the periodic orbit is unstable, or hyperbolic, the eigenvalues come as $(\lambda, 1/\lambda)$ with $\lambda \in \mathbb{R}$. Likewise, when the orbit is stable, or elliptic, they will come as a pair of complex conjugates with a magnitude of 1. For the one-electron mode, which is 1.5 DOF, $\mathbf{J}$ is a 4×4 matrix, since we must treat $(t, \mathcal{E})$ as a conjugate pair along with (x, p). The stability of the orbit is determined by the eigenvalues associated with the x and p directions and the t and $\mathcal{E}$ directions will have eigenvalues of unity.

Parabolicity: It is also possible for an orbit to be neither stable nor unstable. Instead, a periodic orbit can be parabolic, which means a linear analysis is insufficient to determine stability and a higher order analysis must be performed. This occurs when its eigenvalues come in pairs of 1.

Periodic orbits exist in phase space and leave their imprint on the dynamics of close by trajectories. By closeby, we mean that in phase space the trajectory itself closely follows the periodic orbit for some period of time before moving away (possibly

towards a different orbit). The amount of time a trajectory will spend closeby a periodic orbit (and what "closeby" means in this sense) depend entirely on the properties of the periodic orbit. For very unstable periodic orbits, their affect on the dynamics is limited because trajectories must get exceedingly close to the orbit to feel its effects, otherwise the trajectory is pulled away very quickly in the unstable direction(s) of the periodic orbit. Typically, stable orbits are not interesting because trajectories simply stay closeby the orbit, repeating the same motion. Typically, slightly unstable orbits are the most interesting, allowing the trajectory to be influenced by the periodic orbit.

A.4.1 Role of manifolds in the dynamics

Unstable periodic orbits have stable ($\mathcal{W}^s$) and unstable ($\mathcal{W}^u$). The stable manifold is the collection of points in phase space, that when evolved forward in time move toward the periodic orbit. Likewise, the unstable manifold is the collection of points in phase space which move toward the periodic orbit when evolved backward in time.

REFERENCES

[1] Atomic data are taken from the NIST website urlhttp://physics.nist.gov/PhysRefData/Handbook/periodictable.htm.

[2] A. l'Huillier and Ph. Balcou. High-order harmonic generation in rare gases with a 1-ps 1053-nm laser. *Phys. Rev. Lett.*, 70:774–777, 1993.

[3] B. Walker, B. Sheehy, L. F. DiMauro, P. Agostini, K. J. Schafer, and K. C. Kulander. Precision measurement of strong field double ionization of helium. *Phys. Rev. Lett.*, 73(9):1227–1230, 1994.

[4] Paul Corkum and Ferenc Krausz. Attosecond science. *Nature Physics*, 3, 2007.

[5] Matthias F. Kling and Marc J.J. Vrakking. Attosecond electron dynamics. *Ann. Rev. Phys. Chem.*, 59:463, 2008.

[6] P. B. Corkum. Plasma perspective on strong field multiphoton ionization. *Phys. Rev. Lett.*, 71(13):1994–1997, 1993.

[7] D. N. Fittinghoff, P. R. Bolton, B. Chang, and K. C. Kulander. Polarization dependence of the tunneling ionization of helium and neon by 120-fs pulses at 614nm. *Phys. Rev. A*, 49(3):2174, 1994.

[8] G. D. Gillen, M. A. Walker, and L. D. Van Woerkom. Enhanced double ionization with circularly polarized light. *Phys. Rev. A*, 64:043413, 2001.

[9] François Mauger, Cristel Chandre, and Turgay Uzer. Strong field double ionization: The phase space perspective. *Phys. Rev. Lett.*, 102(17):173002, 2009.

[10] I .V. Hertel, T. Laarmann, and C. P. Schulz. Ultrafast excitation, ionization and fragmentation of C_{60}. *Adv. At. Mol. Opt. Phys.*, 50:219–286, 2005.

[11] John M. Greene. A method for determining a stochastic transition. *J. Math. Phys.*, 20:1183, 1979.

[12] Ihar Shchatsinin, Tim Laarmann, Gero Stibenz, Günter Steinmeyer, Andrei Stalmashonak, Nick Zhavoronkov, Claus Peter Schulz, and Ingolf V. Hertel. c_{60} in intense short pulse laser fields down to 9 fs: Excitation on time scales below e-e and e-phonon coupling. *J. Chem. Phys.*, 125(194320):194320, 2006.

[13] W. Becker and H. Rottke. Many-electron strong-field physics. *Contemporary Physics*, 49(3):199–223, 2008.

[14] K. J. Schafer, Baorui Yang, L. F. DiMauro, and K. C. Kulander. Above threshold ionization beyond the high harmonic cutoff. *Phys. Rev. Lett.*, 70(11):1599–1602, 1993.

[15] M. Tu Kuchiev. Atomic antenna. *JETP Lett.*, 45:404–406, 1987.

[16] Phay J. Ho, R. Panfili, S. L. Haan, and J. H. Eberly. Nonsequential double ionization as a completely classical photoelectric effect. *Phys. Rev. Lett.*, 94(9):093002, 2005.

[17] Tenio Popmintchev, Ming-Chang Chen, Dimitar Popmintchev, Paul Arpin, Susannah Brown, Skirmantas Alisauskas, Giedrius Andriukaitis, Tadas Balciunas, Oliver D. Mucke, Audrius Pugzlys, Andrius Baltuska, Bonggu Shim, Samuel E. Schrauth, Alexander Gaeta, Carlos Hernandez-Garcia, Luis Plaja, Andreas Becker, Agnieszka Jaron-Becker, Margaret M. Murnan, and Henry C. Kapteyn. Bright coherent ultrahigh harmonics in the kev x-ray regime from mid-infrared femtosecond lasers. *Science*, 336:1287–1291, 2012.

[18] Paul B. Corkum. Recollision physics. *Phys. Today*, 64(3):36, 2011.

[19] C. Figueira de Morisson Faria and X. Liu. Electron-electron correlation in strong laser fields. *J. Modern. Opt.*, 58:1076–1131, 2011.

[20] D. Farrelly and T. Uzer. Ionization mechanism of Rydberg atoms in a circularly polarized microwave field. *Phys. Rev. Lett.*, 74(10):1720, 1995.

[21] J. C. Keck. Variational theory of reaction rates. *Adv. Chem. Phys.*, 13:85, 1967.

[22] T Uzer, C Jaffé, J Palacián, P Yanguas, and S Wiggins. The geometry of reaction dynamics. *nonlinearity*, 15(4):957–992, 2002.

[23] Charles Jaffé, Shinnosuke Kawai, Jesús Palacián, Patricia Yanguas, and Turgay Uzer. A new look at the transition state: Wigner's dynamical perspective revisited. *Adv. Chem. Phys.*, 130A:171–216, 2005.

[24] P. Cvitanović, R. Artuso, R. Mainieri, G. Tanner, and G. Vattay. *Chaos: Classical and Quantum*. Niels Bohr Institute, Copenhagen, 2008.

[25] A. Kamor, F. Mauger, C. Chandre, and T. Uzer. How key periodic orbits drive recollisions in a circularly polarized laser field. *Phys. Rev. Lett.*, 110:253002, 2013.

[26] Haruo Yoshida. Construction of high order symplectic integrators. *Physics Letters A*, 150(5,6,7):262, 1990.

[27] J. Javanainen, J. H. Eberly, and Qichang Su. Numerical simulations of multiphoton ionization and above-threshold electron spectra. *Phys. Rev. A*, 38(7):3430–3446, 1988.

[28] R. Panfili, J. H. Eberly, and S. L. Haan. Comparing classical and quantum dynamics of strong-field double ionization. *Opt. Express*, 8(7):431–435, 2001.

[29] A.J. Lichtenberg and M.A. Lieberman. *Regular and Stochastic Motion*. Applied Mathematical Sciences. Springer-Verlag, New York, 1983.

[30] V.I. Arnold. Proof of a theorem of A.N. Kolmogorov on the invariance of quasi-periodic motions under small perturbations of the Hamiltonian. *Russ. Math. Surv.*, 18:9–36, 1963.

[31] J. Moser. On invariant curves of area-preserving mappings of an annulus. *Nachr. Akad. Wiss. Goett., Math.-Phys. Kl. IIa*, 1:1–20, 1962.

[32] A.N. Kolmogorov. On the conservation of quasi-periodic motions for a small change in the Hamiltonian function. *Dokl. Akad. Nauk SSSR*, 98:527–530, 1954. (in russian).

[33] F. Mauger, C. Chandre, and T. Uzer. Dynamics of recollisions for the double ionization of atoms in intense laser fields. *Phys. Rev. A*, 81(6):063425, 2010.

[34] G.D. Birkhoff. On the periodic motion of dynamical systems. *Acta Mathematica*, 50:359–379, 1927.

[35] F. Mauger, A. Kamor, C. Chandre, and T. Uzer. Mechanism of delayed double ionization in a strong laser field. *Phys. Rev. Lett.*, 108:063001, 2012.

[36] F. Mauger, A. Kamor, C. Chandre, and T. Uzer. Delayed double ionization as a signature of hamiltonian chaos. *Phys. Rev. E*, 85:066205, 2012.

[37] S. Haessler, J. Caillat, and P. Salières. Self-probing of molecules with high harmonic generation. *J. Phys. B.*, 44:203001, 2011.

[38] P. Agostini and L.F. Dimauro. Atoms in high intensity mid-infrared pulses. *Contemporary Physics*, 49:179–197, 2010.

[39] Manfred Lein. Molecular imaging using recolliding electrons. *J. Phys. B.*, 40:135–173, 2007.

[40] F. Mauger, C. Chandre, and T. Uzer. Recollisions and correlated double ionization with circularly polarized light. *Phys. Rev. Lett.*, 105(8):083002, 2010.

[41] Xu Wang and J. H. Eberly. Elliptical polarization and probability of double ionization. *Phys. Rev. Lett.*, 105:083001, 2010.

[42] L. B. Fu, G. G. Xin, D. F. Ye, and J. Liu. Recollision dynamics and phase diagram for nonsequential double ionization with circularly polarized laser fields. *Phys. Rev. Lett.*, 108:103601, 2012.

[43] Charles W. Clark, Eric Korevaar, and Michael G. Littman. Quasi-penning resonances of a Rydberg electron in crossed electric and magnetic fields. *Phys. Rev. Lett.*, 54(4):320–322, 1985.

[44] J. E. Howard. Saddle-point ionization and the Runge-Lenz invariant. *Phys. Rev. A*, 51(5):3934–3946, 1995.

[45] Wilhelm Becker, XiaoJun Liu, Phay Jo Ho, and Joseph H. Eberly. Theories of photoelectron correlation in laser-driven multiple atomic ionization. *Rev. Mod. Phys.*, 84:1011–1043, 2012.

[46] Xu Wang and J. H. Eberly. Elliptical trajectories in nonsequential double ionization. *New J. Phys.*, 12:093047, 2010.

[47] C. Guo, M. Li, J. P. Nibarger, and G. N. Gibson. Single and double ionization of diatomic molecules in strong laser fields. *Phys. Rev. A*, 58:R4271–R4274, 1998.

[48] Chunlei Guo and George N. Gibson. Ellipticity effects on single and double ionization of diatomic molecules in strong laser fields. *Phys. Rev. A*, 63:040701, 2001.

[49] L. Forró and L. Mihály. Electronic properties of doped fullerenes. *Rep. Prog. Phys.*, 64:649–699, 2001.

[50] I. V. Hertel, I. Shchatsinin, T. Laarmann, N. Zhavoronkov, H.-H. Ritze, and C. P. Schulz. Fragmentation and ionization dynamics of C_{60} in elliptically polarized femtosecond laser fields. *Phys. Rev. Lett.*, 102(2):023003, 2009.

[51] V. R. Bhardwaj, P. B. Corkum, and D. M. Rayner. Recollision during the high laser intensity ionization of C_{60}. *Phys. Rev. Lett.*, 93:043001, 2004.

[52] G. W. Hill. Researches in the lunar theory. *Am. J. Math.*, 1:5, 1878.

[53] E. Doron and S.D. Frischat. Semiclassical description of tunneling in mixed systems: Case of the annular billiard. *Phys. Rev. Lett.*, 75:3661–3664, 1995.

[54] A. Kohler and R. Blümel. Annular ray-splitting billiard. *Phys. Lett. A*, 238:271–277, 1998.

[55] R. W. Robinett. Periodic orbit theory analysis of the circular disk or annular billiard: Nonclassical effects and the distribution of energy eigenvalues. *Am. J. Phys.*, 67:67–77, 1999.

[56] C. Dembowski, H.-D. Gräf, A. Heine, R. Hofferbert, H. Rehfeld, and A. Richter. First experimental evidence of chaos-assisted tunneling in a microwave annular billiard. *Phys. Rev. Lett.*, 84:867–870, 2000.

[57] M. Hentschel and K. Richter. Quantum chaos in optical system: The annular billiard. *Phys. Rev. E*, 66:056207, 2002.

[58] G. Gouesbet, S. Meunier-Guttin-Cluzel, and G. Grehan. Periodic orbits in hamiltonian chaos of the annular billiard. *Phys. Rev. E*, 65:016212, 2001.

[59] R. E. de Carvalho, F. C. Souza, and E. D. Leonel. Fermi acceleration on the anular billiard. *Phys. Rev. E*, 73:066229, 2006.

[60] R. E. de Carvalho, F. C. de Souza, and E. D. Leonel. Fermi acceleration on the anular billiard: a simplified version. *J. Phys. A.*, 39:3561–3573, 2006.

[61] M. Robnik and M. V. Berry. Classical billiards in magnetic fields. *J. Phys. A.*, 18:1361–1378, 1985.

[62] O. Meplan, F. Brut, and C. Gignoux. Tangent map for classical billiards in magnetic fields. *J. Phys. A.*, 26:237–246, 1993.

[63] H. Kunz and N. Berglund. Integrability and ergodicity of classical billiards in a magnetic field. *J. Stat. Phys.*, 83:81–126, 1996.

[64] L. G. G. V. Dias da Silva and M. A. M. de Aguiar. Periodic orbits in magnetic billiards. *Eur. Phys. B.*, 16:719–728, 2000.

[65] M. Aichinger, S. Janecek, and E. Räsänen. Billiards in magnetic fields: A molecular dynamics approach. *Phys. Rev. E*, 81:016703, 2010.

[66] P. J. Morrison and A. Wurm. Nontwist maps. *Scholarpedia*, 4(9):3551, 2009.

[67] D. del Castillo-Negrete, J. M. Greene, and P. J. Morrison. Area preserving nontwist maps: periodic orbits and transition to chaos. *Physica D.*, 91:1–23, 1996.

[68] P. J. Morrison. Magnetic field lines, hamiltonian dynamics, and nontwist systems. *Phys. Plasmas*, 7:2279–2289, 2000.

[69] J. Laskar. Frequency analysis for multi-dimensional systems. global dynamics and diffusion. *Physica D*, 67:257–281, 1993.

[70] M. J. Puska and R. M. Nieminen. Photoabsorption of atoms inside c_{60}. *Phys. Rev. A*, 47:1181–1186, 1993.

[71] D. Bauer, F. Ceccherini, A. Macchi, and F. Cornolti. c_{60} in intense femtosecond laser pulses: Nonlinear dipole response and ionization. *Phys. Rev. A*, 64:063203, 2001.

[72] M. Ruggenthaler, S. V. Popruzhenko, and D. Bauer. Recollision-induced plasmon excitation in strong laser fields. *Phys. Rev. A*, 78:033413, 2008.

[73] A. S. Baltenkov, U. Becker, and A. Z. Msezane. Effects of fullerene (c_{60}) potential and position of the atom (a) on spectral characteristics of endohedral atoms a@c_{60}. *J. Phys. B.*, 43:115102, 2010.

[74] Y. B. Xu, M. Q. Tan, and U. Becker. Oscillations in the photoionization cross section of c_{60}. *Phys. Rev. Lett.*, 76:3538–3541, 1996.

[75] E. Tosatti and N. Manini. Anomalous attachment of low-energy electrons to c_{60}. *Chem. Phys.Lett.*, 223:61–64, 1994.

[76] F. Mauger, C. Chandre, and T. Uzer. From recollisions to the knee: A road map for double ionization in intense laser fields. *Phys. Rev. Lett.*, 104(4):043005, 2010.

[77] D. N. Fittinghoff, P. R. Bolton, B. Chang, and K. C. Kulander. Observation of nonsequential double ionization of helium with optical tunneling. *Phys. Rev. Lett.*, 69(18):2642–2645, 1992.

[78] Th. Weber, H. Giessen, M. Weckenbrock, G. Urbasch, A. Staudte, L. Spielberger, O. Jagutzki, V. Mergel, M. Vollmer, and R. Dörner. Correlated electron emission in multiphoton double ionization. *Nature*, 405:658–661, 2000.

[79] K. Kondo, A. Sagisaka, T. Tamida, Y. Nabekawa, and S. Watanabe. Wavelength dependence of nonsequential double ionization in he. *Phys. Rev. A*, 48(4):R2531–R2533, 1993.

[80] S. Larochelle, A. Talebpour, and S. L. Chin. Non-sequential multiple ionization of rare gas atoms in a ti: Sapphire laser field. *J. Phys. B.*, 31:1201–1214, 1998.

[81] C. Cornaggia and Ph. Hering. Nonsequential double ionization of small molecules induced by a femtosecond laser field. *Phys. Rev. A*, 62(2):023403, 2000.

[82] Merrick J. DeWitt, E. Wells, and R. R. Jones. Ratiometric comparison of intense field ionization of atoms and diatomic molecules. *Phys. Rev. Lett.*, 87:153001, 2001.

[83] J. Rudati, J. L. Chaloupka, P. Agostini, K. C. Kulander, and L. F. DiMauro. Multiphoton double ionization via field-independent resonant excitation. *Phys. Rev. Lett.*, 92:203001, 2004.

[84] Andreas Becker and Farhad H. M. Faisal. Mechanism of laser-induced double ionization of helium. *J. Phys. B.*, 29:L197, 1996.

[85] A. Becker and F. H. M. Faisal. Interplay of electron correlation and intense field dynamics in the double ionization of helium. *Phys. Rev. A*, 59(3):R1742–R1745, 1999.

[86] J. B. Watson, A. Sanpera, D. G. Lappas, P. L. Knight, and K. Burnett. Nonsequential double ionization of helium. *Phys. Rev. Lett.*, 78(10):1884–1887, 1997.

[87] Demetris G. Lappas and Robert van Leeuwen. Electron correlation effects in the double ionization of he. *J. Phys. B.*, 31:L249, 1998.

[88] R. Panfili and W.-C. Liu. Resonances in the double-ionization signal of two-electron model atoms. *Phys. Rev. A*, 67(4):043402, 2003.

[89] M. Lein, E. K. U. Gross, and V. Engel. Intense-field double ionization of helium: Identifying the mechanism. *Phys. Rev. Lett.*, 85(22):4707–4710, 2000.

[90] B. Feuerstein, R. Moshammer, D. Fischer, A. Dorn, C. D. Schröter, J. Deipenwisch, J. R. Crespo Lopez-Urrutia, C. Höhr, P. Neumayer, J. Ullrich, H. Rottke, C. Trump, M. Wittmann, G. Korn, and W. Sandner. Separation of recollision mechanisms in nonsequential strong field double ionization of ar: The role of excitation tunneling. *Phys. Rev. Lett.*, 87(4):043003, 2001.

[91] Li-Bin Fu, Jie Liu, Jing Chen, and Shi-Gang Chen. Classical collisional trajectories as the source of strong-field double ionization of helium in the knee regime. *Phys. Rev. A*, 63:043416, 2001.

[92] J. Chen, J. H. Kim, and C. H. Nam. Frequency dependence of non-sequential double ionization. *J. Phys. B.*, 36(4):691, 2003.

[93] Thomas Brabec, Misha Yu. Ivanov, and Paul B. Corkum. Coulomb focusing in intense field atomic processes. *Phys. Rev. A*, 54(4):R2551–R2554, 1996.

[94] Krzysztof Sacha and Bruno Eckhardt. Pathways to double ionization of atoms in strong fields. *Phys. Rev. A*, 63(4):043414, 2001.

[95] Phay J. Ho and J. H. Eberly. Classical effects of laser pulse duration on strong-field double ionization. *Phys. Rev. Lett.*, 95(19):193002, 2005.

[96] R. Panfili, S. L. Haan, and J. H. Eberly. Slow-down collisions and nonsequential double ionization in classical simulations. *Phys. Rev. Lett.*, 89(11):113001, 2002.

[97] J. Liu, D. F. Ye, J. Chen, and X. Liu. Complex dynamics of correlated electrons in molecular double ionization by an ultrashort intense laser pulse. *Phys. Rev. Lett.*, 99:013003, 2007.

[98] Fritz Ehlotzky. Atomic phenomena in bichromatic laser fields. *Phys. Rep.*, 345(4):175–264, 2001.

[99] Moshe Shapiro and Paul Brumer. *Principles of the Quantum Control of Molecular Processes*. Wiley-VCH, 2003.

[100] L. Ko, M. W. Noel, J. Lambert, and T. F. Gallagher. Two-mode multiphoton transitions. *J. Phys. B.*, 32(14):3469–3483, 1999.

[101] J. E. Howard. Theory of two-frequency microwave ionization of hydrogen atoms. *Phys. Lett. A*, 156(6):286–292, 1991.

[102] A. Haffmans, R. Blümel, P. M. Koch, and L. Sirko. Prediction of a new peak in two-frequency microwave "ionization" of excited hydrogen atoms. *Phys. Rev. Lett.*, 73(2):248–251, 1994.

[103] David Petrosyan and P. Lambropoulos. Phase control of photoabsorption in optically dense media. *Phys. Rev. Lett.*, 85(9):1843–1846, 2000.

[104] M. Ivanov, P. B. Corkum, T. Zuo, and A. Bandrauk. Routes to control of intense-field atomic polarizability. *Phys. Rev. Lett.*, 74(15):2933–2936, 1995.

[105] L. Sirko, S. A. Zelazny, and P. M. Koch. Use of the relative phase in a bichromatic field pulse to control a quasienergy gap. *Phys. Rev. Lett.*, 87(4):043002, 2001.

[106] Leszek Sirko and Peter M. Koch. Control of common resonances in bichromatically driven hydrogen atoms. *Phys. Rev. Lett.*, 89(27):274101, 2002.

[107] Victor S. Batista and Paul Brumer. Coherent control in the presence of intrinsic decoherence: Proton transfer in large molecular systems. *Phys. Rev. Lett.*, 89(14):143201, 2002.

[108] P. M. Koch, S. A. Zelazny, and L. Sirko. Dependence on relative phase for bichromatically driven atoms. *J. Phys. B.*, 36(24):4755–4772, 2003.

[109] C. Rangan, A. M. Bloch, C. Monroe, and P. H. Bucksbaum. Control of trapped-ion quantum states with optical pulses. *Phys. Rev. Lett.*, 92(11):113004, 2004.

[110] V. Constantoudis and C. A. Nicolaides. Stabilization and relative phase effects in a dichromatically driven diatomic morse molecule: Interpretation based on nonlinear classical dynamics. *J. Chem. Phys.*, 122(8):084118, 2005.

[111] Seung Min Park, Shao-Ping Lu, and Robert J Gordon. Coherent laser control of the resonance-enhanced multiphoton ionization of hcl. *The Journal of chemical physics*, 94:8622, 1991.

[112] Andrea D. Bandrauk, Szczepan Chelkowski, and Sebastien Goudreau. Control of harmonic generation using two-colour femtosecond-attosecond laser fields: quantum and classical perspectives. *J. Mod. Opt.*, 52:411 – 428, 2005.

[113] Andreas Assion, T Baumert, M Bergt, T Brixner, B Kiefer, V Seyfried, M Strehle, and G Gerber. Control of chemical reactions by feedback-optimized phase-shaped femtosecond laser pulses. *Science*, 282(5390):919–922, 1998.

[114] Gabriel G Carlo, Giuliano Benenti, Giulio Casati, and Dima L Shepelyansky. Quantum ratchets in dissipative chaotic systems. *Physical review letters*, 94(16):164101, 2005.

[115] S. L. Haan, R. Grobe, and J. H. Eberly. Numerical study of autoionizing states in completely correlated two-electron systems. *Phys. Rev. A*, 50(1):378–391, 1994.

[116] X. Wang and J.H. Eberly. Effects of elliptical polarization on strong field short pulse double ionization. *Phys. Rev. Lett.*, 103:103007, 2009.

VITA

Adam Kamor was born and raised in Atlanta, Ga. He received a B.Sc. in Physics from Georgia Tech in 2009, and then immediatley began his PhD in physics at the same university. He has been working with Drs. Turgay Uzer and Cristel Chandre since the summer after his undergraduate graduation and it is this work which has matured and developed into this thesis. In addition to his love of physics, he has a passion for motorcycle repair and restoration.